

NOTE TO USERS

This reproduction is the best copy available.

UMI[®]

University of Alberta

**Effect of Welding Parameters on the Plasma Transferred Arc Welding (PTAW) Process
for Autogenous Beads and 410SS-WC Overlays**

by

Matthew Allen Russell Yarmuch



A thesis submitted to the Faculty of Graduate Studies and Research in partial fulfillment of
the requirements for the degree of Master of Science

in

Welding Engineering

Department of Chemical and Materials Engineering

Edmonton, Alberta

Fall 2005



Library and
Archives Canada

Bibliothèque et
Archives Canada

Published Heritage
Branch

Direction du
Patrimoine de l'édition

395 Wellington Street
Ottawa ON K1A 0N4
Canada

395, rue Wellington
Ottawa ON K1A 0N4
Canada

Your file *Votre référence*

ISBN: 0-494-09319-6

Our file *Notre référence*

ISBN: 0-494-09319-6

NOTICE:

The author has granted a non-exclusive license allowing Library and Archives Canada to reproduce, publish, archive, preserve, conserve, communicate to the public by telecommunication or on the Internet, loan, distribute and sell theses worldwide, for commercial or non-commercial purposes, in microform, paper, electronic and/or any other formats.

The author retains copyright ownership and moral rights in this thesis. Neither the thesis nor substantial extracts from it may be printed or otherwise reproduced without the author's permission.

AVIS:

L'auteur a accordé une licence non exclusive permettant à la Bibliothèque et Archives Canada de reproduire, publier, archiver, sauvegarder, conserver, transmettre au public par télécommunication ou par l'Internet, prêter, distribuer et vendre des thèses partout dans le monde, à des fins commerciales ou autres, sur support microforme, papier, électronique et/ou autres formats.

L'auteur conserve la propriété du droit d'auteur et des droits moraux qui protègent cette thèse. Ni la thèse ni des extraits substantiels de celle-ci ne doivent être imprimés ou autrement reproduits sans son autorisation.

In compliance with the Canadian Privacy Act some supporting forms may have been removed from this thesis.

Conformément à la loi canadienne sur la protection de la vie privée, quelques formulaires secondaires ont été enlevés de cette thèse.

While these forms may be included in the document page count, their removal does not represent any loss of content from the thesis.

Bien que ces formulaires aient inclus dans la pagination, il n'y aura aucun contenu manquant.


Canada

Abstract

The influence of welding parameters on the plasma transferred arc welding (PTAW) process was investigated. Autogenous welds (i.e., no added material) were completed with variations in heat input, plate chemistry, and welding gases. An operating map was produced that identified operating zones and regions where fusion flaws formed. A weld bead humping phenomenon was observed and investigated; the effects of minor alloying elements and welding gas compositions are discussed. Next, an understanding of process behaviour was sought for PTA overlay welding of martensitic 410 stainless steel, with and without tungsten carbide, as the cladding material. Using argon for the plasma, carrier, and shielding gases, standard operating conditions were determined by optimizing the torch motion, arc energy, and powder delivery. Gas compositions were then varied with additions of helium, hydrogen, nitrogen and carbon dioxide. The changes in the effective heat input, oxidation/reduction behaviour and weld bead formation were recorded with video photography.

Acknowledgment

I would like to acknowledge and thank Dr Barry Patchett for inspiring me to enter graduate school and complete research in the area of welding engineering. Your guidance, knowledge, and experience were instrumental in completing this project. A special thanks goes to Dr Doug Ivey for his constant support and guidance during the day-to-day experiments and data analysis. Thanks to Clark Bicknell for sharing his practical welding knowledge and experience.

Financial support provided to this project by the Natural Sciences and Engineering Research Council (NSERC) of Canada and Syncrude Canada Ltd. is gratefully acknowledged.

Special thanks goes to the Syncrude Canada for allowing me to use their research facilities. In particular, thank you to Shane Hoskins, Stefano Chiovelli, Mike Anderson, and the rest of the Materials and Equipment Group for their guidance and mentorship. Special acknowledgment is given to Robert Skwarok for his assistance in completing the video photography.

I would like to personally thank my parents and family for their unwavering support throughout this experience. Finally, a very special thanks goes to my fiancée Audra for her unequivocal encouragement and patience during my studies.

Table of Contents

Chapter 1 – Introduction and History	1
1.1 History of Joining and Welding	1
1.2 Overview of Welding Processes and Energy Sources	4
1.3 Overall Project Objectives and Scope.....	6
Chapter 2 – General Literature Review	7
2.1 Arc Physics Review	7
a. Importance of Arc Physics to Welding.....	7
b. The Welding Arc Column.....	8
c. Operating Modes for Thermionic Arcs.....	15
d. Non-Thermionic Electron Emission	16
e. Plasma Jet Phenomenon.....	18
f. Electric Arc Power Sources	20
2.2 Arc Welding Process.....	22
a. Gas Tungsten Arc Welding Process (GTAW).....	22
b. Gas Metal Arc Welding (GMAW)	24
c. Plasma Transferred Arc Welding (PTAW).....	28
2.3 Welding Gases and Properties	36
a. Importance to Arc Welding	36
b. Welding Gas Properties	37
2.4 General Literature Review Summary	47
CHAPTER 3 – Part 1: PTAW Autogenous Welding	48
3.1 Project Objectives	48

3.2	Previous Investigations of PTAW	48
3.3	Summary	52
3.4	Materials and Equipment	53
	a. Materials	53
	b. Equipment	57
	c. Metallurgical Samples	59
	d. Calibration of equipment	61
3.5	Experimental Procedure and Results	67
	a. Heat Input Variations	67
	b. Humping Flaw Mechanism Investigation	71
	c. Autogenous Operating Maps	74
	d. Plate Chemistry and Doping Experiments	79
3.6	Discussion	83
	a. Comparison of Heat Input Equation vs. Operating Map	83
	b. Weld Bead Humping	85
	c. Effect of Plate Chemistry on the Humping Mechanism	95
	d. Effect of Welding Gas Composition	107
3.7	Conclusions	113
3.8	Recommendations for Future Work	116
CHAPTER 4 – Part 2: PTA Welding of MMC Overlays		117
4.1	Project Objectives	117
4.2	Literature Review	118
	a. Metal Matrix Composites	118
	b. Wear Applications in the Alberta Oil Sands	119

c.	Comparison of MMC Surfacing Techniques	120
d.	Previous Studies for PTAW Surfacing	124
4.3	Summary	134
4.4	Materials and Equipment	135
a.	Material	135
b.	Equipment	135
c.	Metallurgical Samples	136
d.	Calibration of Equipment	138
4.5	Experimental Procedure and Results	140
a.	Introduction	140
b.	Developing Standard Welding Conditions	141
c.	Gas Composition Variations	143
4.6	Discussion	160
a.	Optimizing Overlay Process Parameters	160
b.	Effect of Gas Composition on Overlay Welding of 410SS	169
c.	Effect of Tungsten Carbide Additions	176
4.7	Conclusions	183
4.8	Recommendations for Future Work	186
Chapter 5 – Summary of Overall Work		189
References		190

List of Tables

Table 1 – AWS Designations for Welding Processes.....	5
Table 2 – Chemical and Physical Properties of Common Arc Shielding Gases	36
Table 3 – Enthalpy and Entropy Changes for Dissociations Reactions	41
Table 4 – Chemical Analysis of Grade 300W Structural Steel	54
Table 5 - Chemical Analysis of Grade 80 Structural Steel - Heat #1	55
Table 6 - Chemical Analysis of Grade 80 Structural Steel – Heat #2	55
Table 7 – Calibration Runs for CNC Welding Table	61
Table 8 –Variability in Actual Welding Speed of the CNC Welding Table	61
Table 9 – Standard GCF Values for Nitrogen Basis.....	65
Table 10 - GCF Values for Gas Mixtures Relative to Nitrogen and Argon	65
Table 11 – Heat Input Welding Parameters.....	67
Table 12 – Welding Parameters for Weld Flaw Investigations	71
Table 13 – Welding Parameters of Autogenous Operating Map.....	76
Table 14 – Experimental Observations of Other Welding Parameters.....	77
Table 15 – Differences in Autogenous Bead Behaviour and Steel Chemistry	79
Table 16 – Welding Parameters for Doping Experiments.....	80
Table 17 – Comparison of Actual Hump Spacing to Capillary Instability Methods.....	92
Table 18 – Survey of PTAW Surfacing MMC Powders	131
Table 19 - Survey of PTAW Surfacing Arc Energy and Powder Feed Rates	132
Table 20 - Survey of PTAW Surfacing Gas Compositions and Flow Rates	133
Table 21 – Nominal Composition of Eutroloy 16410 Powder	135
Table 22 – PTAW Surfacing Parameters.....	140

Table 23 – Welding Parameters Variations of 410SS Powder Material.....	141
Table 24 - Standard Welding Parameters, Cross-section, and Bead Profile for 410SS..	142
Table 25 - Standard Welding Parameters, Cross-section, and Bead Profile for 410SS-WC MMC.....	142
Table 26 – Gas Testing Matrix for 410SS Overlay Welding.....	144
Table 27 – Gas Testing Matrix for 410SS-WC MMC Welding.....	144
Table 28 – Summary of 410SS Fusion Flaws and Other Overlay-to-Base Material Observations	150
Table 29 – EDX Summary for U11 Sample	153
Table 30 – Summary of 410SS-WC Fusion Flaws and Other Overlay-to-Base Material Observations	156
Table 31 – EDX Summary for W1 Sample	159
Table 32 – Thermal Properties of Common Engineering Materials.....	177

List of Figures

Figure 1 – Voltage and Current Ranges for Electrical Discharges and Arcs	8
Figure 2 – Non-Consumable Thermionic Cathode Welding Arc: Regions of the Arc and Arc Voltage Behaviour (electrode negative polarity)	9
Figure 3 – Heat Transfer Contributions to Anode in GTAW	10
Figure 4 – Arc Column Non-Ohmic Behaviour	13
Figure 5 – Non-linear Arc Voltage-Length Relationship	13
Figure 6 – Temperature for Thermionic Emission as a Function of Element and Current Density	16
Figure 7 – Schematic of Five Common Types of Non-consumable Electrode Arc Modes	16
Figure 8 – Schematic of Electromagnetic Lorentz Force Generation.....	19
Figure 9 – Arc Pressure Gradient: Lorentz Forces in Regions of Changing Current Density	19
Figure 10 – Welding Power Sources: Characteristic Voltage-Amperage Curves	21
Figure 11 – Schematic of GTAW Process.....	23
Figure 12 – Schematic of GMAW Process.....	25
Figure 13 – GMAW Equipment	25
Figure 14 – Schematic Illustration of Globular and Small Droplet Spray Transfer	26
Figure 15 - Typical Metal Transfer Droplet Frequency as a Function of Arc Current.....	27
Figure 16 – Rising Arc Characteristic Curve with a Constricted Arc	29
Figure 17 – Schematic Comparison of a GTAW and PTAW Torch.....	29
Figure 18 – Comparison of Temperature Profiles for Constricted and Non-constricted Arcs	30
Figure 19 – Relative Tolerance in Standoff of GTAW and PTAW	32

Figure 20 – Plasma Arc Welding Modes: Transferred and Non-Transferred	33
Figure 21 – Schematic of Melt-in Mode for PTAW.....	34
Figure 22 – Keyhole Welding Geometry for High Energy Density Processes.....	34
Figure 23 – Tolerance Ranges for Welding Current and Plasma Gas Flow Rate for Keyhole PTAW.....	35
Figure 24 - Schliren Photographs of Argon and Helium Gas Shielding During Arc Welding.....	38
Figure 25 – Required Shielding Gas Flow Rate as a Function of Helium Content	38
Figure 26 – Arc Potential as a Function of Shielding Gas Content	41
Figure 27 - Typical Heat Content as a Function of Gas Temperature for Diatomic and Monatomic Gases (left); Energy content as a Function of Gas Temperature for Various Gases (right).....	42
Figure 28 – Thermal Conductivity of Common Welding Gases	43
Figure 29 – Thermal Conductivity of Nitrogen	44
Figure 30 – PTAW Equipment Assembly	57
Figure 31 – PTAW Eutronic GAP 3000 AC/DC Power Source	58
Figure 32 – Cross-Section of GAP E 52 Torch	58
Figure 33 – Calibration Curve for CNC Welding Table Motion.....	62
Figure 34 – Variable External Resistance (R2D2): Top View and Internal Schematic ...	63
Figure 35 – Voltage-Current Curve of Eutronic GAP 3000 AC/DC Constant Current Power Source	64
Figure 36 – Relationship Between Gas Mixture Flow and Calibrated Argon Flow.....	66
Figure 37 – Macro-Images of Run A: Welds A1 to A5.....	69
Figure 38 – Macro-Images of Run B: Welds B1 to B5	69
Figure 39 – Run A Weld Dimensions.....	70

Figure 40 – Run B Weld Dimensions	70
Figure 41 – Stereo-image (left) and SEM image (right) of B2 Slag Material	71
Figure 42 – Macro-Images of Run G: Welds G1 to G5.....	72
Figure 43 – Weld G4 Cross-section Macro-images of Bead Humps.....	73
Figure 44 – Arc Images of Secondary Arc (left) and Reverse Metal Transfer (right).....	73
Figure 45 – Schematic of Autogenous Operating Map Experiments	75
Figure 46 – Operating Map as a Function of Current and Welding Speed.....	77
Figure 47 – Effect of Gas Composition on Autogenous Bead Behaviour	78
Figure 48 – Schematic of Doping Plates.....	80
Figure 49 – Bead Behaviour for Doping Plate Experiment #1	81
Figure 50 - Bead Behaviour for Doping Plate Experiment #2.....	82
Figure 51 – Low Speed Stable Gouging Regime – No Weld Bead Humping.....	88
Figure 52 - High Speed Humping Regime –Weld Bead Humping	88
Figure 53 – Video Captures of Weld Bead Humping Mechanism	89
Figure 54 – Marangoni Flow: Surface Tension Driven Convective Fluid Flow	97
Figure 55 - Video Captures of Twin-Bead Humping Mechanism.....	100
Figure 56 – Predicted Marangoni Fluid Flow for a Thin Film Weld Pool	101
Figure 57 – Behaviour of a Wetting System.....	103
Figure 58 – Behaviour of a Non-Wetting System	103
Figure 59 – Apparent Contact Angle of Humping Peaks	104
Figure 60 – Change in Wetting Behaviour with Surface Active Elements	104
Figure 61 – Weld Pool Shape with Ar-10% Hydrogen Plasma Gas.....	108
Figure 62 – Macro Views of Autogenous Welds Completed with Ar-10% Hydrogen Plasma Gas.....	110

Figure 63 – Autogenous Weld with Ar-H ₂ Plasma Gas & Ar-CO ₂ Shielding Gas.....	111
Figure 64 – Effect of CO ₂ Shielding Gas During Autogenous Welding	111
Figure 65 – Classification of Common Modes of Wear	120
Figure 66 - Surface Heat Treatments and Surface Coatings.....	121
Figure 67 – Schematic of Spray Processes	122
Figure 68 – Surface Buildup	122
Figure 69 - Industrial Thermal Spray Surfacing Techniques.....	122
Figure 70 – Commercially Applicable Surfacing Techniques.....	123
Figure 71 – Optimization Flow Chart for PTAW Surfacing Process Parameters and Coating Behaviour	124
Figure 72 – Influence of Operating Process Parameters on MMC Coating Formation..	126
Figure 73 – PTAW Anode with 45° Trailing Powder Ports: Cross-section (left) Bottom View (top)	136
Figure 74 – “Saw Tooth” Torch Weaving Pattern.....	138
Figure 75 – Actual “Saw Tooth” Torch Pattern.....	138
Figure 76 – Powder Hopper and Delivery System	138
Figure 77 – Deposition Rate as a Function of Carrier Gas Flow Rate (lpm) & Wheel Speed (%).....	139
Figure 78 – Overlay Cross-Sectional Macro-Properties.....	145
Figure 79 - As-Welded Macrographs of 410SS Overlays with Argon Shielding Gas ...	145
Figure 80 - As-Welded Macrographs of 410SS Overlays withCO ₂ Shielding Gas.....	146
Figure 81 - Macrographs of Cleaned 410SS Overlays with Argon Shielding Gas	146
Figure 82 - Macrographs of Cleaned 410SS Overlays withCO ₂ Shielding Gas.....	147
Figure 83 – Cross-section macrographs of 410SS Overlays with Argon Shielding Gas	148

Figure 84 – Cross-section macrographs of 410SS Overlays with CO ₂ Shielding Gas...	148
Figure 85 – Cross-sectional Properties of 410SS	149
Figure 86 – 410SS Argon Standard (P8.2): Overlay Tie-in Lack of Fusion Flaw	150
Figure 87 – 410SS Argon Standard (P8.2): Interface Porosity and Cracking at Overlay Center.....	151
Figure 88 – 410SS Argon-Helium Plasma Gas (P9.1): Overlay Tie-in Flaws.....	151
Figure 89 –Argon-Hydrogen Plasma and Carrier Gas (P9.3): Good Interface and Tie-in Fusion.....	151
Figure 90 – 410SS with Argon-Carbon Dioxide Shielding Gas (U11): Typical Interface Fusion Flaws	152
Figure 91 – SEM Image of Sample U11.....	152
Figure 92 - Macrographs of Cleaned 410SS-WC MMC Overlay with Argon Shielding Gas	154
Figure 93 - Cross-section macrographs of 410SS-WC MMC Overlays.....	155
Figure 94 - Cross-sectional Properties of 410SS-WC MMC Overlays.....	156
Figure 95 – Micrographs of Poor Tie-In Fusion (Left, Sample W1, 50X), Good Carbide Distribution (Center, Sample W1, 50X), and Poor Carbide Distribution (Right, Sample W10, 50X).....	157
Figure 96 – Micrographs of Good Interface Fusion with Composite Region (Left, Sample W1, 300X), Variable Interface Fusion (Center, Sample W6, 100X), & Excellent Tie-In Fusion (Right, Sample W4, 50X)	157
Figure 97 – Micrographs of Interface Porosity and Cracking (Left, Sample W11, 50X), and Surface Cracking and Porosity (Right, Sample W12, 50X).....	157
Figure 98 – SEM Backscattering Electrons (BSE) Imaging of Sample W1.....	158
Figure 99 – 410SS-WC Cross Sections and Weaving Patterns: Dependence on Velocity Vectors	164

Figure 100 – Dependence of Total Welding Time on Torch Velocity and Dwell Time	165
Figure 101 – Effect of Current Variations on the Overlay Surface	166
Figure 102 – Operating Voltage Range for Different Gas Mixtures During 410SS Overlay Welding.....	167
Figure 103 – Effect of Motion, Powder, Arc Energy on Overlay Appearance	169
Figure 104 – Argon Standard - Weld Bead Interface	174
Figure 105 – Argon-Helium Carrier Gas - Weld Bead Interface.....	174
Figure 106 – Argon-Hydrogen Carrier Gas - Weld Bead Interface.....	174
Figure 107 – Excessive Oxidation and Flaw Formation with Ar-CO ₂ Shielding Gas (1.5 seconds).....	175
Figure 108 – Data Variability of 410SS Overlay Welding.....	176
Figure 109 – Macro Picture of 410SS-WC (left) and 410SS Welded with Identical Parameters.....	177
Figure 110 - Bend Test Samples – Cracking Failure (left) & Spallation Failure (right)	180

Chapter 1 – Introduction and History

In order to discuss the relatively specialized operation of the plasma transferred arc welding (PTAW) process, this general literature review will first outline the industrial and scientific background of arc welding. General principles related to arc physics, process parameters, and welding gas properties will be explored. In subsequent sections, two unique applications of PTAW are explored: *Part 1: PTAW Autogenous Welding* and *Part 2: PTA Welding of Metal-Matrix Composite (MMC) Overlays*. A literature review is completed for those sections to introduce the application and explore previous works complete therein.

1.1 History of Joining and Welding

The history of welding and joining can be conveniently divided into three eras: the blacksmith era, development of fusion techniques (circ. 1880 to 1940), and the scientific and technology era (1940 to present) [1]. Prior to the scientific era, metals were joined together without parent material fusion, i.e., without melting the base material. There is evidence of the joining of gold and iron dating to ancient times, even as far back as 1000 B.C. [2] The methods utilized were the blacksmith techniques of brazing, soldering, riveting, and forge welding. Brazing and soldering are accomplished by melting a filler material, with a melting point lower than the solidus temperature of the base material, which is drawn into the weld joint via capillary action and solidifies to form the joint. Forge welding techniques deform metal mechanically while the surfaces are in intimate contact, usually at high temperature. The use of fluxing agents, such as sand, aid in the disruption of the surface oxides and allow virgin (clean) material to bond on contact.

The ability to focus energy in a localized area facilitated melting of the parent material and modern fusion welding was born. Scientific investigations into the nature of electricity, completed near the start of the 19th century by Sir Humphrey Davy, produced the first documented electric arc between two carbon electrodes using a battery [3]. After there were many discoveries, accidental and intentional, which were the origins of modern welding processes. The first electric resistance weld was completed by Elihu Thomson during an accidental discovery during a lecture at the Franklin Institute (Philadelphia) in 1887 and was later patented. Between 1880 to 1890 Auguste de Meritens and his Russian student, Nikolai Benardos, used carbon arc processes to weld lead and steel and obtained French (1881), British (1885) and American (1887) patents. Attempts to replace the carbon electrode with a consumable electrode, whereby metal is transferred across the arc, is credited to C.L. Coffin of Detroit who patent the process is 1897. The development of a consumable electrode arc melter by N.G. Slavianoff in 1892 is considered the precursor of the modern Shielded Metal Arc Welding (SMAW) process. These early welding processes were inherently unstable and provided poor shielding of the weld zone that led to embrittled weldments (i.e., atmospheric oxygen and nitrogen contamination).

In early 1900, the introduction of metal electrodes coated with grease, lime (CaO), and even rust by Strohmenger (U.K.) and Oscar Kjellberg (Sweden, Founder of ESAB) improved arc stability and provided some atmospheric shielding. Later the chemist Le Chatelier recognized that the high temperature combustion reaction of oxygen and acetylene was sufficient to melt and weld steel, while the carbon dioxide and water vapour produced shielded the weldment area. Previous work completed by Edward Blass

in 1887 was the first known use of shielding gases, both neutral and reducing, to protect the weld zone from excessive oxidation [4]. Welding was now seen as a viable and repeatable process that was superior to the typical blacksmith techniques (particularly riveted fabrication).

Development of improved fluxes, coatings, and techniques for the storage of welding gases initiated further developments in gas welding and cutting. The adoption of welding processes by the American Society of Mechanical Engineers Boiler and Pressure Vessel Code (ASME-BPVC) led to increased welded fabrication and production. Significant developments during the two World Wars produced welding techniques such as gas tungsten arc welding (GTAW), gas metal arc welding (GMAW), and submerged arc welding (SAW) that are still in use today.

After 1940, the use of scientific principles and research programs led to significant advancements in welding technology. The importance of quality assurance, automation, and characterization of weldment properties now plays an increasing important role. There is much emphasis on automated welding, robotics, and hybrid-processes. The latest developments include high-energy intensity processes such as electron beam (EBW) and laser beam welding (LBW). Most recently in 1991, The Welding Institute (U.K.) invented friction welding that uses mechanical force to expose and bond clean material without base metal melting, and therefore can be considered a descendent of one of the oldest forms of joining: forge welding.

Of particular importance to the work completed herein was the development of “plasma arc” welding and cutting processes. In 1923, Gerdien and Lotz completed some of the

first known work using an apparatus to physically constrict an electric arc [5]. These early experiments showed that a significant increase in arc energy can be obtained, which results in higher plasma temperatures and increased arc light intensity. The first commercial development of the modern plasma welding process was patented by Robert Gage in 1957 [6]. This practical application simulated further development, including the feeding of filler wire or strips into the plasma column to form a stream of molten metal for welding, spraying, and overlaying [7]. Eventually this led to plasma spray processes and, with the use of powder consumables, the modern incarnation of the plasma transferred arc welding (PTAW) process investigated herein.

1.2 Overview of Welding Processes and Energy Sources

The basic requirements for producing a sound weld has not changed throughout history; provide a clean surface and the necessary energy for fusion. The former is obtained through proper sample preparation and in-situ physical protection or gas shielding. The latter is acquired via one of the following four energy sources: electricity, mechanical action, chemical reactions, and radiant energy [1]. The American Welding Society (AWS) acronyms and initialisms for the vast majority of commercial welding processes are summarized in Table 1. A detailed discussion of the entire spectrum of welding processes and the relevant energy sources is beyond the scope of this dissertation. Attention will be given to the common arc welding gas-shielded processes to compare and explore the welding parameters of interest.

Table 1 – AWS Designations for Welding Processes [1,8]

AWS Designation	Process Name	Other Common Designations
<i>Arc Welding Processes – Electricity</i>		
EGW	ElectroGas Welding	
FCAW	Flux Cored Arc Welding	
FW	Flash Welding	
GTAW	Gas Tungsten Arc Welding	TIG, Heliarc
GMAW	Gas Metal Arc Welding	MIG, MAG
GMAW-S	GMAW Short-Circuit	Dip Transfer, CO ₂ welding
GMAW-P	GMAW Pulsed	Pulse Welding
PAW	Plasma Arc Welding	PTAW
PGMAW	Plasma GMAW	Plasma-MIG
SAW	Submerged Arc Welding	SubArc
SAW-S	SAW - Series	Series Welding
SMAW	Shielded Metal Arc Welding	Stick Welding, MMAW
SW	Stud Welding	
<i>Electric Resistance Welding Processes - Electricity</i>		
RSEW	Resistance Seam Welding	ERW
ESW	ElectroSlag Welding	Slag Welding
RPW	Resistance Projection Welding	
RSW	Resistance Spot Welding	Spot Welding
UW-HF	Upset Welding-High Frequency	
<i>Solid State Welding (SSW) Processes – Mechanical Action</i>		
CW	Cold Welding	
DFW	DiFfusion Welding	Diffusion Bonding
EXW	Explosive Welding	
FOW	FORge Welding	Hammer Welding
FRW	FRiction Welding	
FSW	Friction Stir Welding	
ROW	Roll Welding	Roll Bonding
USW	Ultrasonic Welding	
<i>Chemical Energy Processes – Chemical Energy</i>		
OFW	Oxy Fuel gas Welding	
OAW	Oxy Acetylene Welding	Gas Welding
TW	Thermit Welding	
<i>High Power Density Processes - Radiant Energy</i>		
EBW	Electron Beam Welding	Beam Welding
LBW	Laser Beam Welding	Laser Welding

1.3 Overall Project Objectives and Scope

The main objective of this research was to investigate the influence of welding parameters on the process behaviour of the plasma transferred arc welding process. The aim was to uncover fundamental relationships, utilizing welding arc physics principles, such that the information obtained would be adaptable to any PTAW installation. In all cases weld bead formation and arc behaviour were recorded with video photography.

In *Part 1: PTAW Autogenous Welding*, exploratory experiments were completed to understand and characterize the welding parameters of influence. Stringer beads were completed on base plates with no filler material, i.e., an autogenous welding system. A flaw formation mechanism was observed and investigated. The influence of base material chemistry, minor alloying elements (i.e., surface active elements), welding gas composition, and the PTA torch configuration on the development of fusion flaws was characterized. A practical engineering application was investigated in *Part 2: PTA Welding of Metal-Matrix Composite (MMC) Overlays*; this was the cladding of steel components for wear applications in the oil sands industry. Exploratory research was completed to understand the effects of motion, arc energy, and powder delivery on the effective heat input during PTA overlay welding. Standard conditions were developed for the welding of 410 martensitic stainless steel (410SS) and a 410SS – tungsten carbide metal matrix composite (MMC) alloy. Utilizing these standardized conditions, the weld overlay development was investigated with additions of helium, hydrogen, nitrogen, and carbon dioxide to the plasma, carrier, and/or shielding gas. Particular attention was given to changes in the effective heat input and oxidation/reduction wetting behaviour.

Chapter 2 – General Literature Review

2.1 Arc Physics Review

a. Importance of Arc Physics to Welding

The electric arc is the most widely used energy source of all welding processes. The welding arc is a self-sustained discharge of ionized gas or plasma, the fourth state of matter, having a relatively low voltage drop and capable of supporting large currents. The full spectrum of plasmas used in commercial and research applications is given in Figure 1. Welding arcs are typically ambient pressure and the potential drop is of the order of 10 – 40 V to satisfy the minimum ionization potential of the gas forming the arc.

The simplest case to consider is the direct current (DC) electric arc with inert gas shielding and a tungsten cathode capable of thermionic emission; the basic schematic is shown in Figure 2. In order to complete the electrical circuit, the current must pass from the tungsten cathode to the base material anode by means of arc plasma. The arc is composed of electrons, ions, atoms, and molecules in rapid movement proportional to the imposed electric field. The arc plasma is a source of heat; it forms the weld pool and often melts the electrode. The temperatures obtained are greater than the melting point of all known metals (i.e., >5000K), while peak temperatures in the arc can range between 15,000 and 30,000K; physically constricted arcs are able to produce temperatures up to 50,000K at high current [3]. The high temperature range and the high velocity flow of the plasma leads to intense chemical reactions and mixing in the weld pool. For consumable electrode processes, the electromagnetic arc forces influence metal transfer from the electrode to the work piece; these forces are partially responsible for mixing of the molten weld pool material. The desire to optimize arc welding efficiency, while

ensuring arc stability, greatly influences the electric arc power source type and design.

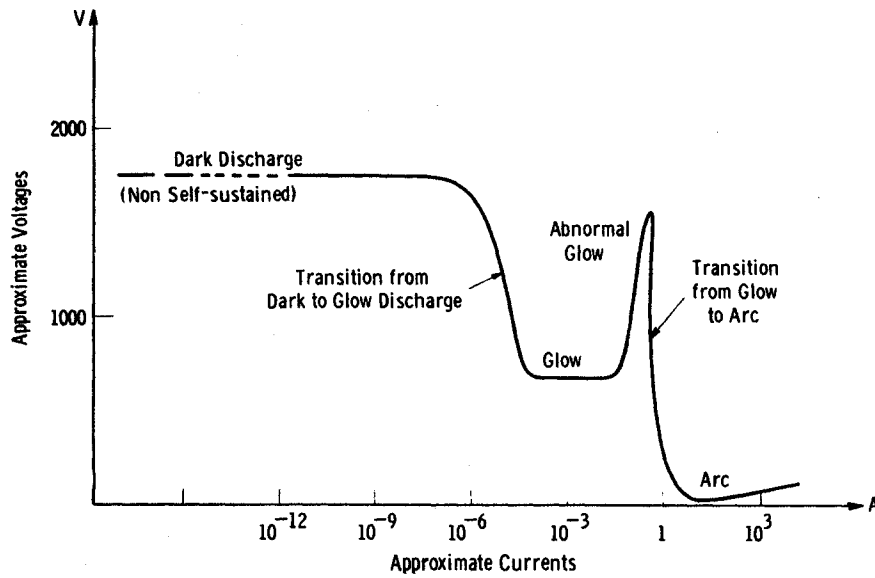


Figure 1 – Voltage and Current Ranges for Electrical Discharges and Arcs [9]

b. The Welding Arc Column

The electric arc, produced by a non-consumable thermionic cathode with electrode negative polarity, can be broken up into five distinct regions: anode spot, anode fall space, arc plasma column, cathode fall space, and cathode spot as shown in Figure 2. The overall mechanism is as follows; electrons produced at the thermionic cathode are accelerated by the cathode fall voltage gradient, and transmit this kinetic energy upon impact with the shielding gases atoms/molecules to produce ions. These ions are then accelerated towards and impact the cathode, which liberates energy and maintains the thermionic temperatures necessary to produce more electrons. Hence, the arc is a “...self-maintained discharge...” [17]. The arc column and anode fall space potential gradients then accelerate the electrons toward the anode spot on the work piece, resulting in the intense heating and formation of the molten weld pool.

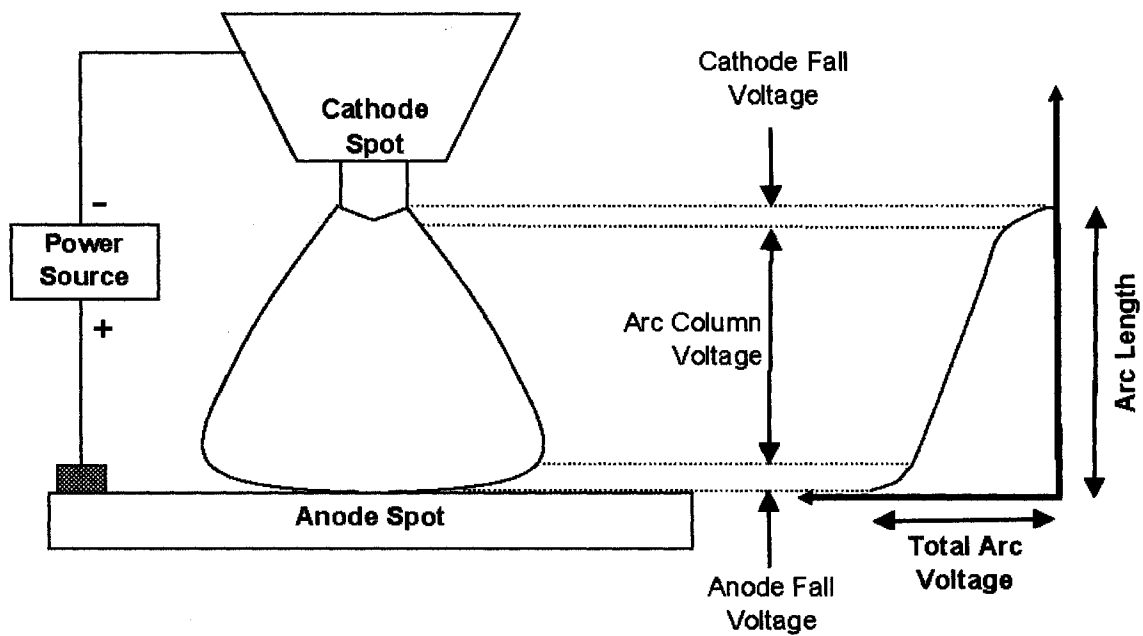


Figure 2 –Non-Consumable Thermionic Cathode Welding Arc: Regions of the Arc and Arc Voltage Behaviour (electrode negative polarity)

The anode spot is the positive electrode (i.e., molten metal) which attracts the negative electrons via the electric field. The electrons are “collected” at this region which leads to intense heating of the anode substrate. The majority of the electron energy is due to the thermionic work function (potential energy) and acceleration from the anode fall space voltage. Additional energy is also liberated from the electrons as they move from higher to lower temperatures, known as the Thompson Effect [10,16]. These electron heating effects are given [12,17] by the following equation:

$$Ha = I \left(\phi + V_a + \frac{3kT}{2e} \right) \quad \text{Equation (1)}$$

Where I is the arc current, ϕ is the anode thermionic work function, V_a is the anode fall

space voltage, and $\frac{3kT}{2e}$ is the electron thermal energy in plasma (Thomson Effect). In addition, there is also heating from conduction, convection, and radiation of the arc plasma to the substrate. The relative heat transfer contributions for GTAW, with 1600W of arc energy and 44.4% efficiency, are shown in Figure 3 [10].

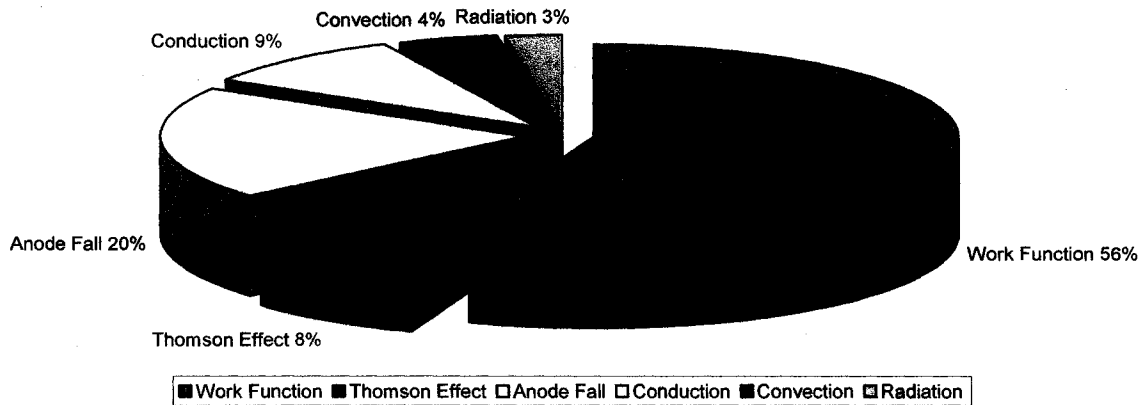


Figure 3 – Heat Transfer Contributions to Anode in GTAW

The small arc region adjacent to the anode spot is termed the anode fall space. This thin layer, estimated to be 1 micrometer, has a negative space charge and is characterized by a steep voltage gradient. Depending on the anode composition and plasma temperature, ions are produced in this region by field ionization and/or by thermal ionization mechanisms [12]. Field ionization is associated with low anode fall space temperatures and high potentials; ionization occurs via relatively few electron-atom interactions. Thermal ionization mechanisms occur as the anode plasma temperature increases and there are increased electron-atom collisions; less potential is required and the anode fall space potential is lowered. The presence of low ionization potential metal ions, due to inevitable vaporization of the anode, causes a drop in the fall space voltage and lower arc

temperatures relative to the idealized solid-copper water-cooled anode [10,11,12]. The net results are a reduction in both the plasma temperatures and anode fall space potential, which lowers overall energy transfer efficiency.

Due to the cooling effect of the electrode, as the plasma approaches the anode the maximum temperature obtained is approximately equal to the anode boiling point. The degree of ionization is directly proportional to the plasma temperature, as described by the Saha equation [3,12,13]. Hence, as the temperature decreases there is a proportional decrease in the percent ionization or particle density per unit volume of welding gas. The drop in ionization results in fewer positive charge carriers and the accumulation of electrons, which creates an effective negative space charge. The steep voltage gradient results from a change in voltage over such a small region, which is required to maintain passage of the current at these lower temperatures [12]. The steep gradient adds a significant amount of kinetic energy to the anode spot, as shown by the Va term in Equation (1). This intense localized heating phenomenon illustrates why the electric arc is suitable for welding.

The arc column is electrically neutral plasma (i.e., without a space charge), consisting of electrons, ions, and neutral atoms or molecules that are in quasi-thermal equilibrium. As electrons are accelerated by the arc potential gradient, they collide with atoms to produce ions that form the electrically neutral plasma. The motion of the lightweight and mobile electrons maintains thermal equilibrium. For example, approximately 1/1000 (0.1%) of the arc current is carried by the slow, heavy ions and can be neglected. The electron mean free path is of the order of 10^{-3} mm and the collision frequency is 10^{11} per second, such that the electron temperature is only slightly above the mean column temperature [12].

Quasi-equilibrium conditions exist since there is some electron drift in-between collisions, where electrons gain energy at the expense of the arc gas, but this effect is only distinct for low pressure arcs [13]. Depending on the current, arc core temperatures range between 5,000 and 50,000K (due to the gradient in gas ionization between 1% to 100% and greater if one considers double and triple ionization [12]). Arc decay, the time for an arc to extinguish at zero current, is of the order of microseconds [12,17], and therefore arc initiation/stability is a practical concern. The presence of low ionization potential elements, such as K^+ and Na^+ or other metal vapours, improves arc starting and arc stability (especially during AC welding), but will lower the core arc column temperature. The voltage gradient, as shown in Figure 2, is uniform along the length of the column for a given arc gas mixture; for example, pure argon typically has a gradient of $\sim 0.7V/mm$ [17]. A welding arc can have an increased potential gradient by increasing the ionization potential (i.e., addition of helium to argon) or using diatomic gases that must first dissociate prior to ionization (i.e., hydrogen or nitrogen additions). The effect of welding gas composition will be discussed further in Section 2.3.

The arc column resistance behaviour is non-linear and non-ohmic as shown in Figure 4. Specifically for GTAW and PTAW, the voltage-current relationship can be broken up into two distinct regions. Region I, which is not a common range for welding, exhibits a sharp drop in voltage with increasing current. This effect is attributed to a combination of the following mechanisms: higher plasma temperatures that increases the electrically conductivity, higher cathode temperatures and improved thermionic electron emission, and an increase in the current carrying cross-section of the arc as the current rises [12]. Region II exhibits a non-linear increasing resistivity relationship, likely caused by

increased current density and greater ion-electron collision frequencies that disrupt the overall flow of current. The slope increase is greater for the physically constricted PTAW arc and the cathode spot mode during GTAW [3,5]. The volt-ampere relationship can be empirically defined [15] by the following equation:

$$V = A + BI + \frac{C}{I} \quad \text{Equation (2)}$$

Where V is the arc voltage, I is the arc current, and A, B, C are empirical constants. In practice, a broad range of volt-ampere characteristic curves are easily obtained by slight variation of welding parameters. For example, the empirical constants A, B, and C vary erratically depending on arc length, anode/cathode chemistry, and control of experimental conditions.

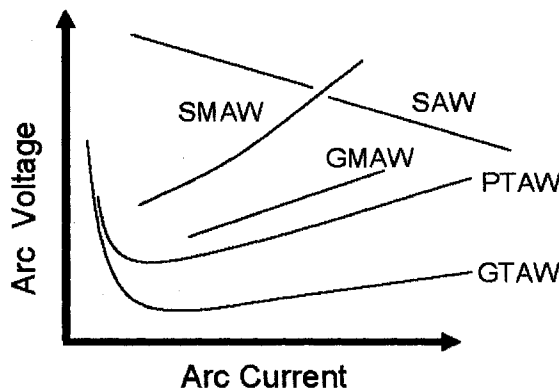


Figure 4 – Arc Column Non-Ohmic Behaviour

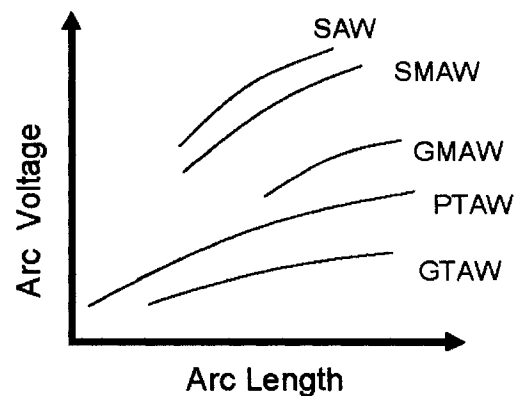


Figure 5 – Non-linear Arc Voltage-Length Relationship

Comparative studies [3,14] have shown that volt-ampere curves are sensitive to slight changes in electrode material, electrode geometry, and cathode mechanisms. Differences in the *total* operating voltage are linked to this variability in the cathode and the anode fall voltage drops. Figure 5 illustrates that arc voltage varies directly with arc length, but

that the relationship is non-linear. The positive relationship is correlated to the arc column voltage gradient (Figure 2); the non-linearity is attributed to variations in the anode/cathode chemistry and plasma jets from both electrodes.

The cathode fall region is the electrical connection between the cathode and the arc column, but is the most poorly understood region of the welding arc. The relative ease of continued production of electrons in this region largely determines arc stability. The region is narrow, of the order of 1 micrometre, with a typical potential difference of approximately 2 – 8 volts [12]. The voltage gradient is steeper than the anode fall region and there is net positive space charge. Positively charged ions, which are produced in the arc column and at the anode spot, are accelerated towards the cathode which raises/maintains the cathode at thermionic temperatures necessary for continued emission. The ion bombardment energy transfer is difficult to quantify numerically since the actual kinetic rebound energy of the ions (i.e., unlike electrons, ions are not always absorbed at the surface), and the total amount of energy of recombination actually liberated is unknown [12].

The cathode spot is the location of electron production at the cathode by thermionic emission; this emission mechanism is only applicable for high-melting-point and low-work-function refractory materials such as carbon, molybdenum, tantalum or tungsten (Figure 6). Upon heating to sufficiently high temperatures, the Richardson-Dushman equation describes current density of the emitted electrons [13]:

$$J(e) = AT^2 \exp\left(\frac{-\phi e}{kT}\right) \quad \text{Equation (3)}$$

Where J is the current density, A is a constant of $6 \times 10^5 \text{ A/m}^2\text{K}^2$ for metals, ϕ is the

thermionic (cathode) work function, e is the charge of an electron, k is the Boltzman's constant, and T is the temperature (K). The negative sign in front of ϕ indicates that the cathode work energy is removed; this cathode cooling effect is often referred to as the "electron evaporation". Note the presence of the anode work function (ϕ) in Equation (1) for heat input to the anode. Typical current densities from tungsten electrodes are of the order of 10^3 A/cm². Utilizing GTAW welding and D.C. electrode negative polarity, approximately 1/3 of the heat is transferred to the cathode electrode and the remaining 2/3 to the anode weld pool [23]. Two non-thermionic emission mechanisms are plasma emission and field emission, and are discussed further in Section 0. Due to local fluctuations in current density and pressure, in practice, two of these mechanisms may be operating simultaneously or the mechanism may change [12].

c. Operating Modes for Thermionic Arcs

Under typical conditions, five distinct modes of operation are possible for the thermionic arc as shown in Figure 7 [13,14]. A detailed explanation of all modes is beyond the scope herein; the following will discuss the major differences of the operating extremes: normal mode and cathode-spot mode [3,13,15]. The cathode tip geometry dictates the nature of the arc; either a hemispherical tip or sharp conical tip, respectively, results in normal operation or cathode-spot mode. The normal mode is stable, occurs over a broad current range, and the arc column takes the form of a truncated cone. The cathode-spot mode involves formation of a dark circular spot on the molten cathode tip, which causes a slight constriction of the cathode plasma and formation of a deep-blue cone of radiation emanating from the cathode. The cathode spot mode exhibits the characteristic bell-shaped arc column; higher arc voltages, increased plasma temperatures, greater electric

field intensity, and increased plasma jet velocities result [3,13,13]. The cathode-spot mode is semi-stable unless 2% thoria-tungsten or similar electrodes are used; but is the most common mode of GTAW operation in practice. The presence of these various operating modes, with subtle differences in behaviour and appearance, may partially explain the discrepancies in experimental data for volt-ampere characteristic curves and volt-arc length measurements discussed previously.

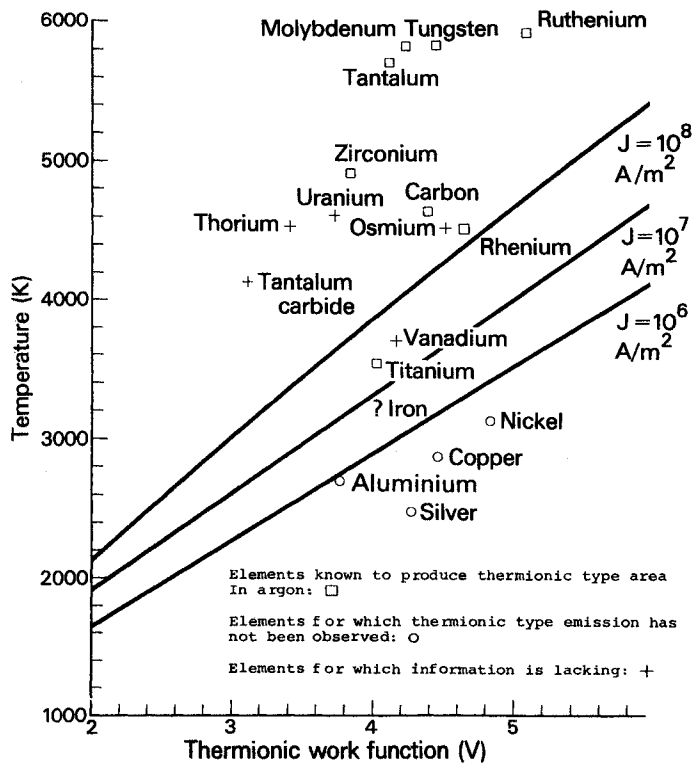


Figure 6 – Temperature for Thermionic Emission as a Function of Element and Current Density [13]

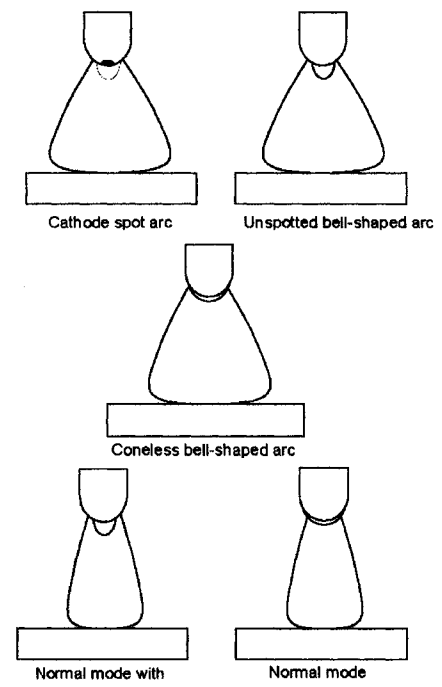


Figure 7 – Schematic of Five Common Types of Non-consumable Electrode Arc Modes [13]

d. Non-Thermionic Electron Emission

The two possible mechanisms to explain electron emission from non-thermionic emitters

are field emission and plasma emission. Plasma emission, which occurs due to plasma impingement on small areas, occurs in low current, high pressure plasmas with non-vaporizing cathodes; these conditions do not exist for typical welding arcs and plasma emission is typically neglected when explaining arc welding [12,13,14].

Field emission occurs for non-thermionic emitters, or cold cathode materials such as steel or aluminum, and is the electron emission mechanism associated with most consumable electrode processes such as GMAW. Emission is promoted by a very high electric field strength proportional to a high current density and a steep potential gradient. The resulting electric field strength theoretically exceeds 10^9 V/m, where the intense field literally rips the electrons out of the relatively cold cathode [16]. The actual mean field strength level encountered during welding is of the order of 10^7 V/m [12]. Therefore, local electric field strength fluctuations in the cathode fall region promote field emission. The resulting cathode spots are very small and highly mobile since they search for areas of high local current density and/or lower field emission requirements, commonly associated with non-metallic oxide particles. The current density at the individual sites is of the order of 10^{11} to 10^{14} A/m², with approximately 10mA current per site and decay times of 5-200ns, while moving at velocities of 10^5 mm/sec [12,14]. These large gradients in motion and current density create strong irregular forces on the cathode, which can result in poor spatial stability and poor metal transfer for consumable electrode processes. In contrast, the cathode spot is relatively large and spatially stable electron emission occurs with thermionic emitters. Lancaster [13,14] has explored various theories, by others, to explain non-thermionic emission, but the mechanism is still not completely understood.

e. Plasma Jet Phenomenon

An important arc phenomenon is the development of the electromagnetic Lorentz force within the arc, which produces high velocity plasma jets in the arc that approach speeds of 100-500 m/s [17]. In 1955, Maecker was able to put forth a theory to explain the plasma-streaming phenomenon [18]. To illustrate, first consider a homogenous cylindrical arc with constant radius and current density as shown in Figure 8. The magnetic field induced by a circular conductor is radial in nature and slowly decreases proportional to the radial distance from the conductor; this is analogous to the magnetic field developed around a current carrying wire. Interaction between the current (J) and magnetic field (B) produces a $J \times B$ force, known as the Lorentz force, which acts upon the charge carriers and tends to compress the current and increase arc plasma pressure. The pressure is proportional to the current and density; compressive force is maximum at points of highest current density [17]. Concurrently, the positive and negative charges in the plasma attempt to expand the arc core with a specific plasma pressure; equilibrium pressure (ΔP) is achieved once this plasma pressure equals the Lorentz compressive force. In a real welding arc, as the arc diverges from the electrode to the base plate, the current density and corresponding Lorentz force decrease (Figure 9). The net result is an axial pressure drop towards the anode surface, i.e., $\Delta P_1 > \Delta P_2 > \Delta P_3$. Plasma fluids respond to this pressure gradient by being pumped and radially accelerated towards the weld pool as jets, given by the following equation:

$$\frac{IJ}{c^2} = \frac{\bar{\rho} v_{\max}^2}{2} \quad (4)$$

Where I is the arc current, J is the current density, $\bar{\rho}$ is the mean plasma density, and

v_{\max}^2 is the resulting maximum plasma jet velocity. This phenomenon is largely dependent on current density gradients and is independent of arc polarity. The plasma jet has an important effect and significance on heat and mass transfer in the welding arc. In addition to the anode spot heating effects, given by Equation (1), the plasma jet effect is a strong convective heat transfer mechanism (see Figure 3). Under special circumstances, relatively equal jets can emanate from both the anode and cathode and, upon collision, deform the arc profile [12]. For consumable electrode processes, such as GMAW, plasma jets and related electromagnetic phenomena largely affect the metal transfer mechanisms. Plasma jets also influence weld penetration, weld pool turbulence and mixing, and contamination via air entrapment. When the arc is physically constricted, as in PTAW, the resulting high velocity gas jets can obtain extremely high speeds and temperatures up to 50,000K [12].

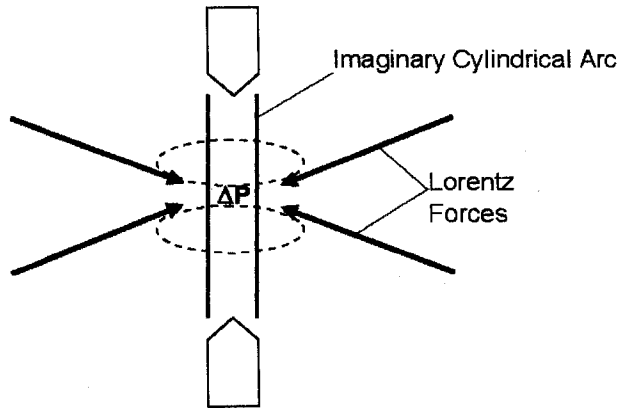


Figure 8 – Schematic of Electromagnetic Lorentz Force Generation [17]

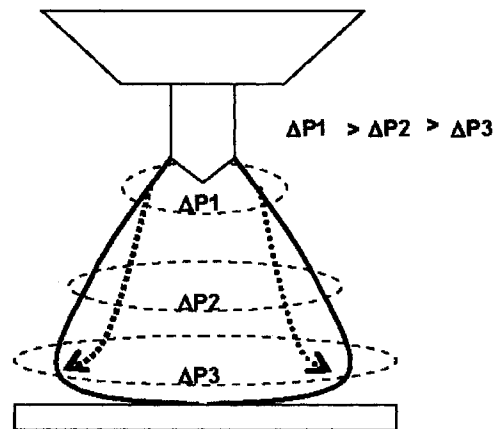


Figure 9 – Arc Pressure Gradient: Lorentz Forces in Regions of Changing Current Density

f. Electric Arc Power Sources

The early power sources were transformer-rectifiers that were large, inefficient, and had limited means for optimization. New inverter, solid-state technologies are small, efficient, and allow for manipulations of operating parameters such as AC wave shape (square or sine wave), frequency modulation, pulse width modulation, phase control, and amplitude control [19]. This improved control has allowed for welding of new materials, new methods (i.e., robotics), and is still an area for potential research.

Power sources are divided into two types: constant current (CC or “droopers”) and constant voltage (CV). As shown in Figure 10, the CC characteristic curve maintains a relatively constant current over a large voltage range and is of particular interest for “hand held” welding processes, such as shielded metal arc welding (SMAW), gas tungsten arc welding (GTAW), and plasma transferred arc welding (PTAW) [19]. As previously discussed, arc voltage and arc length are proportionally related. Thus, if the CC curve is vertical then electrode manipulation (i.e., arc length changes or ΔV) does not effectively change the arc current ($\Delta A \sim 0$). Experienced welders may utilize a more gradual slope or “droop” to manipulate arc voltage and current simultaneously to obtain desired consumable melting rates or penetration characteristics. Consumable electrode, semi-automatic processes typically require the use of CV power sources. These processes include gas metal arc welding (GMAW), flux-cored arc welding (FCAW), submerged arc welding (SAW), and electroslag welding (ESW). A CV power source is utilized for consumable electrode processes because if the wire feed rate suddenly changes, the arc current (and burn-off rate of the consumable electrode) changes inversely. For example, a sudden increase in wire feed speed causes a shorter arc length

and corresponding decrease in voltage, but the CV power source compensates via an increased current and electrode burn-off rate to avoid a short-circuit until the correct arc length is re-established.

The nature of the CC power source is ideal for investigating the effect of welding gas mixtures on the arc voltage-current relationship. By setting the standoff and current constant, the corresponding voltage ranges are compared as a function of the gas mixture. A constant voltage power source would not be feasible for this application since a small change in voltage (ΔV) results in a significant change in current (ΔA). Hence, changes in gas mixtures will affect both the voltage and current simultaneously and the true effect of the mixture itself is less clear.

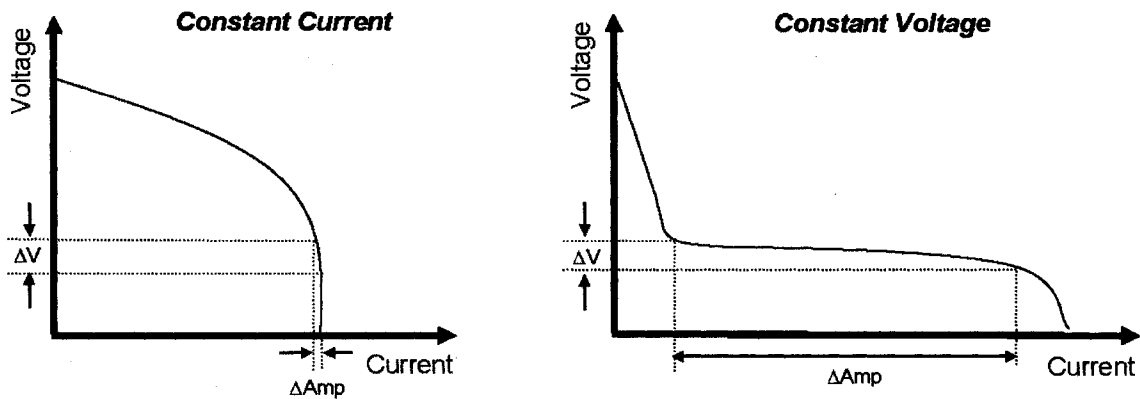


Figure 10 – Welding Power Sources: Characteristic Voltage-Amperage Curves

2.2 Arc Welding Process

a. Gas Tungsten Arc Welding Process (GTAW)

The GTAW process is the simplest method for completing electric arc welding, and is similar to the thermionic arc schematic given in Figure 2. A “free burning” electric arc is struck between the tip of a non-consumable tungsten electrode and the work piece. After entering the arc environment, the shielding gas is ionized to produce conductive plasma and provides protection from atmospheric oxidation/contamination to the weld zone (see Figure 11). Most GTAW is completed with a hand-held torch, although automated and robotic systems are used extensively in some industries, such as automotive and pressure equipment fabrication. It is standard to utilize constant current power sources, and avoid drastic changes in current with relatively small changes in voltage (i.e., slight hand movements). When welding with electrode negative polarity, the use of a tungsten-alloy electrode elevates electron emission characteristics and improves the electrodes current capacity. The most common addition is 2% thorium oxide, which has a lower thermionic work function (see Figure 6) and does not melt so that the cathode-spot operating mode is stabilized [13]. Other additions that are used to improve arc starting, stability, and decrease weldment contamination include cerium and lanthanum; zirconium oxide is a common addition for AC and electrode positive polarity welding [20]. GTAW is a very versatile process [8]; high-quality welds can be completed with most ferrous and non-ferrous materials, in all positions, with or without the addition of welding filler metal, and can be completed on thin gauge (<1 mm) sheet material [21].

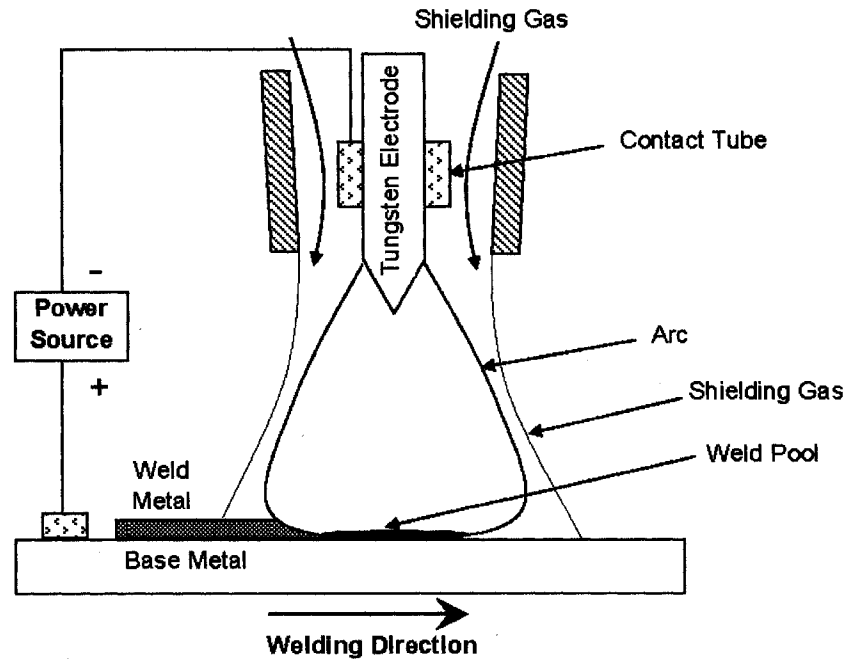


Figure 11 – Schematic of GTAW Process

The arc energy melts the substrate and filler rod to form welds with highly controlled heat input. Relevant welding parameters include arc voltage, welding current, travel speed, shielding gas composition and flow rate. The quantity of welding energy is directly proportional to the current and voltage, and inversely proportional to the welding speed; the basic relationship is given by the heat input equation:

$$\text{Heat Input (J / mm)} = \frac{\text{Voltage (V)} \times \text{Current (Amp)}}{\text{Welding Speed (mm / s)}} \times \text{Efficiency (fraction)} \quad (5)$$

When using direct current electrode negative (DC-EN) polarity approximately 1/3 of the heat input is at the electrode and the remainder enters the work piece [23], but these are not exact ratios since actual heat distribution depends on both arc gap and total arc power [11]. The use of DC electrode positive (DC-EP) polarity reverses the direction of travel of the charged species. The field emission mechanism is responsible for electron

generation at the work piece, a cold cathode material. This action will “clean” refractory oxides off the surface, such as those found on aluminum and magnesium, and results in much cleaner welds. This effect also occurs during alternating current (AC) welding; depending on the phase balance (i.e., ratio of EP to EN) variable heat distributions between the electrode and work piece are possible [22]. With electrons now heating the tungsten electrode during EP, the current density is limited to a maximum value to avoid electrode melting and degradation. The most common industrial shielding gases are inert or reducing mixtures of Ar, He, N₂, and/or H₂ [23]. The use of oxidizing shielding gas mixtures is not possible since they will readily oxidize the tungsten electrode and create excessive arc instability. The effect of welding gas mixtures on arc behaviour will be discussed further in Section 2.3. The major drawback of GTAW is its low productivity when compared to consumable electrodes processes (such as GMAW). In most applications the filler rod is not energized, has lower melting rates, and production decreases. However, the high quality welds, excellent versatility, and relatively low equipment costs results in extensive use of GTAW industrially.

b. Gas Metal Arc Welding (GMAW)

Unlike GTAW that utilizes a non-consumable electrode, the GMAW process establishes an electric arc between the molten weld pool and a consumable electrode wire. Externally supplied shielding gas (or gas mixtures) floods the area to protect the arc and mitigate contamination of the molten weld pool as shown in Figure 12. Using appropriate shielding gases, electrode sizes, and welding parameters, virtually all commercially important metals can be welded, in all positions, by this process in semi-automatic or automatic modes (i.e., robotics). Surfacing consumables include metal strips for

performing large cladding operations, such as internal cladding of pressure equipment [24]. Unfortunately, the relatively complicated equipment setup (Figure 13) can limit applications for this technique.

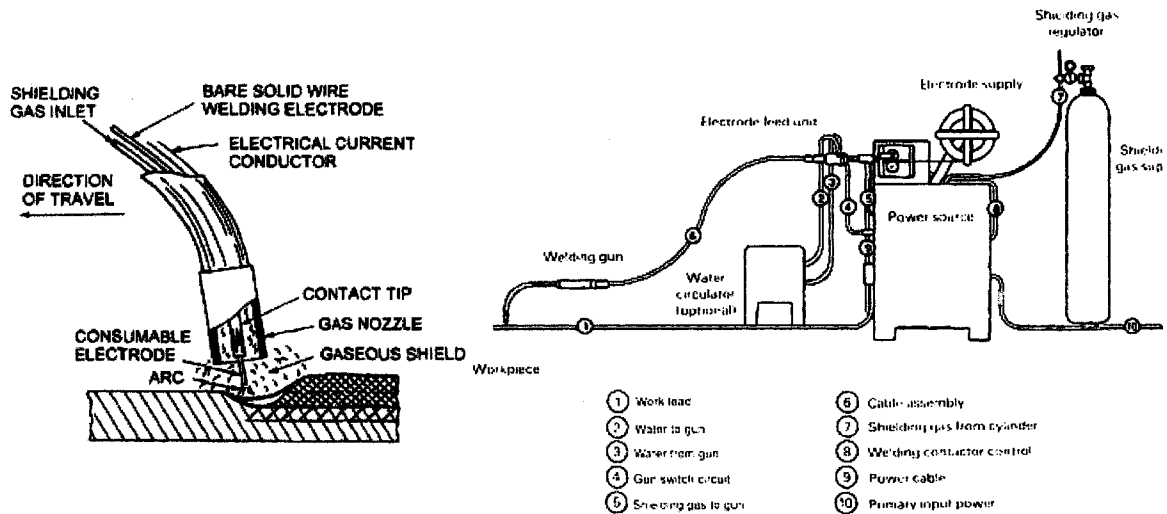


Figure 12 – Schematic of GMAW Process [8]

Figure 13 – GMAW Equipment [21]

The GMAW process characteristics are best described by the metal transfer mode. Using DC-EP polarity, electrons stream towards and subsequently melt the solid bare wire. A molten tip forms that is transferred to the work piece via four different metal transfer modes: globular, spray (small droplet), pulsed, and short-circuit (dip) transfer. Although DC-EN produces the highest electrode melting rates, it is not used because the cathode spots are highly mobile and the resulting irregular forces adversely affect metal transfer [12,14]. Oxygen (1-5%) and/or carbon dioxide gas (5-25%) are often added to the shielding gas to produce a slightly oxidizing arc environment. Oxidation of the weld pool and formation of low thermionic work function oxides promote stable field emission during DC-EP. For these reasons, the use of a purely inert mixture of helium or argon is not common practice.

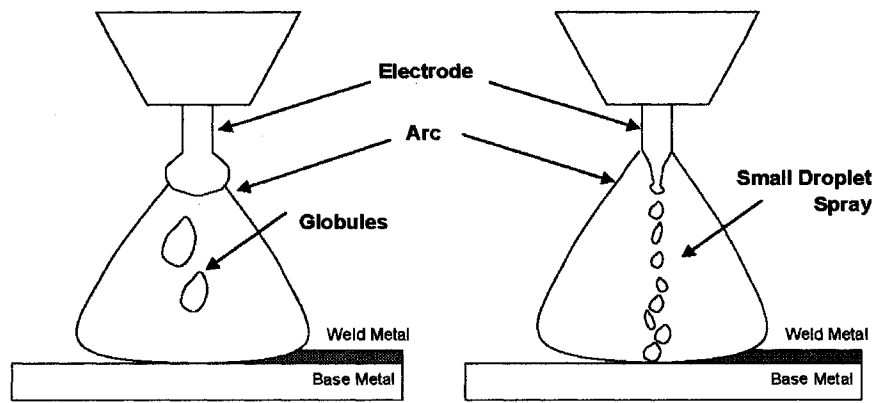


Figure 14 – Schematic Illustration of Globular and Small Droplet Spray Transfer

During globular transfer, droplets larger than the electrode diameter form at relatively low current, and are transferred due to the interactions of gravitational, electromagnetic (i.e., Lorentz forces), and drag forces from the flow of the shielding gas [25]. This type of transfer will occur if the current is below the transition level, regardless of the shielding gas composition. Above the transition current, the spray (or small droplet transfer) mode spontaneously occurs where metal transfers as an axial stream of fine droplets emanating from the tapered end of the electrode. These concepts are illustrated in Figure 14 and Figure 15; the current transition level rises as the electrode diameter increases and/or the electrode extension (stick out) decreases [26]. This transfer mechanism is only possible by using an argon-dominating mixture; the low thermal conductivity of the gas allows the arc to expand around the tip and promote plasma jet assisted metal transfer [27]. Gases with high thermal conductivity, such as helium or carbon dioxide, do not envelope the tip and stabilize the molten globule, and therefore globular or short-circuit transfer will occur [28]. References are available to choose the correct gas mixture(s) to obtain a particular mode of metal transfer for all common engineering alloys [29,30,31,58].

By using real-time pulsations of the current it is possible to alternate between spray and globular transfer, the so-called GMAW-Pulsed mode. At the lower “background” current level, given as I_G in Figure 15, a droplet is formed at the end of the electrode to the desired size. At the higher pulsed current level, I_S , the molten material is propelled as small droplets and increased heat is transferred to the plate to aid with fusion. During short-circuiting (dip) mode, metal is transferred only during a period where the electrode is in direct contact with the weld pool (i.e., no metal is transferred across the arc gap). Depending on various process parameters, such as current, electrode diameter, composition, extension, and shielding gas composition, short-circuiting frequencies (SCF) range from 20 to 200Hz [32]. Small, fast-freezing welds are produced with relatively low heat input. The resulting weldments are well adapted for thin sections, out-of-position welding, and bridging or tacking large root openings. This mode of transfer typically requires the use of CO_2 , Argon- CO_2 , and helium-based mixtures to avoid spray transfer, and is a common transfer mode utilized in many industries.

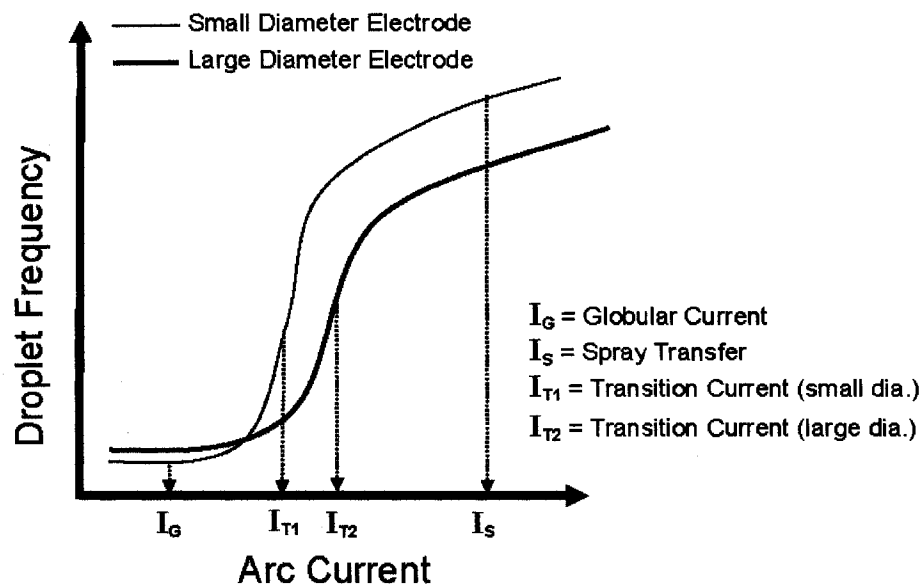


Figure 15 - Typical Metal Transfer Droplet Frequency as a Function of Arc Current

c. Plasma Transferred Arc Welding (PTAW)

i. Characteristics of the Constricted Arc

Based on the previous discussion on arc physics, for stable arc behaviour it is necessary to produce and maintain the required cross section of conducting charge carriers. If the arc cross section is increased, while keeping the current constant, charge density and gas temperature is lowered; the reverse is true if the cross section is reduced [12]. Thus, by physically restricting the arc with a water-cooled copper anode (i.e., heat sink) the arc column area is reduced and electrical resistance increases; arc voltages increase, power dissipation rises, and the core temperature increases to maintain the flow of current [38].

In 1923, Gerdien and Lotz experimented with physically constricted arcs to produce light sources with greater intensity [5]. In 1955, the constricted arc was applied to manual and automated cutting, where the strong plasma jet force mechanically expelled the molten material while the shielding gas prevented excessive oxidation of the cutting interface [33]. In 1957, Robert Gage was first to patent both the plasma torch design and process [6]; others soon followed with novel torch modifications and designs [34]. It was immediately recognized that the constricted arc provided a superior heat-transfer advantage, with heat transfer rates nearly ten times greater than conventional methods such as the oxy-fuel welding system [35]. Automated PTA pipe joint welding and cutting of steel, stainless steel, aluminum, and nickel alloys were rigorously developed in the 1960's [36]. The higher plasma temperatures achieved were due to an increased expenditure of energy, illustrated by the sharply rising voltage-current curve in Figure 16. Higher voltage values and a steeper characteristic curve (see Figure 5) are a result of the physical constriction forcing more charge-carriers to flow to maintain arc stability,

compared to a “free burning” arc. The greater energy density leads to higher arc temperatures, typically ranging from 20,000K for 100 A to over 50,000K for 1450 A [37]. Due to the inherent stability and stiffness of the columnar arc, PTAW covers a wide range of applications and operating mode ranging from 0.1A micro-plasma welding to high deposition applications operating at 450A with up to approximately 15kW of power.

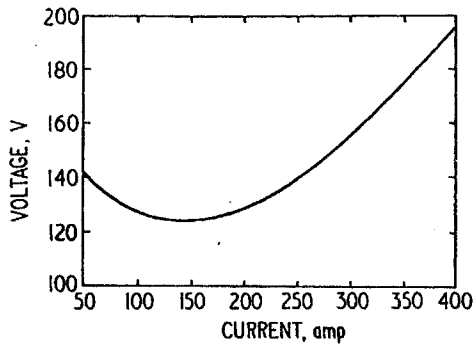


Figure 16 – Rising Arc Characteristic Curve with a Constricted Arc [5]

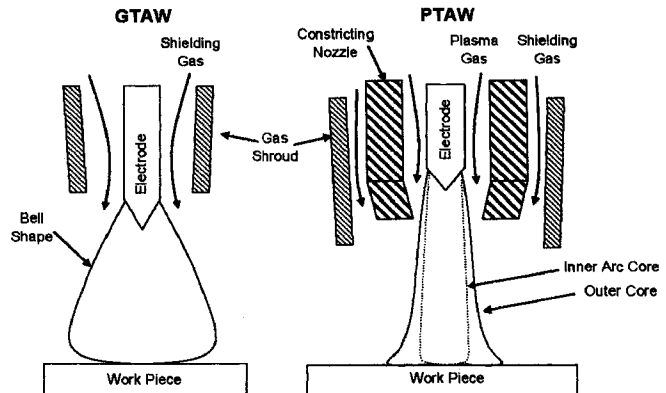


Figure 17 – Schematic Comparison of a GTAW and PTAW Torch

ii. Comparison to GTAW

Since PTAW is an extension of the GTAW, there are inherent similarities and distinct differences between the two processes. As shown in Figure 17, the combination of a setback electrode, a constricting nozzle, and auxiliary shielding gas physically constrict the arc. GTAW forms a conical or “bell” shaped arc, while PTAW forms a columnar shape with an inner arc core surrounded by a cooler sheath [34]. In order to avoid excessive anode melting and erosion, the arc column does not actually touch the nozzle. Rather, an annular layer of relatively cool, non-conductive (i.e., non-ionized) gas surrounds and positions the arc column, provides electrical and thermal insulation, and is necessary to avoid nozzle failure [38]. Hence, when compared to GTAW the current

density, temperature profile, and energy density are greatly increased; for example, power densities of $3 \times 10^{10} \text{ W/m}^2$ have been reported [13]. As shown in Figure 18, even a moderately constricted arc introduces a 30% increase in temperature and a 100% increase in voltage. Physical constriction also intensifies the plasma jet phenomenon, with jet velocities greater than that naturally occurring during the cathode spot mode of GTAW, which leads to greater penetration and deposition rates (i.e., higher welding speeds). The constriction acts as a pump, sucking cool gas from the cathode and propelling it towards low-pressure regions in the form of a plasma jet (see Figure 9). By varying the welding current, plasma gas flow rate, and welding speed, the plasma jet velocity is altered to suit the application and operating mode [12].

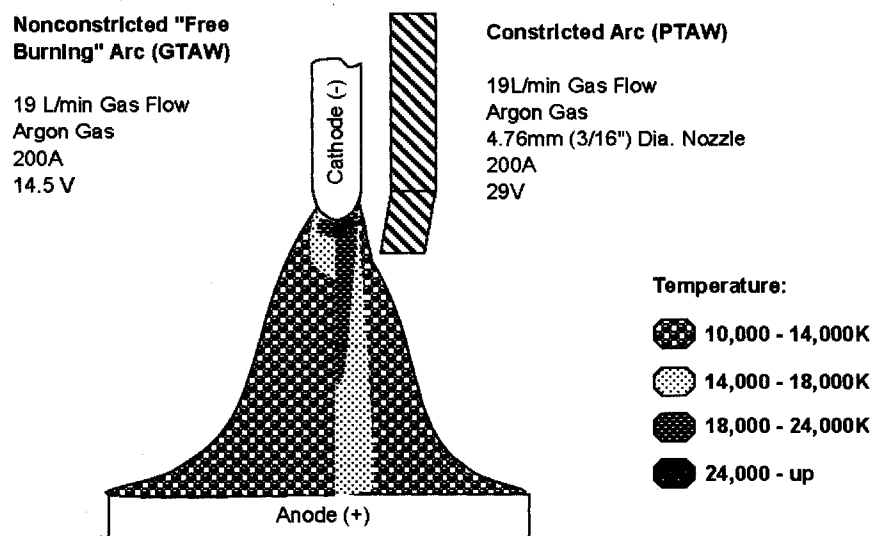


Figure 18 – Comparison of Temperature Profiles for Constricted and Non-constricted Arcs [38]

The constricted arc is much more stable and tolerant of arc length variations than GTAW for the entire range of operating currents and voltages. For example, at low currents GTAW requires a very short arc length, which is prone to instability, arc wandering, and

short-circuiting due to slight variations in the torch-to-work distance [39]. As shown in Figure 19, these slight changes also produce a large variation in the area of arc impingement on the work piece due to the conical arc shape. In comparison, the PTAW arc is columnar in nature, relatively stiff and less prone to these problems. For example, to produce a 20% change in arc cross-sectional area, the PTAW standoff must vary by 1.2mm, while a GTAW arc needs only a 0.12mm variation [40]. GTAW is limited to a minimum current level of 1A with the use of transistor controlled power sources; PTAW is stable down to 0.1A for micro-plasma welding of thin gage metals [39]. Since the electrode of the PTAW torch is recessed (hidden) behind both the gas shroud and constricting nozzle it is protected from physical damage. Work piece contamination, i.e., transmission of tungsten material to the weld pool causing the formation of inclusions, is also mitigated. During low current GTAW, where short arc lengths are required, it is common operator error to contact and subsequently contaminate the weld pool; likewise at high current due to excessive electrode tip heating and melting (especially if DC-EP or AC polarity is utilized). Due to the stable PTAW arc column, improved cooling capacity of the torch nozzle, and protection of the torch body, tungsten contamination is mitigated. The auxiliary shielding gas protects the arc, molten pool, and solidifying weld bead; the plasma gas flow, alone, is too turbulent and the area of impingement too narrow to provide adequate shielding. Hence, constricted arc welding tends to be more versatile, stable over a larger range of current and voltage, and able to operate with higher or lower deposition rates when compared to GTAW. PTAW has many more operating techniques and current modes when compared to GTAW that increases its versatility. The largest disadvantages of PTAW, when compared to GTAW, include the greater capital and

maintenance equipment costs, owing to more complex equipment setup and design [42].

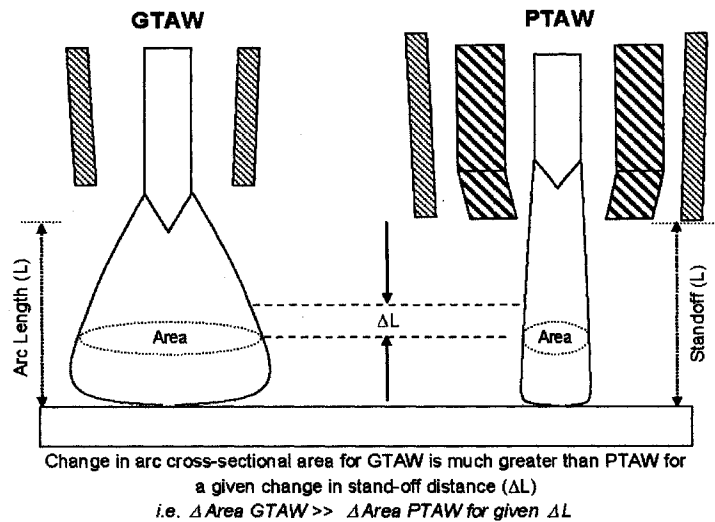


Figure 19 – Relative Tolerance in Standoff of GTAW and PTAW

iii. Operating Modes and Process Characteristics

During constricted arc welding, the process can be operated using either a transferred or non-transferred arc [41,42]. As shown in Figure 20, the transferred arc initiates an electrical connection between the electrode and the work piece and is, by far, the most common mode of operation. During non-transferred operation the arc is electrically connected to the constricting anode via external or internal grounding. The former is common for high gas flow rates and shorter nozzles, while the latter occurs for low flow rates and long nozzles [38]. This mode severely shortens torch life, but is necessary for applying coatings on non-conductive materials. The arc energy is “blown” onto the work piece via the shielding gas, which results in low energy transfer efficiency. Non-transferred mode is prone to “arc wander”, as the arc jumps among anode spots along the length of the copper nozzle. The non-transferred arc, also known as a pilot arc, is commonly used for initiating and stabilizing the main transferred arc. First, a high

frequency discharge ignites the low-current pilot arc between the electrode and the anode nozzle to energize the system. After the proper standoff is obtained, the pilot is blown to the work piece via the plasma gas. During most transferred arc operation, the pilot arc is extinguished once the main transferred arc is stabilized.

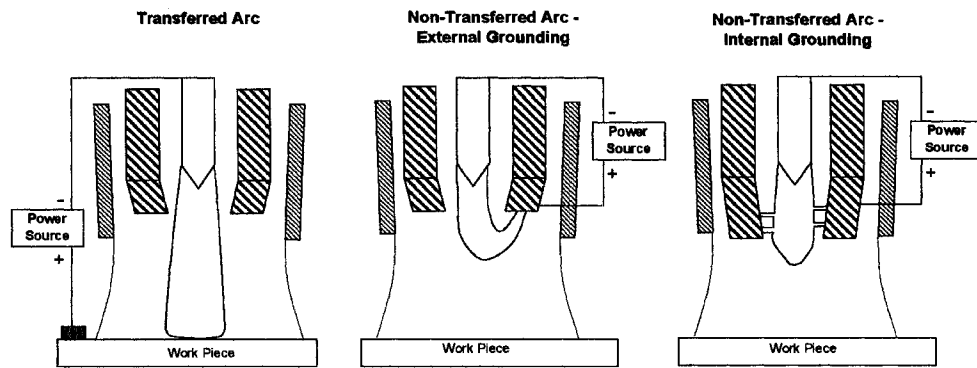


Figure 20 – Plasma Arc Welding Modes: Transferred and Non-Transferred

PTAW allows two different operating techniques; the melt-in mode and the keyhole mode [41]. During the “melt-in” mode, plasma impinges upon and penetrates into the work piece surface to form a molten pool; this technique is analogous to the classical form of GTA welding (see Figure 21). By sufficiently increasing the current and plasma gas flow, the arc completely penetrates the work piece and forms a concentric keyhole through the thickness [34,43]. As the arc travels forward, surface tension forces cause the molten weld metal to flow around the arc and re-solidify behind the keyhole (see Figure 22). Keyhole welding can be completed on mild steel for thicknesses up to 9.5mm [41], while thicknesses greater than that will require additional passes. There are specialized, proprietary nozzles that facilitate penetration up to 15mm for stainless steel alloys [13]. Other high power density processes, such as electron bead welding (EBW) and laser bead welding (LBW), are also able to form a keyhole weld. High-current GTAW is unable to produce the energy density and plasma jet velocity required to form a keyhole, and

instead forms fusion flaws [44].

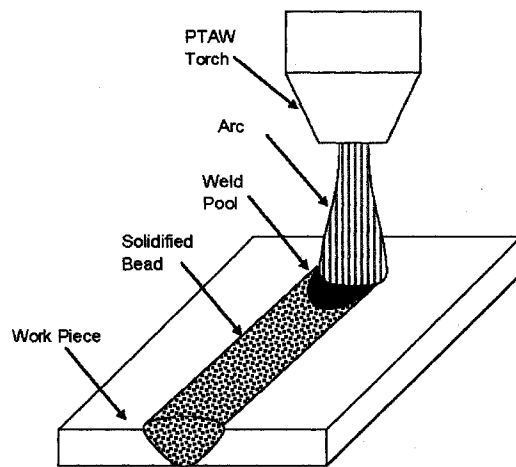


Figure 21 – Schematic of Melt-in Mode for PTAW

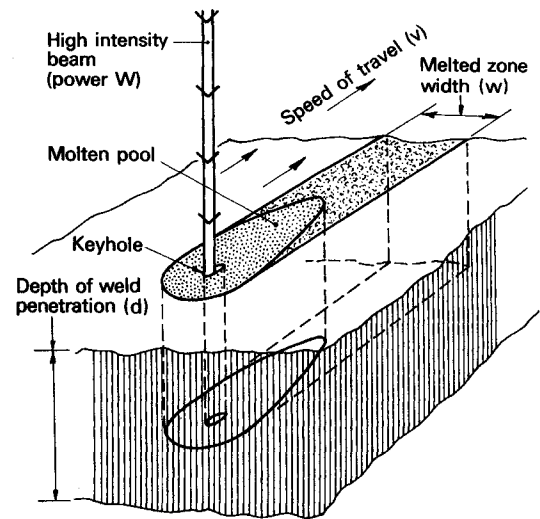


Figure 22 – Keyhole Welding Geometry for High Energy Density Processes [13]

PTAW is often further categorized based on the current level into three modes: micro-plasma, medium-current plasma, and keyhole plasma [42,45]. The micro-plasma mode is usually defined as the current range from 0.1 to 15 A, while medium-current mode includes up to 100 A; both these modes are completed with the melt-in technique. The keyhole plasma mode is typically above 100 A, but there is some inherent degree of overlap between these ranges due to the interactions of the other process parameters. For example, 70 A on a 2 mm (0.08 in.) steel sheet will result in keyhole formation, but only if the correct electrode diameter, vertex angle, and nozzle orifice diameter are selected while the optimized plasma gas flow rates are used within a specific range of welding speeds [42].

The most common polarity used is DC-EN, either continuous or pulsed current, utilizing a constant current power source. DC-EP is limited to low current applications to avoid electrode tip melting. A variable polarity plasma arc (VPPA) welding technique is

utilized for aluminum and manganese alloys, where the EP cycle removes the tenacious, stable refractory oxides (i.e., cathode sputtering) to produce exceptionally clean welds [46,47]; this method has even been used for space shuttle construction [48]. The use of square wave AC improves arc stability and eliminates rectification problems prone to sine wave AC welding. To regulate electrode and nozzle erosion, the maximum operating current is reduced below the torch rating associated with DC-EN. For example, a 175A DC-EN rated torch would have its current reduced by 43%, or down to 100A AC with 30% electrode positive half cycle, to maintain the proper electrode tip configuration [45]. The pulsed current mode, for both DC and AC polarity, is often used for keyhole welding. The peak current is used to penetrate the material and establish the keyhole, while the lower background current allows for the weld metal to cool; heat diffuses away and the weld metal partially solidifies to stabilize the keyhole. Utilizing pulsed current prevents complete melt-thru (i.e., cutting) and increases the useable range of tolerable welding parameters; for example, as shown in Figure 23 the tolerance box for continuous keyhole welding is half that of pulsed current operation.

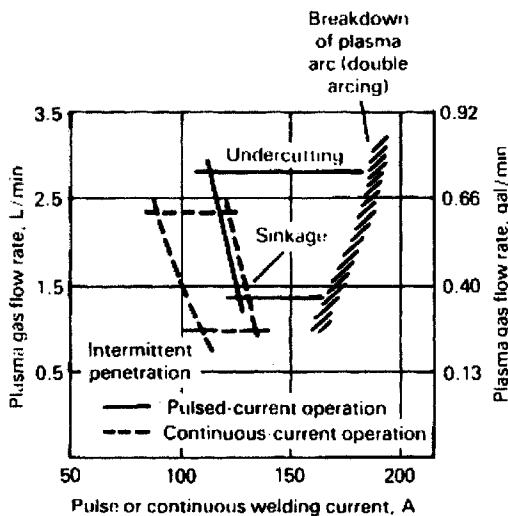


Figure 23 – Tolerance Ranges for PTAW Keyhole Welding [45]

2.3 Welding Gases and Properties

a. Importance to Arc Welding

As discussed in Section 1.1, the first shielding medium used was the gaseous products of oxyacetylene or oxyhydrogen combustion, and usually consisted of hydrogen, water vapour, carbon monoxide, and carbon dioxide [49]. The relative content of these combustion products can produce oxidizing, neutral, or reducing atmospheres and allows for specialized gas mixtures to suit specific materials. However, in modern welding processes the shielding gases are produced either via decomposition of a flux material or by direct metering into the weld zone. Argon, helium, carbon dioxide, nitrogen, hydrogen, and oxygen are by far the most common welding gases utilized during shielded arc welding, although other gases such as chlorine, fluorine, and freon gases have been investigated [50,51]. Table 2 lists the chemical and physical properties of interest for welding applications.

Table 2 – Chemical and Physical Properties of Common Arc Shielding Gases [12,13, 52,58,76]

Gas		Molecular Weight	Specific Gravity	Density g/L	Ionization potential eV	Dissociation Potential eV	Reactivity
Argon	Ar	39.95	1.38	1.78	15.7	-	Inert
Carbon dioxide	CO ₂	44.01	1.53	1.98	14.4	4.3	Oxidizing
Helium	He	4	0.14	0.18	24.5	-	Inert
Hydrogen	H ₂	2.016	0.07	0.09	13.5	4.5	Reducing
Nitrogen	N ₂	28.01	0.97	12.50	14.5	9.8	Active
Oxygen	O ₂	32	1.11	1.43	13.2	5.1	Oxidizing

Although the primary functions of the welding gases are to provide shielding from atmospheric contamination and provide a medium for stable arc operation, selection of the gas(es) has a significant influence on welding process behaviour and performance [53]. Previously in Section 2.1, the influence of the gas mixture on arc physics, arc

stability, and metal transfer was introduced. Other factors that are affected by changing the gas composition include welding production (increased travel speeds, deposition rates, arc efficiency), improved weld quality (weld penetration, flaw formation, bead profile, reduced spatter, and surface appearance), and the chemical/mechanical properties (corrosion resistance, strength, ductility, and toughness). Another increasingly important consideration is the generation of excessive welding fumes and ozone during welding [54]. The importance of the chemical and physical properties of welding gases will be expanded below.

b. Welding Gas Properties

The chemical and physical properties most relevant for arc welding are those that have the largest effect on arc stability, shielding effectiveness, arc energy, heat transfer, and weld pool behaviour.

i. Specific Gravity or Gas Density

Specific gravity (SG) is defined as the ratio of the density of a gas in relation to air, and is a relative indication of how well a mixture will displace the atmosphere during welding. This is important for protecting both the weld pool and electrode. At arc temperatures most gases and all metals are chemically active and a number of gas-metal reactions can ensue, which leads to porosity, inclusion formation, excessive oxidation, embrittlement, and dealloying of the weldment [17,55,56,76]. For both GTAW and PTAW the electrode must be protected from oxidation, or excessive arc instability will develop. The relative importance of gas density is shown by the comparison of argon (SG = 1.4) and helium (SG = 0.14). As shown in Figure 24, argon is very effective in engulfing the weld zone; helium, which is ten times less dense, abandons the region in a turbulent manner and is

much more prone to contamination under strong cross-draft conditions [76]. The net result is that when 25-30% or greater helium content is used, increased flow rates are required to simulate the same shielding effectiveness, as shown in Figure 25. Although hydrogen has a lower density, the same problems are not encountered since hydrogen content rarely exceeds 20% where the increased flow would be required [57].

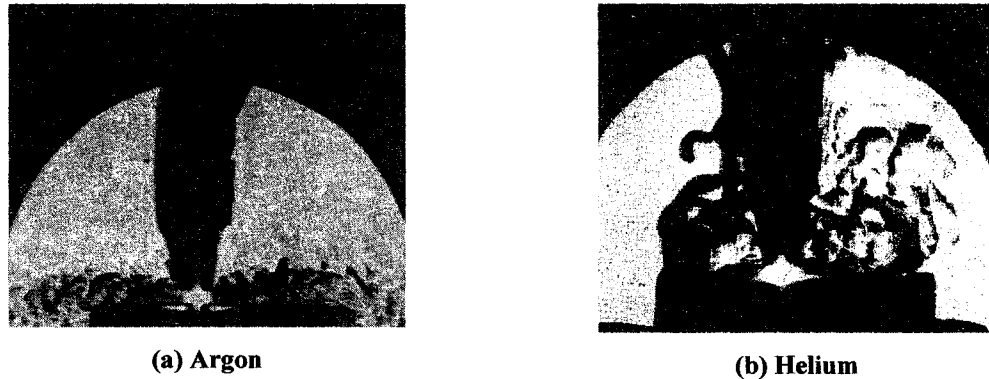


Figure 24 - Schlieren Photographs of Argon and Helium Gas Shielding During Arc Welding [49]

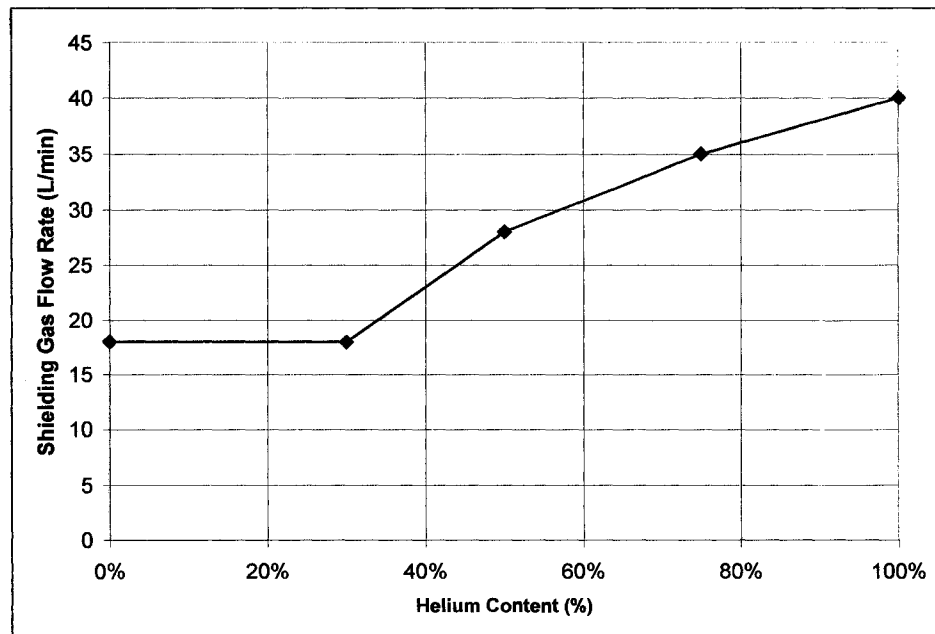


Figure 25 – Required Shielding Gas Flow Rate as a Function of Helium Content [57]

ii. Shielding Gas Efficiency - Gas Purity and Gas Flow

Typically, most industrial shielding gas mixtures have 99.9% purity, but depending on the particular metal being welded the importance of purity changes [58]. The residual elements, such as trace O₂ and N₂ in argon, are typically by-products from a fractional distillation process. Mild steel and copper are examples of metals with relatively high tolerances to contaminants, while aluminum and magnesium have a reduced tolerance to certain residual elements. Titanium and zirconium are examples of metals with extremely high sensitivity to impurities and extensive gas purging/shielding “glove box” systems are required [1,49].

Ensuring a proper shielding gas flow regime is required to provide adequate shielding. The importance of laminar flow as the shielding gas exits the torch nozzle, and avoiding air entrainment has been examined by other authors [53,59,60]. The shielding gas flow regime is expressed by the Reynolds number [59]:

$$R = \frac{Dv\rho}{\mu} \quad 6)$$

Where R is the Reynolds Number, D is the tube diameter, v is the average velocity, ρ is the gas density, and μ is the gas viscosity. If the Reynolds number for the gas flowing within the torch shroud exceeds 2300, then shielding gas effectiveness is greatly reduced due to turbulent flow. Hence, the inherent effectiveness of a shielding gas is partially related to its density and viscosity. For typical welding conditions the critical argon gas velocity, for transition to turbulent flow, is of the order of 1.5 to 2.5 m/s. Turbulent flow intensifies the progressive entrainment of air that subsequently enters the weld pool; greater entrainment occurs as the nozzle-to-work distance increases. Due to high plasma

jet velocities of the order of 100m/s, turbulent flow unquestionably exists within the central arc core region. However, plasma jet velocities decrease radially from the core [12], and laminar flow in the unionized, shielding gas region surrounding the arc is possible. The gas flow regime is also affected by the torch/nozzle design and gas delivery systems [59]. Often authors will provide “rules of thumb” for determining flow rates [60]; others have been created nomograms that predict the optimum flow rate to avoid excessive waste, while avoiding the formation of fusion flaws [61].

iii. Ionization Potential & Dissociation Reaction

The welding arc is maintained by the flow of current in a conductive medium of ionized gas. Arc stability, ease of initiation, and tolerance to sudden changes in length are directly linked to the ionization potential of the gas. The ionization potential is the energy required to remove an electron from the gas atom, normally expressed in the units of electron volts. Diatomic gases must first dissociate to the monatomic state, which is achieved by absorbing enough energy to rupture the valence bond holding the atoms together [13]. Dissociation and ionization are treated as separate reactions with their own associated energy level. As shown by the values listed in Table 2, argon arcs are much easier to initiate and are generally more stable, especially when used with variable polarity, than helium or diatomic gases [49,60].

As discussed in Section 2.1b, the ionization potential directly influences the arc column voltage gradient, which directly dictates the arc voltage (or maximum stable arc length). For example, the ionization potentials of monatomic elemental argon and hydrogen are 15.76 and 13.60 eV, respectively, yet the voltage gradients in argon and hydrogen are typically 0.7 V/mm and 4 V/mm, respectively [12,13]. The effect of the addition of

hydrogen to argon and helium is shown in Figure 26; the dominate effects of hydrogen on arc voltage are evident.

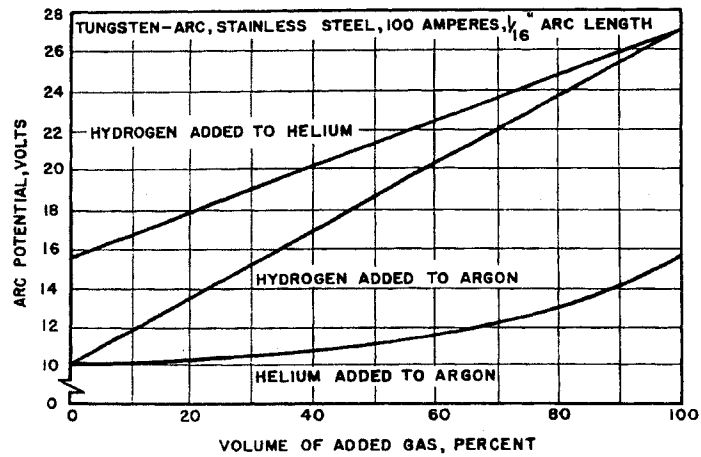


Figure 26 – Arc Potential as a Function of Shielding Gas Content [49]

The higher arc voltages are directly linked to the energy necessary to initiate and maintain dissociation of the hydrogen molecules, as shown by the endothermic enthalpy and entropy changes in Table 3.

Table 3 – Enthalpy and Entropy Changes for Dissociations Reactions [62]

	ΔH°	ΔS°
Reaction	(J/mol)	(J/K*mol)
$H_2 = 2H$	460,410	122.93
$O_2 = 2O$	513,460	134.89
$N_2 = 2N$	966,670	136.44
$CO_2 = CO + 1/2 O_2$	271,580	81.17
$H_2O = H_2 + 1/2 O_2$	253,550	58.87
NOTE: Free-energy change: $\Delta G = \Delta H^\circ - T \cdot \Delta S^\circ$		

The energy content of the diatomic gases increases substantially by virtue of molecular dissociation; large quantities of energy are added to the system to facilitate these

reactions with relatively small increases in temperature (see Figure 27). Upon cooling and recombination, this extra energy is liberated to the work piece; this additional energy transport mechanism increases productivity (i.e., penetration and speed) during welding and cutting [12,58,60]. For example, GTAW weld penetration of 304 stainless steel can increase over 50% with the addition of only 4 vol.% hydrogen to argon [63]. Diatomic mixtures are good for thick sections or materials with high thermal conductivity (such as aluminum or copper) as long as no deleterious gas-metal reactions occur (see Section 2.3b.v).

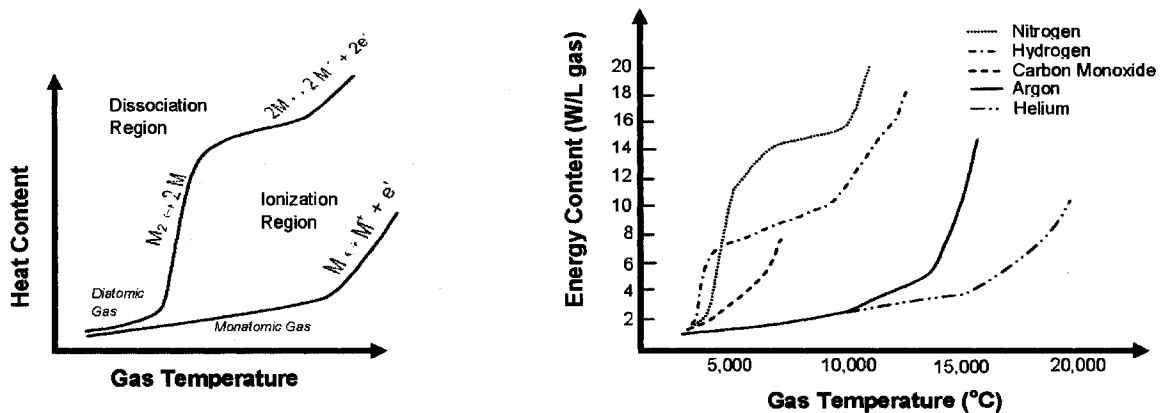


Figure 27 - Typical Heat Content as a Function of Gas Temperature for Diatomic and Monatomic Gases (left); Energy content as a Function of Gas Temperature for Various Gases (right) [35]

iv. Thermal Conductivity

Thermal conductivity is a measure of the relative ease by which a gas can dissipate heat. This property will influence radial heat loss from the arc column and heat transfer efficiency between the plasma and the weld metal or powder. Helium and dissociable gases have higher average conductivities when compared to argon, and therefore the plasma heat can be transmitted through a smaller volume of gas. This phenomenon affects the overall arc shape and size for free-burning arcs; additions of helium,

hydrogen, and nitrogen reduce arc diameter while length is proportional to the ionization potential [12,64]. As discussed in Section 2.2b, thermal conductivity determines the metal transfer mode for GMAW; plasma jet assisted metal transfer only occurs in argon dominated gas mixtures where the lower overall thermal conductivity permits envelopment of the electrode tip [27,28]. Higher thermal conductivity gases constrict the arc plasma, relative to argon, which leads to higher energy concentration [65]. Hence, greater penetration and travel speeds are possible with diatomic gases due to the combined affects of the dissociation/ionization reactions and higher thermal conductivities [57,66].

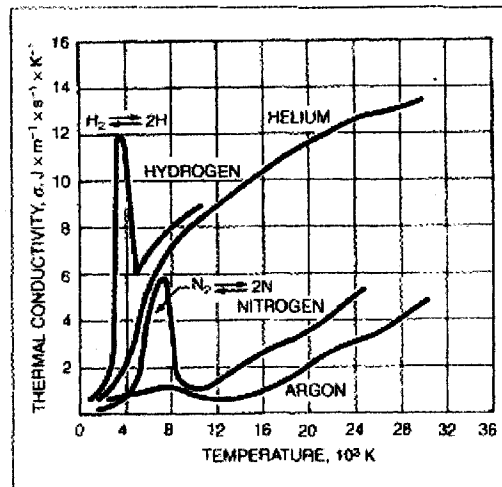
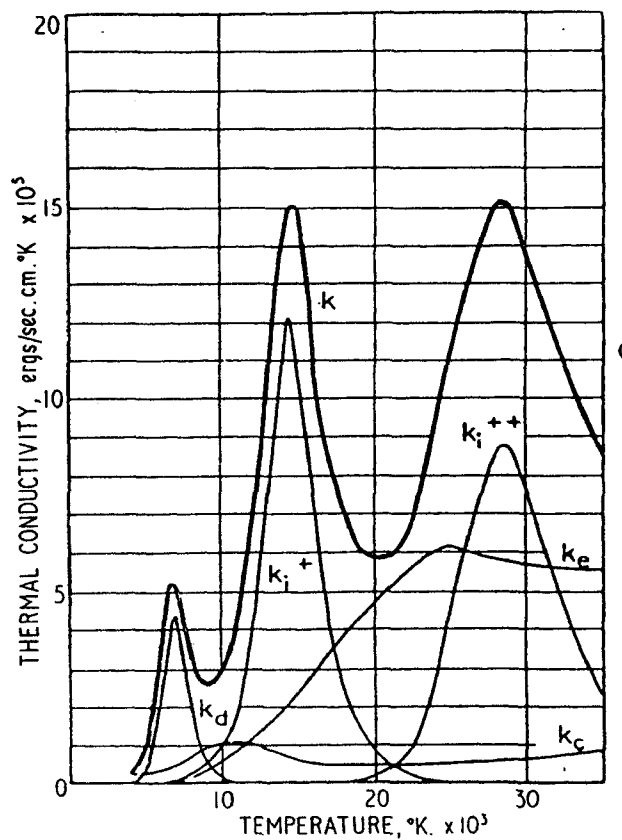


Figure 28 – Thermal Conductivity of Common Welding Gases [8,52]

Dissociable gases also experience “spikes” in the thermal conductivity, as shown for nitrogen in Figure 29, which are correlated to the dissociation and ionization reactions. As discussed above, diatomic gases consume large amounts of energy for relatively small changes in temperature during these reactions, which increases the effective thermal conductivity of the gas. This results in a steep thermal conductivity gradient as a function

of temperature at each spike. Hence, up the temperature gradient and towards the arc core there is a sharp transition to much higher thermally conductive plasma; this leads to the formation of an internal sub-structure or inner core with a clearly defined boundary that can be observed experimentally [12].



k_e The classical conductivity due to the microscopic motions of the atoms and ions
 k_e The classical conductivity due to the microscopic motions of the electrons
 k_d Conductivity due to the diffusion of molecules and associated atoms
 k_i^+ Conductivity due to the diffusion of electrons and singly ionized atoms
 k_i^{++} Conductivity due to the diffusion of electrons and doubly ionized atoms

Figure 29 – Thermal Conductivity of Nitrogen [12]

v. Gas Reactivity and Physiochemical Behaviour

At arc temperatures, all known metals are chemically active. However, noble gases such

as argon and helium are non-reactive, insoluble in the molten metal, and have no direct chemical effect on the weld pool. Physiochemical behaviour, such as molten pool surface tension, is only *indirectly* affected by changes in arc and pool temperature for inert gases. For example, the hotter arc and higher weld pool temperatures associated with helium gas mixtures reduces molten pool surface tension and viscosity, which improves wetting, fluidity, and reduces fusion flaws such as undercutting [67].

Both oxygen and carbon dioxide are oxidizing gases; recall that carbon dioxide will dissociate into carbon monoxide and oxygen at arc temperatures. These gases will oxidize the weld pool, a common reaction observed during the welding of steel. However, if chemically active de-oxidizing element such as aluminum, silicon, magnesium, and titanium are present the excess oxygen becomes “tied-up” in the form of stable oxides. Some oxidation potential has been found to improve fluidity, bead coalescence and reduce undercutting; which was attributed to the lowering of the liquid-to-air interface energy (or surface tension) [40,49]. Surface tension of molten steel droplets was also reduced in the presence of shielding gases containing oxygen and carbon dioxide during GMAW [68]. Oxygen or carbon dioxide cannot be utilized to establish the arc for non-consumable electrode processes such as GTAW and PTAW. Tungsten alloy electrodes will become excessively oxidized at thermionic temperatures, which leads to reduced cathode spot stability (i.e., cathode shifting), and tungsten erosion and contamination of the weld pool [49]. A slightly oxidizing environment is employment during the consumable electrode process (GMAW) to improve arc stability and allow for spray metal transfer during the welding of steels [69,70]. However, excessive oxidizing potential in the shielding gas has a negative influence on weldment

strength, impact toughness, fatigue behaviour, and corrosion resistance for steels, stainless steels, and reactive materials such as titanium [1, 57].

Surface oxides are reduced by the addition of hydrogen gas to the arc zone, which improves the bead surface appearance. The use of hydrogen gas for welding of austenitic stainless steels (300 series) is common practice as it improves fluidity, bead contour, and eliminates undercutting [49,60,76]. Cleaner welds are produced because chromium oxide is reduced, leaving greater chromium content in the weld metal and water vapour by-products. These effects occur although it has been found that hydrogen additions increase the surface tension of stainless steel under welding conditions [71]. Often 15% or less hydrogen is recommended due to the deleterious metallurgical effects of excessive dissociable hydrogen to some welds. For example, ferritic and martensitic alloys are susceptible to hydrogen assisted cracking (HAC) and porosity, while titanium can become embrittled, and both aluminum and tough pitch copper are prone to porosity formation [1,57,60,76].

Nitrogen additions, ranging from 10% to 20%, exhibit high heat input and efficiency due to the molecular recombination energy, and are very popular for high diffusivity materials such as copper [72]. Unlike oxidizing gases, nitrogen does not exert adverse effects on the tungsten electrode [49], and the weld pool surface tension remains unchanged relative to argon [71]. Nitrogen absorption and the subsequent porosity in ferritic materials is primarily a function of the oxidizing potential of the shielding gas stream [73,74]; ferritic weld metals deposited in an arc atmosphere of 6% nitrogen generally lead to porosity [70]. The use of nitrogen gas is often avoided due to possible formation of nitrides in ferrous and reactive materials, which causes weld embrittlement

and loss of corrosion resistance [75,76,77]. Hence, gas mixture combinations must be carefully selected to mitigate fusion flaws.

2.4 General Literature Review Summary

The major principles of welding history, arc physics, non-consumable and consumable welding processes, and gas properties were outlined in the general literature review. The unique operating parameters associated with the constricted arc were also explored, and the various modes of PTAW operation were introduced. With the fundamental understanding of these industrial and scientific principles, the specialized operation of PTAW can be investigated. In subsequent Chapters, two unique applications of PTAW will be explored: *Part 1: PTAW Autogenous Welding* and *Part 2: PTA Welding of Metal-Matrix Composite (MMC) Overlays*. An introductory literature review is completed for those sections to introduce the application and explore previous works completed therein.

CHAPTER 3 – Part 1: PTAW Autogenous Welding

3.1 Project Objectives

Based upon the forthcoming review, it will become clear that the majority of investigations into plasma transferred arc welding (PTAW) are based on the keyhole mode of operation. The portion of the literature based on the melt-in technique is typically concerned with micro-plasma welding [78,79]. Hence, the transition region between micro-plasma and keyhole operation, or normal plasma operation, becomes the focal point for this autogenous welding study. Utilizing a simple “bead-on-plate” system, i.e., no filler material added, the autogenous weld behaviour and bead formation were a direct result of interactions between the base material, process parameters, and welding arc. This experimental method provided optimal means to explore process parameters of influence, such as base material composition, heat input, arc constriction, and gas composition. Finally, a repetitive and reproducible weld flaw was found to form under certain operating conditions. The capstone was to understand this humping flaw formation mechanism, determine the welding parameters of influence, and finally eliminate its formation.

3.2 Previous Investigations of PTAW

The fundamentals parameters and early developments for the plasma transferred arc process were introduced in Chapter 2. The following outlines the work of others to further advance the science and technology of PTAW. The initial work completed during the 1970s was concerned with optimizing keyhole operation. To summarize, work was completed to utilize automated feedback control systems to optimize operation [80], monitor keyhole stability [81], and develop heat transfer efficiency models [82]. In

more recent years, others have advanced the modeling of plasma arc heat transfer [83,84], simulated weld pool flow and keyhole stability [85,86,87], and proposed methods for optimizing overall operation [88].

In the 1980s and 1990s, studies were completed to characterize the operating characteristics of the transferred arc system. Choi [89] examined transferred arc behaviour in a specially designed chamber and confirmed the strong relationship between arc length and voltage, and that the gas plasma flow rate appears to have a greater influence on voltage, compared to the effect of current. It was recommended that different gas mixtures be investigated to understand changes in operating characteristics. Mehmetoglu and Gauvin [90] determined the potential distribution along the arc length. The general shape of the curve mirrored Figure 2; the cathode fall region was relatively large compared to the anode fall region. They also stressed the interdependence of the arc voltage gradient on both current and plasma gas velocity. For the conditions examined, plasma temperatures were of the order of 20,000K and plasma jet velocities reached 100-200 m/s; this data correlates well with the values discussed in Section 2.1. Richardson [91] conducted experiments with a transferred arc system at elevated pressures (i.e., greater than ambient). Both argon and helium/argon plasma gas mixtures were used. Process behaviour, system efficiency, and weld bead characteristics were determined for various pressures and compared to GTAW behaviour.

There has been much interest into the optimization of variable polarity plasma arc (VPPA) operation throughout the 1980s and 1990s. Hou [92] was able to ascertain the flow patterns of the welding gas under various conditions to minimize undercutting weld flaws during VPPA keyhole operation. A modified torch design that optimizes shielding

gas efficiency and requires lower flow rates was presented. Arc efficiency for VPPA was found to vary from 0.47 to 0.60 in the experiments completed by Evans [93]. Other works in the area included the determination of the dominant cathode cleaning mechanism and heat transfer efficiency as a function of polarity [46,47]. Martinez *et al.* [94] explored the variation in aluminum melt size through systematic changes in both the plasma and shielding gas for VPPA; differences in both arc shape and melt zone size were obtained by varying argon and helium content in the shielding and plasma gas streams.

In order to exploit process benefits of the constricted arc, there have been hybrid-process developments that combine PTAW with another welding process. A common example is the plasma gas metal arc welding process (PGMAW), also known as plasma-MIG, developed at the Philips Research Laboratories in the Netherlands around 1969 [95]. This process utilizes a main plasma torch in transferred mode, while consumable wire is fed into the constricted arc area, melted, and transferred to the weld pool. If the filler wire is energized with a separate power source, the melting rate and deposition efficiency increase. Areskoug and Widgren [96] showed that by varying torch head oscillation and motion patterns this process can be utilized for cladding operations. Schultz [97] introduced an intermediary process between GTAW and PTAW, known as TIG with dual shielding. This process does not use a solid copper nozzle to constrict the arc, but rather relies on the “kinetic confinement” of the auxiliary shielding gas. Under specific conditions, advantages over both GTAW and PTAW were observed, such as reduced distortion and higher welding speeds. Another unique development for plasma arc welding was the use of a third gas stream emanating from the center of a hollow tungsten electrode, which stabilizes the arc, increases tolerances to arc length changes, and

helium, and hydrogen gas mixtures for the keyhole welding of aluminum, stainless steel, and high strength steel. They found that the specific gas combinations that optimized productivity and process efficiency were strongly dependent on the base material, i.e., 50% increased production for 316L was achieved with argon – 50% helium. A significant conclusion was that argon-helium mixtures had narrow operating windows during which the keyhole operation was stable; they also recommended that the benefits of such mixtures be investigated for the plasma melt-in technique.

There has been comparatively less work completed on either understanding or improving the PTAW melt-in technique with autogenous welds. To date, researchers and industry must rely on GTAW behaviour to approximate PTAW process operation. For example, a comprehensive analysis was completed by Key [106] to determine the dependence of arc shape and weld dimensions on both the cathode geometry and shielding gas. It was determined that arc shape varies considerably with the electrode vertex angle, and can range from the classical “bell” shape to a more constricted form; weld dimensions were strongly influenced by the gas composition. It has not been verified what effect a physically constricted arc has on these interrelationships. Hence, the range of operation between micro-plasma and the keyhole mode was chosen for the following experiments. Due to the lack of data in the literature, the results will be compared to similar GTAW studies where appropriate.

3.3 Summary

To date, the majority of investigations into plasma transferred arc welding are based on the keyhole mode of operation. The region between micro-plasma and keyhole operation remains relatively unexplored and unknown. The following bead-on-plate experiments

aim to better understand the effects of welding parameters on process behaviour, bead development, and flaw formation.

3.4 Materials and Equipment

a. Materials

Three different types of steel were used during the autogenous welding investigations. The first type was basic structural plate of type CSA G40.21-2004 Grade 300W in 12.7 mm (1/2 in) gauge thickness, the specified and actual plate chemistries are given in Table 4. Two different heats of ASTM A656 – Grade 80 structural steel were used; these microalloyed steel heats were produced via thermo-mechanical controlled processing (TMCP) techniques. The composition of Heat #1 is given in Table 5 and Heat #2 in Table 6; the thicknesses were 12.7 mm (1/2 in) and 7.9 mm (5/16 in) respectively. All elements, except cerium, nitrogen and oxygen, were determined via spark analysis. Oxygen and nitrogen content was determined using the LECO nitrogen/oxygen analyzer. Cerium was determined using inductively coupled plasma - mass spectrometry (ICP-MS). The compositions were within specification limitations.

Table 4 – Chemical Analysis of Grade 300W Structural Steel

Element		Plate Chemistry	
		G40.21 - Grade 300W Spec. Requirements:	Actual Heat Composition
C	Carbon	0.22 max.	0.18
Mn	Manganese	0.5 – 1.50	0.61
P	Phosphorous	0.04 max.	0.011
S	Sulphur	0.05 max.	0.031
O	Oxygen	Not Specified	0.024
Si	Silicon	0.40 max.	0.20
Al	Aluminum	Not Specified	<0.003
Ti	Titanium	Not Specified	<0.001
V	Vanadium	*Note	0.001
Cr	Chromium	Not Specified	0.12
Ni	Nickel	Not Specified	0.11
Co	Cobalt	Not Specified	0.007
Mo	Molybdenum	Not Specified	0.031
Nb	Niobium	*Note	<0.001
N	Nitrogen	Not Specified	<0.01
Cu	Copper	Not Specified	0.32
W	Tungsten	Not Specified	0.008
Ca	Calcium	Not Specified	<0.0002
B	Boron	Not Specified	<0.0002
As	Arsenic	Not Specified	0.004
Sn	Tin	Not Specified	0.014
Ce	Cerium	Not Specified	<0.0001
Fe	Iron	Not Specified	Balance
*Note: grain refining elements – 0.10 max.			

Table 5 - Chemical Analysis of A656 Grade 80 Structural Steel - Heat #1

Element		Plate Chemistry	
		A656 Spec. Requirements:	Actual Heat Composition
C	Carbon	0.18	0.052
Mn	Manganese	1.65	1.09
P	Phosphorous	0.025	0.007
S	Sulphur	0.035	0.003
O	Oxygen	Not Specified	0.016
Si	Silicon	0.60	0.13
Al	Aluminum	Not Specified	0.032
Ti	Titanium	Not Specified	0.002
V	Vanadium	0.08	0.001
Cr	Chromium	Not Specified	0.074
Ni	Nickel	Not Specified	0.16
Co	Cobalt	Not Specified	0.009
Mo	Molybdenum	Not Specified	0.059
Nb	Niobium	0.008 – 0.10	0.035
N	Nitrogen	0.020	<0.01
Cu	Copper	Not Specified	0.37
W	Tungsten	Not Specified	0.014
Ca	Calcium	Not Specified	0.0025
B	Boron	Not Specified	<0.0002
As	Arsenic	Not Specified	0.004
Sn	Tin	Not Specified	0.017
Ce	Cerium	Not Specified	<0.0001
Fe	Iron	Not Specified	Balance

Table 6 - Chemical Analysis of A656 Grade 80 Structural Steel – Heat #2

Element		Plate Chemistry	
		A656 Spec. Requirements:	Actual Heat Composition
C	Carbon	0.18	0.064
Mn	Manganese	1.65	1.52
P	Phosphorous	0.025	0.014
S	Sulphur	0.035	0.006
O	Oxygen	Not Specified	0.016
Si	Silicon	0.60	0.15
Al	Aluminum	Not Specified	0.033
Ti	Titanium	Not Specified	0.033
V	Vanadium	0.08	0.037
Cr	Chromium	Not Specified	0.21
Ni	Nickel	Not Specified	0.27
Co	Cobalt	Not Specified	0.012
Mo	Molybdenum	Not Specified	0.29
Nb	Niobium	0.008 – 0.10	0.087
N	Nitrogen	0.020	<0.001
Cu	Copper	Not Specified	0.39
W	Tungsten	Not Specified	0.024
Ca	Calcium	Not Specified	0.0031
B	Boron	Not Specified	<0.0002
As	Arsenic	Not Specified	0.008
Sn	Tin	Not Specified	0.041
Ce	Cerium	Not Specified	<0.0001
Fe	Iron	Not Specified	Balance

b. Equipment

The PTAW autogenous experiments were carried out using a Eutronic GAP 3000 AC/DC constant current power source, EP 1 powder feeder, and GAP E 52 torch, as shown in Figure 30 and Figure 31. The thoriated-tungsten electrode was 4mm in diameter; ground to an angle of 20° with a 0.5 mm diameter tip. The electrode setback distance was maintained at 1 mm above the lower edge of the plasma nozzle bore for all experiments. The torch was stationary and the work piece was moved via a computer numerically controlled (CNC) welding table. Torch motion, welding speed, and the torch-to-work distance were set prior to each weld run. All runs were recorded using a Sony DXC-390 1/3-type three-chip CCD digital camera with 770 (horizontal) by 500 (vertical) effective picture elements operating at 30 frames per second with a shutter speed of 1/4000. The filter pack included one polarizing filter, three ND4 and one ND2 neutral density filters, and a P-452 protective lens with a welders clear cover plate. High magnification images were obtained using a C-mount video microscope lens. Ambient lighting, which floods the entire weld zone, was provided by an ARRISUN 12 HMI light source.

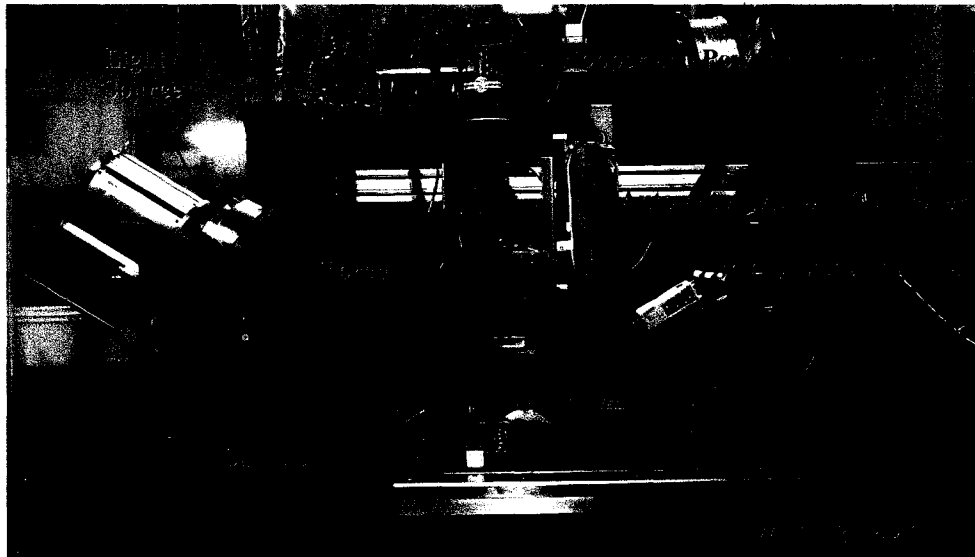


Figure 30 – PTAW Equipment Assembly

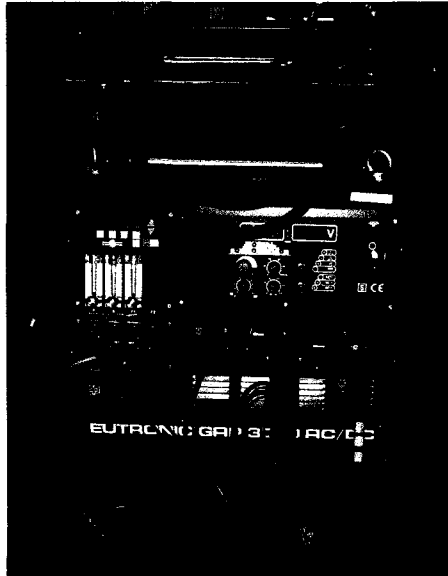


Figure 31 – PTAW Eutronic GAP 3000 AC/DC Power Source

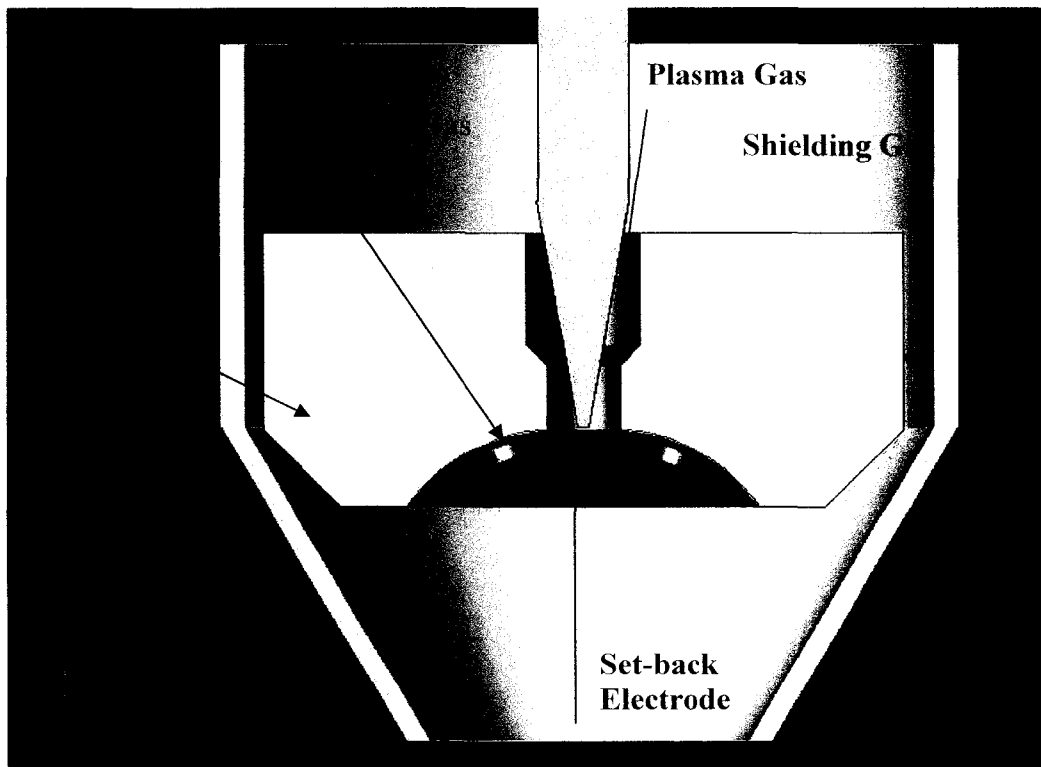


Figure 32 – Cross-Section of GAP E 52 Torch

c. Metallurgical Samples

i. Macro-Samples

All samples that were prepared solely for macro-analysis were not mounted in bakelite and were prepared manually. Progressively finer SiC sand papers, i.e., 240, 320, 400, and 600 mesh grit, were used for grinding of specimens. When moving from coarser to finer paper, the specimen was thoroughly rinsed with water to clean off contaminants. The sample was also rotated 90° degrees between stages in order to recognize when coarse scratches were replaced with fine ones. Samples were then given a rough polish with 6µm diamond in a water-based carrier. As required, fine polishing was completed with 1µm diamond and 0.05µm alumina in water-based carriers. The samples were then photographed using a Nikon FinePix digital camera. As required, a Bausch & Lomb stereoscope was used for higher magnification macro images.

ii. Micro-samples

All samples that were difficult to handle or required micro-analysis were mounted in 38 mm (1.5 in) Bakelite molds using a Struers automated sample mounter with all parameters set to resin specifications. The samples were then ground and polished according to the following procedure with a Buehler Automet 2 Polisher:

1. Grinding

Medium:	200 – 600 grit SiC sandpaper
Time:	3 minutes
Wheel Speed:	240 rpm
Force:	31 N/sample (7 lbs/sample)
Wheel Direction:	Counter clockwise
Sample Direction:	Clockwise

2. Rough Polishing

Medium:	6 μ m diamond in water-based carrier
Time:	3 – 5 minutes
Wheel Speed:	180 rpm
Force:	22 N/sample (5 lbs/sample)
Wheel Direction:	Counter clockwise
Sample Direction:	Clockwise

3. Fine Polishing I

Medium:	6 μ m diamond in water-based carrier on nylon cloth
Time:	3 – 5 minutes
Wheel Speed:	180 rpm
Force:	22 N/sample (5 lbs/sample)
Wheel Direction:	Counter clockwise
Sample Direction:	Clockwise

4. Fine Polishing II

Medium:	1 μ m diamond in water-based carrier on nylon cloth
Time:	3 – 5 minutes
Wheel Speed:	180 rpm
Force:	22 N/sample (5 lbs/sample)
Wheel Direction:	Counter clockwise
Sample Direction:	Clockwise

5. Fine Polishing III

Medium:	0.05 μ m alumina in water-carrier on micro-polishing cloth
Time:	3 – 5 minutes
Wheel Speed:	180 rpm
Force:	22 N/sample (5 lbs/sample)
Wheel Direction:	Counter clockwise
Sample Direction:	Clockwise

In between each stage, the sample was cleaned via thorough rinsing in water and acetone.

All samples were etched with a 2% Nital solution. The micro-images were captured using an Olympus PMG 3 microscope and Quartz PCI V.5 imaging software.

d. Calibration of equipment

i. Table Motion

The CNC table motion was calibrated to ensure proper welding speeds were obtained in the x- and y-direction as indicated in Figure 30. Depending on the camera view required, welds were completed in either the x- or y-direction. A series of runs was completed, as shown in Table 7, with stationary reference points to find the disparity between the CNC speed setting and the actual speed of the table.

Table 7 – Calibration Runs for CNC Welding Table

Speed Setting		Travel Time (s)	Actual Speed	
mm/s	in/s		mm/s	in/s
6.4	0.25	31.4	6.4	0.25
12.7	0.50	15.8	12.7	0.50
19.1	0.75	10.4	19.2	0.76
25.4	1.00	7.8	25.6	1.01
31.8	1.25	6.3	31.7	1.25
38.1	1.50	5.2	38.5	1.51
38.1	1.50	5.1	39.1	1.54
44.5	1.75	4.5	44.2	1.74
44.5	1.75	4.5	44.2	1.74

Next, a series of runs was completed at a constant welding rate of 12.7 mm/s (0.5 in/s) to determine the average deviation of the actual table speed. As shown in Table 8, the average deviation of travel time is very low.

Table 8 – Determination of the Variability in Actual Welding Speed of the CNC Welding Table

Speed Setting		Travel Time (s)	Actual Speed	
mm/s	in/s		mm/s	in/s
12.7	0.50	15.8	12.7	0.50
12.7	0.50	15.7	12.8	0.50
12.7	0.50	15.7	12.8	0.50
12.7	0.50	15.8	12.7	0.50
12.7	0.50	15.6	12.8	0.50
Average:		15.7	13	0.50
Average Deviation		0.05	0.04	0.002

Note: Average deviation is the average of the absolute deviations of data points from their mean and is a measure of the variability in a data set.

The following calibration curve (Figure 33) was produced from this data and illustrates the extremely low percent error associated with the table motion. Hence, in all experimental data the welding speed indicated is, in-fact, the true welding speed obtained and no correction factors are required.

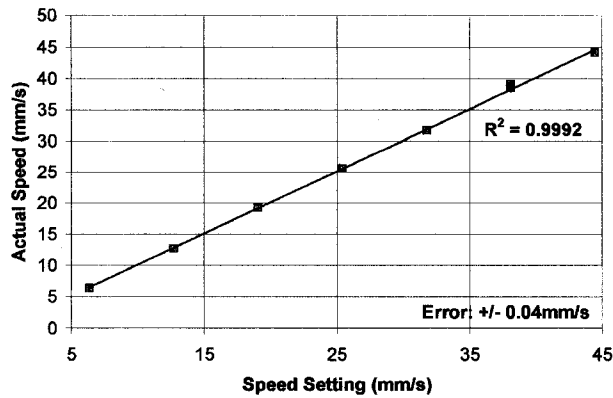


Figure 33 – Calibration Curve for CNC Welding Table Motion

ii. Power Source

The static voltage-current characteristics curve of the Eutronic GAP 3000 AC/DC power source was determined. As mentioned in Section 2.1f, constant current (CC) power sources can have slight “droop” in their voltage-current curve by changing the internal inductance (also known as slope control). The true nature of the CC power source was therefore sought. An external resistance was formed (nicknamed R2D2) and the power source initiated a current to complete the circuit. R2D2 has various resistance settings that simulate the welding arc, which can have differing resistance depending on the particular welding conditions. As shown in the top view of Figure 34, there are 19 electrical contact points along the middle, and two side points labeled “A” and “B”. The internal schematic illustrates that by varying the contact points in the circuit, 38 unique

resistance levels typical for welding arcs are obtainable. By completing a circuit at all 38 resistance “steps”, the power source static characteristics can be quantified.

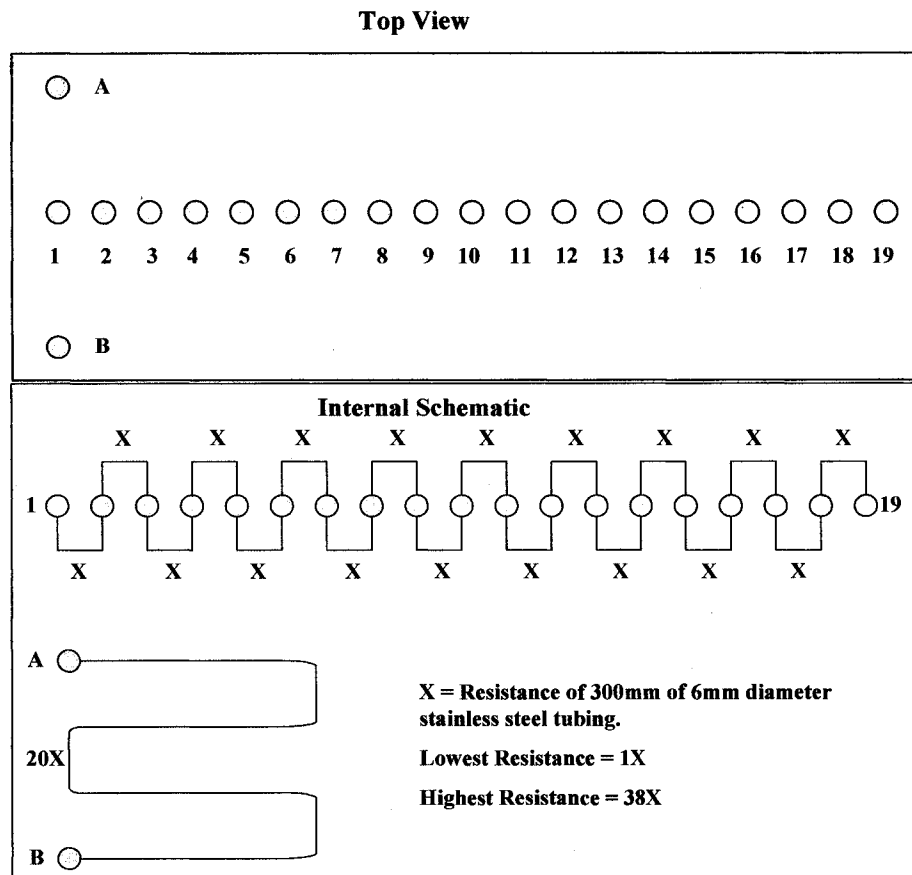


Figure 34 – Variable External Resistance (R2D2): Top View and Internal Schematic

As shown in Figure 35, the power source produces a constant curve for currents levels of approximately ≤ 125 A. At high currents and voltages there is some slight droop to its behaviour, but constant current behaviour is obtained up to 30V. During most PTAW operations it is uncommon for the voltage to exceed 30-35V, since such a large standoff results in poor shielding. Thus, for practical welding purposes it can be stated that the Eutronic GAP 3000 AC/DC is a true constant-current power source.

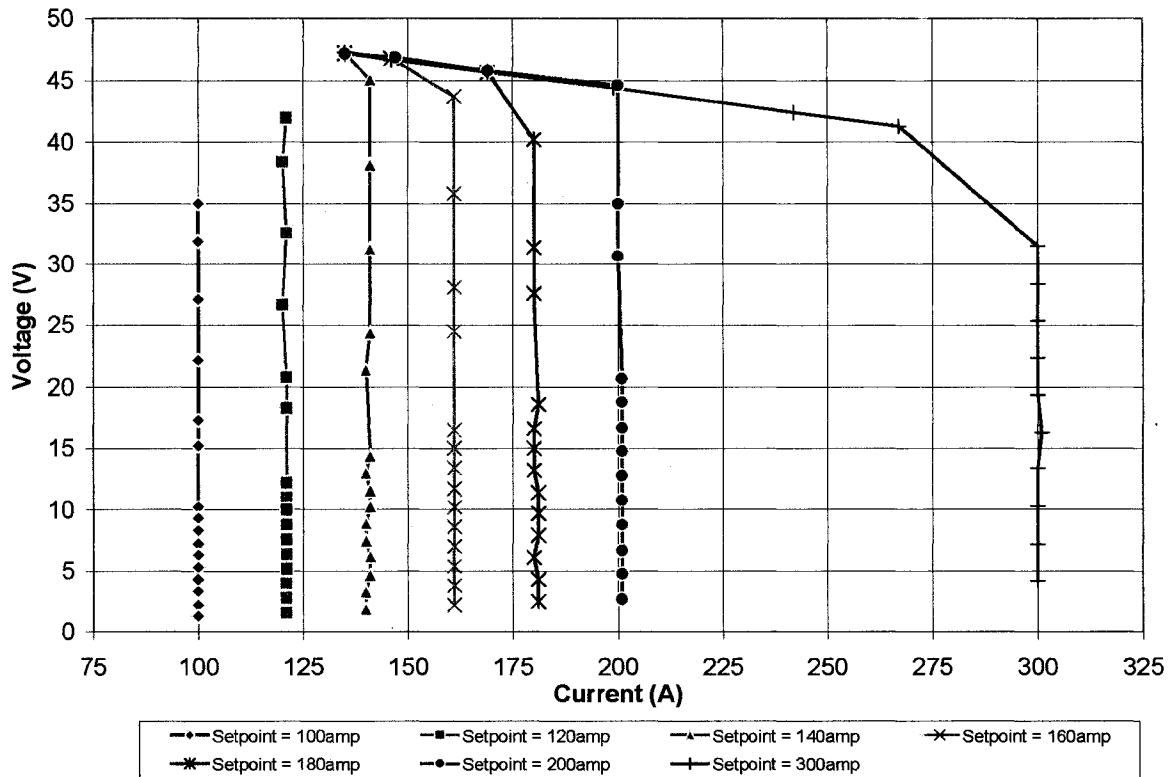


Figure 35 – Voltage-Current Curve of Eutronic GAP 3000 AC/DC Constant Current Power Source

iii. Gas Flow Rates

The gas flow valves on the GAP 3000 were previously calibrated for argon flow only. Various experimental gas mixtures were used and gas correction factors were calculated [107,108]. The gas correction factor is not simply the weighted average of each component, but rather calculated (relative to nitrogen) by the following equation:

$$GCF = \frac{0.3106(a_1s_1 + a_2s_2 + \dots + a_ns_n)}{a_1d_1c_{p1} + a_2d_2c_{p2} + \dots + a_nd_nc_{pn}} \quad (7)$$

Where a_1 to a_n are the fractional flows (or compositions) of gases 1 to n ; s_1 to s_n are the molecular structure factors; d_1 to d_n are the standard densities; and c_{p1} to c_{pn} are the specific heat capacities. These values can be readily obtained from various industrial handbooks. Molecular structure correction factors are: 1.030 for monoatomic gases,

1.000 for diatomic gases, 0.941 for triatomic gases, and 0.880 for polyatomic (four or more atoms) gases. The gas correction factors (GCF) relative to a nitrogen basis are easily calculated; these standard GCF values are given in Table 9.

Table 9 – Standard GCF Values for Nitrogen Basis

Standard GCF	
Argon	1.39
Carbon Dioxide	0.7
Helium	1.45
Hydrogen	1.01
Nitrogen	1

The GCF for a gas mixture of known composition or partial flow rates can be calculated by the following equation [108]:

$$GCF(mixture) = a_1 \times GCF_1 + a_2 \times GCF_2 + \dots + a_n \times GCF_n \quad (8)$$

Where a_1 to a_n are the fractional flows (or compositions) of gases 1 to n, and GCF_1 to GCF_n are the gas correction factors of gases 1 to n. The calculated GCF values for the gas mixtures used in these experiments are summarized in Table 10.

Table 10 - GCF Values for Gas Mixtures Relative to Nitrogen and Argon

Gas Mixture	GCF - Nitrogen Basis	GCF - Argon Basis
100% Argon	1.39	1.0
Ar-20% CO ₂	1.252	0.901
Ar-25% He	1.405	1.011
Ar-10% H ₂	1.352	0.973
Ar-25% N ₂	1.2925	0.930

Since the flow valves on the power source were calibrated for pure argon flow, these gas correction factors must be converted from the nitrogen to an argon basis. This is accomplished by dividing each value by the standard argon GCF (i.e., 1.39), as shown in Table 10. These final gas conversion factors determine the linear relationship between the

calibrated argon flow and actual gas mixture flow; the disparity between the two values is largest at high gas flow rates. Note that the slopes of the lines in Figure 36 are the GCF values (argon basis) for the respective gas mixture.

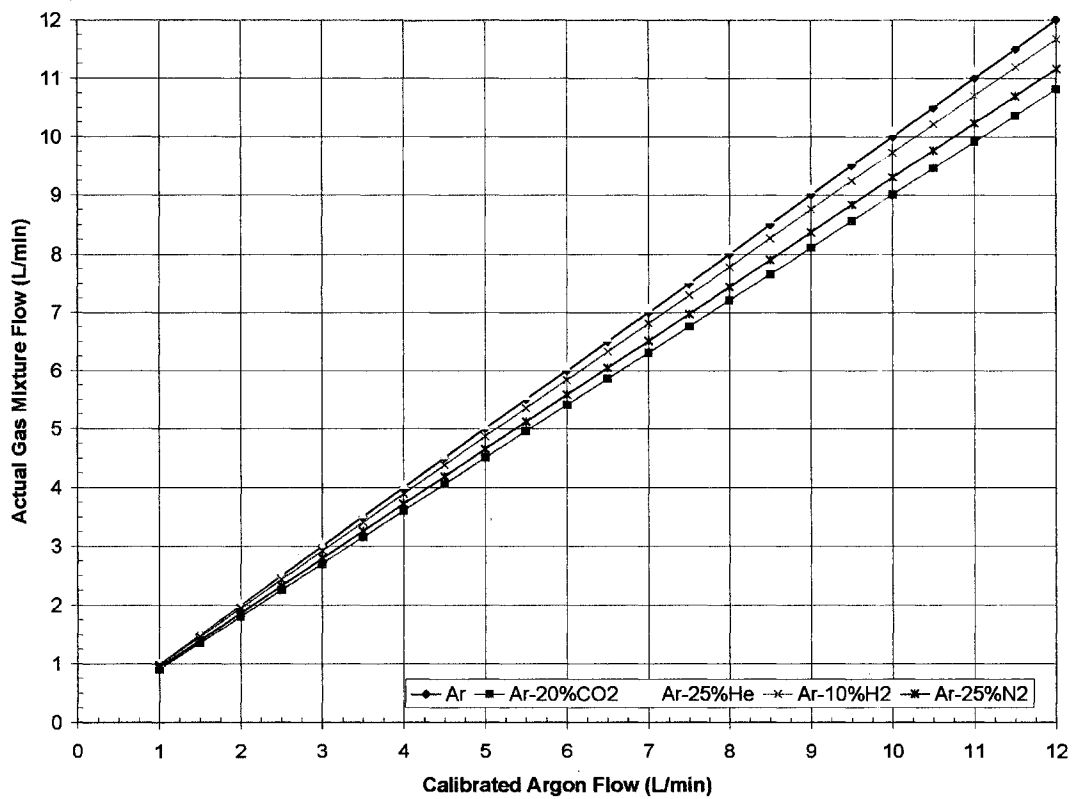


Figure 36 – Relationship between Gas Mixture Flow and Calibrated Argon Flow

3.5 Experimental Procedure and Results

a. Heat Input Variations

i. Experimental Procedure

The most common method to characterize welding conditions is the heat input equation, which was first introduced in Chapter 2. The experiments were aimed at comparing only the nominal heat input; therefore the efficiency was assumed to be 100%. The autogenous welds were completed on Grade 80 – Heat #1 microalloyed steel with nominal dimensions of 300mm x 77mm x 13mm (12in x 3in x 0.5in). Based on previous experience, the currents indicated in Table 11 were known to be insufficient for keyhole welding steel of this thickness. The parameters for welds A1 to A5 and B1 to B5 were selected so that a series of nominal heat inputs could be compared. The current and voltage were chosen so that identical welding speeds were used for a given heat input, i.e., weld A1 and B1 were both completed at 15.6 mm/s and so on.

Table 11 – Heat Input Welding Parameters

Weld ID	Current (Amp)	Voltage (V)	Welding Speed (mm/s)	Welding Speed (in/s)	Nominal Heat Input (kJ/mm)
A1	130	30	15.6	0.61	0.25
A2	130	30	8.0	0.31	0.5
A3	130	30	5.2	0.20	0.75
A4	130	30	4.0	0.16	1.0
A5	130	30	2.6	0.10	1.5
B1	170	23	15.6	0.61	0.25
B2	170	23	8.0	0.31	0.5
B3	170	23	5.2	0.20	0.75
B4	170	23	4.0	0.16	1.0
B5	170	23	2.6	0.10	1.5

The current level was set on the GAP 3000, while the arc voltage was maintained via the use of an automated voltage controller (AVC); this device is shown in Figure 30. The AVC controls the torch standoff (z-direction) to maintain a constant voltage during

welding by utilizing a continuous feedback loop based on the output voltage of the power source. During experimentation, the AVC semi-continuously adjusted the torch standoff to maintain the desired voltage set point. However, these fluctuations were minimal (<1mm) and it was verified experimentally that the AVC had no noticeable effect on arc behaviour and bead development. The nominal heat input was varied by adjusting the welding speed, while the current and voltage remained constant for the entire weld. For all the autogenous welds, pure argon gas was used for the plasma and shielding streams with flow rates of 2.5 L/min and 10 L/min, respectively. The carrier gas stream had no flow, although positive argon pressure was maintained to avoid contamination of the welds. All the autogenous beads were cross-sectioned and cut lengthwise (i.e., the longitudinal direction) and prepared utilizing the metallographic techniques described earlier. In addition to micro and macro analysis, some welds were examined with the scanning electron microscope and energy dispersive x-ray analysis (SEM-EDX). Note that during EDX analysis an ultra-thin window detector was used, which can detect the presence of light elements (such as carbon, oxygen, and nitrogen), but it is difficult to quantify the exact composition; therefore, the chemical quantities reported herein are not exact values.

ii. Results

Marco samples were prepared from each autogenous welding run and they are presented in Figure 37 and Figure 38. It is apparent that the welds A1 to A5 ("Run A") are distinctly different from the other comparable heat input welds B1 to B5 ("Run B"). Run A exhibits almost no penetration and bead formation is irregular and of poor quality. Run B formed a repeating, flawed weld bead with regions of poor fusion and expelled weld

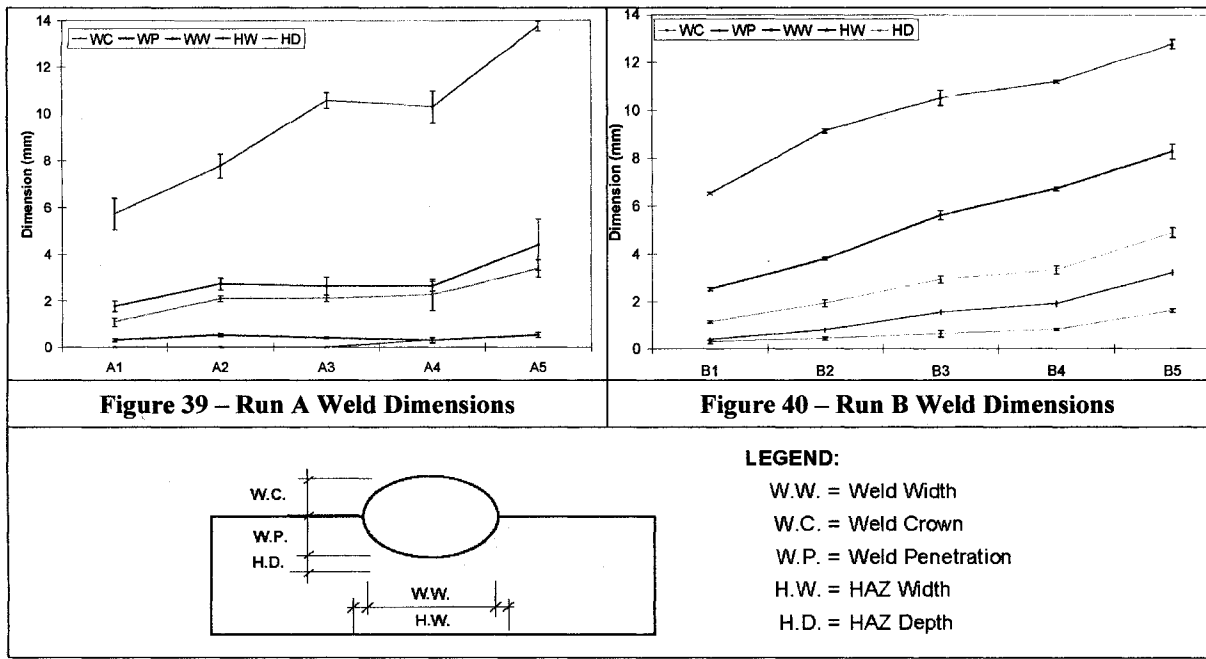
metal. This “stepped” flaw formation mechanism has been observed for other welding processes and was identified as the bead humping mechanism [109,120].



Figure 37 – Macro-Images of Run A: Welds A1 to A5



Figure 38 – Macro-Images of Run B: Welds B1 to B5



The dimensions of the welds from Run A and Run B were determined and are illustrated in Figure 39 and Figure 40. The heat affect zone (HAZ) dimensions are of the same order and are quite comparable. The weld dimensions for Run B were consistently higher than Run A. Metallographic analysis indicated the presence of slag material, or an “oxide nub”, on the bead surface as shown in Figure 41. Video analysis confirmed the presence of slag material on the weld surface during welding. Weld B2 and B4 were selected for SEM-EDX analysis. EDX analysis indicated the presence of oxygen, and the following deoxidizers: silicon, aluminum, calcium, titanium, and manganese.

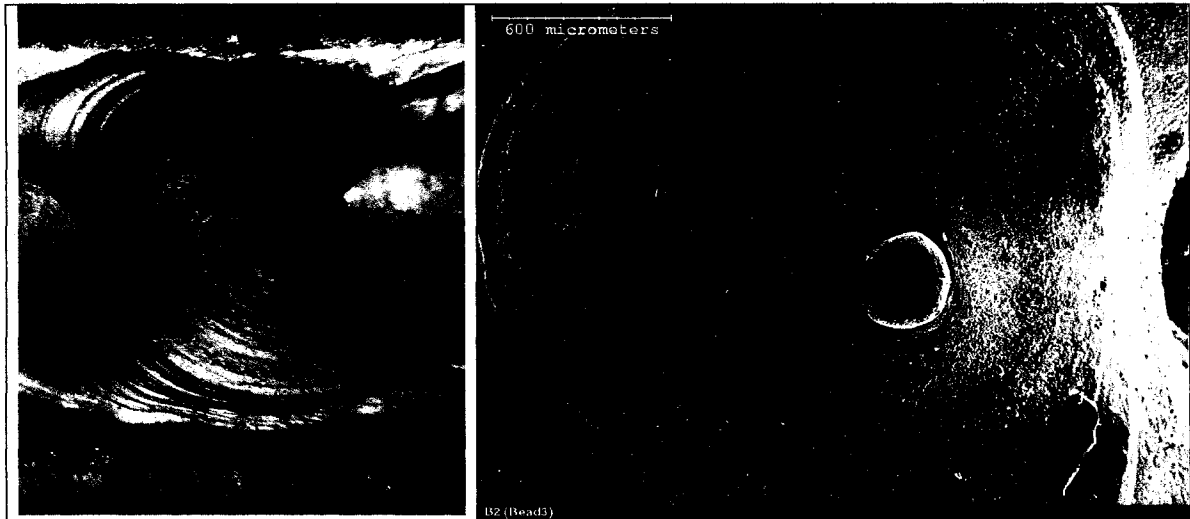


Figure 41 – Stereo-image (left) and SEM image (right) of B2 Slag Material
(Arrow indicates location of oxide nub)

b. Humping Flaw Mechanism Investigation

i. Background and Experimental Procedure

A reproducible flaw mechanism was observed during the previous round of welding and was subsequently investigated. The same materials and procedures as described above were utilized for welds G1 to G5 (“Run G”). As indicated in Table 12, 25V was selected to increase the standoff distance since occasional short-circuits between the bead hump and the torch were observed during Run B at 23V.

Table 12 – Welding Parameters for Weld Flaw Investigations

Weld ID	Current (Amp)	Voltage (V)	Welding Speed (mm/s)	Welding Speed (in/s)	Nominal Heat Input (kJ/mm)
G1	170	25	17.0	0.67	0.25
G2	170	25	8.5	0.33	0.50
G3	170	25	5.7	0.22	0.75
G4	170	25	4.3	0.17	1.0
G5	170	25	2.8	0.11	1.50

ii. Results

The autogenous beads for Run G are shown in Figure 42; note the similarity to Run B. All welds exhibit a repeatable humping weld flaw; weld G1 (0.25 kJ/mm) also contains undercutting flaws. The weld bead and HAZ dimensions were of the same order as Run B, but were excluded for brevity. Weld G4 was cross-sectioned at 2 mm intervals so that the bead hump behaviour could be further analyzed; the results are given in Figure 43. The cross-sections clearly indicate poor wetting of the base material by the weld bead; undercutting and lack of fusion flaws are noted on many of the cross-sections. Digital images were also taken of the arc (Figure 44). The images clearly show a secondary arc, reverse metal transfer, and confirm the presence of an inner core and an outer cooling sheath.

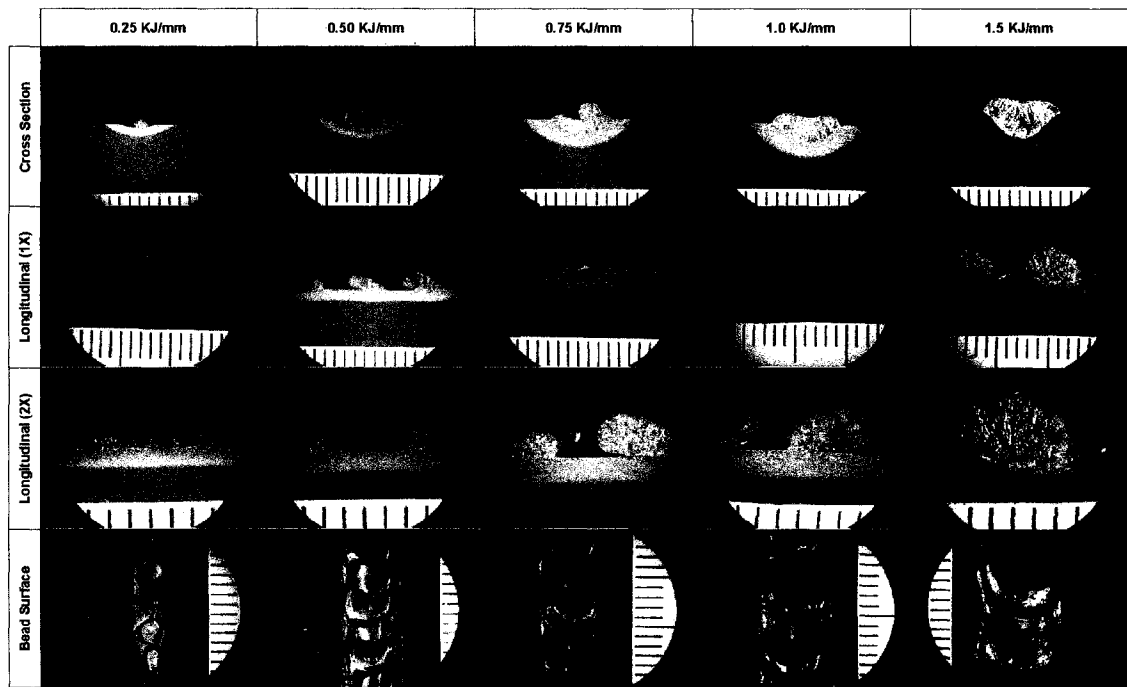


Figure 42 – Macro-Images of Run G: Welds G1 to G5

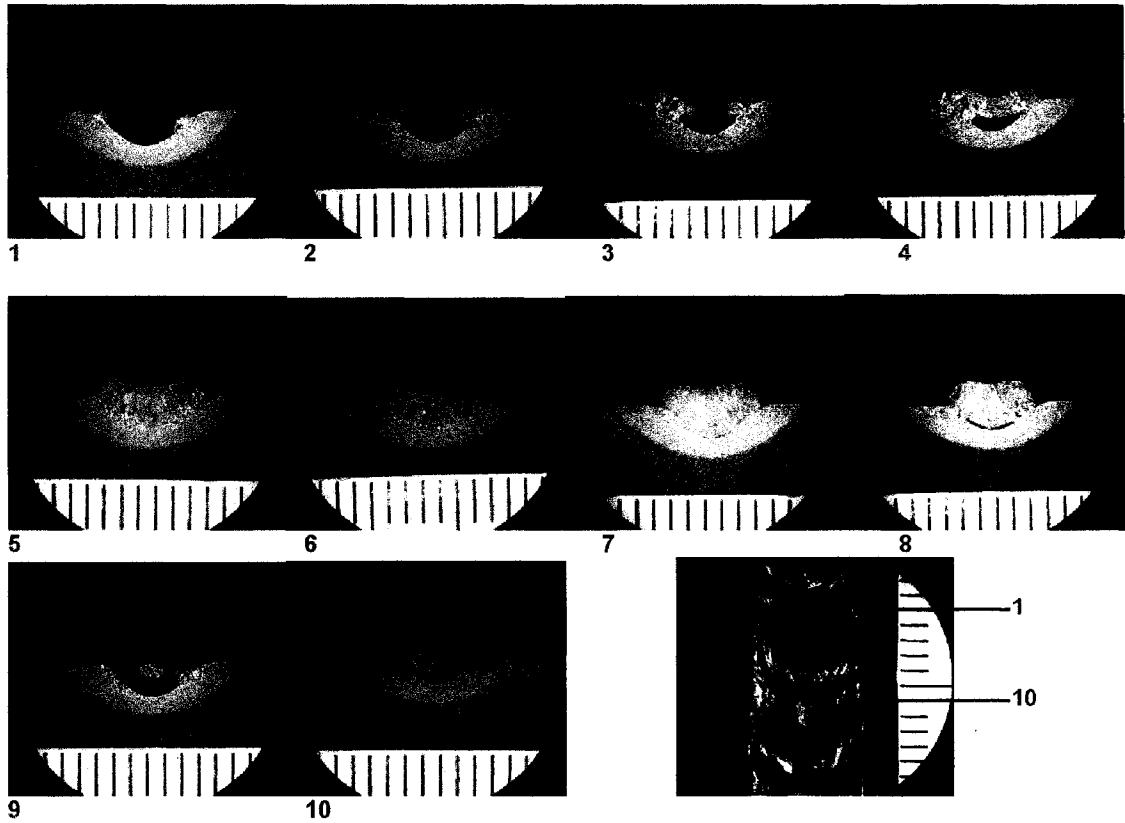


Figure 43 – Weld G4 Cross-section Macro-images of Bead Humps



Figure 44 – Arc Images of Secondary Arc (left) and Reverse Metal Transfer (right)

c. Autogenous Operating Maps

i. Experimental Procedure

Based on the formation of flaws observed during the heat input comparison, an operating map was experimentally determined for the Grade 80 – Heat #2 microalloyed steel. In Part 1 of Table 13, various combinations of current and welding speed were attempted and the resulting bead behaviour was observed and digitally recorded. In lieu of a constant voltage, these experiments were conducted with a constant standoff of 8mm. The use of a constant standoff is common practice when developing operating maps for plasma arc welding [102,105]. Based on previous experience, below approximately 80 A there was not much base metal melting for the range of welding speeds selected; 80A was selected as the minimum value and 300A was the maximum output of the GAP 3000. Autogenous stringer beads were completed with a pure argon plasma gas flow of 2 L/min and shielding flow of 10 L/min; positive argon pressure was maintained for the carrier gas. During each weld run, the arc was initiated and stabilized at the initial current level. As the torch progressed along the work piece, at the prescribed welding speed, the current was increased by 5 A every 25 mm; this concept is illustrated in Figure 45. The plate was cooled to ambient temperatures between successive beads. At the lower welding speeds (<1.3 mm/s), it was possible to break through the material via the keyhole mode. Those runs denoted with an asterisk (i.e., *R3.2, *R6.4, and *R9.4) were completed with the plate elevated off the table to allow the arc to pass completely through. The current at which the keyhole formed was recorded, but no attempt was made to stabilize the behaviour. In Part 2 of Table 13, the influence of other process parameters on the threshold of flaw formation was investigated. All the experiments were completed at a

constant welding speed of 2.5 mm/s (0.10in/s) and all other variables remained constant, unless otherwise noted. The current range of 80 – 120 A was investigated to determine how and if flaw formation was affected. In Part 3 the influence of the plasma and shielding gas composition was investigated for a constant welding speed of 2.5 mm/s (0.10in/s) for the current range of 80 to 200 A. All other variables remained constant.

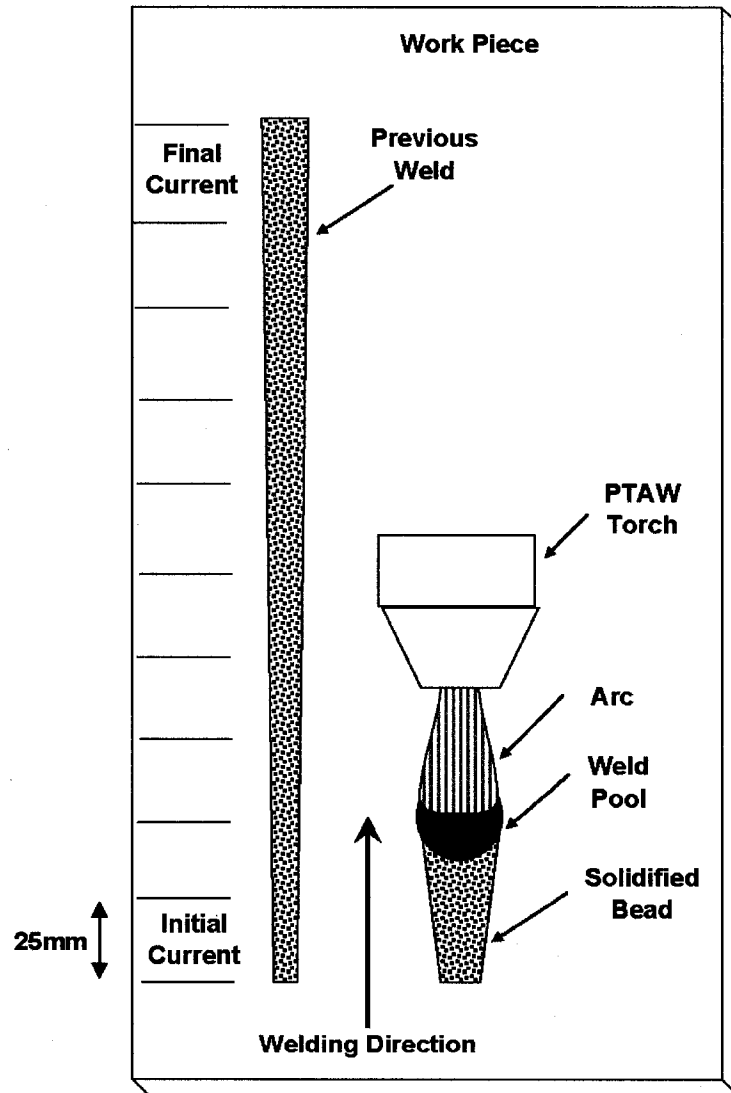


Figure 45 – Schematic of Autogenous Operating Map Experiments

effect of changing other process parameters on bead behaviour; these observations are based on video and metallographic analysis. Figure 47 illustrates the effect of changing plasma and shielding gas composition on bead development.

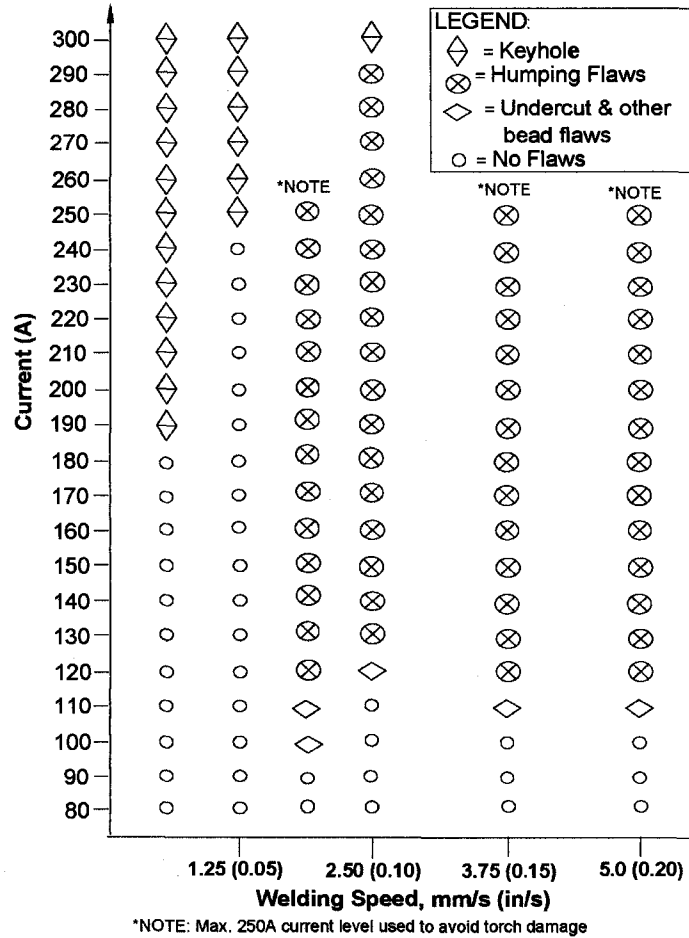


Figure 46 – Operating Map as a Function of Current and Welding Speed

Weld ID	Original Variable	Experimental Variable	Observations
S2	PG = 2 L/min	PG = 1 L/min	Weld dimension relatively unchanged; Flaw formation relatively unchanged
S3	SG = 10 L/min	SG = 5 L/min	Increase in weld width and depth; Flaw formation relatively unchanged
S4	PG = 2 L/min	PG = 3 L/min	Large increase in weld width and depth; Flaw formation at lower currents
S5	E.S.B. = 1mm	E.S.B. = 0 mm	Reduced weld width and depth; Flaw formation at higher currents
S6	E.S.B. = 1mm	E.S.B. = 3 mm	Significant increase in weld width and depth; Flaw formation at lower currents



Table 14 – Experimental Observations of Other Welding Parameters

d. Plate Chemistry and Doping Experiments

i. Background and Experimental Procedure

During the previous experiments, the autogenous bead behaviour of the Grade 80 – Heat #1 and the 300W structural steel were found to be distinctly different. In particular, the humping bead flaw mechanism was fundamentally different under identical welding conditions (Table 15). It was theorized that surface active elements, specifically oxygen and sulfur, were responsible for the behaviour observed. The Mn/S and Al/O ratios of the 300W steel were noticeably lower, and the net total de-oxidant level was reduced. Hence, doping experiments were completed whereby manganese and aluminum were artificially added to the weld zone to initiate a change in weld bead formation.

Table 15 – Differences in Autogenous Bead Behaviour and Steel Chemistry

	CSA 300W Plate %C = 0.18 %Mn = 0.61 %S = 0.031 %O = 0.024 %Al = < 0.003		A656 Grade 80 – Heat #1 %C = 0.052 %Mn = 1.09 %S = 0.003 %O = 0.016 %Al = 0.032
	Mn/S ratio = 20 Al/O ratio = 0.0125		Mn/S ratio = 363 Al/O ratio = 2
	De-oxidants: %Si = 0.20 %Al = <0.003 %Ti = <0.001 %V = 0.001 %Ca = <0.0002		De-oxidants: %Si = 0.13 %Al = 0.032 %Ti = 0.002 %V = 0.001 %Ca = 0.0025
“Twin Bead”		“Single Bead”	

Two different doping plates were machined from the 300W steel as shown in Figure 48. Various hole diameters, spacings, and welding currents were attempted in Doping Plate #1 since optimal experimental conditions were not known. PTAW autogenous beads were completed on the top surface of the plate, and the arc impinged directly into the

holes filled with the doping powder; welding parameters are indicated in Table 16.

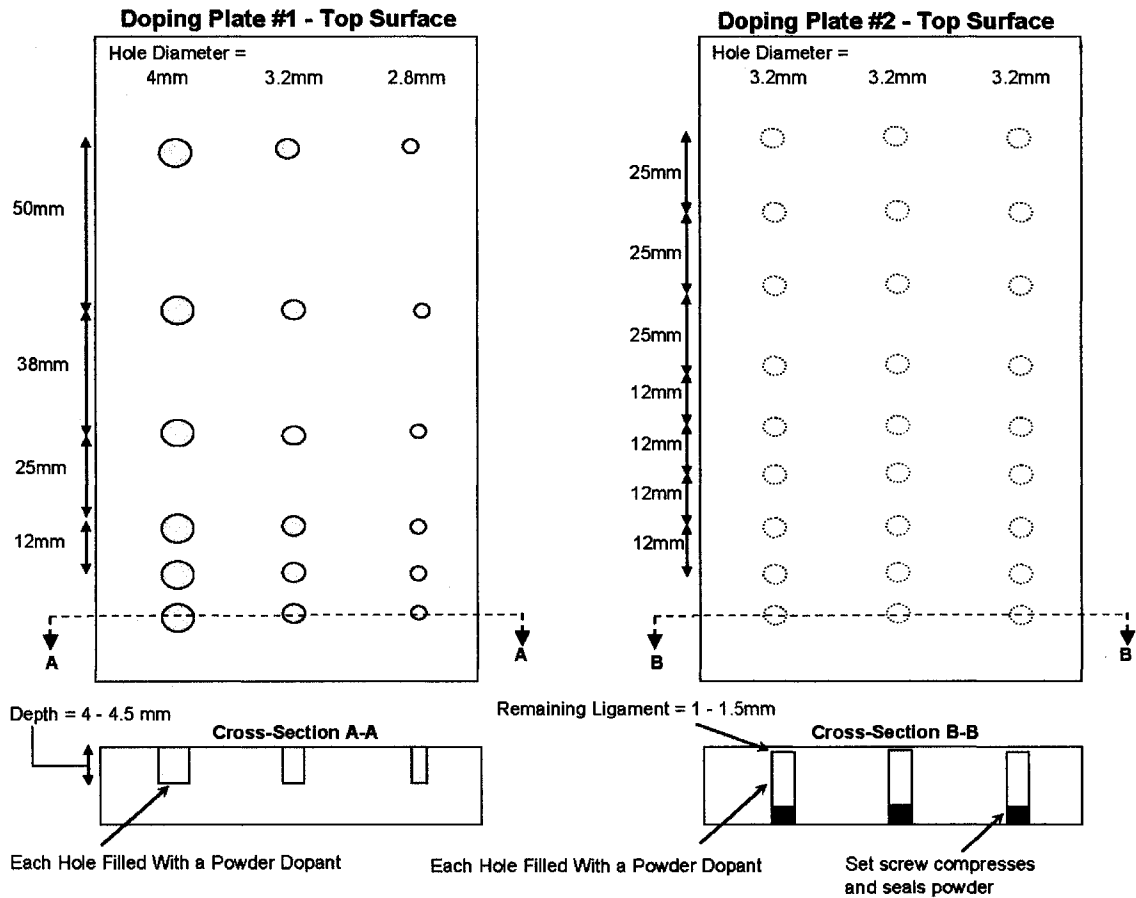


Figure 48 – Schematic of Doping Plates

To avoid the excessive powder losses experienced earlier, a slightly modified plate design was employed for Doping Plate #2. The welding parameters utilized are summarized in Table 16. The hole diameter and spacing that produced the best results during the first doping experiment were utilized for the second doping plate experiment.

Table 16 – Welding Parameters for Doping Experiments

Weld ID#	Hole Dia.	Powder	Amp	Other Parameters
N4	4.0 mm	99.9% Al	170A	Welding speed = 4.3 mm/s Standoff = 8mm Plasma Gas = 2.5 L/min Argon Shielding Gas = 10 L/min Argon Carrier Gas = Argon Purge Nominal Heat Input = 1.0 kJ/mm
N5	3.2 mm	Al-23%Mn	140A	
N6	2.8 mm	99.9%Mn	130A	
X1	3.2 mm	99.9% Al	170A	
X2	3.2 mm	Al-23%Mn	170A	
X3	3.2 mm	99.9%Mn	170A	

The doping holes were drilled from the backside until a 1-1.5mm ligament remained, were filled with the doping powder, and a set screw was used to compress and seal off the powder. Hence, instead of the strong plasma jet force expelling the powder, the ligament was melted and the powder was “drawn” into the weld pool.

ii. Results

The autogenous bead behaviour for Plate Design #1 is shown in Figure 49. The first few weld humps directly after the dopant hole were notably changed; thereafter the powder dopant was sufficiently diluted out of the weld metal. As the hole spacing and hole diameter were reduced, the influence of the powder on weld pool behaviour and bead development was intensified. The 4.0 mm diameter holes were too large and the plasma jet expelled the powder, resulting in excessive powder residue.

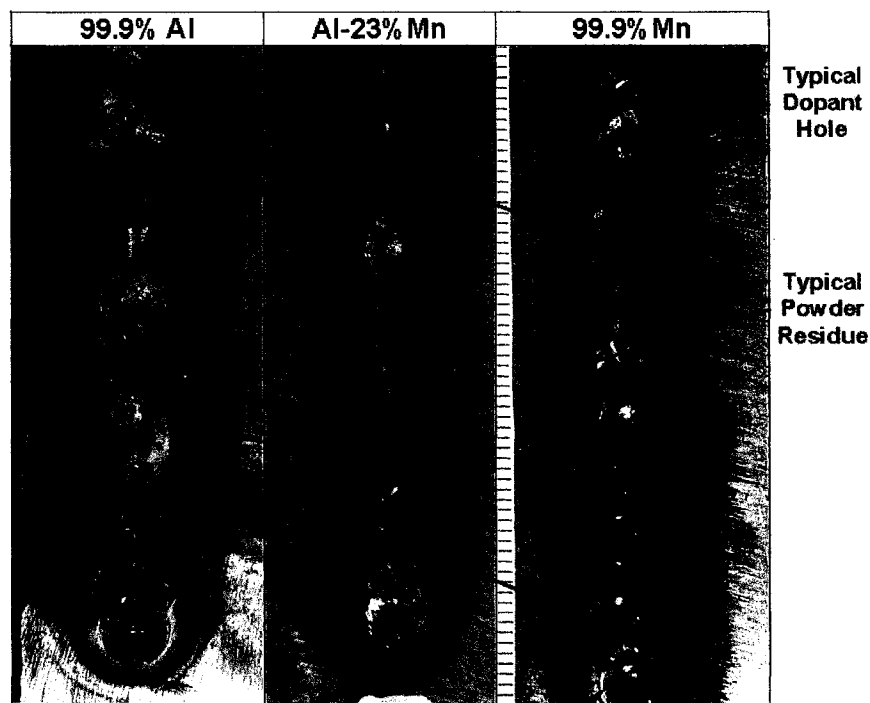


Figure 49 – Bead Behaviour for Doping Plate Experiment #1

The typical bead behaviour for Plate Design #2 is summarized in Figure 50. Much cleaner and consistent welds were obtained, with no powder losses, and the bead behaviour confirmed the results obtained earlier.

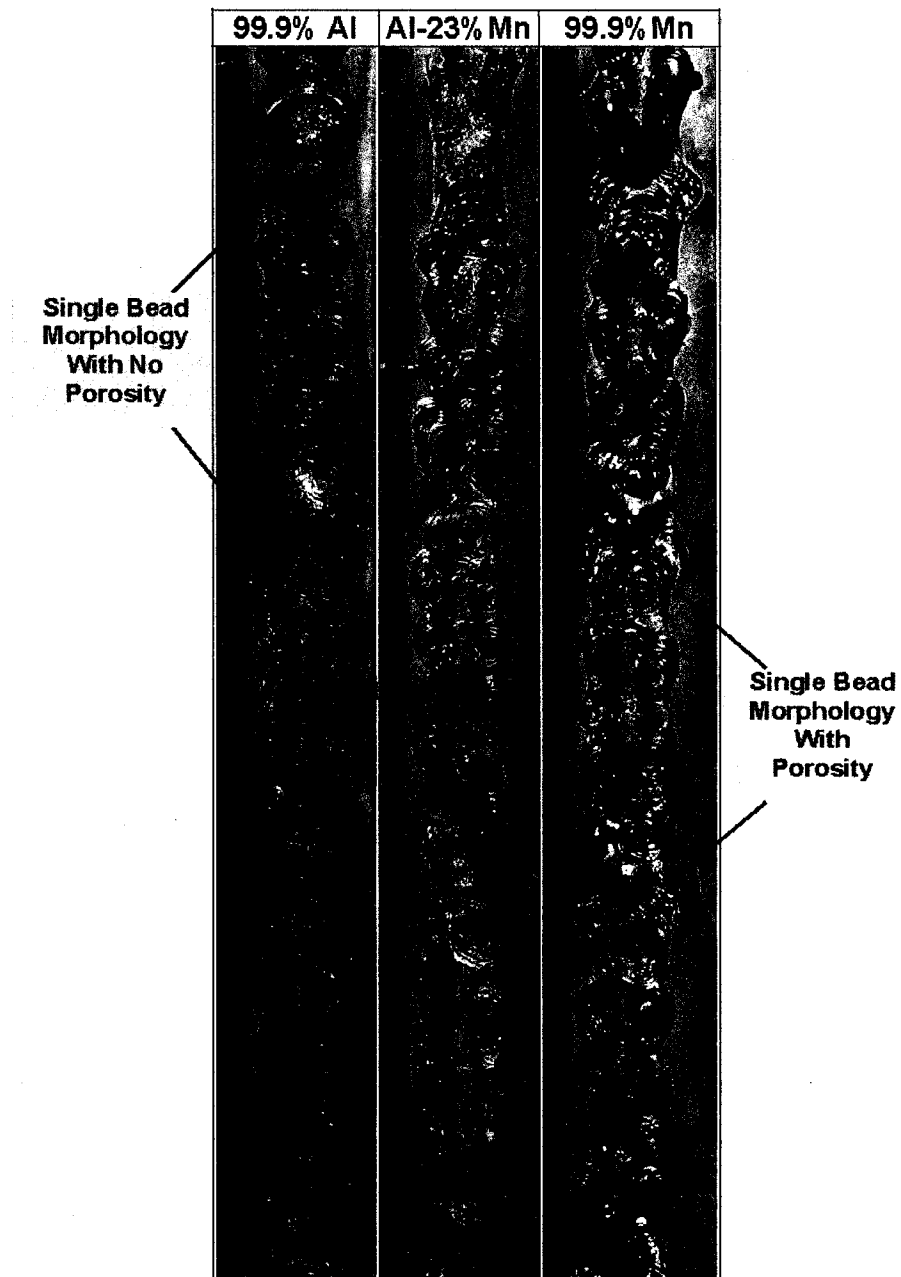


Figure 50 - Bead Behaviour for Doping Plate Experiment #2

3.6 Discussion

a. Comparison of Heat Input Equation vs. Operating Map

The heat input equation has found wide range acceptance for many welding processes such as GTAW, GMAW and SMAW. Within a range of practical operation, the equation adequately calculates the quantity of energy entering the weld zone. For example, the use of SMAW electrodes at the specified welding speed, current, and voltage will produce consistent results that are predicted by the heat input equation. The equation has found acceptance in many construction codes and standards (e.g. ASME, CSA, etc.). A survey of the literature indicates that the equation is also applied to PTAW. However, unlike the previous example, our experiments suggest that the equation does not adequately describe process and weld behaviour.

Figure 39 and Figure 40 illustrate that the heat affected zone (HAZ) dimensions from Run A and Run B are of the same order and quite comparable. However, the weld bead dimensions, shape, and in-situ behaviour (i.e., obtained via video analysis) exhibit no commonality. The smaller weld dimensions in Run A are linked to poor arc column stability at the relatively high standoff required to maintain a 30V argon arc. The anode spot “danced” around the work piece as it searched for stabilizing oxides. The irregular weld bead surface patterns (Figure 37) are a result of this unstable arc behaviour. Run B had a significant increase in weld dimensions, but only if one measures the bead hump; molten material was expelled between each hump as shown in Figure 38. The nominal heat input equation was unable to predict these weld size differences or the formation of flaws. Some could argue that by determining the welding process efficiency, as indicated in the heat input equation, one could account for these differences. However, in doing so

the efficiency term simply becomes an empirical “fudge factor” that correlates output (weld bead dimensions) with input (welding parameters) without addressing the underlying arc processes and metallurgical principles. These fudge factors would only be applicable within the specific range of welding parameters examined. The equation is too simple to address the many interrelationships that exist between the process parameters during autogenous welding. Note that this inadequacy is further exacerbated during the PTAW surfacing of overlay materials as discussed in Chapter 4. Therefore, a significant conclusion is that the *true* quantity of energy delivered to the work piece is not adequately calculated by the heat input equation during PTA welding. The equation can be utilized to “index” welds for relative comparisons, i.e., 0.25 kJ/mm is very different from 1.5 kJ/mm, but is a poor indicator of weld quality or dimensions for the PTAW process.

The operating map method was a more effective means of assessing and comparing welding parameter interactions. This method is an extension of the keyhole envelopes developed by past authors [102,103], but with the emphasis on the intermediate range between micro-plasma and keyhole welding. The operating map identified regions of good operation and flaw formation for a relatively large range of parameters. As shown in Figure 46, at welding speeds less than 1.9 mm/s (0.075 in/s) no flaws formed. The welding speed of 1.9 mm/s was a transition point where the “humping threshold” was at the lowest current; operation under these conditions is not recommended. Above 1.9 mm/s, undercutting and weld humping limits the maximum allowable operating current. This maximum current appeared to decrease slightly with increased weld speed; further work is required to verify this behaviour. This trend, therefore, limits productivity since

all industrial applications aspire to maximize welding speed and current level simultaneously. The use of operating maps also provided a sound method for understanding the interactions between other welding parameters and the resulting influence on the formation of fusion flaws. The dependence of the humping threshold on other process parameters will be discussed further in Section 3.6b.iv.

b. Weld Bead Humping

i. Background

The desire to increase productivity and reap the economic benefits has led to various studies of welding processes at high welding speeds and currents. However, the benefits are limited due to the appearance of fusion flaws such as undercutting, single bead humping, twin bead humping, and tunnel porosity. In 1968, Bradstreet [109] was the first to report weld bead humping during high current GMAW. Since then there have been other investigations into these fusion flaws for GTAW, GMAW, and laser welding applications. There are no known investigations for the PTAW process. Therefore, the following will introduce the relevant previous investigations to allow for comparisons to the PTAW behaviour.

During most welding, the classical hemispherical weld pool is formed with very little depression of the top free surface (i.e., less than 1mm). During GTA welding at currents greater than 200 – 250A, there is a sudden and rapid increase in penetration with increased current that has been studied by many investigators [110,111,112,113]. These investigations explored how the depressed pool shape and penetration is affected by the interrelationships of current, Lorentz force, plasma jets, welding speed, convection and arc pressure. These models illustrated that depressed pool behaviour was both complex

and significantly different from undepressed pool behaviour. When the depressed pool turns into a thin-film under the arc, there is a greater propensity towards formation of humping-like flaws and undercutting. This phenomenon was observed during a study of low-pressure GTAW beads [114] and confirmed at ambient pressure [115]. This thin film is commonly referred to as the “gouging” region and was also observed during narrow-groove GMAW [116] and autogenous GMAW [109,117]. Humping has also been investigated for non-arc welding processes such as laser welding [118,119]; analysis proved that capillary instability, or the width-to-length ratio of the pool, governs humping behaviour. Mendez *et al.* [44,120] recently developed a model for high-current GTAW bead humping that closely resembled the observations of PTAW humping. Hence, it became the basis for the humping mechanism proposed below.

ii. The Humping Mechanism

Based upon metallographic and video analysis, the bead humping mechanism was characterized for PTAW. Figure 46 illustrates that at low welding speeds <1.9 mm/s (0.075 in/s) no flaws are formed. In this regime, the weld pool becomes progressively depressed with an increase in current until a thin film forms at high current. The proposed mechanism is described in Figure 51. A gouging region is formed due to the penetrating action of the constricted arc. The arc force is proportional to the square of the welding current [112]; hence, Lorentz forces and plasma jet pressure expels molten material to the edges and rear of the pool. During gouging the arc directly heats the film, while the solid work piece acts as a large heat sink. Hence, if there is an imbalance in this energy transfer, due to gradients in arc energy, then a small region of prematurely solidified weld metal can form. The timescale for this solidification has been estimated to be on the order

of milliseconds [44]. If any solidified regions form at low welding speeds, there is sufficient time for these disturbances to be “repaired”. The flow of metal in the liquid rim provides the continuous source of molten material. The welding speed of 1.9 mm/s is a transition point where the “humping threshold” was at a minimum. The pool instability was the result of the weld oscillating between the low speed stable gouging regime (Figure 51) and the high speed humping regime (Figure 52). Video recordings showed that stable gouging would be randomly replaced by humping, and occasionally revert back to stable gouging. This mode of operation is not recommended for practical applications.

At welding speeds ≥ 1.9 mm/s the molten metal flow rate from the gouging region to the rear of the weld puddle is insufficient to “repair” solidified regions (see Figure 52). At high speeds and current, the thin film is pushed further to the rear of the weld zone where there is less direct heating from the arc. The resulting energy imbalance caused premature solidification. Due to the insufficient flow of molten material and poor wetting of the solidified regions, as determined by video analysis shown in Figure 53, the solidified regions expand and effectively disrupt molten metal flow. Continuous gouging forms weld side pools that coalesce to form a new weld bead hump and the process is repeated. The maximum operating current appeared to decrease slightly with increasing weld speed, possibly due to inadequate molten material flow to the rear of the weld pool. This trend was observed by others [114,115], and needs to be verified over a large range of welding speeds.

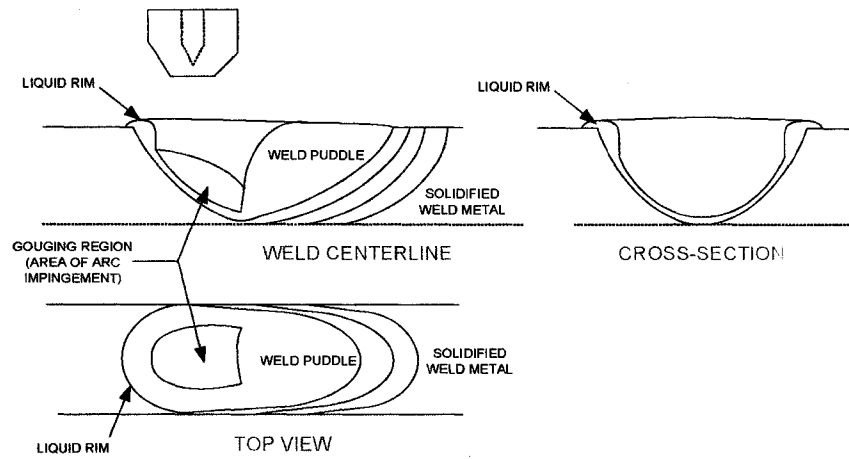


Figure 51 – Low Speed Stable Gouging Regime – No Weld Bead Humping

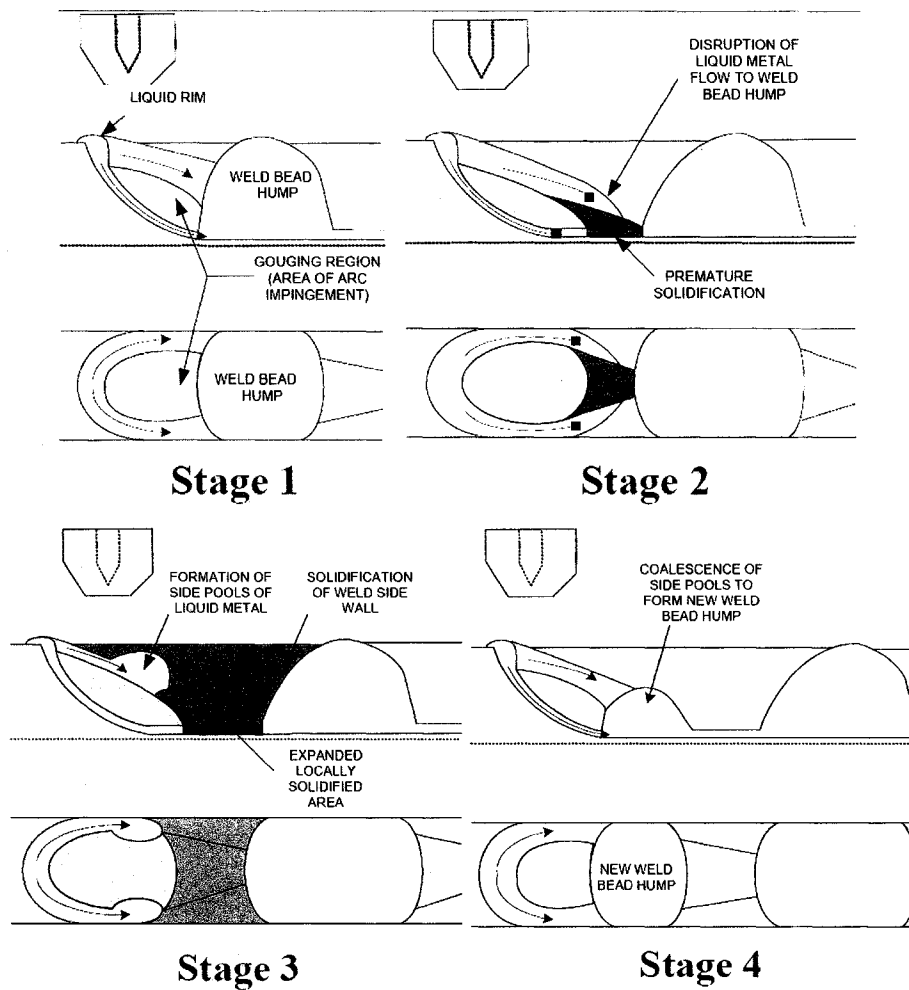


Figure 52 - High Speed Humping Regime - Weld Bead Humping

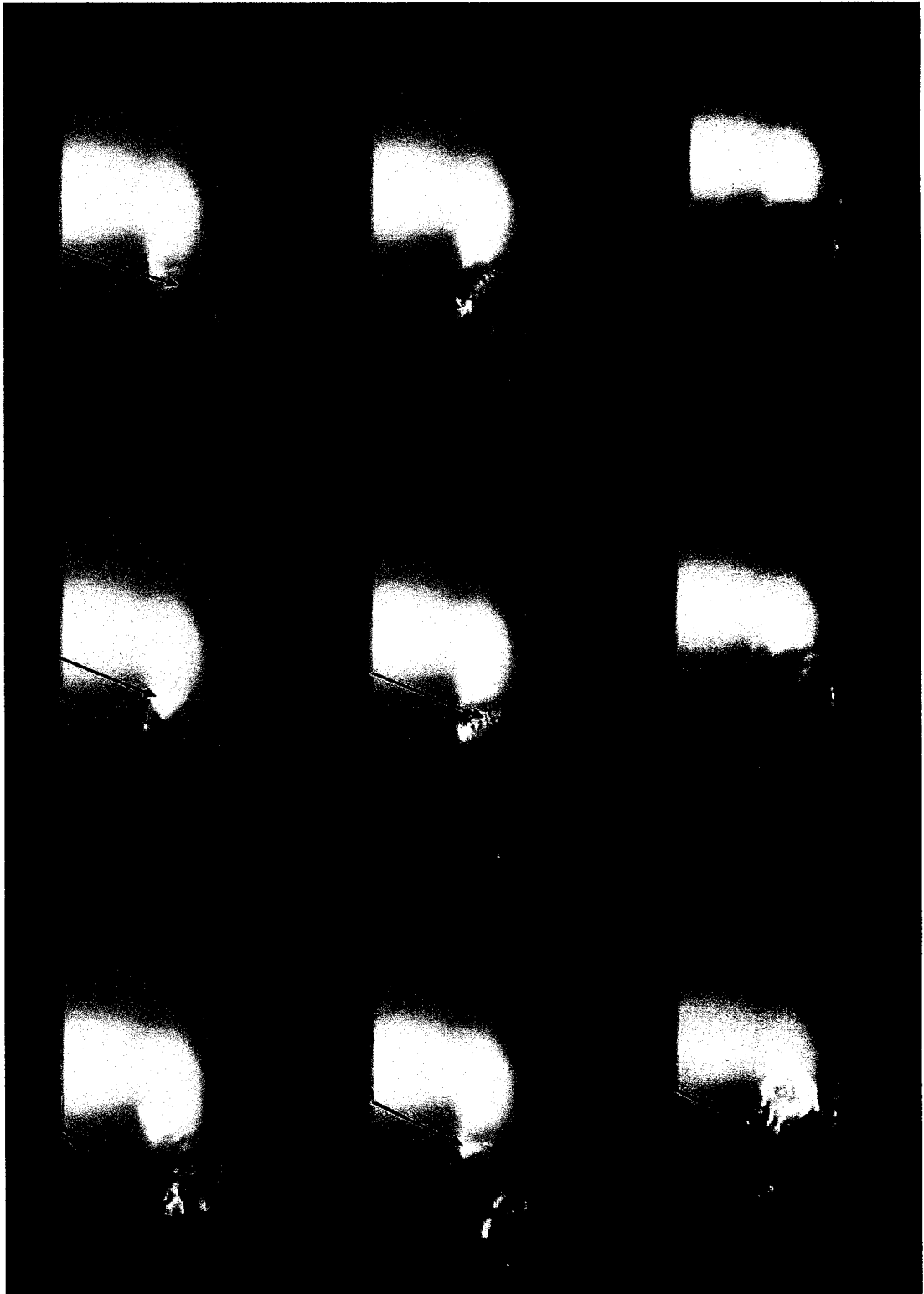


Figure 53 – Video Captures of Weld Bead Humping Mechanism (approx. 1.5 seconds)

iii. Comparison to Others

The high-current GTAW humping model proposed by Mendez *et al.* [44,120] is based on a balance between hydrostatic, capillary, and arc pressure forces at the transition line between the thin film and the molten puddle. The effect of Marangoni, electromagnetic, and buoyancy forces were considered to have a secondary influence on the trailing region and were not included in their model. As the transition line is pushed to the rear of the arc, there is insufficient heat to prevent premature solidification and humping initiates. This correlates well with the observations during PTAW humping. However, the fact that electromagnetic forces were not included in the model is questionable, since they are known to influence pool behaviour significantly, i.e., such as forming a depressed weld pool shape [112], and influence convective fluid flow [121]. The validity of these assumptions was not experimentally verified. Perhaps the model will be expanded in the future to encompass more of the many interrelated arc phenomena affecting weld bead behaviour.

In the work of Savage *et al.* [115], three different GTAW current ranges were observed. At currents <250A, the maximum welding speed was limited by undercutting flaws (i.e., higher speeds were required for humping). From 250A – 400A welding speed was limited by humping with no undercutting and at >400A welding speed was limited by undercutting prior to humping. In the operating map completed here (Figure 46), the limiting flaw was undercutting of the weld bead. Further work is required to identify if the flaw behaviour changes over a larger range of welding speeds. Savage *et al.* were unable to find a direct correlation between the travel speed limit and the absolute value of the arc force. In the model proposed for PTAW, the importance of fluid flow to the rear

of the arc has been emphasized. Future work could confirm whether this is, in fact, a controlling factor on the upper limit of welding speeds for GTAW.

During PTAW, the physically constricted arc has a large influence on the likelihood for weld hump formation. The greater concentration of energy and increased velocity of the plasma jet flow drastically lowers the combinations of welding current and speeds that produce humping flaws when compared to GTAW and GMAW. For example, humping flaws for GMAW are observed with currents on the order of 400 – 550A at 10.5 – 65 mm/s travel speeds [109]. This represents a significant increase when compared to the humping threshold range summarized in Figure 46. This difference could be attributed to the presence of alloying elements and added weld metal mass (i.e., volume) from the consumable wire, which changed the weld bead behaviour (see discussion on capillary instability below). However, similar increases were also observed during autogenous GTAW, where the humping threshold fell into the range of 5 – 15 mm/s and 250 – 500A [115]. Although the test conditions were not identical, such a drastic change in the operating envelope is likely due to the high energy density and penetrating effects of the constricted arc.

As mentioned earlier, capillary instability is sometimes used to quantify humping behaviour. The two known works were completed by Bradstreet [109] for GMAW and Gratzke [118] for laser welding. Bradstreet applied Rayleigh's theory (1896) on the instability of a free liquid cylinder of radius (R) that is maintained only by surface tension and is suspended freely in space. Since the exact shape of the molten pool is variable, it is approximated as a cylinder. The liquid cylinder will become unstable when the wavelength of a disturbance exceeds its circumference. The critical length is given as: L_C

= $2\pi R$. Gratzke then extended this theory to a partially bounded cylinder to account for the fact that the weld contacts the base material. The modified critical length is: $L_C = 2\pi R \cdot f(\varphi_o)$, where $f(\varphi_o) = (1 - (\pi / (2(\pi - \varphi_o))))^{-0.5}$ and $2\varphi_o$ equals the angle subtended at the cylinder center by the bounded region. The application of these analysis techniques is summarized in Table 17. As indicated, there is no correlation between the average PTAW hump spacing and the predicted minimum for either the Bradstreet or Gratzke Method. The Gratzke Method breaks down for those welds where φ_o exceeded 90° . These discrepancies are likely due to the assumption to approximate the weld pool with a liquid cylinder, and the assumption to ignore other influences of the plasma arc, particularly the dominating effects of the constricted arc. Therefore, a significant conclusion is that capillary instability cannot be used to explain humping behaviour during PTA welding of autogenous welds.

Table 17 – Comparison of Actual Hump Spacing to Capillary Instability Methods

Weld ID	Avg. Bead Radius mm	Angle (φ_o)		Bradstreet Method Minimum spacing $2\pi R$	Gratzke Method		Actual avg. Spacing mm
		Degree	Radians		$f(\varphi_o)$	Minimum spacing $2\pi R f(\varphi_o)$	
G1	0.81	50	0.87	5.1	1.39	7.01	3.41
G2	2.61	90	1.57	16.4	-	-	6.41
G3	3.22	82.5	1.44	20.2	2.60	52.64	6.37
G4	3.56	100	1.75	22.3	-	-	6.52
G5	4.06	104	1.82	25.5	-	-	9.44

NOTE: $f(\varphi_o)$ cannot be calculated for angles greater than or equal to 90 degrees

iv. Effect of Other Welding Parameters

Based on previous investigations [13,44,115,120], the welding speed threshold for GTAW bead humping can be influenced by various process parameters. The welding speed limit is increased with lower current, shorter arc length, a properly conditioned

electrode, reduced electrode diameter and increased vertex angle, orientating the electrode in the forward direction (i.e., forehand technique), or using a magnetic field to angle the arc forward. These results indicate that the electrode configuration and the resulting arc behaviour strongly influence flaw formation. Therefore, PTAW process parameters that significantly influence arc behaviour were examined to discover if the humping threshold was affected.

As summarized in Table 14 the influence of other welding process parameters was obtained for the welding speed of 2.5 mm/s. Note that a similar response is expected for other welding speeds. Other authors [102,103] cite the importance of plasma gas flow on process behaviour during keyhole welding. For the range of 1 L/min to 3 L/min, the plasma flow rate had a minimal effect on bead development and the humping threshold. This is likely because the gas speeds obtained due to the plasma gas flow are relatively low and benign when compared to the plasma jet velocities, i.e., an order of magnitude difference. At much higher plasma flows, the mechanical “cutting action” of the plasma gas may have a larger influence on the humping threshold; this could be investigated in future work. Reducing the shielding gas flow appears to have a small effect on arc and bead behaviour. As discussed, the shielding gas flows provide protection from atmospheric contamination and the “cooling” action partially constricts the plasma gas column (i.e., the shielding blanket acts as a heat sink). It was theorized that by lowering the flow rate, and reducing the arc constriction slightly, the gouging ability of the arc would be reduced. This effect was not observed and the humping threshold remained unchanged. It is possible that by reducing the flow rate, less energy was lost to the gas stream and more energy was transferred to the weld pool, which mitigated the formation

of prematurely solidified regions. The electrode set back had a dominating effect on the weld bead behaviour. With an increased electrode setback, the physical constriction of the arc increased proportionally, which led to an increased energy density and plasma jet velocity. Greater penetration was observed via video analysis, and the weld dimensions were enlarged. This is to be expected since the ability to form a PTA keyhole weld is improved as the electrode setback is increased. By escalating the penetrating ability of the arc, for the same current level, the propensity towards gouging the base material and forming a depressed pool, in-lieu of melting and forming an un-depressed weld pool, is greatly amplified. Therefore, the critical combination of current and welding speed that produces a thin-film prone to flaw formation (i.e., humping threshold) is lowered as electrode setback is increased. The opposite was obtained when the electrode set back and arc constriction was reduced.

A unique observation found via video and metallurgical analysis was the formation of a secondary “backwards acting” arc emanating from the rear of the weld pool (see Figure 44). SEM analysis confirmed that the slag material was rich in deoxidants such as Ti, Al, Si, and Mn. Video analysis confirmed that the “oxide nubs” floated to the pool surface and were present during welding. These low work function oxides formed the anode spots for the secondary arc. A localized region of high current density formed at the oxide nubs, which resulted in the formation of a current density gradient. As discussed earlier, formation of Lorentz forces is dependent only on the existence of a current density gradient and is independent of polarity. Therefore, the Lorentz forces developed from the oxide nubs were “backwards” acting, which led to reverse plasma jet action and reverse metal transfer. Significant amounts of weld metal collected on the torch during

autogenous runs, even though the torch never contacted the weld pool. Previous investigators have made similar observations where reverse plasma jets can greatly affect metal transfer and arc shape [17]. Based upon the weld longitudinal profile (see Figure 42), it appears that the weld bead hump is pulled “up and back” towards the torch. It is proposed that the secondary arc and the associated reverse Lorentz force had a stabilizing effect on the bead hump that further impairs wetting of the base material and lowers the humping threshold. Further work is required to verify this supposition and properly quantify what effect, if any, the reverse Lorentz force has on bead development.

c. Effect of Plate Chemistry on the Humping Mechanism

Based on the video and metallurgical data, it is believed that surface tension driven “Marangoni” fluid flow does not affect flaw formation when operating with a depressed thin-film pool. Rather, it is proposed that the physiochemical behaviour, i.e., surface tension and wetting behaviour of the thin-film strongly influence the type of fusion flaws created. The use of different base materials, weld pool dopants, and different gas mixtures confirmed the proposed mechanism.

i. Background

The majority of theoretical and experimental work regarding weld pool fluid flow has been established for GTA welding with a non-depressed weld pool. The four primary forces driving fluid flow include buoyancy forces, electromagnetic or Lorentz forces, aerodynamic drag forces from the arc plasma, and surface tension forces [121]. In the classic paper by Heiple and Roper [122] a model for weld pool convection, based on surface tension drive fluid flow, was successfully developed; the importance of minor alloying additions was also emphasized. The model is based largely on the work

completed by Marangoni in the late 19th century, where it was demonstrated that if a surface tension gradient exists on the surface of a liquid, the fluid is drawn along the surface up the tension gradient (i.e., from regions of low to high surface tension).

The Heiple and Roper model states that surface tension gradients exist on the weld pool because surface tension decreases with temperature; this forms a negative surface tension temperature coefficient. As shown in Figure 54 (top diagram) the temperature is maximum directly under the arc and coolest near the edges, which pulls fluid from the center to the edges; the resulting weld has a high width-to-height ratio. The addition of surface active elements (group VI of the periodic table) to iron-based alloys can greatly influence this fluid convection behaviour by lowering the fluid surface tension, and producing a positive surface tension temperature coefficient. Although there is a decrease in system entropy due to the preferential segregation of surface active elements in lieu of homogenous mixing, the net free energy change for the system is negative and limited only by kinetic mechanisms [123]. At low temperatures near the pool edges, the surface active elements will lower the surface tension. The concentration of these elements becomes progressively lower towards the center of the pool due to high temperature losses (i.e., they are burned off), as shown by the middle diagram in Figure 54. If the weld pool reaches sufficiently high temperature, 2025°C for sulphur and 2370°C for oxygen, the concentration drops to levels whereby it is no longer surface active and the original melt behavior is restored [122]. This type of behaviour is illustrated in the lower diagram of Figure 54 where T_0 is the temperature where the element is no longer surface active. Welds with sufficiently high surface active elements produce greater weld penetration and the convection flow patterns are complementary to the electromagnetic

Lorentz force. In previous investigations [26,121,122,123,124,125,126,127] the common surface active elements examined for steel and stainless steel include sulfur, oxygen, selenium, and tellurium. Common reactive elements utilized to chemically “tie-up” or remove these active elements include aluminum, cerium, calcium, silicon, and manganese. These reactive elements will preferentially tie-up either oxygen or sulphur (or both), and have proven to be able to mitigate the effects of these surface active elements. Hence, the use of these reactive elements is an effective means of modifying surface tensions and/or Marangoni flow.

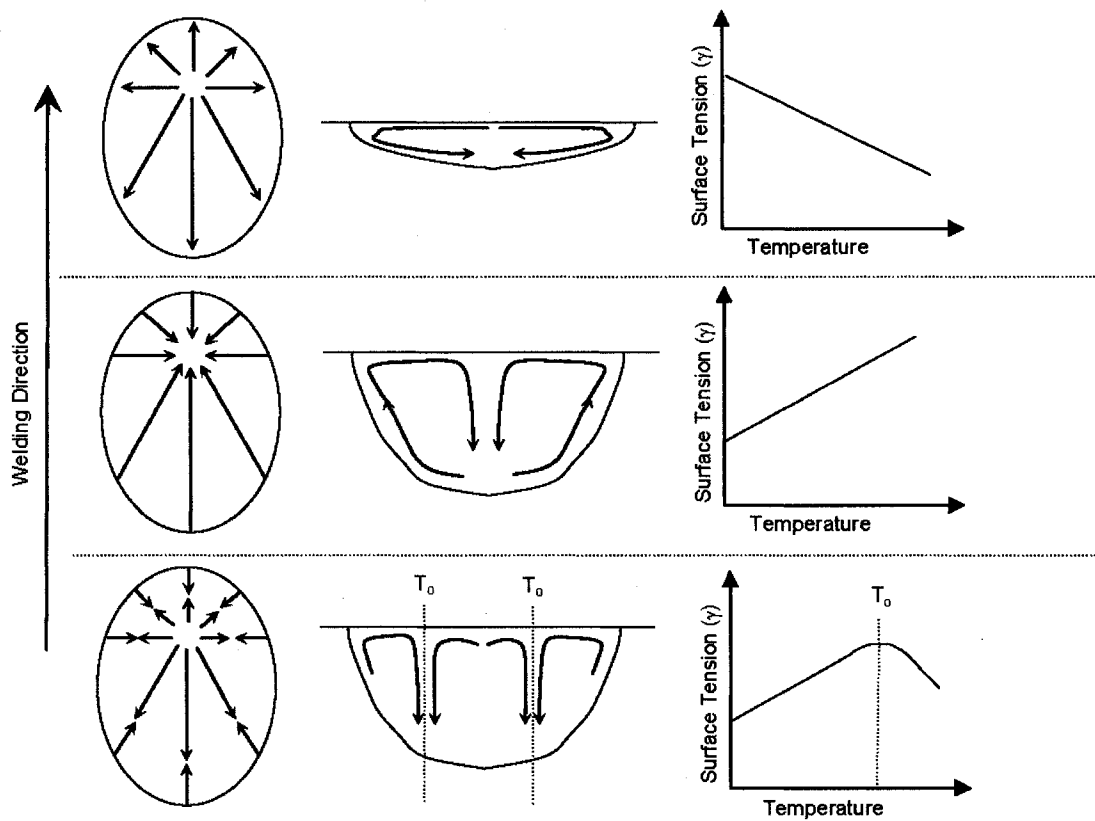


Figure 54 – Marangoni Flow: Surface Tension Driven Convective Fluid Flow

The preceding discussion illustrates that the Marangoni flow mechanism has been well established for most GTA welding applications. However, the effect of surface active elements and reactive dopants has not been investigated, to the author's knowledge, for PTA welding. In addition, there have been very few investigations for high current GTA with depressed weld pools. Heiple and Roper [128] noted that with large additions of sulphur the GTA weld pool became depressed and the molten material was transported to the rear of the pool. They state that since the weld pool surface tension resists the plasma jet force, the reduction in surface tension (due to the sulphur additions) increased the effect of the plasma jet and allowed for greater penetration. Mendez *et al.* [44] attempted to assess the influence of sulphur additions for the humping mechanism during high current GTA welding. The threshold for humping and undercutting was reduced with high sulphur content, which they attributed to inwards Marangoni flow and the formation of a prematurely solidified rim at the edges of the pool that prevented wetting and caused undercutting. However, they also found that weld penetration in high current GTAW was independent of sulfur concentration and concluded that Marangoni forces were not dominant in that regime. They did not explain these somewhat contradictory results. They also observed a higher effective weld bead contact angle when welding with high sulphur, which indicates that the liquid metal is less wetting. This contradicts the common belief that a lower surface tension will always improve wettability; they were unable to explain this behaviour. Based on these results, the actual role Marangoni flow plays during high current GTA humping is unclear. In the discussion below the wetting behaviour and the importance (or lack thereof) of Marangoni flow during PTAW autogenous humping will be discussed.

ii. Effect of Surface Active Elements on Humping Behaviour

The difference in the weld bead humping pattern produced on different base materials was introduced in Table 15. The humping mechanism that produced the “single bead” pattern was described in detail in Section 3.6b.ii. The video data from Figure 53 illustrates that a “single bead” forms due to coalescence of the expelled molten material at the rear of the pool. Figure 55 is video data that captures the formation of “twin bead” humping flaws with the weld porosity shown in Table 15. Similar to the single bead humping mechanism, molten steel is expelled from the gouging region due to the strong plasma jet force. However, the twin beads do not coalesce at the rear of the weld pool. Other unique observations of the twin-bead humping mechanism include:

- Twin humping only occurred when welding 300W steel and the threshold current was lower when compared to the single bead humping mechanism for Grade 80 microalloyed steel. This confirms that free surface active elements were partially responsible for the behaviour.
- Metal flow was erratic prior to the formation of the twin beads, and wetting behaviour was poor. A solid, continuous rim of liquid steel does not form around the arc; rather, small droplets form that poorly wet the substrate. The twin beads solidify with high aspect ratios (i.e., the beads are relatively tall & narrow) and rarely coalesce to fill-in the central arc gouge. The arc easily expelled molten material during gouging with low fluid resistance (i.e., low viscous drag). This behaviour indicates the molten steel has low surface tension and poor wettability; therefore, physicochemical behaviour directly influences flaw formation.

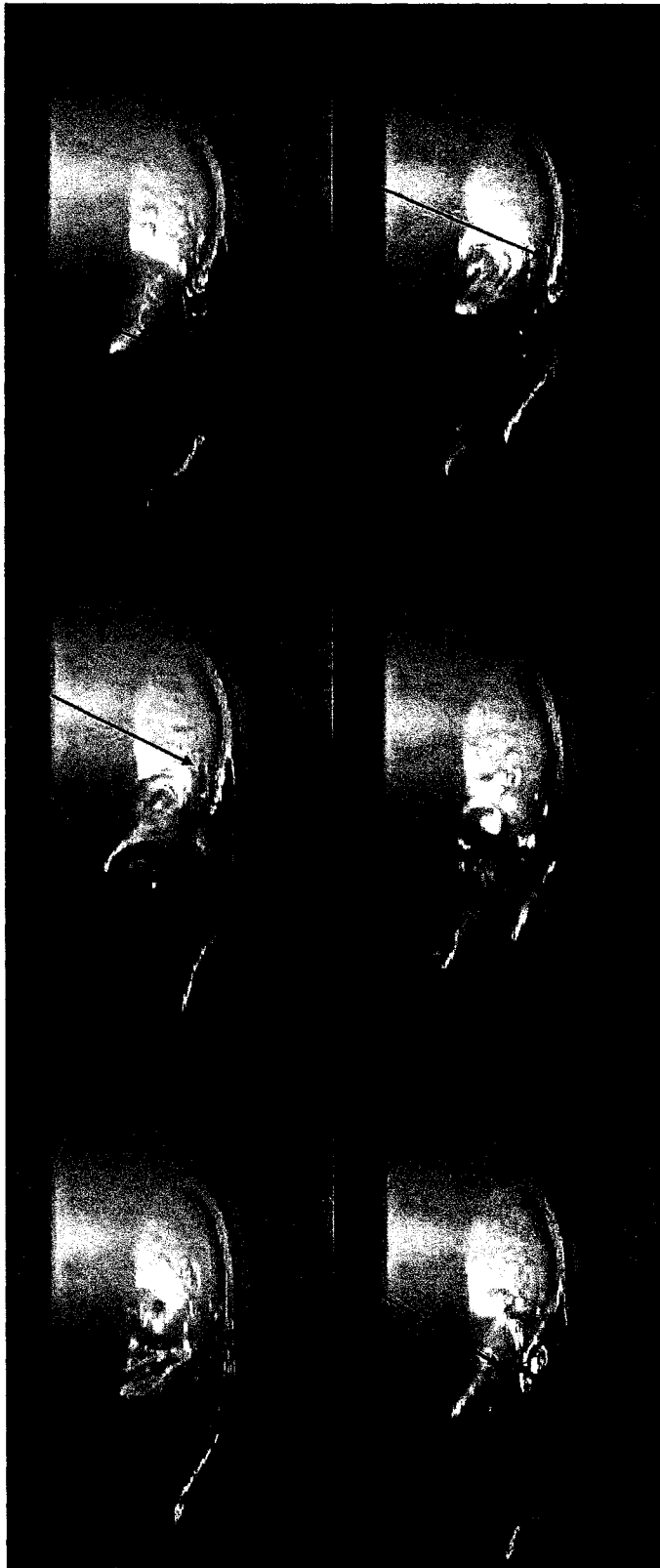


Figure 55 - Video Captures of Twin-Bead Humping Mechanism (approx. 1.5 seconds)

The behaviour during twin bead formation directly contradicts what is predicted from the Marangoni theory on surface tension driven flow. The free surface active oxygen and sulphur created a positive surface tension gradient where metal *should have* flowed from the edges of the pool to the arc center; this concept is illustrated in Figure 56. However, Figure 55 illustrates that the metal beads formed along the upper edges of the groove rarely coalesce at the rear of the pool. The flow of the thin film directly opposes the surface tension gradient. Marangoni flow, alone, also inadequately explains the single bead humping behaviour previously discussed in Section 3.6b.ii. Figure 56 predicts that without surface active elements the weld metal should be expelled from the gouging region and concentrate near the edges of the weld pool. Figure 53 illustrates that the fluid flow is again opposite to the surface tension gradient. Hence, it can be concluded that Marangoni driven flow is not a factor during autogenous PTAW bead humping. This correlates with the findings of Heiple and Roper [121,128], who stated that at sufficiently high current the Lorentz force will dominate fluid flow and the influence of trace active elements becomes less important.

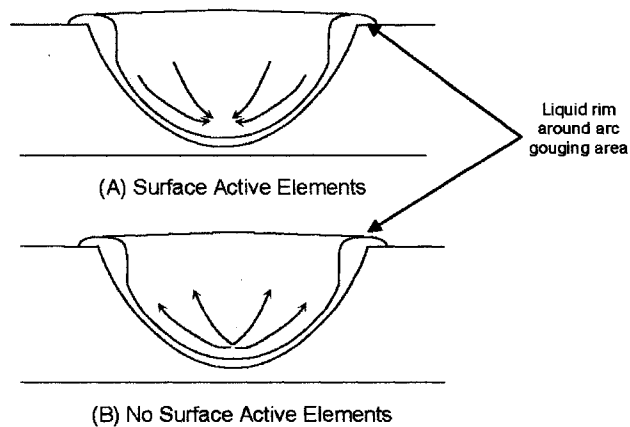


Figure 56 – Predicted Marangoni Fluid Flow for a Thin Film Weld Pool (Cross-section)

iii. Twin Bead Humping Mechanism

An alternative mechanism was sought to explain the formation of twin bead humping while welding 300W structural steel with free surface active elements. The influence of oxygen and sulphur on the surface tension of molten steel and iron is well established; hence, it was theorized that the physiochemical wetting behaviour of the molten weld pool could explain the humping behaviour.

The erratic behaviour, poor fluidity, and low viscous drag of the molten pool prior to forming the twin beads can be rationalized by considering the changes in the overall surface tension of the weld pool. As discussed earlier, Heiple and Roper [121,128] state that the weld pool surface tension will directly counter the impinging plasma jet force (or pressure). It has been established that the constricted arc is very penetrating due to a high energy density and strong plasma jet force. Therefore, the reduction in surface tension of the pool (due to surface active elements) would decrease the resistance to the arc force. This mechanism explains the poor fluidity and low viscous drag of the weld metal during the twin bead humping process. However, this mechanism does not adequately explain the lack of weld bead coalescence, formation of small droplets around the arc gouging rim, or the poor wetting of the work piece by the molten steel when welding the 300W steel.

To explain this behaviour, the dynamics of the physiochemical capillary wetting were examined. Figure 57 illustrates the behaviour of a molten material that wets a solid substrate. The definition of a wetting system is arbitrary, but is typical indicated by $\gamma_{LS} < \gamma_{SV}$ or $\theta < 90^\circ$. The angle the liquid obtains is dependent on the force balance at the junction near the edge of the droplet, which can be described by the following equation:

$\gamma_{LS} + \gamma_{LV}\cos\theta - \gamma_{SV} = 0$. The table accompanying Figure 57 summarizes how the contact angle will be changed if only one component of this balance is altered; hence, it is possible to create a system that is more or less wetting. If the force balance changes sufficiently so that $\gamma_{LS} > \gamma_{SV}$ and $\theta > 90^\circ$, then a non-wetting system is produced as shown in Figure 58. The behaviour is described by $\gamma_{SV} + \gamma_{LV}\cos(180 - \theta) - \gamma_{LS} = 0$; the table illustrates how the system can become more or less wetting.

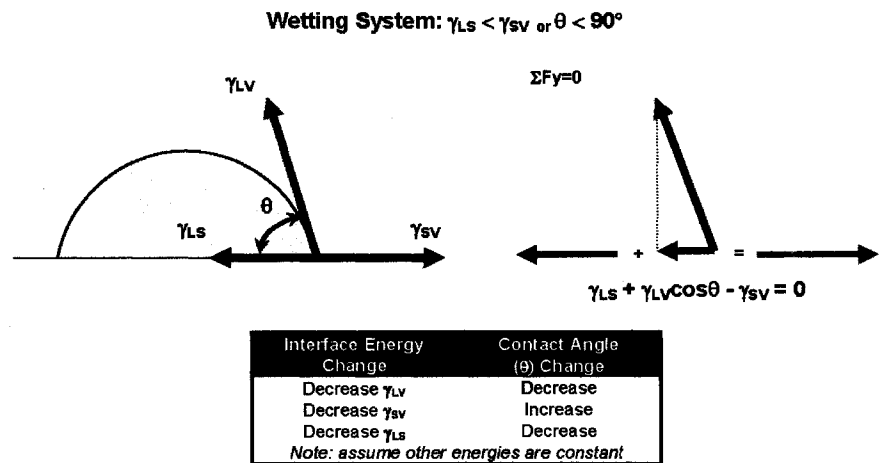


Figure 57 – Behaviour of a Wetting System

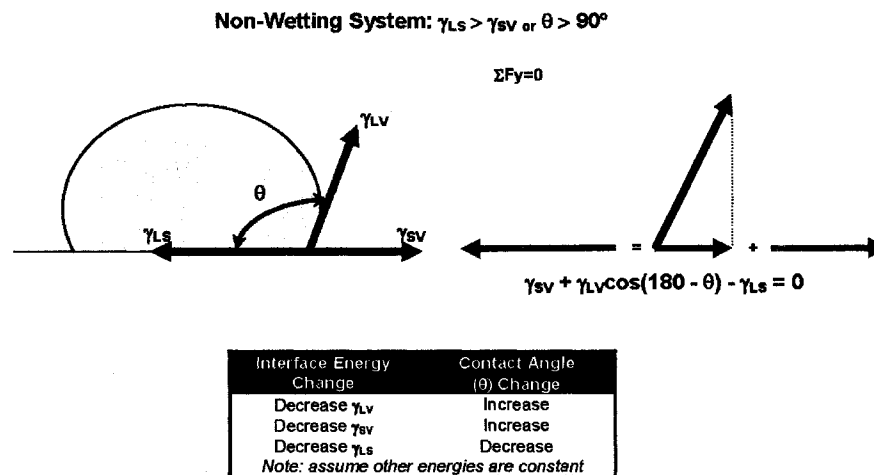


Figure 58 – Behaviour of a Non-Wetting System

Figure 59 illustrates the typical contact angles of the bead humps. Both steel systems exhibit relatively poor wetting characteristics with relatively high contact angles. In particular, the twin bead humps consistently have the *largest* contact angles.

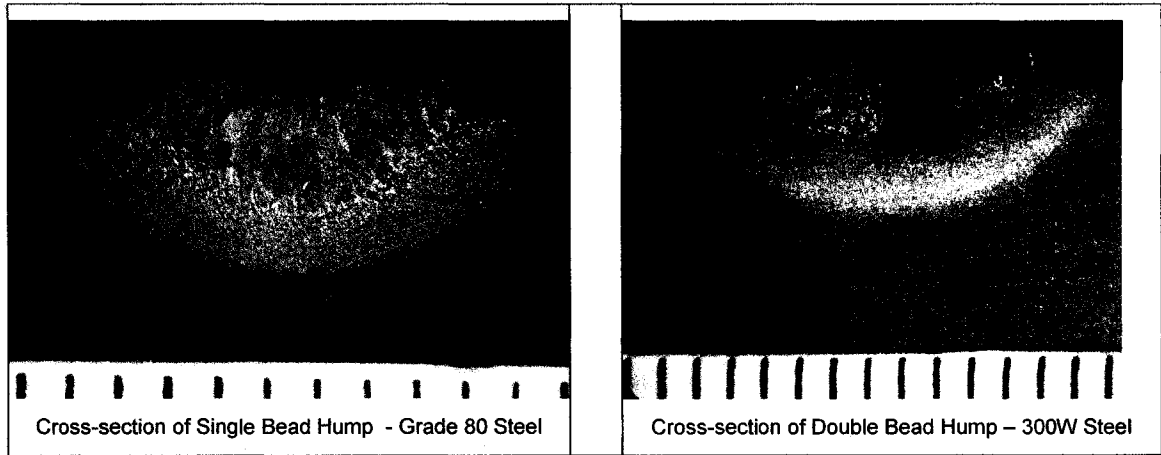


Figure 59 – Apparent Contact Angle of Humping Peaks

This shift towards higher contact angles or poor wetting has been attributed to the decrease in surface tension of the weld pool as a result of free surface active elements. For a non-wetting system, in order to maintain the force balance while reducing the surface tension, the contact angle must increase (assuming that the other interface energies remain relatively constant). This change in wetting behaviour is illustrated in Figure 60.

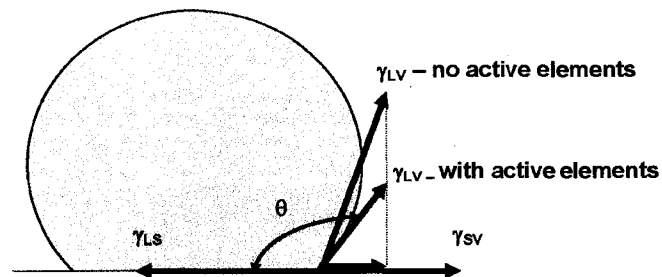


Figure 60 – Change in Wetting Behaviour with Surface Active Elements

This concept emphasizes the importance of considering all the interface energies when assessing wetting behaviour. Most literature is concerned only with modification of the liquid surface tension, likely because it can be readily measured via common experimental techniques [132], and most investigations immediately assume that a reduced surface tension will always bring about improved wetting behaviour. However, thorough analysis requires consideration of the balance between all the interface energies. The relationship between the contact angle and surface active elements was previously investigated by Humenik and Whalen [129]. They compiled data that demonstrated that the contact angle of a non-wetting ferrous liquid would increase with the addition of sulphur, even though the surface tension decreased. This correlates well with the concept illustrated in Figure 60. This concept likely also explains the increase in contact angle for high sulphur 304 austenitic stainless steel weld metals as reported by Mendez *et al.* [44]. Unfortunately, insufficient chemistry, metallurgical and video data was published to allow for a rigorous analysis. Humenik and Whalen also emphasize that a reduction in surface tension does not always produce improved wetting; reducing the solid-liquid interfacial energy is the most effective means for promoting wetting behaviour in an inherently non-wetting system (see Figure 58). These concepts were quantified in the work of Lee and Morita [130], where molten steel droplet surface tension and contact angles were measured on a CaO substrate, a strong desulphurizer. CaS formed at the interface yielded improved wetting, despite the fact that the droplet surface tension simultaneously increased due to the reduction in surface active element concentration. This data illustrates that investigations into wetting behaviour require analysis of all the interface energies.

To confirm that it was *only* the influence of surface active elements that led to twin bead formation, doping experiments with reactive elements were conducted. The results in Figure 49 and Figure 50 clearly indicate that the addition of reactive elements can modify behaviour considerably. The aluminum dopant formed a scum layer due to the reaction with oxygen, sulphur and other alloying elements; the formation of a scum layer has been reported by others [122]. There was a reduction in porosity due to the deoxidizing nature of aluminum. Immediately following the dopant hole, there was an increased tendency for the material to coalesce and form a single bead due to improved wetting of the base material as per Figure 60. Note the similarity between these beads in Figure 49 and Figure 50, and the typical single bead behaviour given in Table 15. After sufficient dilution, the effect disappears and twin bead formation resumes. The use of the Al-23%Mn powder also produced similar results. The use of manganese alone did not produce a scum layer, did not reduce porosity, and did not modify bead behaviour to the same extent as aluminum although the trend appears to be similar. This correlates well with the data presented by Mills and Keene [127] where large additions of manganese are required to appreciably affect the surface active behaviour of sulphur. Therefore, in the future it is recommended that a larger variety of dopants be used, such as calcium, cerium, aluminum, titanium, manganese, and mixtures therein. In conclusion, the doping experimental results confirm that surface active elements modify the physiochemical wetting behaviour of the weld bead during humping as proposed in Figure 60. Improved wetting behaviour led to single bead formation while reduced wetting initiated twin bead formation.

d. Effect of Welding Gas Composition

In the original investigation for GMAW, Bradstreet [109] found that humping only occurred under normal welding conditions in the presence of oxygen, either from the welding gas or from surface oxides. The presence of a deoxidant eliminated hump formation. During high current GTA welding, Savage *et al.* [115] observed that the humping threshold was significantly higher with 100% helium shielding gas. There is no known work regarding the influence of hydrogen additions on the humping mechanism. In the work investigated here, the influence of different plasma and shielding gas compositions on the PTAW humping mechanism will be discussed.

Based on the work of Savage *et al.* [115], it was theorized that the humping threshold would be increased via the addition of 25% helium to the plasma gas. However, as shown in Figure 47, the weld is slightly wider compared to pure argon but the humping threshold and bead behaviour remains essentially unchanged. It is likely that the addition of 25% helium to only the plasma gas was, unfortunately, insufficient to produce large-scale changes. It should be noted that the drastic increase in the humping threshold when using 100% helium, as observed by Savage *et al.*, was not related to the arc force and they did not determine the underlying cause. In future work, the humping threshold should be determined as a function of various helium contents up to 100% to obtain, if any, desirable effects.

As shown in Figure 47, the addition of 10% hydrogen to the plasma or carrier gases eliminated humping but led to weld bead porosity. The weld width and depth are noticeably increased due to the high heat input dissociation/recombination reaction. The weld bead is noticeably cleaner and the surface oxides are removed due to the chemically

reducing nature of the mixture. The reasons for the elimination of weld humping are believed to be three-fold: (1) the high heat input of the hydrogen plasma, (2) the increase in pool surface tension, and (3) changes in physiochemical wetting behaviour of the pool in a reducing atmosphere.

It has been well established that hydrogen additions will produce greater heat input; increased energy density, and productivity improvements close to 40% have been observed during keyhole welding [131]. During autogenous welding, this extra energy translates into greater work piece melting and increased bead dimensions. It was determined earlier that the formation of a prematurely solidified region and insufficient metal flow to the rear of the pool were the underlying causes of weld humping. However, the extra energy from the hydrogen additions quickly “repaired” any prematurely solidified regions. Figure 61 illustrates the typical pool shape and the abundant quantity of weld metal present.

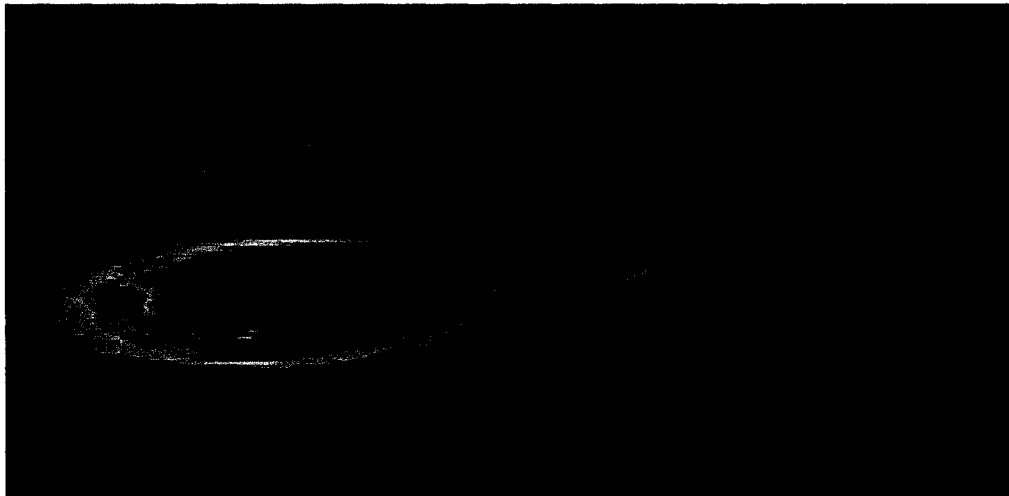


Figure 61 – Weld Pool Shape with Ar-10% Hydrogen Plasma Gas

The shape of the weld pool is quite different from that observed when welding with argon

plasma gas (see Figure 53). A thin film does not develop; rather a depressed pool similar to that encountered during high current GTAW is formed. The current was increased until keyhole formation, and undercutting or humping flaws never occurred. As discussed earlier, Heiple and Roper [121,128] stated that the liquid surface tension will directly counter the impinging plasma jet pressure and Lorentz force. Hence, hydrogen additions appear to increase the surface tension of the weld pool, which increases resistance to the formation of a thin film. An increase in stainless steel surface tension with hydrogen, under welding conditions, was qualitatively proven by Wen and Lundin [132], and attributed to a reduction in free surface active oxygen concentration. These results also correlate well with the doping experiments completed earlier, where it was proven that surface active elements lowered surface tension and intensified the effect of the plasma jet and Lorentz force on the pool depression.

The final factor contributing to the elimination of weld bead humping was the change in physiochemical wetting behaviour. As shown in Figure 61, the weld pool readily wets the base material. Video analysis also proved that the leading edge of the base material was chemically reduced prior to melting and being drawn into the weld pool, i.e., the base metal surface energy γ_{sv} was increased. It is postulated that the reducing atmosphere simultaneously lowered the solid-to-liquid interface energy γ_{ls} by reducing interface contaminants. Therefore, the system shifted from non-wetting (or $\gamma_{sv} < \gamma_{ls}$ as per Figure 58) to wetting (or $\gamma_{sv} > \gamma_{ls}$ as per Figure 57), even though the liquid surface tension increased. This behaviour reinforces the concepts introduced in Section 3.6c and illustrates that a thorough analysis of wetting behaviour requires consideration of all three interacting interface energies. The common belief that a reduction in surface tension

will *always* bring about better wetting is contradicted when considering the influence of hydrogen gas.

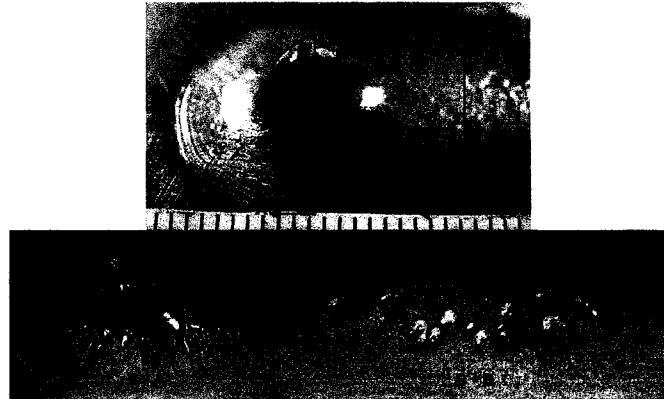


Figure 62 – Macro Views of Autogenous Welds Completed with Ar-10% Hydrogen Plasma Gas

A drawback of utilizing hydrogen as the plasma or shielding gas was the formation of porosity at the rear of the welding pool (see Figure 61). As shown in Figure 62 the weld volume contained excessive porosity (B-B); after the arc was extinguished the hydrogen pressure was sufficient to push the weld metal upwards to form a tall, hollow peak (A-A). This phenomenon results from the absorption, super-saturation, and rejection of hydrogen during solidification due to a reduced solubility compared to liquid iron. The hydrogen porosity mechanism proposed by Salter and Milner [133] stated that hydrogen was first absorbed in the high-temperature “active zone” below the electrode. This saturated liquid metal was transported to the edges/rear of the pool due to convective forces, and porosity formed at the solidification front due to a buildup of hydrogen pressure. The results of the experiments completed here agree with this theory. As shown in Figure 47, the use of helium as a plasma or shielding gas had no effect on the formation of porosity. The use of Ar-20% CO₂ shielding gas was effective in reducing the formation of porosity as shown in Figure 63. The oxidizing CO₂ gas likely reacted with the “excess” hydrogen that

had previously caused the porosity during solidification, and formed water vapour that was transported away by the shielding gas. Weld spatter and occasional surface oxides were formed during solidification, but weld pool wetting behaviour was relatively unaffected. The use of Ar-10% H_2 and Ar-20% CO_2 was the only combination whereby all weld metal flaws (i.e., undercutting, humping, and porosity) were completely eliminated. Martikainen and Moisio [131] found that this same combination of gases produced the most uniform appearance and regular penetration during optimization of keyhole welding.

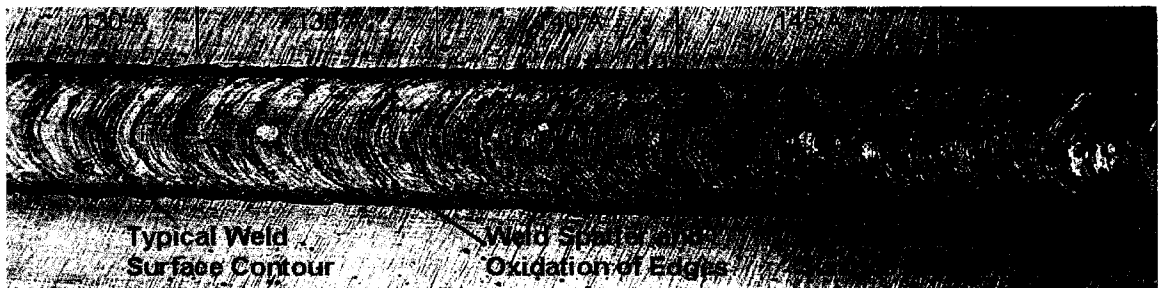


Figure 63 – Autogenous Weld with Ar- H_2 Plasma Gas & Ar- CO_2 Shielding Gas (130A-145A)

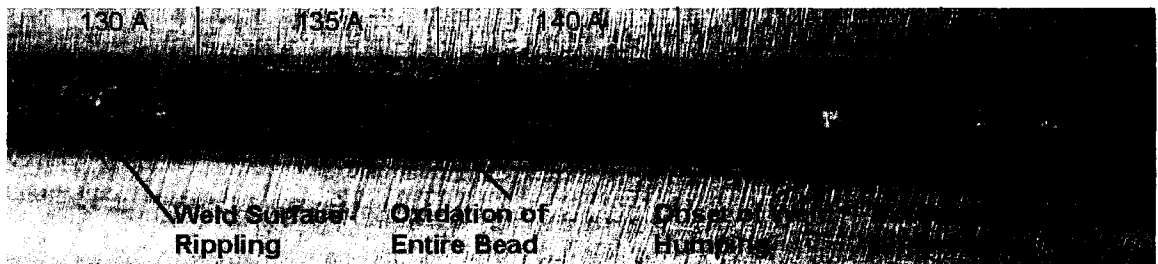


Figure 64 – Effect of CO_2 Shielding Gas during Autogenous Welding (130A-145A)

Based on the results of Bradstreet [109], the use of Ar-20% CO_2 was expected to exacerbate the humping phenomenon. Conversely, this shielding gas medium, with argon or Ar-He plasma gas, actually increased the humping threshold current. This improvement is attributed to the recombination energy for the dissociable gas increasing

the quantity of weld metal formed that “repaired” prematurely solidified regions (as discussed above for hydrogen). However, the oxidizing nature of carbon dioxide caused undercutting, surface oxidation, and surface rippling¹ as shown in Figure 64. Poor wetting behaviour was also observed due to the balance of interface energies. Weld pool surface tension, γ_{LV} , was reduced due to free surface active oxygen. The base metal near the leading edge of the pool was chemically oxidized and the solid-vapour interface energy, γ_{SV} , was reduced; therefore, a non-wetting system ($\gamma_{SV} < \gamma_{LS}$ as per Figure 58) was established. At sufficiently high current, the beneficial effects of the recombination energy were undermined by the poor physiochemical wetting behaviour of this system, which led to weld hump formation as shown in Figure 64.

¹ Surface rippling is an uneven or step-like surface profile due to the poor ability of the liquid metal to wet on previously solidified weld metal.

3.7 Conclusions

- The *true* quantity of energy delivered to the work piece is not adequately predicted by the heat input equation during PTA welding. Large differences in weld size are obtained for the same nominal heat input value; the equation also does not aid in the prediction of fusion flaws.
- The operating map method can be used to predict PTA weld behaviour and provides an excellent forum for comparing the relative influence of the process parameters. The combinations of speed and current that initiate flaws are readily identified.
- The PTAW behaviour in the thin film regime was characterized for low and high welding speeds. The humping mechanism was attributed to the formation of a premature solidified region and disruption of molten metal to the rear of the pool
- The PTAW humping mechanism correlates well with previous work completed for humping of high current GTAW. The critical combinations of current and welding speed that initiate humping are much lower for PTAW compared to GTAW and GMAW. Although capillary instability describes the humping phenomenon for GMAW and laser welding, there is no correlation with PTAW humping.
- For the range examined, plasma and shielding gas flow rates were found to have a minimal effect on the humping threshold and weld dimensions. Increased electrode set back intensified arc constriction, which increased the arc penetrating ability and lowered the humping threshold. Formation of a secondary, backwards acting arc appears to stabilize the bead hump, although further work is required to quantify this effect.

- Two different humping flaws were formed: single bead and twin bead, which depended on the base material chemistry and concentration of free surface active elements. However, surface tension driven “Marangoni” fluid flow does not influence bead behaviour or flaw formation when operating with a depressed thin-film pool. Physiochemical behaviour, i.e., surface tension and wetting behaviour, of the thin-film strongly influences the type of fusion flaws created.
- Two successful weld doping techniques were developed and utilized in these experiments. The results confirmed that surface active elements modify the physiochemical wetting behaviour of the weld bead during humping. Improved wetting behaviour led to single bead formation, while reduced wetting initiated twin bead formation.
- Addition of 25% helium to the plasma gas had no noticeable effect on bead formation or the humping threshold.
- Addition of 10% hydrogen to the plasma or shielding gas eliminated weld humping due to the following: (1) the high heat input of hydrogen plasma, (2) an increase in pool surface tension, and (3) changes in physiochemical wetting behaviour of the pool in a reducing atmosphere.
- Ar-10%H₂ and Ar-20%CO₂ were the only combinations whereby all weld metal flaws (i.e., undercutting, humping, and porosity) were completely eliminated.
- At sufficiently high current, with Ar-20%CO₂ shielding, the beneficial effects of the recombination energy were undermined by the poor physiochemical wetting

behaviour of this system, which led to weld hump formation.

- A thorough analysis of wetting behaviour requires consideration of all three interacting interface energies. The common belief that a reduction in surface tension will *always* bring about better wetting can be contradicted.

3.8 Recommendations for Future Work

- Analysis of humping behaviour needs to be completed over a larger range of welding speeds. It can be verified how the maximum current (i.e., humping threshold) is affected by weld speed. The influence on the humping threshold of other process variables, such as plasma gas, shielding gas, and arc constriction, need to be verified over a larger range of welding speeds.
- The unique secondary arc observed during PTAW needs to be investigated to determine what effect, if any, the reverse Lorentz force has on weld bead development.
- Further investigations of the humping mechanisms for different grades and heats of steel is required to confirm and expand upon the single and twin bead humping mechanisms presented here. In addition, doping experiments with calcium, cerium, aluminum, titanium, manganese, and mixtures thereof could also modify the humping flaw mechanism considerably.
- Judging by the strong influence of gas composition on bead behaviour, the operating map for a new type of plasma and/or shielding gas would likely change considerably.
- The humping threshold should be determined as a function of various helium contents up to 100% to obtain, if any, desirable effects.
- It may be possible to utilize lower hydrogen content and still eliminate humping while not forming porosity.

CHAPTER 4 – Part 2: PTA Welding of MMC Overlays

4.1 Project Objectives

The second part of this thesis is centered on studying the effects of PTA welding parameters for a practical engineering application. The plasma transferred arc surfacing technique has been investigated by others, but most often the primary focus is on the wear and/or corrosion resistance of the coating. Work to the present has concentrated on the metallurgical effects of carbide type, carbide fraction in the deposit, carbide dissolution effects and binder alloy composition [134,135], all in order to increase wear/corrosion resistance to suit engineering applications, such as oil sands abrasion [136]. However, there are only a few studies where the *main* objective is developing a greater understanding of welding parameter influences [137]. Some investigators utilize factorial techniques to predict overlay quality [138,139], which demonstrate interrelationships between variables but often do not explore the underlying principles. Other experimenters who investigate process parameters retain most of the information and a small amount has been published in the open literature. In particular, little has been done in any jurisdiction on the effects of plasma, carrier and shielding gas compositions on process behaviour. What information is available appears to concentrate on the effects of gas flow rate [140], and changes in gas composition are rarely mentioned or any possible benefits are discounted [141]. Therefore, a systematic study was employed to understand the effects of welding parameters on overlay development and properties. The interactions of torch motion, arc energy, and powder delivery on deposit formation were sought. Finally, the influence of gas composition on process behaviour was determined, utilizing video recording and metallurgical analysis of the overlay.

4.2 Literature Review

a. Metal Matrix Composites

Ceramic – metal composites are defined as a heterogeneous combination of a ceramic phase(s) with metal(s) and/or alloy(s) [142,143]. Within this broad category, an entire material genre exists, with various ceramic-metal composite classifications such as “cermets”, “cemented carbides”, “hard metals”, and “metal matrix composites”. The use of these classifications is largely historical, with highly subjective distinctions; hence, the terms are often used interchangeably and inconsistently in the literature. For brevity, the term metal matrix composite (MMC) will be used herein.

The concept of reinforcing a metal with a ceramic is relatively old, and is analogous to fiber-composite reinforced polymers. For wear applications, the goal of the MMC is to combine the beneficial properties of the ceramic (i.e., high wear resistance and hardness) with that of the metal matrix (i.e., ductility and adhesion). Homogeneous microstructures and strong bonding between metal and ceramic are required for uniform load bearing and transfer. Matrix – reinforcing phase compatibility strongly affects microstructure and wear properties. Greenhut and Haber [142] emphasize the following compatibility factors:

1. Composition, structure, and grain size of the matrix;
2. Ceramic surface character, i.e., shape, roughness, porosity;
3. Ceramic volume fraction, size, and orientation;
4. Wetting and chemical bonding between carbide grains and matrix;

Depending on the application and intended service of the component, the relative

importance of the compatibility factors will vary. These factors are also strongly affected by the technique employed during surfacing.

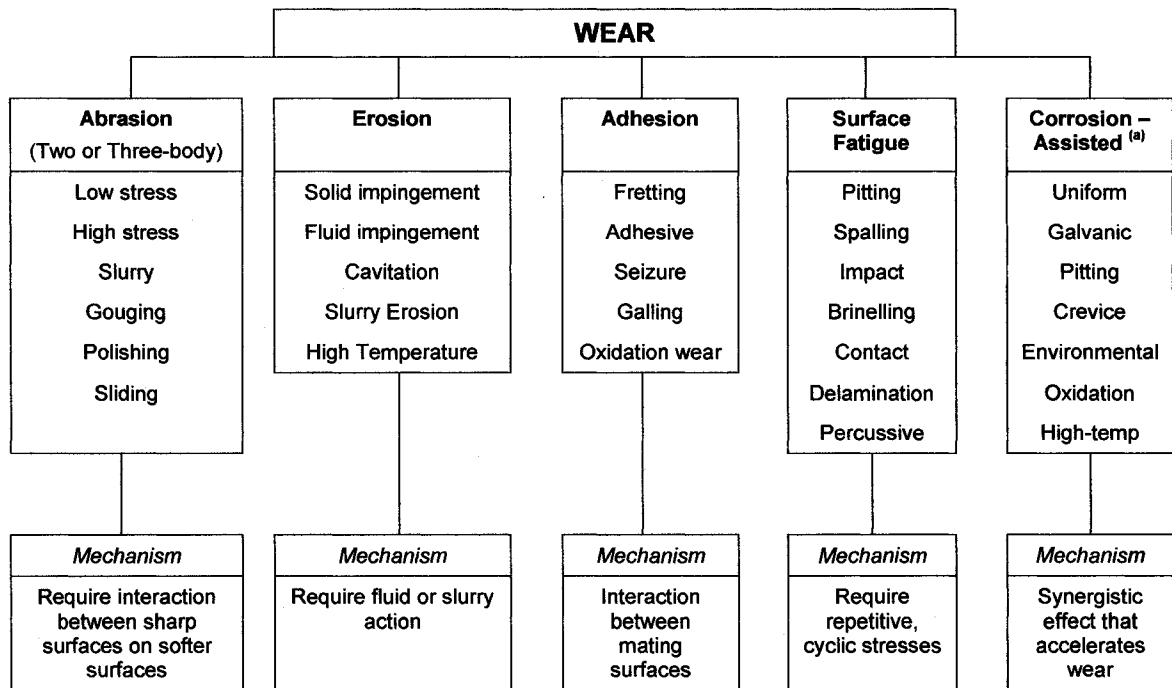
b. Wear Applications in the Alberta Oil Sands

In the mining and oil sands industry, wear mechanisms are responsible for costly component damage and equipment repair. Wear attack alone is responsible for higher production costs; in excess of \$50 million is spent at Syncrude's Fort McMurray operations per year in equipment repairs/replacement [136,144]. During oil sands processing, the equipment and machinery must be tolerant enough to handle two tonnes of oil sands for every barrel of refined oil produced [145]. Production goals could not be achieved without protective coatings for key production equipment, and oil sands processing would be unprofitable. Hence, there is a strong driving force for continued development of MMC materials [146] and optimization of the PTAW technique for application of the MMC to equipment and parts.

The science of wear falls within the genre of tribology: "the science and technology of interacting surfaces in relative motion", which includes consideration of friction, wear, and lubrication [147]. The classification of wear modes, mechanisms, and models is highly variable in the literature. As shown in Figure 65, which is a compilation from various references [146,147,148,149,150], a large regime of wear mechanism exists for common engineering applications. During oil sands operations wear regimes range from low and high stress abrasion, to gouging abrasion, and very severe adhesion (galling) on equipment such as rock crushers and earthmoving equipment [144,151]. Other concerns include slurry abrasion and erosion, and high temperature erosion. Most damage in oil sands operation is due to fine hard particles, such as quartz (SiO_2), zircon (ZrSiO_2), and

rutile (TiO₂) [144,152]. Depending on the particular wear mode, different wear mechanisms exist. Proper microstructural development and wear testing, such as ASTM G65 for measuring abrasive wear resistance of materials, are essential for ensuring component longevity.

Figure 65 – Classification of Common Modes of Wear



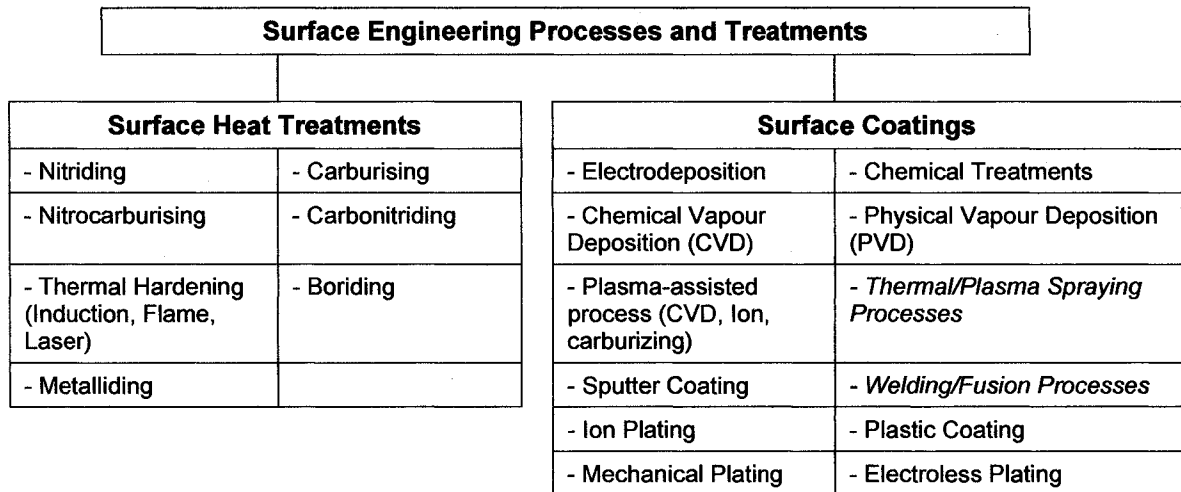
NOTE (a): Environmental corrosion includes stress-corrosion cracking (SCC), hydrogen embrittlement, micro-organism induced corrosion, sulfidation, organic/inorganic acids, etc.

c. Comparison of MMC Surfacing Techniques

Wear resistant materials generally have high hardness and low toughness, which makes processing, forming, and cost-effective production of complex shapes difficult. As a result, much work has been completed to develop techniques for applying wear resistance coatings onto component surfaces. These production methods are broadly divided into two categories: surface heat treatments and surface coatings. In the former, the inherent substrate composition/chemistry with proper heat treatment produces the desired surface

properties. Often these surface modification techniques are accompanied by the diffusion of elements, e.g. carbon or nitrogen, into the hardened surface. The latter includes methods to deposit MMC material onto the substrate. Applicable processes for these two categories are summarized in Figure 66. A detailed discussion of each process is beyond the scope of this review. However, the two families of surface coatings that are relevant to these discussions are thermal/plasma spraying and welding/fusion processes.

Figure 66 - Surface Heat Treatments and Surface Coatings [148,149,153]



Thermal/plasma spray processes use a high-energy heat source, either combustion of gases or an electric arc, that melts the coating material before it is propelled at high velocity onto the substrate material [154,155]. The non-transferred mode of plasma arc operation falls within this category. The droplets impact onto and are cooled by the surface before adhering to surface irregularities, solidifying, and forming a mechanical bond [148]. General schematics of the spray process are shown in Figure 67 and Figure 68; the most common types are summarized in Figure 69.

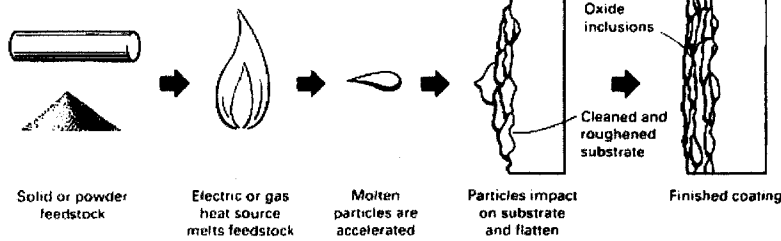


Figure 67 – Schematic of Spray Processes [155]

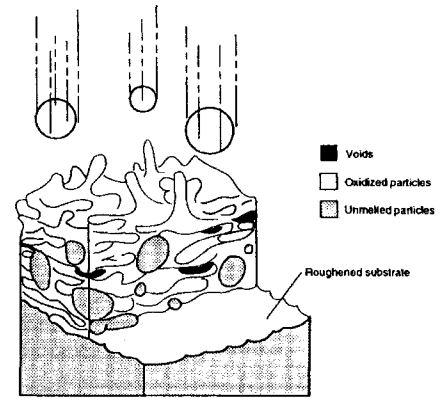


Figure 68 – Surface Buildup [155]

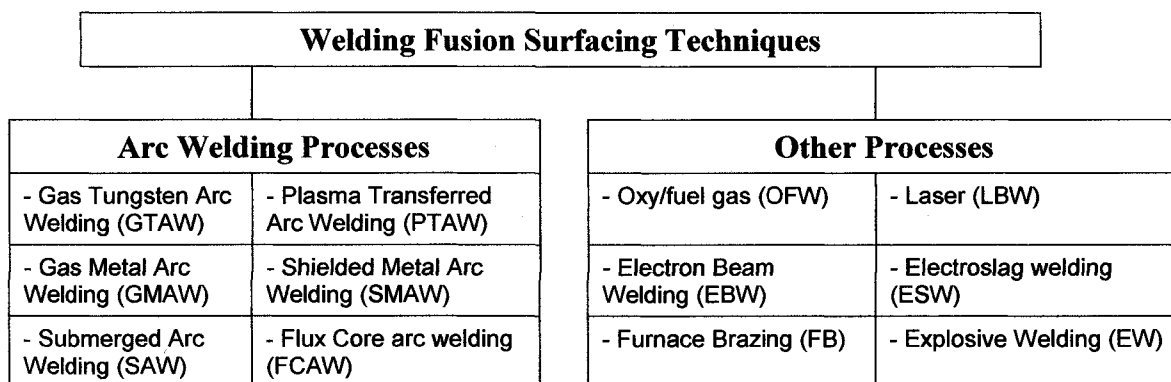
Proper process selection is based on numerous factors such as surface quality, costs, productivity, etc. Coatings are not melted into the surface and processes exist for both metallic and nonmetallic materials with very little heat input to the component, provided the proper surface preparation and parameter selection are completed. The main limiting factors are mechanical bond strength (generally 34 – 48 MPa) rather than a metallurgical bond, and coating thickness is limited to 1 – 2.5 mm. Coatings ranging from 3 – 5 mm are easily achieved with PTA surfacing [152]. Hence, thermal/plasma sprayed MMC coatings have found applications in the oil sands industry, but are generally not robust enough to handle more severe service in the oil sands industry.

Figure 69 - Industrial Thermal Spray Surfacing Techniques [148,153,149,155]

Thermal Spray Surfacing Techniques			
Gas Combustion Processes		Arc/Plasma Processes	
- Oxy-fuel wire (OFW)	- Oxy-fuel rod	- Plasma arc powder (PA)	- Electric arc wire (EAW)
- Oxy-fuel powder (OFP)	- Oxy-fuel jet powder	- Atmospheric plasma spraying (APS)	- Inert Plasma Spraying (IPS)
- Detonation gun (D-Gun)	- High-velocity oxy-fuel (HVOF)	- Vacuum Plasma Spraying (VPS)	- Underwater Plasma Spraying (UPS)
		- High-Power Plasma Spraying (HPPS)	

Weld surfacing techniques produce a metallurgical bond and “clad” the substrate with a relatively thick layer of MMC material². Weld surfacing processes cover a wide spectrum of operation, including manual, semi-automatic, mechanized, or fully-automatic arc-welding and non-arc processes, as shown in Figure 70 [148,157]. Examples have been documented where optimized PTA MMC overlays have extended the life of industrial components used in oil sands operations from 300 – 700% with significant lifetime cost reductions [145,156]. Process selection depends on substrate and coating material compatibility, weldability, costs, and desired productivity.

Figure 70 – Commercially Applicable Surfacing Techniques



There are benefits and disadvantages to using either thermal/plasma spraying or welding/fusion processes, and within each group certain processes are adaptable to specific applications. As a result, there are handbooks [154,155,157], industry standard practices [149], and texts [148] that provide guidelines and algorithms to aid the selection process.

²In welding literature, the terms hardfacing, surfacing, cladding, and overlaying are often interchangeable.

d. Previous Studies for PTAW Surfacing

The majority of PTAW investigations have concentrated on metallurgical characterization, wear/corrosion behaviour, and weldability tests for new alloy (powder) development [140,158,159,160,161,162]. A full discussion of these studies is beyond the scope of this literature review. There are relatively few investigations where the main objective is to understand the effects of process parameters on overlay development and properties. The following will discuss these studies and the relative importance to the work completed herein.

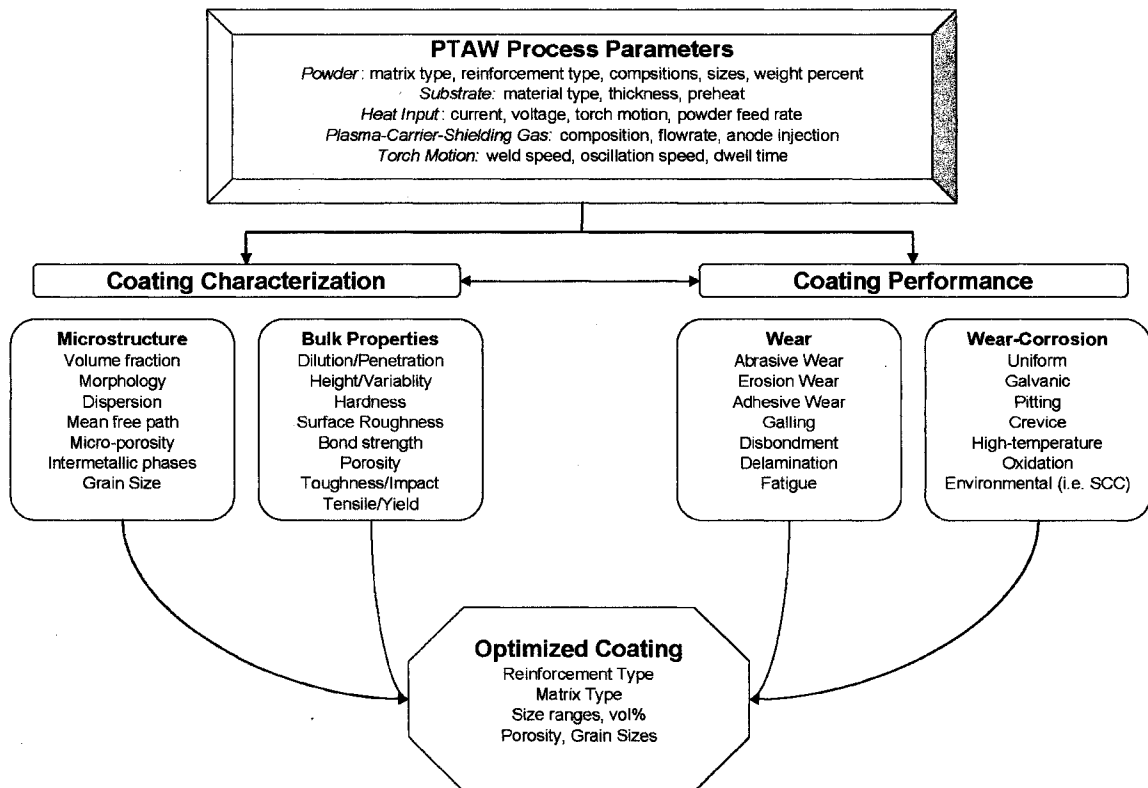


Figure 71 – Optimization Flow Chart for PTAW Surfacing Parameters and Coating Behaviour

Figure 71 lists the major PTAW process parameters that directly influence coating characteristics and behaviour. Also listed are common microstructural and bulk

properties that are investigated, and the engineering wear/corrosion regimes for which the coatings are intended. Taken as a whole, this flow chart illustrates the main constraints to develop a viable coating and fully characterize its formation and properties. Figure 71 also illustrates the wide scope of experiments that could be completed to achieve many interacting objectives (i.e., high productivity with excellent corrosion behaviour).

The following survey (Table 18, Table 19, and Table 20) summarizes the common process parameters investigated by others for ferrous alloy systems. Investigations into MMC overlay welding onto aluminum and titanium base materials are also areas of active research [158,159,166,163]. Although some authors discuss optimizing MMC coatings [171], there is no known method or protocol for establishing optimum welding parameters. The most thorough analysis of the interacting process parameters was completed by Deuis *et al.* [164]; Figure 72 defines the influence of PTA process parameters on the formation, properties, and structure of PTA welded MMC overlays. Note the relatively large range of process parameters listed in Table 19 and Table 20. Parameters are very subjective and variable depending on materials, equipment, and investigator methods. Hence, one of the objectives of the work completed here was to explore the interrelationships of torch motion, powder delivery, and arc energy, or the effective heat input, during PTAW. In particular, a motion optimization protocol was developed that will allow for standardized investigations in the future.

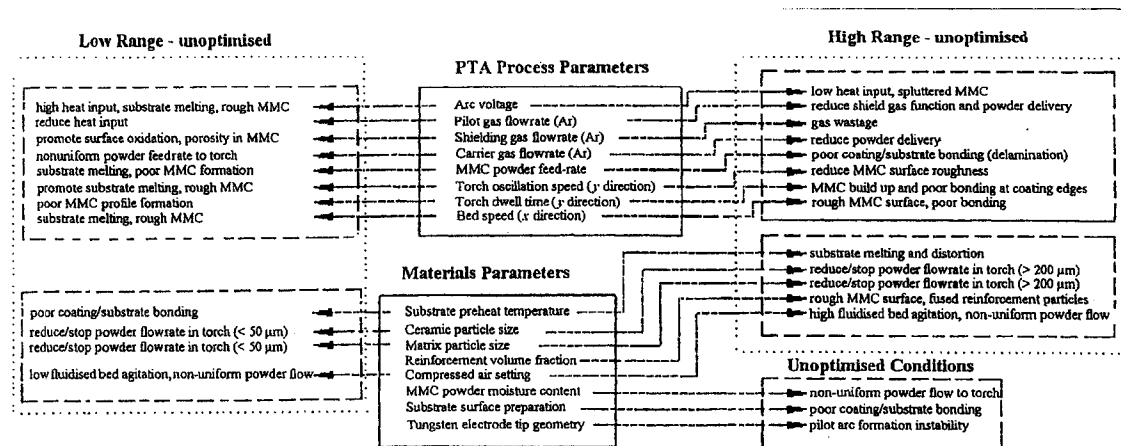


Figure 72 – Influence of Operating Process Parameters on MMC Coating Formation [164]

Table 18 lists the common welding consumables utilized during PTAW surfacing. Normally materials are powdered mixtures of matrix and carbide, and there are many common industrial mixtures (e.g., stellite). Powder volume fractions are chosen to suit the final engineering application. Often the matrix and carbide particle size ranges are investigated. Hallen *et al.* [171] state that a size range of 53 – 180 μm produced minimal dilution and penetration, which resulted in the best coating properties. Deuis *et al.* [140] recommend 50 – 150 μm to ensure proper powder flowability. Babiak *et al.* [134] determined that maximum melting efficiency and minimal dilution was achieved with particles sizes of 100 – 200 μm . These three ranges overlap, but the variability is likely due to differences in powder composition, and other welding parameters such as arc energy and motion. The most common carbide type is tungsten carbide (WC or W_2C). However, Sasaki *et al.* [175] selected VC because of its comparatively lower specific gravity reduces the “carbide settling” effect associated with heavy tungsten-based carbides. Gradients in overlay properties, such as carbide distribution, hardness, and wear behaviour are avoided. Wu *et al.* [180] investigated the behaviour of a number of

reinforcing particles: TiC (74-149 μm), VC (74-149 μm), NbC (74-108 μm), WC (74-149 μm), MoC (74-149 μm), Cr-C (74-149 μm), SiC (74-177 μm), ZrB₂ (<74 μm), and Al₂O₃ (108 - 177 μm). Developing new MMC compositions and characterizing their behaviour is an area of active research.

Table 19 lists the typical PTA process parameters and powder feed rates. Specific to the melt-in overlay PTAW technique, based on the deposition rate, the following classes of operation are used: MPTA (micro-PTA), PTA (standard-PTA), and HPTA (high power PTA) [140,171]. Note the similarity of these classes to the generic current modes described in Section 2.2c.iii. During MPTA the deposit penetration and dilution are minimized, producing a finer grain structure when compared to standard-PTA. Typical parameters include current from 1 – 50 A with up to 1kg/hr (17 g/min) maximum deposition rate [79]. Standard-PTA covers the largest and most common range of parameters, with 50 – 300 A and up to 7 kg/hr (117g/min) deposition. HPTA mode involves currents of 300 - 500A and deposition rates up to 12–15 kg/hr, which is comparable to submerged arc welding (SAW) techniques. However, HPTA has the added benefits of much lower dilution (<20%) and a finer microstructure compared to SAW, which approaches 25-40% dilution with a relatively coarse structure and relatively thicker coatings must be employed to obtain proper surface characteristics [188]. It is common practice to optimize current to suit a given powder mixing-ratio and particle size, based largely on minimizing dilution while ensuring proper physical bead appearance [174]. However, no agreed upon or standardized techniques exist for completing this process, largely due to variations in torch design, operation, and

experimental methods.

Due to the complex nature of the PTAW process, there are a large number of interrelated welding parameters. Many statistical techniques have been employed to explore these interrelationships and provide algorithms to optimize overlay development. The factorial techniques completed by Harris and Smith [141] developed quantitative relationships between process parameters and overlay quality, which were verified experimentally. Current, standoff, powder feed rate, weld speed, and oscillation width were identified as the main controlling parameters. Dehaut and Rochette [165] determined that three parameters have a notable effect on metallurgical quality: the main arc current, powder feed rate, and the surface area covered by the torch. The factorial experiments completed by Herrström *et al.* [138] assessed welding variable influence on overlay properties. For the range of experiments completed, the largest influences on dilution and hardness were current and plasma gas flow; weld width was highly dependent on current and weld speed; deposit height was strongly influenced by plasma gas, weld speed, and current. The fundamental reasons for these statistical relationships were not explored. Marimuthu and Murugan [139] applied a five level factorial technique to the hardfacing of valve seat rings; graphical aids were presented for selection of appropriate process parameters to obtain a desired level of quality.

Matsuda *et al.* [166] determined practical operating ranges as a function of welding current and powder feed rate. The range of operation was also affected by the carbide type; NbC and TiC had the largest operating range while the window for SiC was considerably narrower. The weldable operating range was enlarged with increased substrate preheat, but above 300°C the operable range either remained constant or

decreased; the cause of this phenomenon is not clear. Penetration became more acicular or finger-like with increased powder feed rates. This is directly linked to greater constriction of the plasma, which increased energy density and elevated penetrating capability. This “thermal pinch effect” was amplified with increased current and preheat. It was observed that porosity only formed when carbide material was added to the matrix material (i.e., there was no porosity when welding only the matrix material). The authors attributed this to moisture contamination, which does not explain why no porosity formed in the previous case. However, porosity formation may be linked to a physiochemical phenomenon or the poor wetting of the carbide particle by the matrix material [140].

Dören and Wernicke [137] completed a study into the effects of particle shape, size, and morphology. The differences in *actual* powder feed rates obtained as a function particle morphology, either angular or spherical, were discussed. A greater mass flow rate was achieved with spherical powder compared to angular, with all other variables constant. The experimenters explored interrelationships between particle type, plasma gas flow, and feed rate, and the subsequent influence on overlay hardness and dilution. Lower particle feed rates, with all other variables constant, were found to increase dilution and reduce overlay hardness; these effects were exacerbated by an increase in current and plasma gas flow. Others have completed analysis of the powder behaviour as it is transported from the torch to the substrate. Xibao and Hua [167] developed a model that predicted particles size ranges that were susceptible to melting and evaporation in the arc column; recommendations were given to reduce particle waste. The theoretical assessment completed by Xibao and Wenyue [168] predicts that the particle velocities in the transferred arc are lower than the plasma jet speeds, and that the velocity obtained

increases with reduced particle size and reduced density. This theoretical evaluation was not verified experimentally.

As shown in Table 20, very little work has been done in exploring different gas compositions for PTAW surfacing applications. Some experimenters [141,171,173,138,178,183,188] utilize hydrogen gas additions for the carrier and/or shielding flows mainly to minimize oxidation of the powder and overlay. These gas additions have been successfully welded on ferritic steels, which indicates that very little diffusible hydrogen remains following PTA surfacing that could cause hydrogen assisted cracking (HAC). To the author's knowledge, no investigations into plasma gas additions have been published in the open literature. Kamalyan *et al.* [169] studied gas porosity and spatter with nitrogen shielding gas; addition of 0.5 – 0.6 wt.% aluminum to the powder reduced porosity to acceptable levels due to formation of stable nitrides, and reduced spatter 6 – 14 times. Wahl and Krauskopf [170] describe various gas combinations for all three gas streams. Selection of these gases is heavily dependent on the materials and applications. They suggest argon and helium mixtures to control plasma temperatures and enthalpies, which directly influence energy density, penetration/dilution, and deposition rates. Argon and hydrogen mixtures are suggested for shielding gases, while argon and nitrogen are recommended for the carrier gas. However, the authors do not provide quantitative data to illustrate the effects of gas composition of overlay development or properties.

Table 18 – Survey of PTAW Surfacing MMC Powders

Substrate	Matrix Powder	Powder Size (µm)	Carbide Type	Carbide Size (µm)	Particle Content (vol.%)	Ref.
Steel	NiCrWC	53-180	WC	-	-	[171]
Steel	Co-based	50-150	WC	42-91	30;20;10	[172]
Steel	Ni-based	50-150	WC	42-91	40;50	[172]
Steel	Ni-based	50-151	WC	42-92	30	[172]
Steel	Ni-based	45-90				[173]
Steel	Stellite 6	25-180	Cr-C	25;53;106	20;30;40	[174]
Steel	Stellite 6	25-180	TiC	25;53;106	20;30;40	[174]
Steel	Co-Cr-Mo	73-220	VC	74-147	20	[175]
Steel	Co-Cr-Mo	<63	VC	<2	20	[175]
Steel	Fe-10Ni-19Cr	200 mesh	VC	200 mesh		[176]
Steel	Fe-10Ni-19Cr	200 mesh	NbC	200mesh	20	[176]
Steel	87Fe-12Cr-0.2Al	200 mesh	VC,NbC	200mesh	30;30	[176]
Steel	87Fe-12Cr-0.2Al	200 mesh	TiC,NbC	200mesh	30;30	[176]
Steel	Stellite 6	63-180	-	-	-	[138]
Steel	NiTi	44-246	NiTi	44-246	50 at%	[177]
304SS	Stellite 6	-	-	-	-	[178]
Steel	C-Cr-Mo-TiC	1-45	TiC	45	-	[179]
Steel	Fe-Cr-C	50-200	-	-	-	[167]
Tool Steel	Colmonoy 88	-	WC	-	17.3 wt%	[79]
Tool Steel	Eutroloy 16112	-	W ₂ C-W	-	59 wt%	[79]
4140	Stellite 6	53-150	-	-	-	[180]
4140	Stellite 12	53-150	-	-	-	[180]
4140	Colmonoy 56	53-150	-	-	-	[180]
4140	Colmonoy 83	53-150	-	-	-	[180]
4140	Comonoy 88	53-150	-	-	-	[180]
Steel	304L	-	CrB	<425	50;67;50	[181]
Steel	304L	-	WVC	45-106	50;67;75	[181]
Steel	Cr-Ni SS	74-149	Various	-	30;5 (wt%)	[182]
Steel	Ni-based	74-149	Various	-	30;5 (wt%)	[182]
Steel	Co-based	74-149	Various	-	30;5 (wt%)	[182]
Steel	Tool Steel	74-108	Various	-	30;5 (wt%)	[182]
410SS	Co-Cr	40-250	WC	<250	-	[183]
304SS	Nitronic 60	-	-	-	-	[184]
Steel	NiCrBSiFeC	100-320	W ₂ C-W	100-200	50	[134]
Tool Steel	Boron	-	Boron	325 mesh	-	[185]
Steel	Metco16C	42-125	-	-	-	[186]
Steel	Stellite 6	53-180	-	-	-	[186]
Steel	Ni-based	150 - 320 mesh	-	-	-	[187]
Steel	Fe-Cr based	60 - 200	-	-	-	[188]
Steel	Ni-Cr based	60 - 200	-	-	-	[188]

Table 19 - Survey of PTAW Surfacing Arc Energy and Powder Feed Rates

Voltage (V)	Torch-to-work Distance (mm)	Current (A)	Preheat (°C)	Powder Feed Rate (g/min)	Ref.
-	15	290	-	200	[171]
-	-	80	-	3 cm ³ /min	[172]
-	-	80	-	2-5 cm ³ /min	[172]
-	-	70	-	2 cm ³ /min	[172]
30 - 50	-	80-160	-	-	[173]
36 - 38	-	133-159	250-300	45	[174]
38 - 40	-	135-172	250-300	45	[174]
-	-	-	-	-	[175]
-	-	-	-	-	[175]
15	-	150	Ambient	20	[176]
27	-	130	Ambient	10	[176]
27	-	130	Ambient	10	[176]
27	-	130	Ambient	10	[176]
6 - 14	6 - 14	115 -130	Ambient	16.7	[138]
-	-	110	Ambient	-	[177]
20.6 - 23	-	90-93	-	26.5	[178]
-	-	80	-	-	[179]
28 - 32	15	100-200			[167]
-	-	25	-	0.3 - 3.0	[79]
-	-	25	-	1.6 - 7.8	[79]
22	-	160	-	25	[180]
22	-	165	-	25	[180]
22	-	135	-	25	[180]
22	-	125	-	25	[180]
22	-	120	-	25	[180]
30	13	190	100	15	[181]
30	13	140	100	15	[181]
30-34	-	145-155	100-200	45	[182]
30-34	-	130-150	250-350	45	[182]
28-34	-	130-160	150-300	45	[182]
28-34	-	130-160	200-300	45	[182]
20 - 22	-	75;200		15;67	[183]
28	-	160-180	260-455	>20	[184]
-	-	100-200	-	22	[134]
-	-	70	-	-	[185]
-	15	120	100	33.3	[186]
-	15	160	100	33.3	[186]
38	-	80	-	60	[187]
-	20	200-400	-	200	[188]
-	20	200-400	-	200	[188]

Table 20 - Survey of PTAW Surfacing Gas Compositions and Flow Rates

Gas Flow-Rate (L/min)			Gas Composition			Ref.
Plasma	Carrier	Shield	Plasma	Carrier	Shield	
3.2	9.5	13	Ar	Ar - 6.5%H ₂	Ar - 6.5%H ₂	[171]
-	-	-	Ar	Ar	Ar	[172]
-	-	-	Ar	Ar	Ar	[172]
-	-	-	Ar	Ar	Ar	[172]
-	-	-	Ar	Ar-H ₂	Ar-H ₂	[173]
4.2	7.98	25.2	Ar	Ar	Ar	[174]
4.2	7.98	25.2	Ar	Ar	Ar	[174]
-	-	-	-	-	-	[175]
-	-	-	-	-	-	[175]
-	-	10	Ar	Ar	Ar	[176]
-	-	-	Ar	Ar	Ar	[176]
-	-	-	Ar	Ar	Ar	[176]
-	-	-	Ar	Ar	Ar	[176]
1-3	2-4	10	Ar	Ar	Ar - 5%H ₂	[138]
1	3	6	Ar	Ar	Ar	[177]
2.33	4.72-7.08	2.36	Ar	Ar-H ₂	Ar	[178]
1	-	9	Ar	-	Ar	[179]
0.25	0.4	-	Ar	Ar	Ar	[167]
0.5	-	9.5	Ar	Ar	Ar	[79]
0.5	-	9.5	Ar	Ar	Ar	[79]
2	2.5	15	Ar	Ar	Ar	[180]
2	2.5	15	Ar	Ar	Ar	[180]
2	2.5	15	Ar	Ar	Ar	[180]
2	2	15	Ar	Ar	Ar	[180]
2	2.5	15	Ar	Ar	Ar	[180]
3.6	-	15	Ar	Ar	Ar	[181]
3.6	-	15	Ar	Ar	Ar	[181]
-	7.98	-	-	Ar	-	[182]
-	7.98	-	-	Ar	-	[182]
-	7.98	-	-	Ar	-	[182]
-	7.98	-	-	Ar	-	[182]
2.5 - 3.5	-	9;9	Ar	-	Ar - 7%H ₂	[183]
-	-	-	-	-	Ar	[184]
-	-	-	-	-	-	[134]
0.5	-	9.4	Ar	-	Ar	[185]
1.5	5	23	Ar	Ar	Ar	[186]
1.2	4	22	Ar	Ar	Ar	[186]
5.8	8	-	Ar	Ar	-	[187]
-	3.5	10	Ar	Ar - 5%H ₂	Ar - 5%H ₂	[188]
-	3.5	10	Ar	Ar - 5%H ₂	Ar - 5%H ₂	[188]

4.3 Summary

Based on the preceding literature review it is clear that PTAW process parameters greatly affect overlay formation and properties. However, an insufficient number of systematic investigations into process behaviour have been completed to date. The areas of particle delivery, torch motion, and gas composition and the resulting affect of overlay development require further exploration.

4.4 Materials and Equipment

a. Material

The CSA 300W and ASTM A656 Grade 80 - Heat #2 structural steels were utilized for the PTAW overlay welding experiments; the compositions were given in Chapter 3. The powder used as the matrix material was Eutectic-Castaloin Eutroloy 16410 martensitic stainless steel (410SS); the composition is given in Table 21. This powder was used for the initial round of experiments. The tungsten carbide material was Kennametal SCNC-069 crystalline tungsten carbide (WC) in the raw powder form with a size range of 80 – 200 mesh. A 65 wt.% WC – 35 wt.% 410SS mixture was manually prepared and mixed thoroughly. This 410SS-WC powder was selected as the MMC overlay powder for the final investigations completed.

Table 21 – Nominal Composition of Eutroloy 16410 Powder

Element		Nominal Composition
C	Carbon	0.15 max
Mn	Manganese	1.00 max
P	Phosphorous	0.045 max
S	Sulphur	0.030 max
Si	Silicon	1.00 max
Cr	Chromium	11.5 – 13.5
Ni	Nickel	0.75 max
Fe	Iron	balance
Hardness = HRC 35; Density = 7.75 g/cc; Grindable finish.		

b. Equipment

The PTAW overlay experiments were carried out with the same Eutronic GAP 3000 AC/DC equipment and recorded with the same Sony DXC-390 digital camera described in Chapter 3. The only change was the use of the EP 1 powder feeder and carrier gas stream to deliver the powder. Calibration of the powder feed equipment is discussed below. A 45° trailing anode nozzle was used as shown in Figure 73. Utilizing rear

ports orientated at 45° towards the electrode minimized the time the powder spent during flight in the hotter arc regions. The amount of carbide dissolution/melting and reaction with the matrix material and/or arc atmosphere are minimized and the original carbide properties are retained.

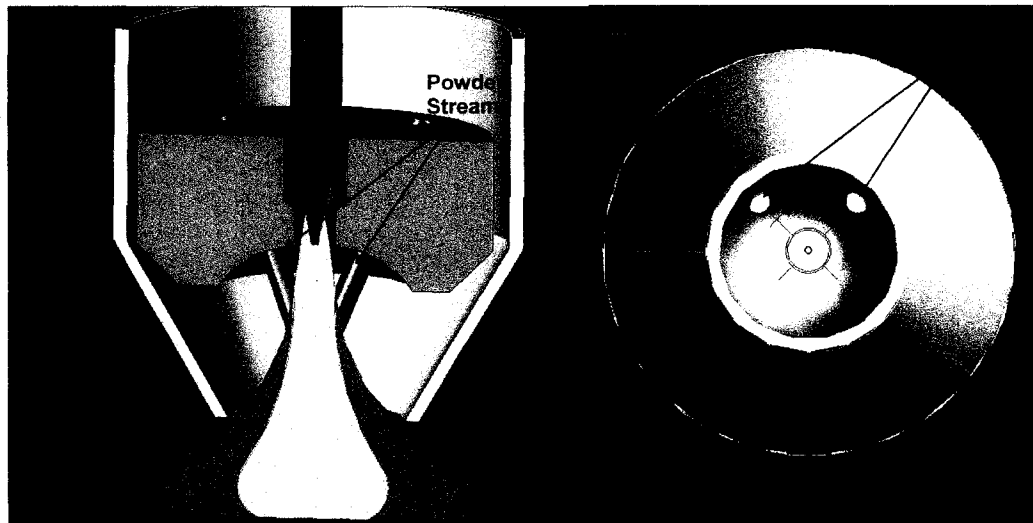


Figure 73 – PTAW Anode with 45° Trailing Powder Ports: Cross-section (left) Bottom View (top)

c. Metallurgical Samples

The 410SS macro and micro-samples were prepared utilizing the same techniques described in Section 3.4c. All 410SS-WC macro- and micro-samples were mounted in 38 mm (1.5 in) Bakelite molds. The samples were then ground and polished according to the following procedure with a Buehler Automet 2 Polisher:

1. Grinding

Medium:	45 μ m Diamond cloth
Time:	5 - 15 minutes
Wheel Speed:	180 rpm
Force:	31 N/sample (7 lbs/sample)
Wheel Direction:	Counter clockwise
Sample Direction:	Clockwise

2. Rough Polishing

Medium:	15 μm Diamond cloth
Time:	5 – 15 minutes
Wheel Speed:	180 rpm
Force:	27 N/sample (6 lbs/sample)
Wheel Direction:	Counter clockwise
Sample Direction:	Clockwise

3. Fine Polishing I

Medium:	1 μm diamond in water-based carrier on nylon cloth
Time:	5 - 10 minutes
Wheel Speed:	180 rpm
Force:	22 N/sample (5 lbs/sample)
Wheel Direction:	Counter clockwise
Sample Direction:	Clockwise

4. Fine Polishing II

Medium:	6 μm diamond in water-based carrier on nylon cloth
Time:	5 – 10 minutes
Wheel Speed:	180 rpm
Force:	22 N/sample (5 lbs/sample)
Wheel Direction:	Counter clockwise
Sample Direction:	Clockwise

5. Fine Polishing III

Medium:	0.05 μm alumina in water-carrier on micro-polishing cloth
Time:	5 - 10 minutes
Wheel Speed:	180 rpm
Force:	22 N/sample (5 lbs/sample)
Wheel Direction:	Counter clockwise
Sample Direction:	Clockwise

After each stage, the sample was rinsed and cleaned with water and acetone. All samples were etched with 2% Nitol solution.

d. Calibration of Equipment

i. Table Motion

Based on previous experience, a “saw tooth” pattern was chosen for the MMC coatings. As shown in Figure 74, two velocity vectors operate independently to determine the actual table/torch displacement, while at each stop/start location the dwell period can be altered. This automated process allows for a large number of weaving patterns and welding speeds to be used. To ensure proper calibration, a pencil was attached to the torch and a dry run (i.e., no arc) of the motion parameters was completed so that the weaving pattern was traced on the paper. Vector analysis was completed on the pattern; the correct weave width, pitch, and angle, and total welding time were confirmed.

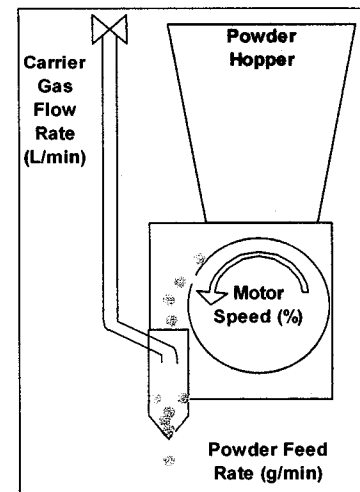
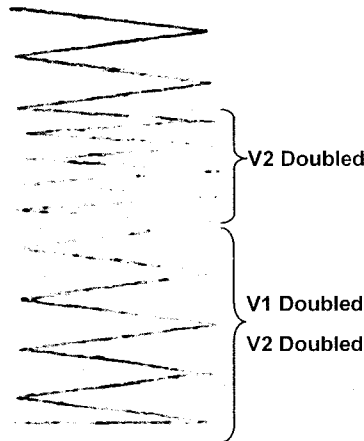
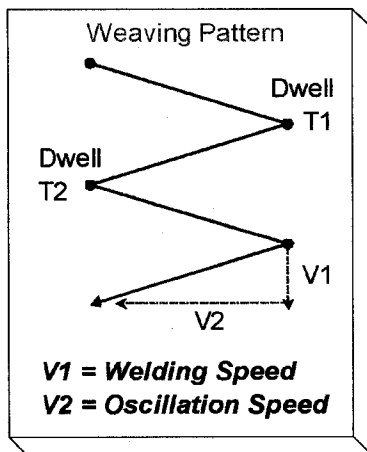


Figure 74 – “Saw Tooth” Torch Weaving Pattern

Figure 75 – Actual “Saw Tooth” Torch Pattern

Figure 76 – Powder Hopper and Delivery System

Figure 75 is an actual trace of the torch motion for a width of 25mm (1 inch). After the initial period, the oscillation speed ($V2$) is doubled which leads to “tighter” stitches. In the next region the welding speed ($V1$) is also doubled and, hence, the original weaving pattern is restored. This linear scalar relationship is important to highlight and will be

discussed in detail later.

ii. Powder Feed Rate

The actual powder rate (g/min) delivered to the welding arc is dependent on the carrier gas flow rate (L/min or lpm) and hopper motor speed (%). The motor speed is controlled as a percentage of the maximum wheel RPM. Dry run experiments were completed for an allotted time and the mass of powder material deposited was measured; the results are summarized in Figure 77.

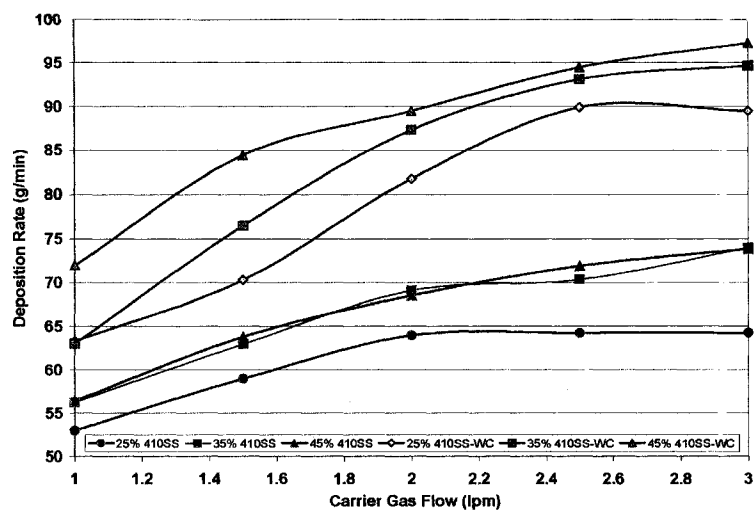


Figure 77 – Deposition Rate as a Function of Carrier Gas Flow Rate (lpm) & Wheel Speed (%)

4.5 Experimental Procedure and Results

a. Introduction

As discussed in Section 4.2, there exists a large range of PTAW process parameters; these are summarized in Table 22. Previous experience provided the initial starting point, but the optimized welding parameters were obtained via systematic “trial and error” experiments. First, the parameters to be investigated were identified (i.e., variables) and those parameters not to be altered were fixed (i.e., constants). Emphasis for this work was exploring the effects of motion, powder feed rates, and welding gas composition on overlay development. The torch motion, arc energy, and powder feed rate experiments will be explained, and the standardized “optimum” parameters are presented. In later sections the influence of different plasma, carrier, and shielding gases on 410SS and 410SS-WC overlay development will be discussed.

Table 22 – PTAW Surfacing Parameters

Parameter	Type	Parameter Group
Substrate Material	<i>Constant</i>	Materials
Matrix Material	<i>Constant</i>	
Reinforcing (carbide) phases	<i>Constant</i>	
Voltage (V)	Variable	Arc Energy
Torch-to-work Distance (mm)	Variable	
Current (Amp)	Variable	
Electrode set back (mm)	<i>Constant</i>	
Preheat (°C)	<i>Constant</i>	
Gas Flow-Rate (L/min)	Variable	Welding Gases and Powder Feed Rates
Gas Composition	Variable	
Wheel Speed	Variable	
Powder Feed Rate (g/min)	Variable	
Cladding Thickness (mm)	Variable	Motion
Welding Speed (mm/s)	Variable	
Oscillation Speed (mm/s)	Variable	
Oscillation Width (mm)	<i>Constant</i>	
Dwell Time (s)	Variable	

b. Developing Standard Welding Conditions

i. Experimental Procedure

The experiments with only 410SS powder were completed on 300W steel; the 410SS-WC experiments were completed on Grade 80 - Heat #2. All experiments were completed with argon gas, so that it could be used as the standard for the welding gas comparisons completed later. The arc was initiated and stabilized, then powder was fed in, and the table motion program was initiated. After the table had traveled approximately 25mm of linear distance, a single variable was changed “on the fly”. The variable was again changed after another 25mm of distance, and so on, over a range of practical/possible operation. The physical appearance of the overlay was assessed using macro analysis techniques. Physical examination of the overlay height, quality of fusion of the overlay edges (i.e., tie-in quality), and formation of flaws were the features examined. Digital video recording was also employed to better understand in-situ arc and overlay behaviour. A large number of experiments were completed, but they will not be included for brevity since many of the changes are subtle and very repetitive. An example of typical experimental runs for 410SS powder is given in Table 23 for reference.

Table 23 – Welding Parameters Variations of 410SS Powder Material

Weld ID	Parameter Varied	Parameter Range	Weld Speed (in/s)	Oscillation Speed (in/s)	Dwell Time (micro-sec)
P1	Oscillation Speed	0.25-0.35-0.45-0.55	0.03	variable	350
P2	Weld Speed	0.025-0.030-0.035-0.040-0.045	variable	0.35	350
P3	Weld Speed	0.045-0.050-0.055-0.060-0.065	variable	0.35	350
P4	Dwell	1000-750	0.035	0.35	variable
P5	Carrier Gas	1.5-1.25-1.0-0.75	0.035	0.35	350
P7	Oscillation Speed	0.2-0.25-0.3-0.35-0.4	0.035	variable	350
P8 - 1	Weld Speed	0.035-0.030-0.028	variable	0.25	350
P8 - 2	Dwell	350-750-1000	0.026	0.25	variable

Current = 160A; Standoff = 8mm; Voltage Range = 20 - 22V; Plasma Gas = 1.25LPM (Ar); Shielding Gas = 1.25 LPM (Ar)

ii. Results

Based upon many experiments, the following standard parameters shown in Table 24 and Table 25 were determined for 410SS and 410SS-WC, respectively.

Table 24 - Standard Welding Parameters, Cross-section, and Bead Profile for 410SS

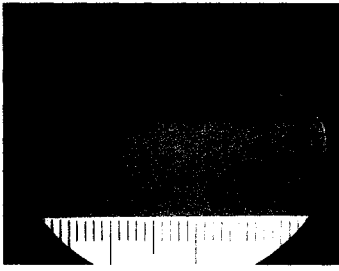

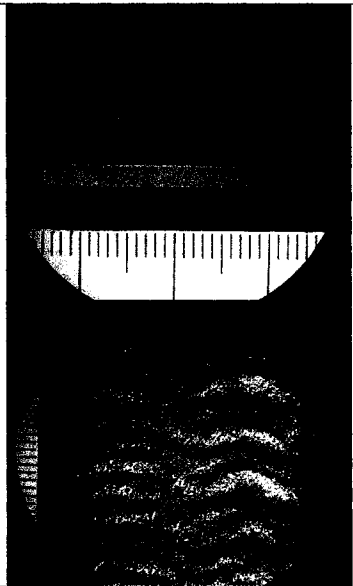
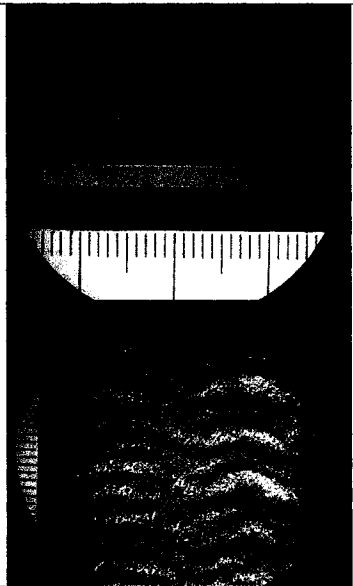
Parameter	Value	Macro Images
Substrate Material	Steel	
Matrix Material	410 SS	
Reinforcing (carbide) phases	n/a	
Voltage (V)	20 – 22	
Torch-to-work Distance (mm)	8	
Current (Amp)	160	
Preheat (°C)	Ambient	
Gas Flow-Rate (L/min)		
Plasma Gas	1.25	
Carrier Gas	1.25	
Shielding Gas	10	
Gas Composition		
Plasma Gas	Argon	
Carrier Gas	Argon	
Shielding Gas	Argon	
Wheel Speed (%)	25	
Powder Feed Rate (g/min)	56	
Cladding Thickness (mm)	3.2	
Welding Speed (mm/s)	0.75	
Oscillation Speed (mm/s)	6.35	
Oscillation Width (mm)	25	
Dwell Time (msec)	350	

Table 25 - Standard Welding Parameters, Cross-section, and Bead Profile for 410SS-WC MMC

Parameter	Value	Marco Images
Substrate Material	Steel	
Matrix Material	410 SS	
Reinforcing (carbide) phases	WC	
Voltage (V)	24 - 25	
Torch-to-work Distance (mm)	12	
Current (Amp)	160	
Preheat (°C)	Ambient	
Gas Flow-Rate (L/min)		
Plasma Gas	3.0	
Carrier Gas	2.0	
Shielding Gas	10	
Gas Composition		
Plasma Gas	Argon	
Carrier Gas	Argon	
Shielding Gas	Argon	
Powder Feed Rate (g/min)	88	
Cladding Thickness (mm)	4.8	
Welding Speed (mm/s)	1.0	
Oscillation Speed (mm/s)	16.5	
Oscillation Width (mm)	25	
Dwell Time (msec)	350	

c. Gas Composition Variations

i. Experimental Procedure

All experiments were completed with the optimized “Argon Standard” parameters described above. The scope of gas mixtures tested for 410SS is shown below in Table 26. Each gas mixture was completed for a minimum length of 75mm (3 inches) to ensure the arc was stabilized and the full powder feed rate was achieved. Due to the deleterious effects of nitrogen as a carrier gas, only one weld was completed with Ar-N₂ as the plasma gas. The first thirteen experiments were completed with argon shielding gas. The Ar-20%CO₂ mixture was not used for either the plasma or carrier gas since it oxidizes the tungsten electrode and leads to excessive arc instability. To ascertain the effect of an oxidizing gas, Ar-CO₂ was used for the shielding stream where it is not in direct contact with the non-consumable electrode. Based on the results of the 410SS, only the specific gas mixtures that were expected to change overlay behaviour were completed for 410SS-WC (Table 27). Physical examination of the overlay height, carbide distribution, quality of fusion of the overlay edges (i.e., tie-in quality), and formation of flaws were examined with micro- and macro-analysis techniques. Macro-analysis was also utilized to determine the overlay properties described in Figure 78. Digital video recording was employed to better understand in-situ arc and overlay behaviour. The mean voltage-operating ranges were also recorded.

Table 26 – Gas Testing Matrix for 410SS Overlay Welding

ID #	Plasma Gas	Carrier Gas	Shielding Gas
P8.2	Ar	Ar	Ar
P11.1	Ar	ArHe	Ar
P10.3	Ar	ArH ₂	Ar
P11.2	Ar	ArN ₂	Ar
P9.1	ArHe	Ar	Ar
P10.2	ArHe	ArHe	Ar
P12.3	ArHe	ArH ₂	Ar
P12.2	ArHe	ArN ₂	Ar
P9.1	ArH ₂	Ar	Ar
P10.1	ArH ₂	ArHe	Ar
P9.3	ArH ₂	ArH ₂	Ar
P11.3	ArH ₂	ArN ₂	Ar
P12.1	ArN ₂	ArHe	Ar
U11	Ar	Ar	ArCO ₂
U12	ArHe	ArHe	ArCO ₂
U13	ArH ₂	ArH ₂	ArCO ₂
Actual gas composition:			
ArHe = 25% He, bal. Argon		ArH ₂ = 10% H ₂ , bal. Argon	
ArN ₂ = 25% N ₂ , bal. Argon		ArCO ₂ = 20%CO ₂ , bal. Argon	

Table 27 – Gas Testing Matrix for 410SS-WC MMC Welding

ID #	Plasma Gas	Carrier Gas	Shielding Gas
W1	Ar	Ar	Ar
W2	Ar	ArHe	Ar
W3	Ar	ArH ₂	Ar
W6	ArHe	Ar	Ar
W5	ArHe	ArHe	Ar
W4	ArHe	ArH ₂	Ar
W8	ArH ₂	Ar	Ar
W10	ArH ₂	ArHe	Ar
W9	ArH ₂	ArH ₂	Ar
W11	Ar	ArN ₂	Ar
W12	Ar	Ar	ArCO ₂
Actual gas composition:			
ArHe = 25% He, bal. Argon		ArH ₂ = 10% H ₂ , bal. Argon	
ArN ₂ = 25% N ₂ , bal. Argon		ArCO ₂ = 20%CO ₂ , bal. Argon	

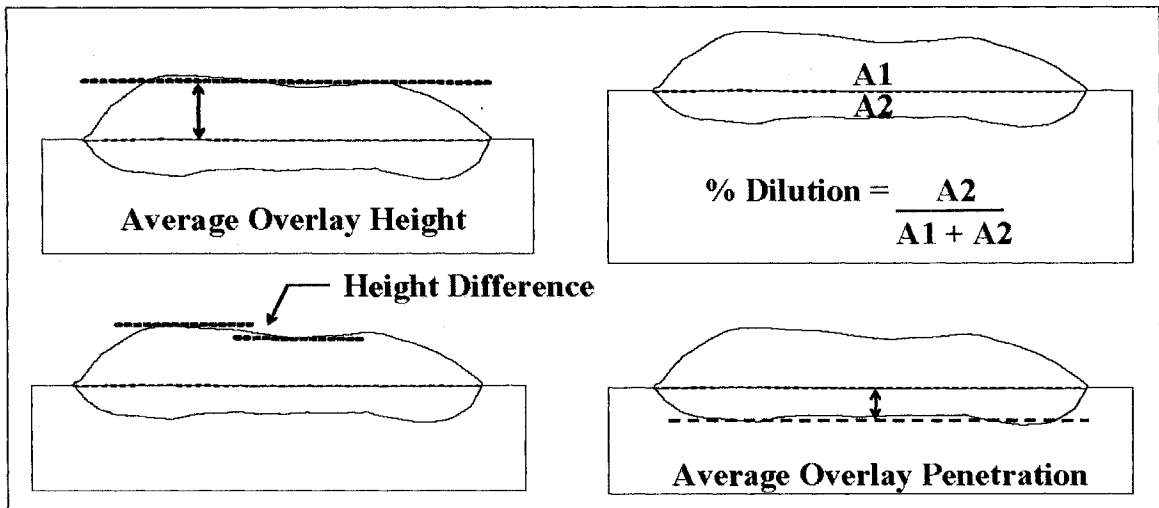


Figure 78 – Overlay Cross-Sectional Macro-Properties

ii. Results – 410SS Gas Mixtures

Surface Macro-Analysis

The as-welded condition of the samples is given in Figure 79 and Figure 80.

Carrier Gas:	Plasma Gas			
	Argon	Ar - 25%He	Ar - 10% H ₂	Ar - 25% N ₂
Argon				
Ar-25%He				
Ar-10%H ₂				
Ar-25%N ₂				

Figure 79 - As-Welded Macrographs of 410SS Overlays with Argon Shielding Gas

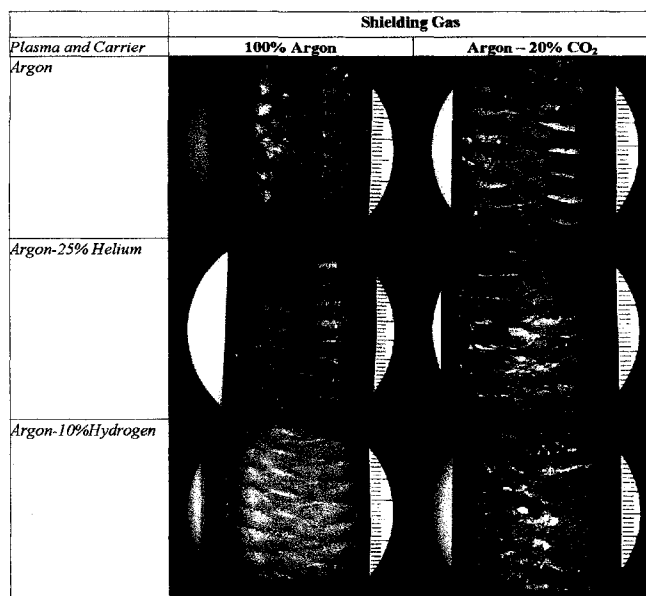


Figure 80 - As-Welded Macrographs of 410SS Overlays with CO₂ Shielding Gas

The specimens in Figure 81 and Figure 82 were wire brushed to remove surface oxides.

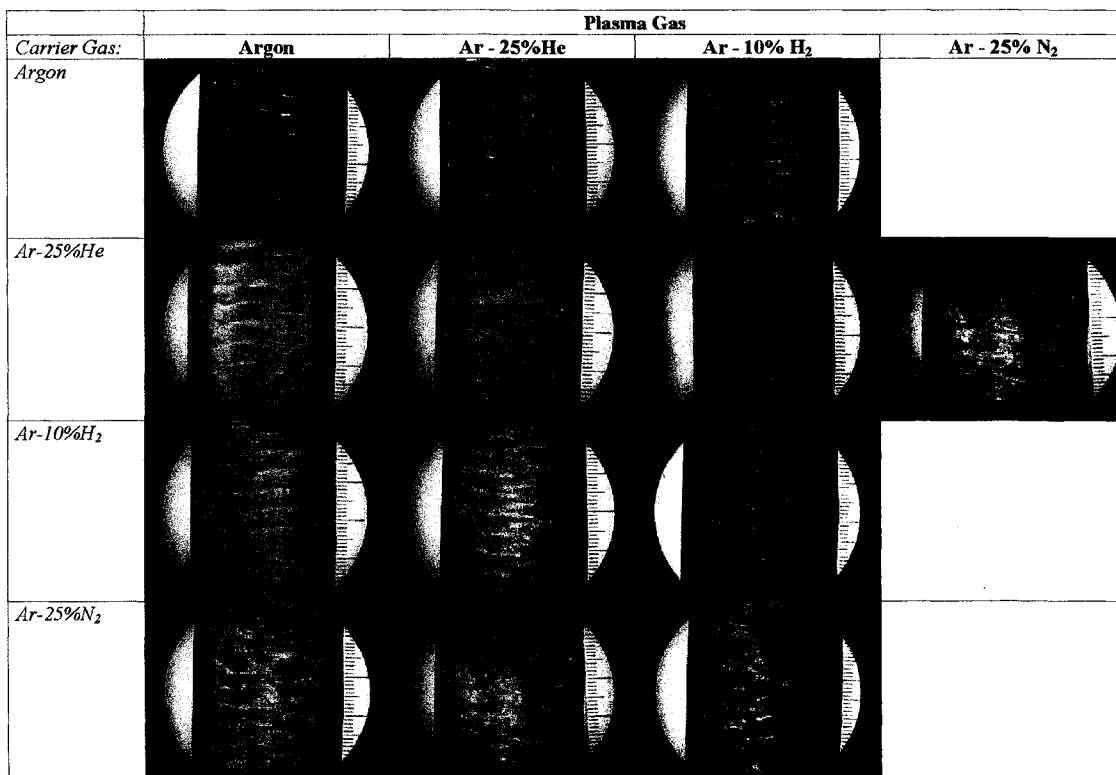


Figure 81 - Macrographs of Cleaned 410SS Overlays with Argon Shielding Gas

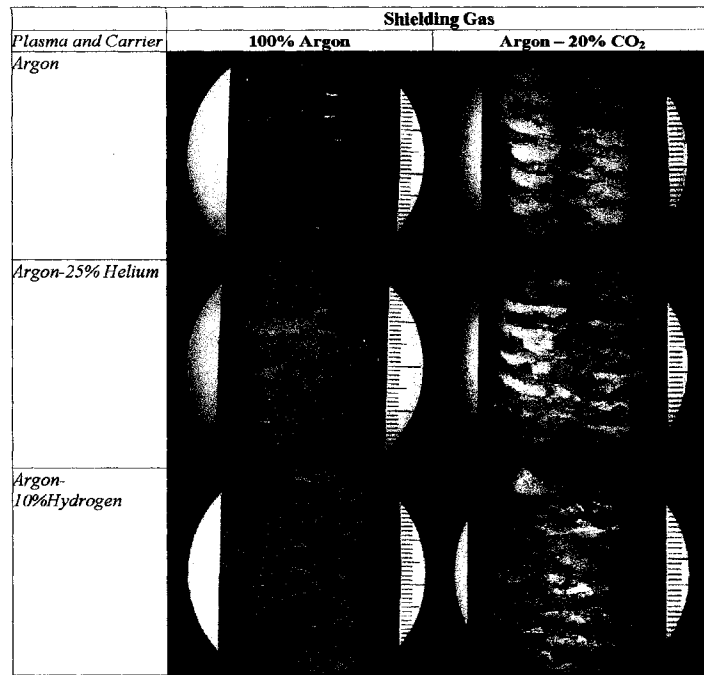


Figure 82 - Macrographs of Cleaned 410SS Overlays with CO₂ Shielding Gas

Cross-sectional Macro Analysis

Sample cross-sections are shown in Figure 83 and Figure 84. The surface porosity that was observed earlier when welding with Ar-N₂ was confirmed to exist throughout the sample volume. The samples welded with Ar-CO₂ shielding gas were found to have both macro flaws and micro flaws. For all overlays that did not have excessive flaws (i.e., porosity), the following properties were determined: average height, percent difference in overlay height, overlay dilution, and average penetration. These results are summarized in Figure 85; the error bars represent the variability in the measuring techniques utilized. Standard metallographic techniques and digital software were used to determine these properties.

Carrier Gas:	Plasma Gas			
	Argon	Ar - 25%He	Ar - 10% H ₂	Ar - 25% N ₂
Argon				
Ar-25%He				
Ar-10%H ₂				
Ar-25%N ₂				

Figure 83 – Cross-section Macrographs of 410SS Overlays with Argon Shielding Gas

Plasma and Carrier Gases	Shielding Gas	
	100% Argon	Argon - 20% CO ₂
Argon		
Argon-25% Helium		
Argon-10%Hydrogen		

Figure 84 – Cross-section Macrographs of 410SS Overlays with CO₂ Shielding Gas

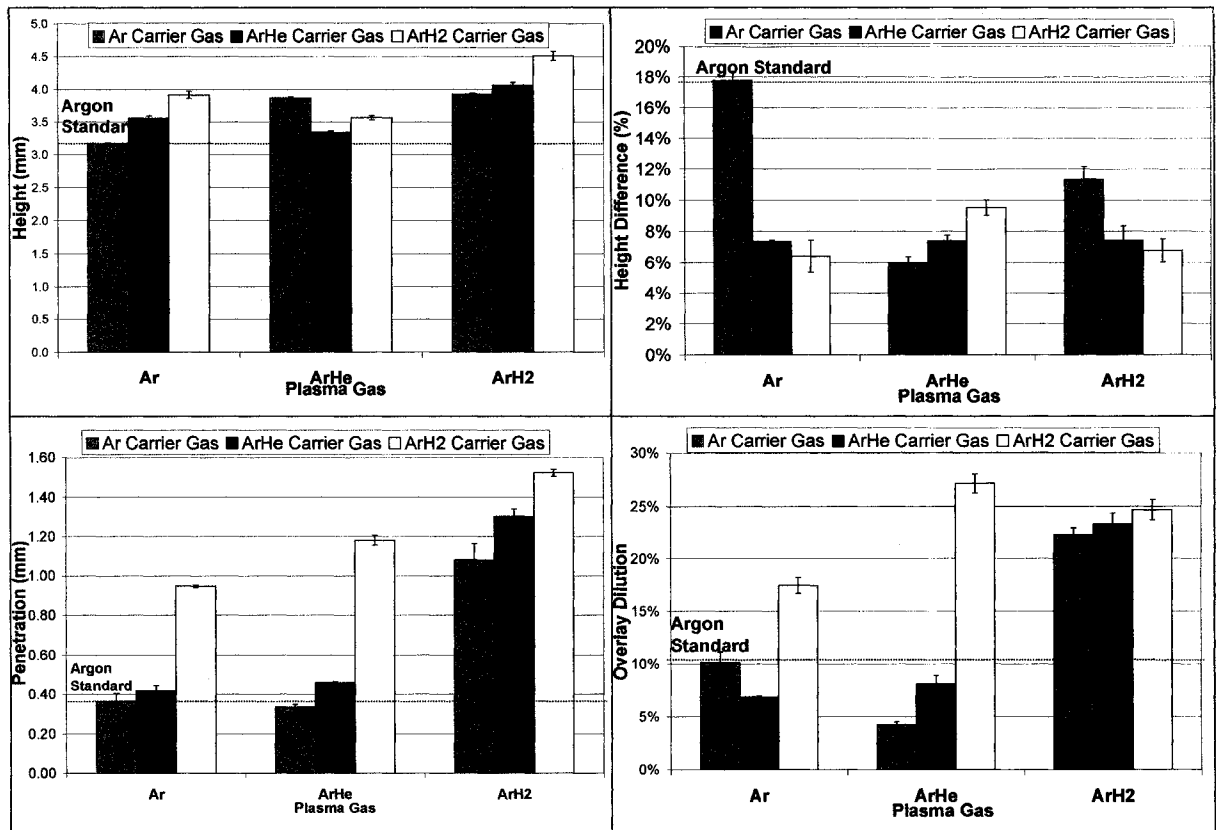


Figure 85 – Cross-sectional Properties of 410SS

Cross-section Micro Analysis

Table 28 summarizes any observed flaws and the nature of the overlay-to-base material interface while welding with 410SS powder material. The use of argon and argon-helium mixtures for the plasma gas had the greatest likelihood for fusion-line flaw formation. For example, samples P8.2 and P9.1 formed lack of fusion type flaws near the overlay edges (i.e., tie-in flaw), as shown in Figure 86, Figure 87 and Figure 88. Conversely, the use of hydrogen, as either a carrier gas or plasma gas, greatly increased the penetrating capabilities of the arc to ensure proper fusion, but at the expense of greater dilution (see Figure 89). Welding with carbon dioxide shielding gas created various oxide-based fusion flaws, as shown in Figure 90, which compromise overlay integrity. This correlates

well with the excessive surface oxidation observed earlier and the entrapment of oxide material was observed during video analysis (see Section 4.6b.iii). The interfacial flaws formed in sample U11 were selected for SEM-EDX analysis.

Table 28 – Summary of 410SS Fusion Flaws and Other Overlay-to-Base Material Observations

ID #	Plasma Gas	Carrier Gas	Shielding Gas	Observations
P8.2	Ar	Ar	Ar	Interface micro and macro porosity and cracks, tie-in lack of fusion flaws
P11.1	Ar	ArHe	Ar	Interface micro and macro porosity and cracks, tie-in lack of fusion flaws
P10.3	Ar	ArH ₂	Ar	Tie-in lack of fusion flaws, minimal porosity
P11.2	Ar	ArN ₂	Ar	Excessive porosity and irregular fusion interface
P9.1	ArHe	Ar	Ar	Tie-in lack of fusion flaws, stringer interface flaws
P10.2	ArHe	ArHe	Ar	Fair fusion interface, minimal porosity
P12.3	ArHe	ArH ₂	Ar	Good interface fusion
P12.2	ArHe	ArN ₂	Ar	Excessive porosity and irregular fusion interface
P9.2	ArH ₂	Ar	Ar	Good interface fusion
P10.1	ArH ₂	ArHe	Ar	Good interface fusion
P9.3	ArH ₂	ArH ₂	Ar	Good interface fusion
P11.3	ArH ₂	ArN ₂	Ar	Excessive porosity and irregular fusion interface
P12.1	ArN ₂	ArHe	Ar	Excessive porosity and irregular fusion interface
U11	Ar	Ar	ArCO ₂	Interface flaws, and tie-in lack of fusion flaws
U12	ArHe	ArHe	ArCO ₂	Interface flaws, and tie-in lack of fusion flaws
U13	ArH ₂	ArH ₂	ArCO ₂	Faire fusion interface, excessive overlay porosity

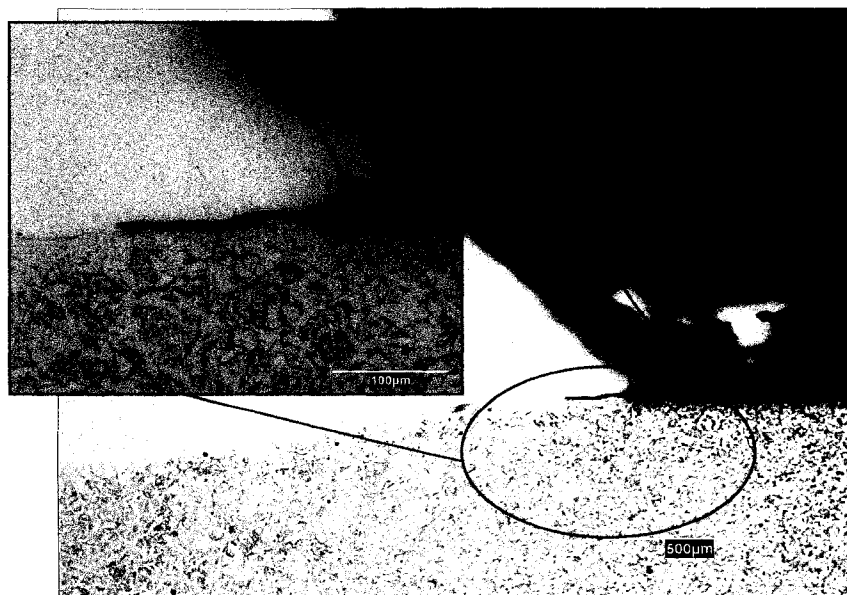


Figure 86 – 410SS Argon Standard (P8.2): Overlay Tie-in Lack of Fusion Flaw



Figure 87 – 410SS Argon Standard (P8.2): Interface Porosity and Cracking at Overlay Center



Figure 88 – 410SS Argon-Helium Plasma Gas (P9.1): Overlay Tie-in Flaws



Figure 89 – Argon-Hydrogen Plasma and Carrier Gas (P9.3): Good Interface and Tie-in Fusion

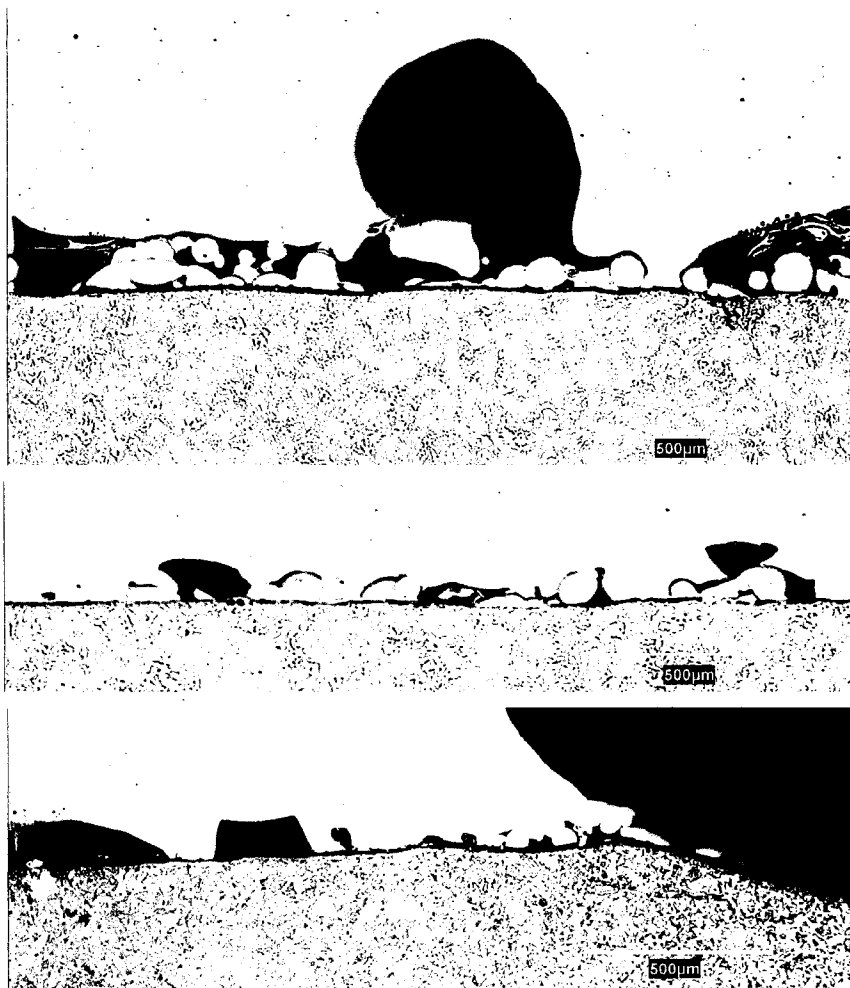


Figure 90 – 410SS with Argon-Carbon Dioxide Shielding Gas (U11): Typical Interface Fusion Flaws

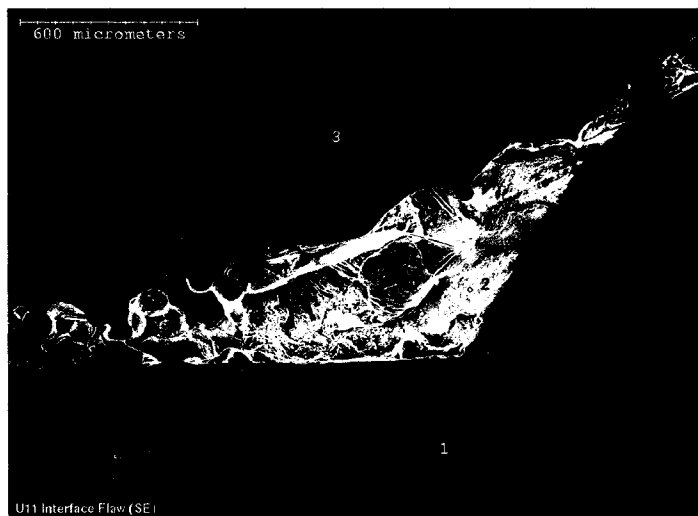


Figure 91 – SEM Image of Sample U11

As shown in Figure 91, a large piece of foreign matter contaminated the interface between the base material (bottom) and overlay (top). Energy dispersive x-ray (EDX) analysis was utilized at the three points indicated to determine the local composition, and the results are summarized in Table 31. The high concentrations of deoxidants and oxygen confirm that the contaminant is an oxide, likely formed on the pool surface during welding.

Table 29 – EDX Summary for U11 Sample (wt. %)

Element	Point 1	Point 2	Point 3
Fe	98%	18%	87%
Mn	1.8%	25%	1.5%
Si	0.2%	16%	0.5%
Cr	-	32%	11%
Al	-	4%	-
O	-	4%	-

iii. Results – 410SS-WC Gas Mixtures

Surface Macro-Analysis

The cleaned condition of the MMC samples is summarized in Figure 92.

Cross-sectional Macro Analysis

Sample cross-sections are shown in Figure 93. Based on the deleterious results obtained when welding the 410SS matrix powder, the use of Ar-N₂ and Ar-CO₂ was limited. Using the same techniques described earlier, the following properties were determined: average height, percent difference in overlay height, overlay dilution, and average penetration as shown in Figure 94.



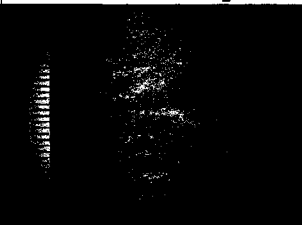
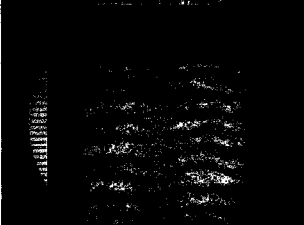

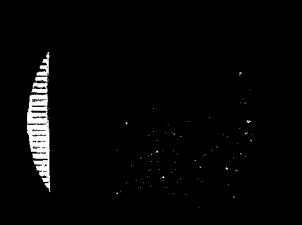
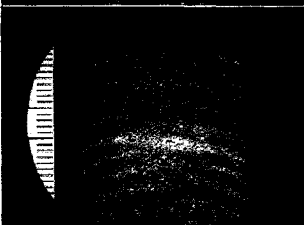
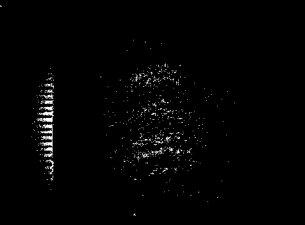

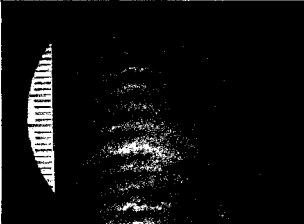
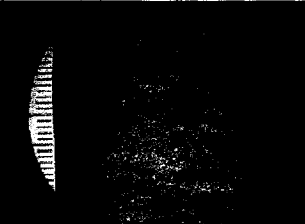
	Plasma Gas		
Carrier Gas:	Argon	Ar - 25%He	Ar - 10% H ₂
Argon			
Ar-25%He			
Ar-10%H ₂			
	Other Gas Mixture Variants		
Argon for all other gases.	Argon-25%N ₂ Carrier Gas	Argon-20%CO ₂ Shielding Gas	
			

Figure 92 - Macrographs of Cleaned 410SS-WC MMC Overlay with Argon Shielding Gas

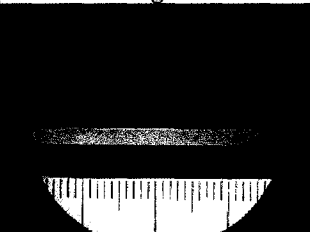
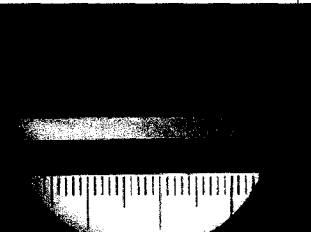
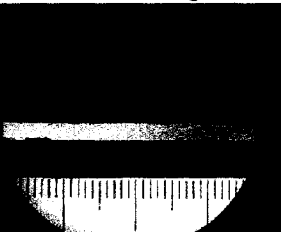
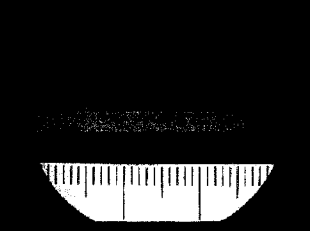
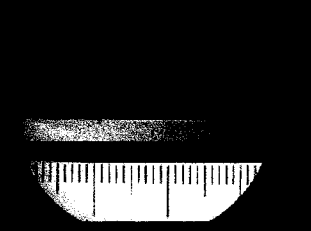

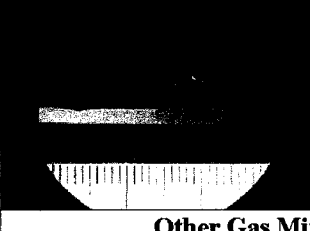

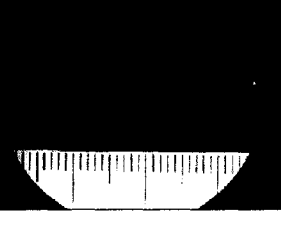
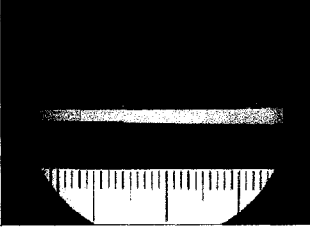

Carrier Gas:	Plasma Gas		
	Argon	Ar - 25%He	Ar - 10% H ₂
Argon			
Ar-25%He			
Ar-10%H ₂			
Argon for all other gases	Other Gas Mixture Variants		
	Argon-25%N ₂ Carrier Gas	Argon-20%CO ₂ Shielding Gas	
			

Figure 93 - Cross-section Macrographs of 410SS-WC MMC Overlays

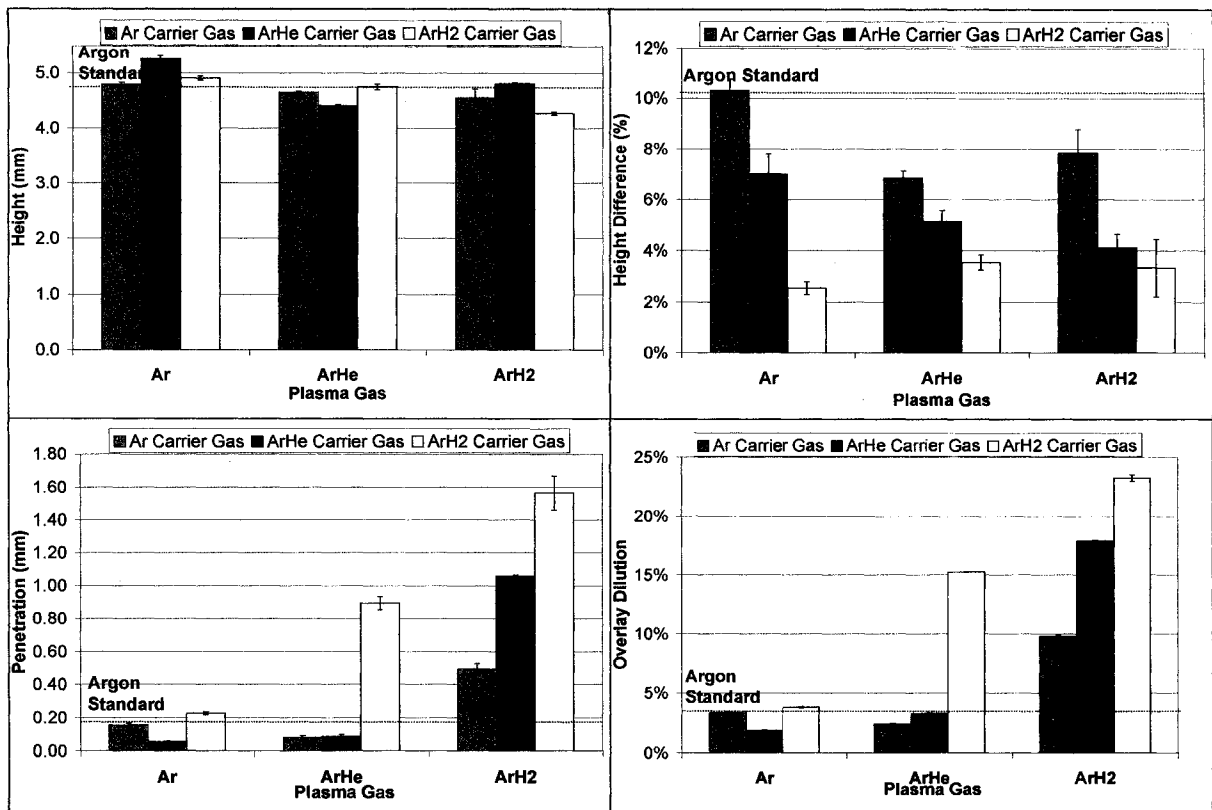


Figure 94 - Cross-sectional Properties of 410SS-WC MMC Overlays

Cross-section Micro Analysis

Table 30 summarizes any observed flaws and the nature of the overlay-to-base material interface while welding with 410SS-WC MMC powder material.

Table 30 – Summary of 410SS-WC Fusion Flaws and Other Overlay-to-Base Material Observations

Weld ID	Interface Quality	Tie-Quality	Carbide Distribution	Porosity	Cracks
W1	Good	Poor	Good	Minimal	None
W2	Poor	Poor	Good	Minimal	None
W3	Excellent	Good	Marginal	None	Several
W6	Poor	Poor	Good	Several	None
W5	Good	Poor	Good	Several	None
W4	Excellent	Excellent	Marginal	None	Minimal
W8	Excellent	Excellent	Marginal	Minimal	None
W10	Excellent	Excellent	Poor	None	None
W9	Excellent	Excellent	Poor	None	Minimal
W11	Poor	Poor	Marginal	Several	Several
W12	Good	Poor	Marginal	Several	Several
<i>Rankings: Poor, Marginal, Good, Excellent</i>				<i>Rankings: none, minimal, several</i>	
NOTE: All samples contained some degree of micro-porosity and micro-cracks of the order of micrometers. Above indicates the tendency for macro-sized porosity or those greater than the average carbide diameter.					

Typical micrographs that illustrate overlay properties and flaws are shown in Figure 95, Figure 96, and Figure 97.

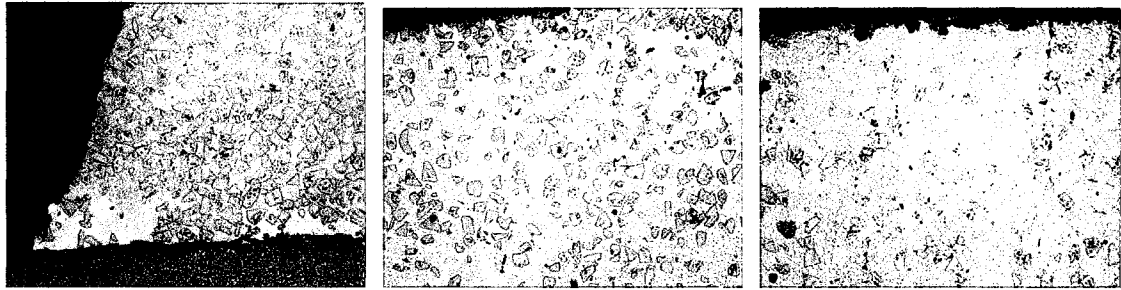


Figure 95 – Micrographs of Poor Tie-In Fusion (Left, Sample W1, 50X), Good Carbide Distribution (Center, Sample W1, 50X), and Poor Carbide Distribution (Right, Sample W10, 50X)



Figure 96 – Micrographs of Good Interface Fusion with Composite Region (Left, Sample W1, 300X), Variable Interface Fusion (Center, Sample W6, 100X), & Excellent Tie-In Fusion (Right, Sample W4, 50X)

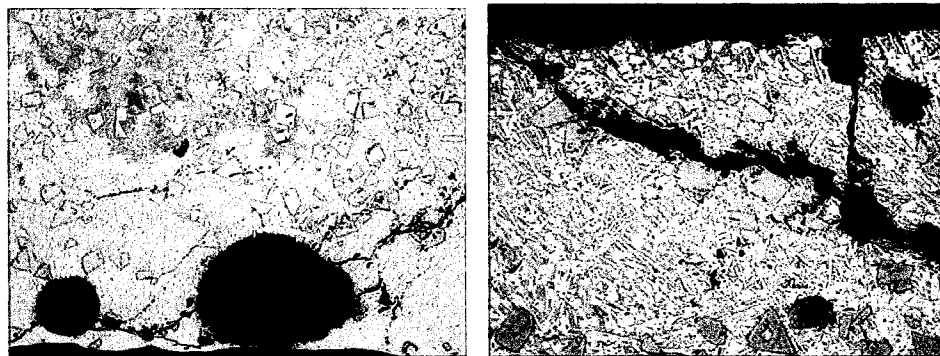


Figure 97 – Micrographs of Interface Porosity and Cracking (Left, Sample W11, 50X), and Surface Cracking and Porosity (Right, Sample W12, 50X)

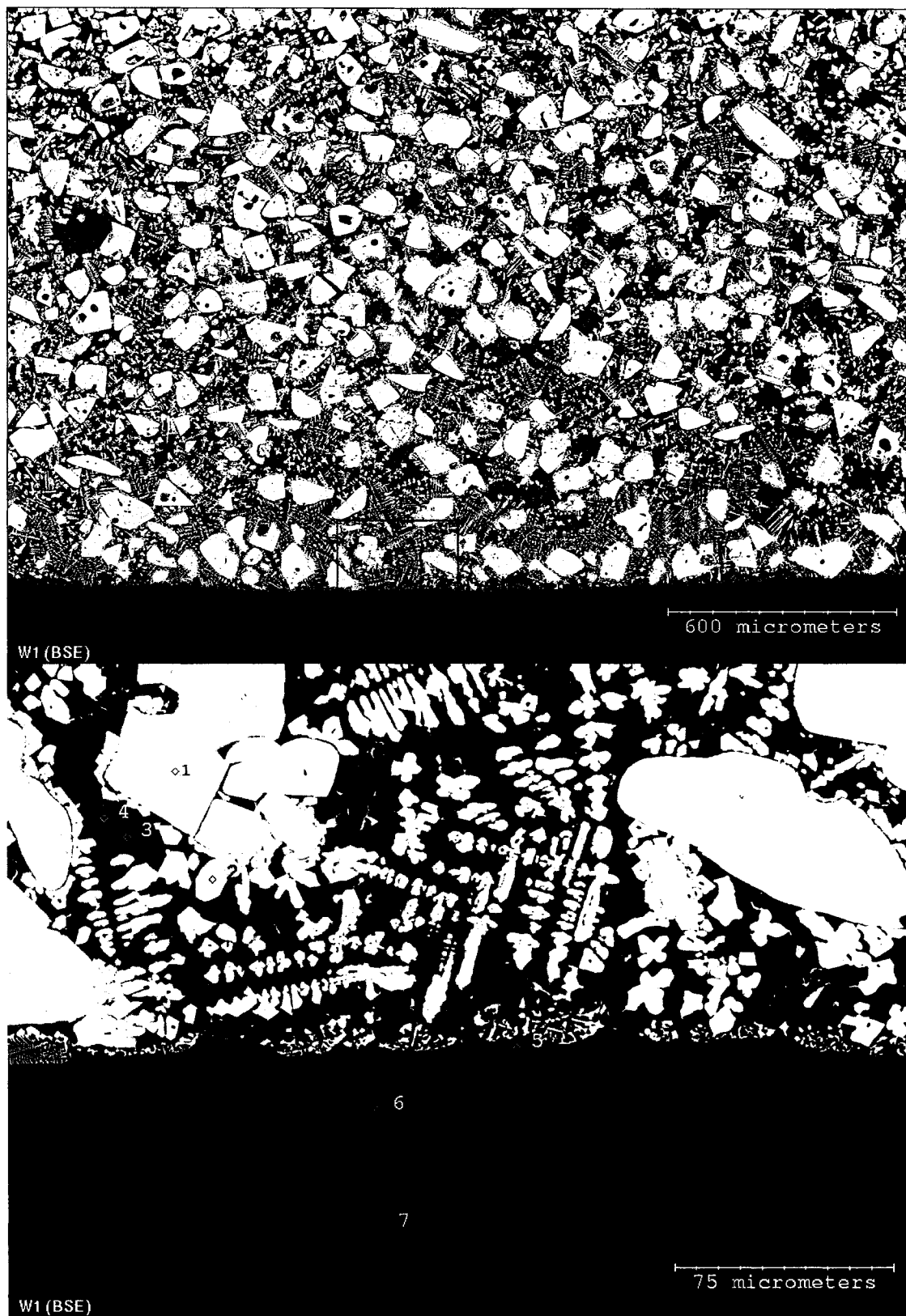


Figure 98 – SEM Backscattering Electrons (BSE) Imaging of Sample W1

As shown in the micrograph on the left in Figure 96, a “composite” interface region formed and a secondary carbide network appeared to exist within the matrix material. The backscattering electron image, Figure 98, confirmed that an intricate secondary carbide network with a unique composition was formed within the 410SS matrix. It was theorized that the tungsten carbide melted during fusion and reacted with the iron and other elements (such as carbon and chromium), and then precipitated as a new phase. EDX was utilized at the seven points indicated to determine the local composition. The elements of interest present are summarized in Table 31. The results indicate that various types of phases were formed within the MMC coating. The “composite” region mentioned earlier contained iron, tungsten and chromium. A trace amount of chromium also diffused out of the overlay and into the base material.

Table 31 – EDX Summary for W1 Sample (wt. %)

Location	Primary Element	Secondary Element	Tertiary Element
1	Tungsten – 95%		
2	Tungsten – 70%	Iron – 24%	Chromium – 3%
3	Iron – 86%	Tungsten – 7%	Chromium – 5%
4	Iron – 60%	Chromium – 21%	Tungsten – 17%
5	Iron – 83%	Tungsten – 12%	Chromium – 3%
6	Iron – 97%	Chromium – 0.23%	
7	Iron – 98%		
Note: All locations contained trace amounts of silicon and/or manganese			

4.6 Discussion

a. Optimizing Overlay Process Parameters

i. Background

Table 22 illustrates that there are a large number of interacting process parameters that affect PTA overlay development. The survey of existing literature indicated that a wide range of parameters are used. There is no known method, procedure, or protocol for determining the heat input or establishing optimum welding process parameters. Another difficulty when evaluating previous work is the lack of normalized parameter(s) for comparison. For example, some authors will perform assessments based on powder feed rates (i.e., productivity), but this is an arbitrary value if the motion and arc energy parameters are not disclosed. Furthermore, there are very few studies that attempt to understand PTA overlaying solely from a welding process viewpoint. The net result is that PTAW surfacing parameters are very subjective and variable depending on materials, equipment, and investigator methods. The following discussion will illustrate that the classical heat input equation is of no value for PTAW surfacing. Instead, it will be shown that torch motion, powder delivery, and arc energy, together, determine the effective heat input for PTA overlay welding systems.

ii. Torch Motion

The idealized torch “saw tooth” motion was introduced in Figure 74. The dependence of overlay development on the velocity vectors V_1 and V_2 is shown in the cross-sectional macrographs of 410SS-WC overlays (Figure 99). With the slowest forward welding speed (V_1), the overlay material simply “piles” on top and does not fuse with or penetrate into the base material. Metallographic examination of the overlay-to-base-material

interface revealed the presence of various fusion flaws. The “tight” torch weaving pattern indicates that although a large amount of energy is added to the system per unit length, the energy does not reach the base plate. The 410SS – 65wt% WC MMC system acts as an insulator between the arc and the base plate material. This is in direct conflict with the classical heat input equation, where the lowest welding speed results in the highest heat input. As previously discussed in Chapter 3, this example highlights that the heat input equation is not applicable for assessing PTAW behaviour, with or without the addition of a powder consumable material. Using the fastest forward speed did not improve the overlay development; the torch motion was excessive for the given powder feed rate. The overlay material does not build up to a desirable height, typically between 3mm to 5mm, and the overlay height exhibits large macroscopic irregularities and a poor cross-sectional profile. The intermediate welding speed provided a better operating point, and when combined with the highest oscillation speed an excellent saw tooth pattern is developed. As indicated, these became the standard motion parameters for welding 410SS-WC in a pure argon atmosphere (see Table 25).

To explore the interrelationships between torch velocity and dwell time, a torch motion optimization diagram was developed as shown in Figure 100. Based on the “Argon Standard” conditions presented above ($V_1 = 1\text{mm/s}$, $V_2 = 16.5\text{ mm/s}$, and dwell time = 350ms), the total welding time per 25 mm was measured and the absolute resultant torch velocity was calculated via Pythagoras’ theorem. The absolute torch velocity was 14 mm/s and the total welding time was 34 seconds (per 25mm section). By multiplying both V_1 and V_2 by the same scalar multiple, the torch velocity shall change but the torch displacement will be identical to the standard (recall that this concept was introduced in

Figure 75). If a scalar multiple of 0.5X is used, the welding time increases by 70% to 58 seconds per 25mm. Hence, the powder feed rate becomes excessive for the given arc energy and the resulting overlay is a “bulge” of material brazed to the base material. There was minimal fusion and this represents a deviation from practical operating conditions. By using the 2X scalar multiple there is a 35% drop in the total welding time. Under these motion conditions the torch velocity is excessive for the powder feed rate and arc energy. Again, this represents deviation from the ideal conditions. For multiples ≥ 3 there is no significant change in the total welding time. For these previous experiments, a dwell time of 350ms was utilized; the practical extremes for normal operation are zero dwell and 1000ms (or 1 second). The resulting welding time curves are also shown in Figure 100 below. As expected, increasing the dwell time will shift the welding time upwards for all scalar multiples. As dwell increases the deviation from an ideal power law relationship increases, as quantified by the R-squared values. Under ideal conditions, the dependence of welding time with velocity is derived below based on the basic motion equation $D = V \times T$, where $D = \text{Distance} = \text{Constant}$, since torch displacement is identical for all scalar multiples. $V = \text{Velocity} = \text{Variable}$, which is linearly dependent on the scalar multiple, and $T = \text{Total Welding Time} = \text{Variable}$, which is dependent on torch velocity. Hence, $T = \frac{\text{Constant}}{\text{Variable}}$ which can be expressed by the general power law equation:

$$y = \frac{A}{x^B} \Leftrightarrow T = \frac{\text{Constant}}{\text{Variable}}$$

For a dwell time of 0ms, the R-squared value approaches unity; the small error encountered is an indication of the equipment “mechanical dwell time”. There is a small,

but authentic, amount of time required to stop the torch head and subsequently continue in a new direction; such an event cannot occur instantaneously. Lastly, further manipulation can be achieved by exploring the final motion operating window, as indicated in Figure 100. Within this window the pertinent overlay characteristics, such as height, width, surface roughness, etc., can be fine-tuned to suit the particular application.

The previous analysis illustrates how the complex interactions between torch motion and powder feed rate can significantly change overlay properties. For a given powder feed rate, it is possible to change overlay development considerably by using different combinations of V1 and V2. These combinations will create a unique torch weave pattern. By using scalar multiples of V1 and V2 and/or changing the dwell time, the total welding time to obtain this unique weave pattern will change which allows for further optimization and improved productivity. This motion optimization procedure provides future investigators with a standardized and reproducible method for assessing the influence of torch motion on overlay formation. Another important parameter that influences the effective heat input is arc energy and is discussed below.

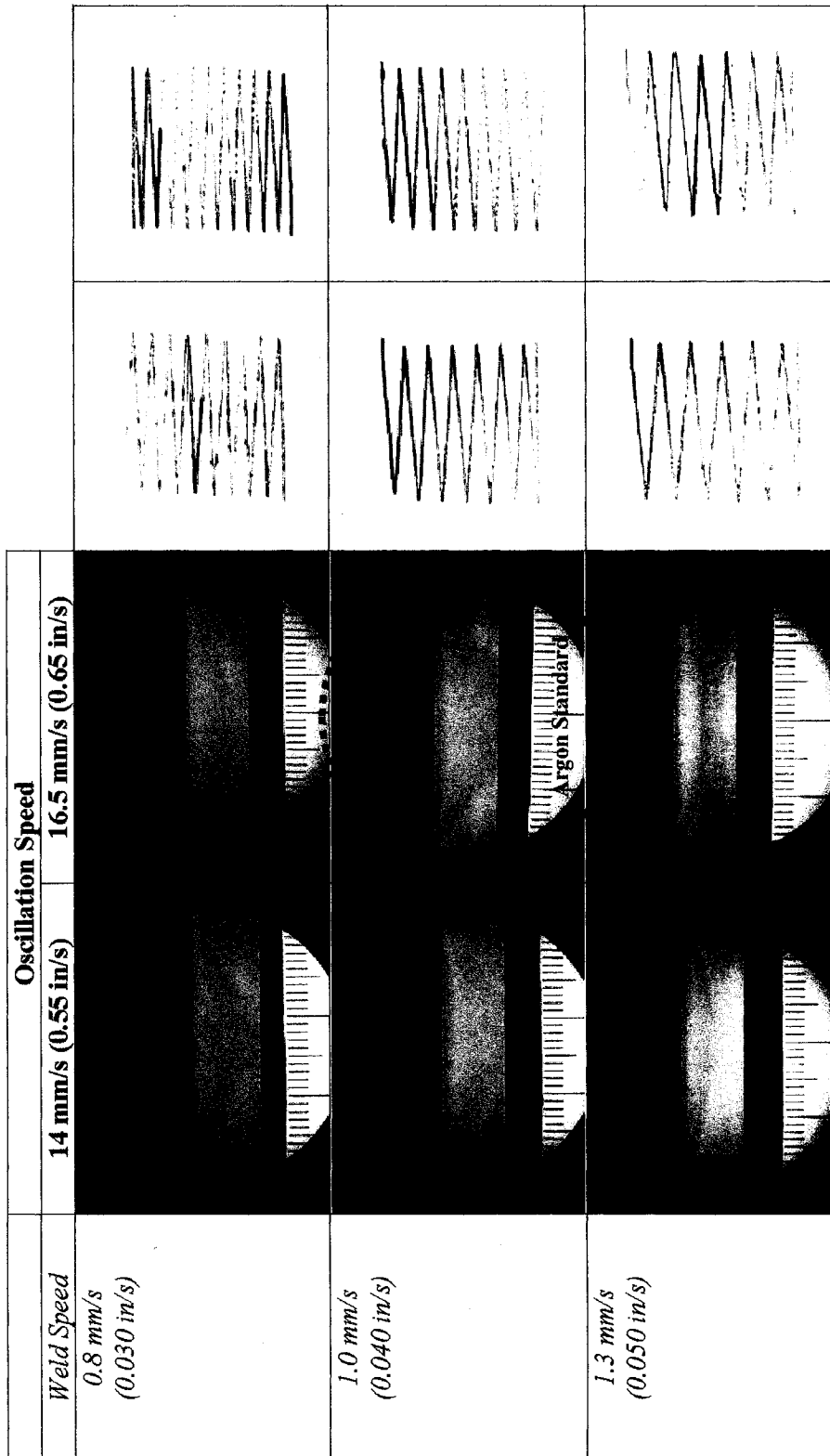


Figure 99 – 410SS-WC Cross Sections and Weaving Patterns: Dependence on Velocity Vectors

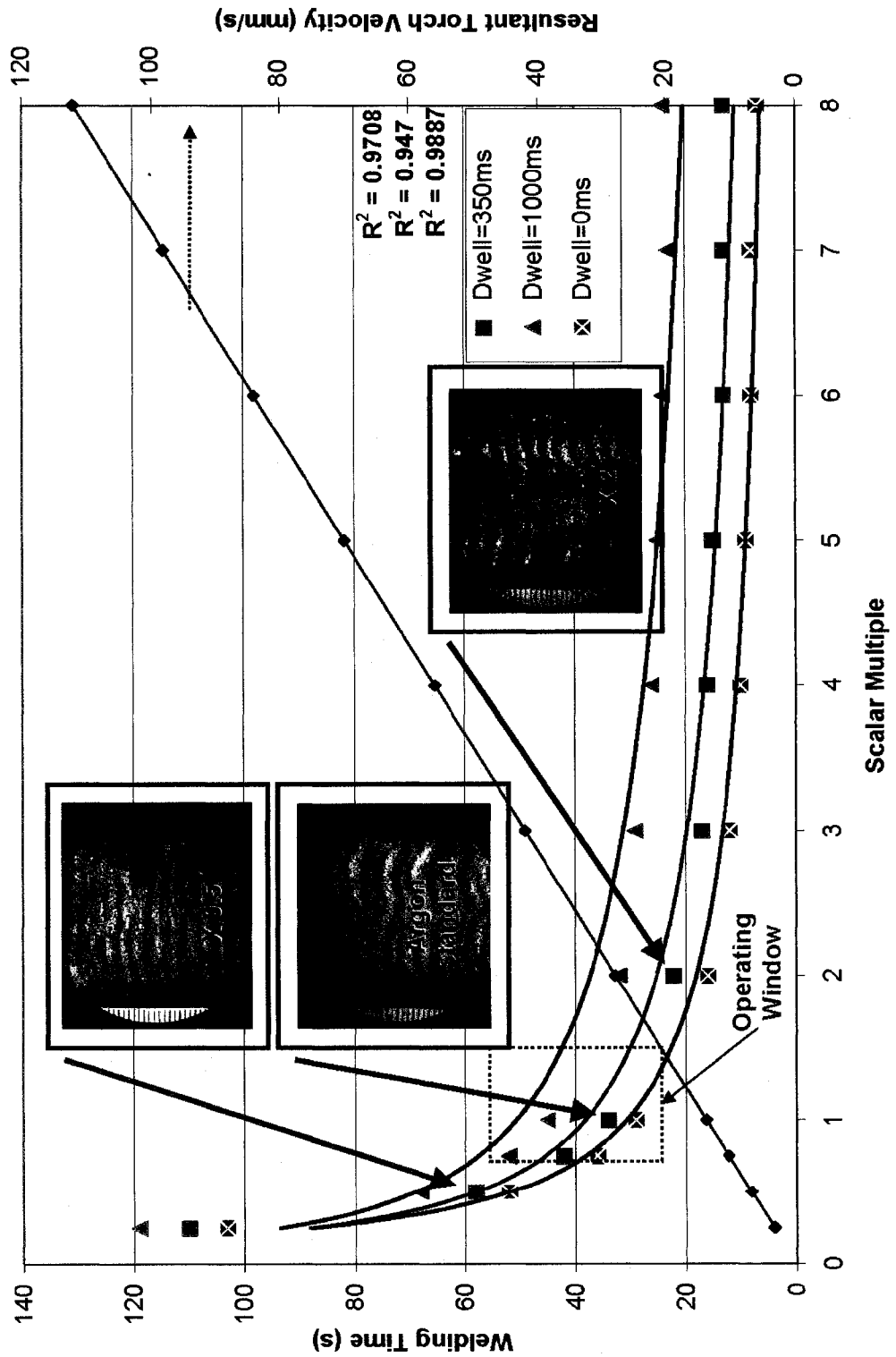


Figure 100 – Dependence of Total Welding Time on Torch Velocity and Dwell Time

iii. Arc Energy

The final component of the effective heat input for PTAW surfacing is the arc energy or power, given by the $V \times I$ (Voltage x Current). After optimizing motion and powder delivery, varying the arc energy changes the effective heat input to both the overlay and base material. This allows one to “fine-tune” overlay properties and obtain a desired product to suit the application. For example, one can obtain a very smooth vs. rough bead surface, minimize dilution or carbide melting, or even increase penetration to avoid lack of fusion and poor tie-in quality. Figure 101 illustrates the influence of welding current on overlay behaviour. With low power the individual bead stitches are clearly evident and the surface is relatively rough. At higher current there is increased melting of previously solidified material and improved overlay fluidity. The resulting overlay formed has more uniform properties and decreased surface roughness. A similar effect can be obtained by altering the arc voltage or standoff.

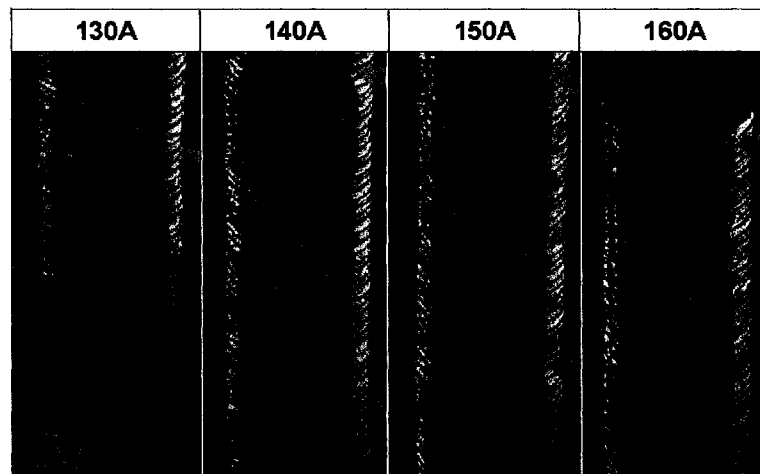


Figure 101 – Effect of Current Variations on the Overlay Surface

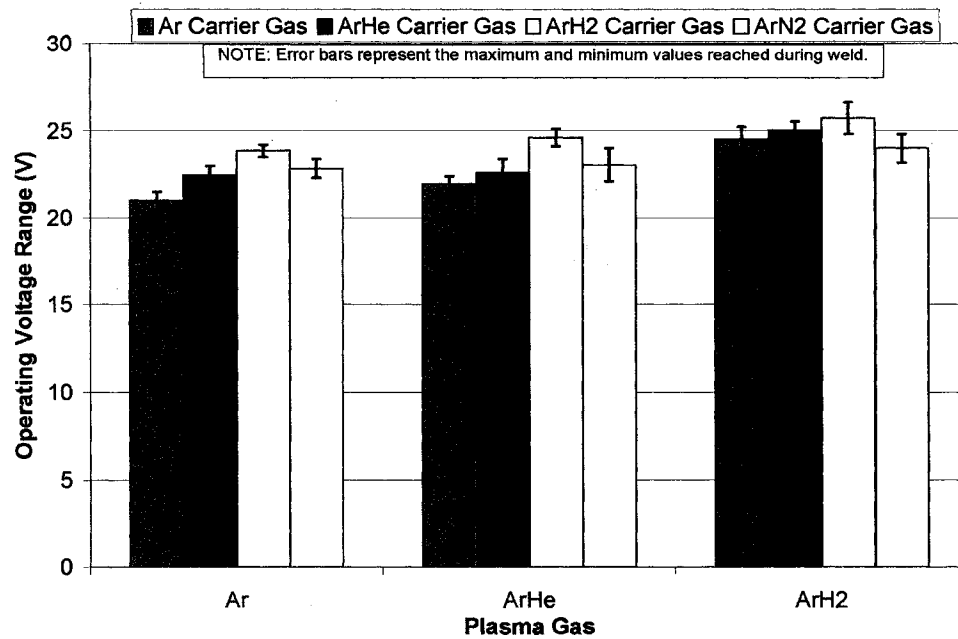


Figure 102 – Operating Voltage Range for Different Gas Mixtures during 410SS Overlay Welding

Our investigations found that increasing voltage was a very effective means of improving bead melting and fluidity, but only within a limited operating range. Similar to previous investigators [172,181,186,167], it was found that the optimal standoff distance ranged from 8 mm to 15mm. Occasional arc instability and reduced overlay shielding occurred if the standoff was greater than this range. Operating below this level resulted in occasional short circuits and low arc energy that limited productivity. As shown in Figure 102, different gas compositions were able to increase the voltage for the same standoff and provide an alternative means for increasing the effective heat input. Note that argon shielding gas was used in all cases. With the argon plasma gas, the voltage progressively increased with the addition of helium, nitrogen, and hydrogen carrier gas streams. The increase in voltage with helium is due to a higher ionization potential compared to argon (24.5 eV vs. 15.7eV). The even larger increases for hydrogen and nitrogen are a result of the molecular dissociation reactions prior to ionization. For these same reasons, the

operating voltage ranges with the argon-helium and argon-hydrogen plasma gases exhibit a “step increase” for all combinations when compared to the argon plasma gas. As will be discussed, this increase in the arc voltage and effective heat input altered overlay development and properties.

iv. Heat Input: Interactions between Torch Motion, Powder Delivery, and Arc Energy

During overlay optimization a large number of exploratory test welds were created to understand the interrelationships between the heat input parameters. The following examples will illustrate that developing a proper overlay requires finding the tolerance range (i.e., tolerance box) for the motion, powder delivery, and arc energy. This is similar to the concepts introduced by Deuis *et al.* [158], as summarized in Figure 72. Significant deviation outside these operating ranges will disturb the effective heat input balance and compromise overlay integrity. Figure 103a illustrates the effect of operating with an arc energy that is too low; there is poor fusion between successive weaves and poor continuity at the overlay edges. There are a number of means for resolving this problem, such as increased arc energy, decreased powder feed rate, or modification of torch motion; all three solutions increase the effective heat input to the overlay system. Figure 103b demonstrates that excessive forward welding speed causes a breakdown in the overlay weaving pattern and loss in overlay height continuity; note the similarity to the X2 multiple shown in Figure 100. This deviation outside of tolerable ranges is significant and it may be difficult to obtain a new combination of arc energy and powder feed rate that could remedy this poor overlay behaviour. Figure 103c shows that by sufficiently reducing the powder delivery feed rate, the extra arc energy is transferred to the base

material, which can create porosity and other fusion flaws. These examples illustrate the strong interrelationships between torch motion, powder delivery, and arc energy during PTA surfacing.

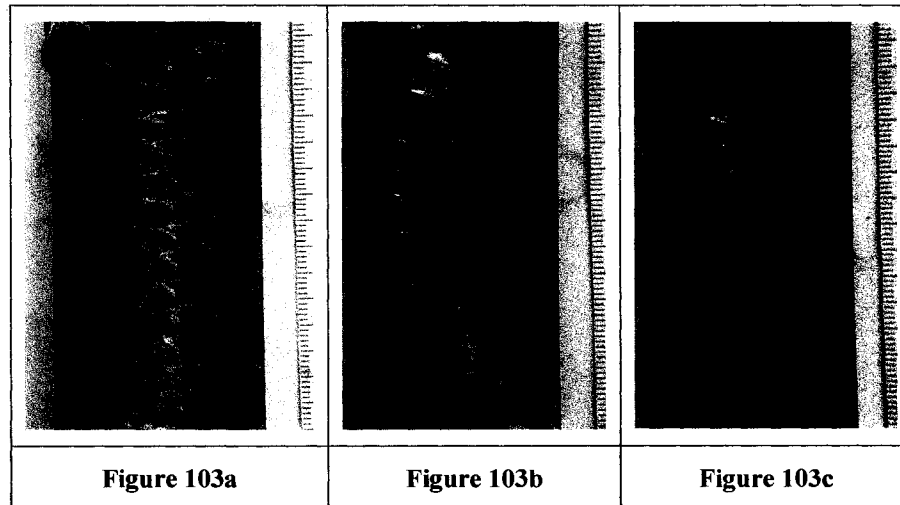


Figure 103 – Effect of Motion, Powder, Arc Energy on Overlay Appearance

b. Effect of Gas Composition on Overlay Welding of 410SS

i. Overlay Surface Appearance

The as-welded condition of the 410SS samples is given in Figure 79 and Figure 80. There are differences in the “macro” appearance of the overlay as a function of the gas mixture. For example, the use of Ar-25%N₂ for both the carrier and plasma gas is not recommended due to excessive porosity formation. It is possible that with a lower percentage of nitrogen or the addition of aluminum powder to the overlay [170] the porosity would be reduced to acceptable levels, but this was not investigated in this study. The cleaned specimens in Figure 81 and Figure 82 illustrate that the oxide formed during welding has a bluish hue. It appears there was an increase in overlay oxidation when Ar-He was used; likely owing to helium’s lower density and greater propensity to float away

and not shield the overlay material as effectively. The use of Ar-H₂ mixtures reduced the amount of oxidation present due to its reducing chemical reactivity. The Ar-CO₂ shielding mixture leads to excessive overlay oxidation. Even after extensive wire brush cleaning, the oxide material could not be removed for the samples welded with Ar-CO₂ shielding gas. A violent reaction occurs when welding Ar-CO₂ and Ar-H₂ together with 410SS. This porosity did not form during autogenous welding, and it is likely the result of a reaction with other alloying elements (i.e., perhaps chromium and/or carbon). The best quality overlay was obtained with argon shielding gas.

ii. Overlay Cross-sectional Macro Properties

The macro properties of the 410SS overlay are summarized in Figure 85. Due to the excessive porosity obtained when welding with the Ar-N₂ gas, it was omitted from the comparisons. In all cases, the “Argon Standard” refers to the standard welding conditions utilized to produce the optimized overlay, as shown in Table 24. All subsequent comparisons will be made to this standard and the effect of the gas composition will be discussed.

The Argon Standard conditions had the lowest average height and largest difference between the minimum and maximum heights. This “saddle effect” can be observed in the overlay cross-section macrographs (Figure 83); relatively high powder waste was also observed during welding. Addition of helium and hydrogen carrier gases to the arc environment (with Ar plasma gas) created higher and more uniform overlay heights. As discussed earlier, the greater heat input required to fuse more of the powder material can be related to the higher operating voltage ranges and increased heat input. This is a significant finding since the majority of literature reports poor, saddle-like profiles for

PTA surfacing. Hence, changing the gas composition is an effective means for reducing powder waste and improving contour.

The use of 10% hydrogen for the plasma gas exhibited a similar increasing trend for the overlay height. The operating voltage had an average increase of approximately 3 volts, which resulted in the 0.7 mm average increase in the overlay height. Additional heat was also added to the system during the exothermic atomic hydrogen recombination reaction. This phenomenon dominates the overlay fusion behavior; any gas combination that uses hydrogen exhibits a substantial increase in dilution and penetration. The industrial standard is to have the percent dilution less than approximately 15%; the use of hydrogen exceeds this arbitrary limit. This trend does not prohibit the use of hydrogen for PTA welding, but indicates that the Argon Standard parameters were not optimized for this level of heat input. For example, manipulation of the powder feed rate and welding speed would lower the overlay dilution. The use of an Ar-H₂ gas composition is practical means of increasing productivity.

It is unclear why during the use of Ar-He plasma gas the trend in overlay height, as a function of carrier gas, does not follow that of the other mixtures. However, an identifiable trend is the drop in overlay percent dilution and penetration, compared to the Argon Standard, with helium plasma or carrier gases; concurrently there was also an increase in overlay height. The only exceptions to this pattern are the dominating penetrating effects of the hydrogen gas recombination reaction discussed earlier. It is postulated that the high thermal conductivity of helium permits more efficient energy transfer to the overlay powder (likely as the powder travels through the arc), in-lieu of transferring heat directly to the base plate. This effect is very desirable for overlay

welding where maximum overlay height and minimum dilution are the ultimate goals. The presence of micro fusion flaws and poor tie-in quality, shown in Figure 88, indicates that the dilution level is too low. However, recall that the operating parameters are for pure argon gases and these flaws could be eliminated through subsequent optimization experiments.

iii. Overlay-to-substrate Wetting Behaviour and Fusion Flaws

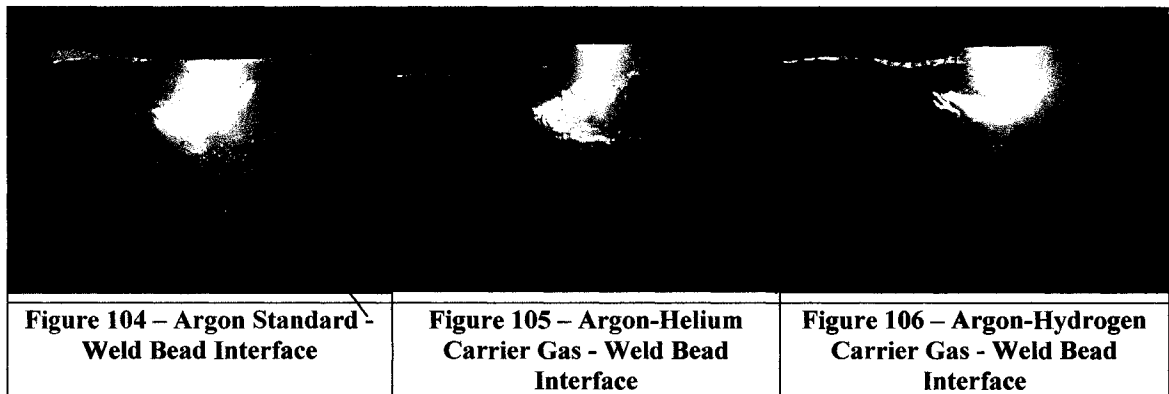
In-situ video observation of the overlay leading edge provided excellent information regarding physiochemical wetting behaviour. The Argon Standard exhibited relatively poor wetting and fluidity. The inert argon atmosphere was susceptible to flaw formation at the overlay interface; video analysis reveals regions where the overlay tends to “ball-up” or create cavities where the liquid did not fully wet the substrate (see Figure 104). In addition, the excessive waste powder, accumulated at the front of the interface, is undesirable since it tends to disrupt the flow of molten material. These issues often translated into the interface flaws shown in Figure 86, Figure 87, and Table 28. Video analysis allowed for the exact location of the arc to be tracked. When the arc impinged directly on the work piece, ahead of the overlay front, the dilution/penetration increased significantly. Conversely, if the arc impinged upon the leading edge of the overlay or the previous weld pass, the molten material acted as thermal insulator to direct heat transfer and was partially responsible for the fusion line flaws noted above. Some authors [138,141] believe that the arc should impinge directly on the weld pool to minimize penetration, while others [171] insist that the plasma arc should be directed just in front of the molten pool to avoid lack of fusion and porosity flaws. Utilizing the video techniques described, it is recommended that the effect of the arc impingement location

be investigated in greater detail in the future. This may eliminate interface fusion flaws and avoid an increase in overlay dilution/penetration.

The addition of inert helium to the carrier gas, Figure 105, produced a slight reduction in waste powder material and increased the pool size; this led to a thicker layer of molten material underneath the arc. However, there was not a substantial change in the wetting behaviour and the overlay was still prone to interface fusion flaws (Figure 88 and Table 28). It is theorized that 25% was insufficient helium content to initiate large, whole-scale changes in bead wetting behaviour. As discussed in Section 3.6d, this gas composition was also ineffective in changing bead behaviour during the humping threshold experiments. In future work it is recommended that other helium contents be attempted, up to 100%, to determine the true influence on interface-to-work wetting behaviour.

The addition of hydrogen brought about a substantial change in the physiochemical wetting behaviour at the interface and reduced powder waste (Figure 106). By creating a situation where the liquid-solid interfacial energy was equal to or less than the solid-vapour interface energy promoted wetting; these concepts were introduced in Section 3.6c. Video analysis proved that surface oxides were chemically reduced ahead of the overlay front, which increased the base metal surface energy, γ_{SV} . It is postulated that the solid-to-liquid interface energy γ_{LS} was also lowered due to the reduction in interface contaminants. Therefore, as γ_{SV} increases while γ_{LS} decreases, the system will become more wetting, even though the liquid surface tension, γ_{LV} , was also increased. This was consistently observed when hydrogen was added to the plasma and carrier gas streams, and a similar effect is expected if hydrogen is added to the shielding gas. Also evident in

Figure 106 is that the arc impinged upon the largest liquid weld pool due to high powder melting rates and low powder losses. It would be expected that dilution/penetration would be minimized. However, the data in Figure 85 and Table 28 contradict this and further reinforce the dominating effects of the hydrogen recombination reaction. Sufficiently high quantities of energy are released by this exothermic reaction so that extremely high penetration and excellent fusion quality are possible (Figure 89). This indicates that productivity can be maximized (i.e., high powder feed rates and motion) without the threat of poor interface fusion quality.



Video and metallurgical analysis was used to ascertain the effect of an oxidizing gas, Ar-CO₂, as the shielding gas. As mentioned earlier, this type of gas mixture was not attempted for the plasma or carrier streams due to the damaging effects on the tungsten electrode. Figure 107 illustrates that wetting behaviour is not improved with the oxidizing stream, while entrapment of surface oxides resulted in interface fusion flaws (see Figure 90 and Table 28). EDX analysis (Figure 91 and Table 29) indicated a high concentration of deoxidants and oxygen, which confirmed that interface contaminant was an oxide-based inclusion. Figure 107 illustrates the mechanism by which the oxide material was entrapped beneath the overlay. Excessive oxidation of the base metal near the leading

edge of the overlay pool caused the solid-vapour interface energy, γ_{sv} , to be reduced. As discussed previously in Section 3.6d, this led to a system where $\gamma_{sv} < \gamma_{ls}$ and overlay wetting ability was reduced. Hence, due to excessive interface fusion flaws and poor physiochemical wetting behaviour, the use of oxidizing shielding gases is not recommend for PTAW overlay applications.

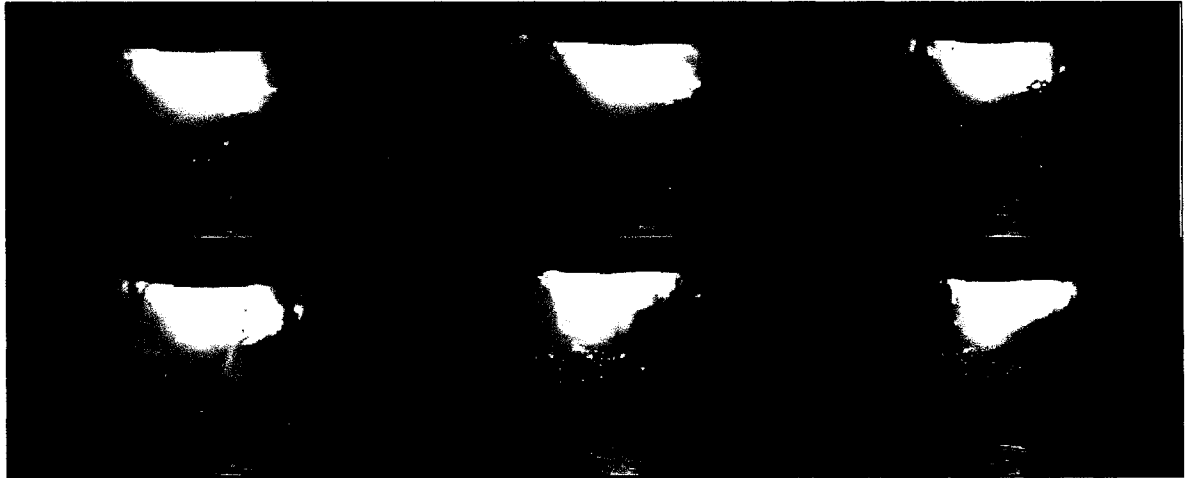


Figure 107 – Excessive Oxidation and Flaw Formation with Ar-CO₂ Shielding Gas (1.5 seconds)

iv. Data Variability

Three different gas combinations were randomly selected and repeated in another welding run to determine data variability. Figure 108 illustrates that: 1) the absolute values of the macro properties will vary from run to run, but 2) the trends within each weld run are reasonably consistent. The variability in the absolute value between welding runs is due to the inherent difficulties in controlling such a large number of interrelated process variables (see Table 22). For example, as discussed in Section 4.6a, the effective heat input is dependent on a large number of parameters and a serious error in controlling one variable or the cumulative effect of a number of variables could bring about a “shift” in the effective heat input. This is the likely cause for the variation from Run 1 to Run 2.

However, the consistency in the trends common to both welding runs is encouraging and illustrates that changing the welding gas composition has significant effects on process behaviour and overlay development.

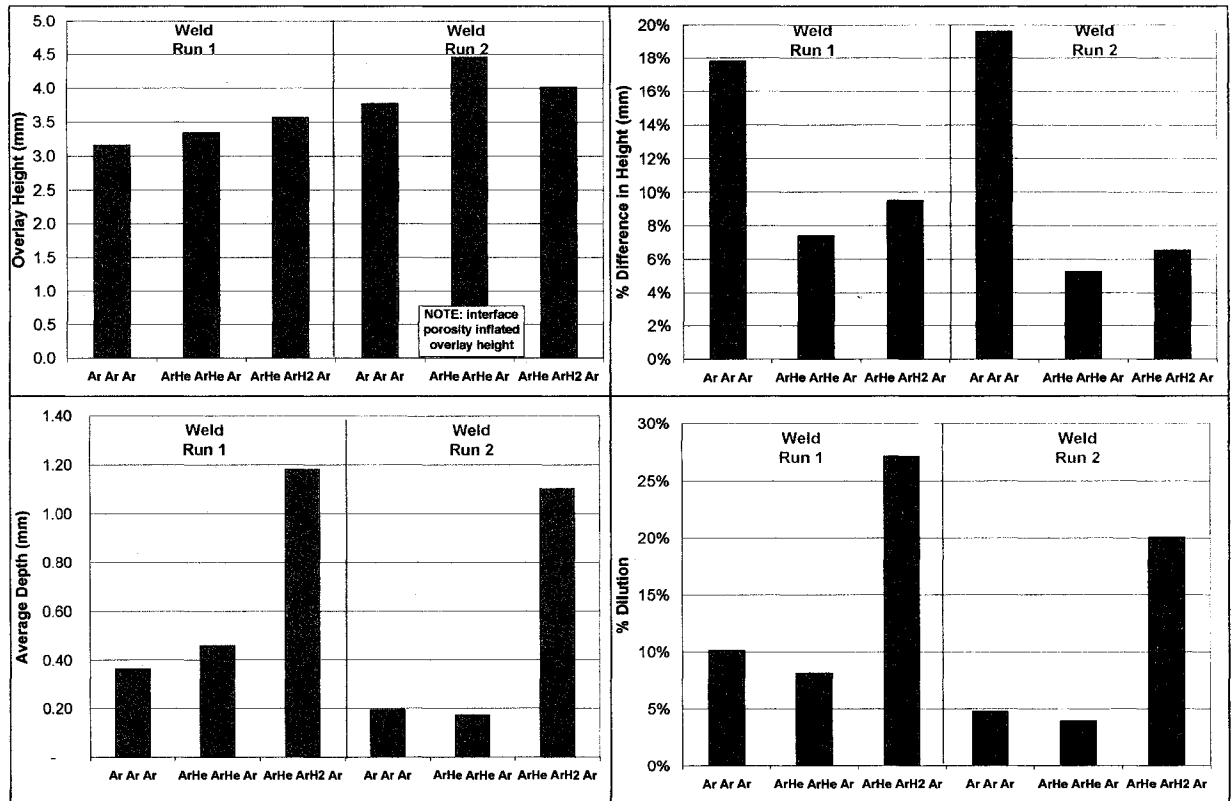


Figure 108 – Data Variability of 410SS Overlay Welding

c. Effect of Tungsten Carbide Additions

i. Thermal Behavior

The addition of 65% weight percent tungsten carbide (WC) to the 410SS matrix material caused a very large change in the overlay thermal behaviour. Tungsten carbide has a very high melting point and a relatively high heat capacity, as indicated in Table 32, and acts as a “heat sink” during PTA overlay welding. For example, due to their high melting temperatures the carbides can absorb large amounts of energy and subsequently release the energy during matrix solidification. This thermal effect can increase arc constriction

and is often called the thermal pinch effect [166]. As will be discussed, the thermal behaviour of WC affects process parameter interactions, the influences of welding gas composition, and metallurgical properties.

Table 32 – Thermal Properties of Common Engineering Materials

	Units	Iron	0.23%C Steel	410 SS	WC
Thermal Conductivity	(W/m K)	80.2	35	27	100
Melting Temperature	(°C)	1530	1510	1510	2850
Latent Heat of Fusion	(J/g)	272	272	272	197
Specific Heat	(J/g C)	0.448	0.486	0.468	0.306
Density	(g/cm ³)	7.9	7.9	7.7	15.8



Figure 109 – Macro Picture of 410SS-WC (left) and 410SS Welded with Identical Parameters

An example that illustrates this thermal effect is shown in Figure 109. Both overlays were completed utilizing the same process parameters optimized for 410SS as summarized in Table 26. The overlay on the right exhibits a good profile, fusion quality and surface appearance; this is to be expected since the parameters were optimized for 410SS powder. The overlay on the left has a poor profile, inadequate fusion, a very rough surface appearance, excessive cracking, and porosity. The main cause was that the effective heat input, as determined by the motion, arc energy, and powder delivery, was insufficient for the WC additions. The combination of process parameters required to produce a sound overlay of comparable height with 65%wt-WC is summarized in Table 27, and is distinctly different than that for pure 410SS. Recommended future work

includes investigating this thermal effect by utilizing progressively higher additions of WC and assessing how the required motion and arc energy is altered; this information would be an integral part of the effective heat input formula for PTA surfacing.

ii. Effect of Gas Composition

The first outcome of changing gas composition was the “stitching pattern” developed on the overlay surface shown in Figure 92. The typical pattern expected for overlays produced via saw tooth motion is given for the Argon Standard. Additions of helium to either the plasma gas or carrier gas have minimal effects. However, additions of hydrogen extended solidification times considerably; the solidification of the overlay in a semi-circular shape is an indication of this effect. If solidification time is extended too much, then the shielding gas may not adequately protect the overlay from surface oxidation. This did not occur during these experiments, but has been reported by others [171]. The increased time required for solidification indicates that a greater quantity of energy was added to the system, likely due to the exothermic recombination reaction and higher operating voltages. The thermal behaviour of WC allows for this extra energy to be stored and slowly released, extending solidification time. As discussed below, this greatly affects overlay macro and micro properties.

Based on the data presented in Figure 93 and Figure 94, many of the trends in the macro cross-sectional properties for 410SS-WC are similar to those described in Section 4.6b for 410SS. However, due to the thermal behaviour of WC, there are some unique developments not previously encountered. First, Figure 94 illustrates that the overlay height did not change considerably as a function of the gas combination. Most combinations were identical, or there were minimal increases or decreases. The percent

height difference decreased, but to a much lower extent than that encountered during 410SS welding. These trends are linked to the thermal absorbing behaviour of WC. In Section 4.6b it was established that the extra arc energy from both the 25%-helium and 10%-hydrogen additions were delivered to the powder as it traveled to the base material. During 410SS-WC welding, however, the WC readily absorbed this extra energy and it did not translate into the greater quantity of powder melting observed with pure 410SS. Increasing helium above 25% and hydrogen above 10% could produce sufficient energy to counteract the thermal pinch effect and increase the overlay height. However, the resulting carbide distribution, overlay dilution and other overlay properties would have to be assessed to ensure proper metallurgical integrity.

In-situ video analysis determined that the arc impinged upon a thin layer of molten material during welding. The relatively low dilution and penetration for both pure argon and Ar-He mixtures illustrate that the MMC was extremely effective at insulating the base material during PTAW. When welding with very low dilution, i.e., less than 5%, it is possible to not develop a properly bonded overlay-to-work interface and form interface flaws (see Table 30). As shown in Figure 96 – Sample W1 & W4, during 410SS-WC overlay welding a “composite” region formed at the interface; EDX analysis revealed that tungsten (~12%) and chromium (~3%) had combined with iron to form the interface. Formation of this composite region is critical to ensure proper bonding. In the vicinity of interface flaws there is a loss of this composite region (see Figure 96 – Sample W6 and Figure 95 – Sample W1). A qualitative method for determining the quality of the overlay bonding, without completing metallographic analysis, is the overlay bend test. This type of test is based on a “go or no go” criteria, corresponding to cracking failure or spallation

failure, respectively, as shown in Figure 110. Hence, to avoid a spallation failure, also called a peeling failure [166], one must ensure that there is sufficient penetration of the base material. The use of hydrogen additions induced a substantial increase in both penetration and overlay dilution during 410SS-WC PTAW (Figure 94); this correlates well with earlier trends. Figure 96 – Sample W4 illustrates excellent tie-in quality while welding with hydrogen additions; Figure 95 – Sample W1 demonstrates poor tie-in fusion in a pure argon atmosphere. The very high penetration power, even though a thick insulating layer formed beneath the arc, is due to the exothermic recombination reaction. Also, the high thermal capacity of the WC stored substantial arc energy that contributed to the longer solidification times and increased penetration/dilution.

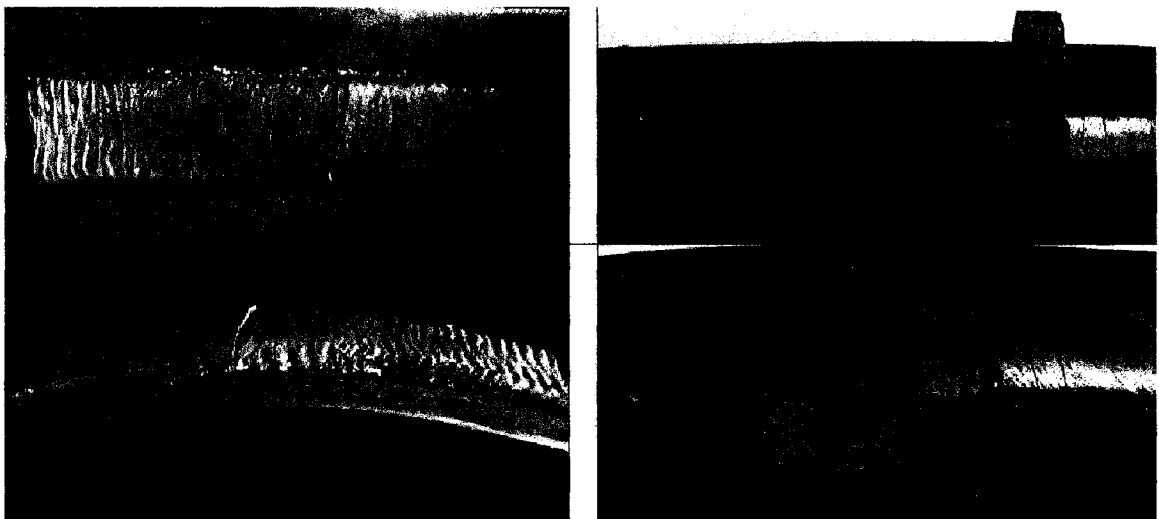


Figure 110 - Bend Test Samples – Cracking Failure (left) & Spallation Failure (right)

Another contributing factor to the overlay dilution and establishing the proper interface was the physicochemical wetting behaviour of the MMC material. The same trends observed during 410SS welding (recall Section 4.6b.iii) were observed with 410SS-WC. The argon atmosphere produced poor wetting characteristic, addition of helium to the

plasma or carrier gas(es) produced very little change, while the reducing hydrogen arc greatly improved wetting behaviour. The use of an Ar-CO₂ shielding gas was found to decrease wetting and led to similar surface and interface oxide inclusion flaws discussed earlier for 410SS (see Figure 97). To ensure proper interface and tie-in fusion, the use of hydrogen is recommended for overlay applications. However, the tendency towards deleterious metallurgical effects, such as hydrogen assisted cracking, must be assessed in future work.

The carbide distributions for the various gas compositions were qualitatively assessed and are summarized in Table 30. An important objective of MMC overlay welding is ensuring a homogenous distribution of carbide throughout the overlay; Figure 95 – Sample W1 shows a desirable carbide distribution. Since tungsten carbide density is twice that of the matrix (see Table 32), the carbide tends to sink to the bottom of the pool. This can form a top surface zone relatively dilute of tungsten carbide (Figure 95 – Sample W10) and a bottom zone with relatively high carbide distribution. This combination is grave for wear applications; the matrix material is easily worn from the top surface layer and the remaining exposed tungsten carbide may have insufficient matrix material to ensure proper resistance to wear, impact, chipping, and micro-fracturing [152,170]. Based on the results here, there is a strong correlation between carbide distribution and overlay solidification time. This intuitively makes sense, since a fast freezing puddle will trap the carbide in a more homogenous manner. However, recall that the process parameters were optimized for pure argon welding only. By obtaining optimal motion, powder delivery, and arc energy parameters for each gas composition, in future work, the carbide distributions may be improved.

4.7 Conclusions

- The classical heat input equation is too simple to predict actual heat input during PTA surfacing. The interrelationships between torch motion, arc energy, and powder delivery determine the effective heat input. A torch motion optimization methodology was developed to determine optimum motion conditions for overlay welding and to standardize comparisons in the future.

- Effect of gas mixtures on 410SS overlay welding:
 - The use of helium decreased shielding efficiency and led to increased overlay oxidation. Hydrogen chemically reduced the amount of oxide present. The use of carbon dioxide for the shielding gas reduced wetting behaviour and led to entrapment of surface oxides and formation of interface fusion flaws. The use of oxidizing shielding gases is not recommended for PTAW overlay applications. Pure argon was the optimum shielding medium.
 - The addition of helium and hydrogen to the plasma and/or carrier gas reduced powder waste, decreased height differences, and eliminated the common “saddle” profile.
 - Argon - 10% hydrogen gas caused an increase in overlay height, reduced powder waste, and increased dilution due to a higher heat input; the exothermic recombination reaction dominated overlay penetration trends. Wetting ability and interface quality were both improved.
 - An argon – 25% helium gas mixture increased overlay height and

decreased dilution due to a higher heat input and thermal conductivity. Energy appears to be transferred to the overlay powder in-lieu of the base material. This effect is very desirable for overlay welding where maximum overlay height and minimum dilution are the ultimate goals. Overlay wetting was not improved and interface fusion flaws were more common.

- Data variability was assessed. The absolute values of the macro properties will vary from run to run, but the trends within each weld run are reasonably consistent.
- The thermal properties of tungsten carbide allow it to absorb and subsequently release large amounts of arc energy during PTAW, which can extend overlay solidification time. The average overlay height and percent height difference did not change considerably as a function of the gas combination due to this thermal absorbing behaviour.
- The 410SS-WC MMC was extremely effective at insulating the base material during PTAW, as illustrated by the relatively low dilution, low penetration, and high interface flaw rate for Ar and Ar-He mixtures. The dominating effects of the hydrogen recombination reaction ensure proper fusion and mitigated interface flaws.
- Formation of a composite interface region with tungsten and chromium is critical to ensure proper overlay-to-work bonding. During metallographic analysis a wide variety of very complex microstructures was observed. A secondary carbide

network was produced in the matrix material via melting, dissolution and precipitation of the original tungsten carbide. There is a strong correlation between carbide distribution and overlay solidification time. As solidification time increases, the carbide settling effect increases, as expected.

4.8 Recommendations for Future Work

- All the 410SS-WC gas combinations should be abrasive wear tested per ASTM G65 to determine the influence of weld gas composition on wear behaviour.
- Investigations into the interaction between torch motion, powder feed rate, and arc energy needs to be continued. A new heat input equation must be developed that better predicts overlay quality.
- The thermal “heat sink” effect of WC needs to be better quantified. The use of progressively higher additions of WC and assessing how the required motion and arc energy are altered would provide valuable information, integral to developing a new heat input equation for PTA surfacing.
- Building upon the torch motion optimization methodology presented here, new methods for controlling torch motion is an unexplored area. Most investigators do not disclose the details of the motion program used, or what algorithms they utilized to develop the optimum operating conditions.
- Arc constriction affected autogenous welding considerably (Chapter 3), but there have been no studies, to the author’s knowledge, on the effects of arc constriction on PTA overlaying. The electrode set back, cathode diameter, nozzle configuration, and the plasma, carrier and shielding gas flows rates will provide useful information regarding overlay development.
- There are several nozzle configurations available from the equipment manufacturer, which alter the number and location of gas ports for the carrier gas, but there is virtually no information giving the effects of these variations on the

formation of a weld deposit. The use of wire consumables with or without powder feed is another unexplored area.

- A wide variety of deposition rates are obtainable for a single carrier gas flow rate. Experiments that explore overlay development with the same deposition rate but obtained via different combinations of carrier gas and wheel speed would be valuable.
- Utilizing the same video techniques, it is recommended that the effect of the arc impingement location (i.e., on or off the weld pool) be investigated to determine if penetration can be minimized while mitigating interface flaw formation.
- More detailed metallurgical analysis, such as microhardness, SEM, and TEM, is required to better understand the complex carbide networks developed in the iron matrix. The influence of these precipitates and phases on the metallurgical and wear properties is of practical value.
- It is recommended that helium contents up to 100% be investigated to discover the true influence of helium on interface-to-work wetting behaviour and overlay properties.
- The use of hydrogen gas shows real promise, however the tendency towards deleterious metallurgical effects, such as hydrogen assisted cracking, must be assessed. Also, a variety of Ar-H₂ mixtures up to 10%-15% should be evaluated to determine the minimum hydrogen concentration that improves overlay penetration and wetting, while minimizing dilution, excessive carbide melting, and secondary phase formation.

- The use of welding gas tri-mixtures, i.e., Ar-He-H₂, for the plasma, carrier, and shielding streams is another area that could be explored. It may be possible to fine-tune a mixture to suit the particular powder, base material, or develop overlay properties to suit unique engineering applications.

Chapter 5 – Summary of Overall Work

Investigations into the behaviour of the PTAW process were completed with the main objective of better understanding the influence of welding parameters on process behaviour. During autogenous experiments, it was found that the heat input equation was inadequate to fully characterize PTAW process behaviour. A better method to characterize behaviour is the use of operating maps, where regions of proper operation and flaw formation are easily identified. A humping flaw mechanism was observed and fully characterized; the influence of welding speed, welding current, base material chemistry, minor alloying elements, torch configuration, and welding gas composition on flaw formation was determined. Recommendations to optimize productivity and mitigate flaws are presented. Experimental results from the PTA surfacing of steel components will aid future investigators that wish to improve MMC coatings for wear applications in the oil sands industry. The effective heat input is best characterized by considering the combined effects and interrelationships of torch motion, arc energy, and powder delivery. A motion optimization methodology was developed and shall provide future investigators with a standardized method for assessing torch motion protocols in the future. Standard conditions were developed for 410SS powder and a 410SS – tungsten carbide metal matrix composite (MMC) alloy. Significant changes in overlay bead development, wetting behaviour, and metallographic properties were obtained. Improvements were found with additions of hydrogen and helium, while nitrogen and carbon dioxide produced detrimental fusion flaws. Future work is required to develop optimized mixtures that improve PTA process behaviour and MMC wear resistance.

References

- 1 Patchett, B.M., Welding Metallurgy, The Metals Blue Book – Welding Filler Metals, 2nd ed., CASTI Pub. and American Welding Society (AWS), 1998.
- 2 Cary, H.B., Modern Welding Technology, 4th ed., Prentice-Hall Pub., 1998.
- 3 Jackson, C.E., “The Science of Arc Welding”, Welding Journal, vol. 29, no. 4, 1960, pp 129s-140s.
- 4 Nunes, Jr., A.C., “Arc Welding Origins”, Welding Journal, vol. 45, no. 7, 1976, pp 566-572.
- 5 Gerdien, H., Lotz, A., “Ueber eine Lichtquelle von sehr hoher Flächenhelligkeit (Source of light giving very high surface intensity)”, Zeitschrift für Technische Physik, vol. 4, no. 4, 1923, pp 157-162
- 6 Gage, R.M., Arc Torch and Process, U.S. Patent 2,806,124, September 10, 1957
- 7 Yenni, D.M., High Pressure Arc Process and Apparatus, U.S. Patent 2,847,555, August 12, 1958
- 8 Kielhorn, W.H. *et al.*, “Survey of Joining, Cutting, and Allied Processes”, AWS Welding Handbook, 9th ed., Volume 1 – Welding Science and Technology, AWS Pub., 2001.
- 9 Hoyaux, M.F., Arc Physics, New York, 1968
- 10 Quigley, M.B.C., Richards, P.H., Swift-Hook, D.T., Gick, A.E.F., “Heat flow to the workpiece from a TIG welding arc”, Journal of Physics D: Applied Physics, Vol. 6, 1973, pp 2250-2258
- 11 Goldman, K., “Electric Arcs in Argon: Heat Distribution”, British Welding Journal, Vol. 10, No. 7, 1963, pp. 343-347
- 12 Milner, D.R., Salter, G.R., Wilkinson, J.B., “Arc Characteristics and their Significance in Welding”, British Welding Journal, vol. 7, no. 2, 1960, pp 73 – 88
- 13 Lancaster, J.F. The Physics of Welding, 2nd Ed., International Institute of Welding - Pergamon Press Pub., 1986
- 14 Lancaster, J.F., “The Physics of Fusion Welding – Part 1: The Electric Arc in Welding”, IEE Proceedings, Vol. 134, Pt. B., No. 5, September 1987, pp 233 - 252
- 15 Goldman, K., “Electric Arcs in Argon”, Physics of the Welding Arc Proceedings, Institute of Welding, London, 1966
- 16 Key, F.J., “Arc Physics of Gas-Tungsten Arc Welding”, ASM Handbook Volume 6 – Welding and Joining, ASM International Pub., 1993
- 17 Milner, D.R., & Apps, R.L., Introduction to Welding & Brazing, Pergamon Press Publ, 1968.
- 18 Maecker, H., “Plasma Streaming in Electric Arcs as a Result of Self-Magnetic Compression”, Z. für Physik, vol. 141, 1955, pp. 198

-
- 19 Grist, F.J., Farrell, W., Lawrence, G.S., "Power Sources", ASM Handbook Volume 6 - Welding Brazing and Soldering, ASM International Pub, 1993
- 20 Anon, AWS A5.12/A5.12M, "Specification for Tungsten and Tungsten Alloy Electrodes for Arc Welding and Cutting", American Welding Society Publ., 1998
- 21 Anon, Arc Welding, ASM Metals Handbook, Desk Ed., 2nd Ed., ASM International, 2000
- 22 Patchett, B.M., "Variable AC Polarity GTAW Fusion Behaviour in 5083 Aluminum", Welding Journal, in press
- 23 G.K. Hicken et al., "Gas Tungsten Arc Welding", Welding Handbook, Vol. 2, Welding Processes. AWS, 8th ed. Pg 74-107
- 24 Budinski, K.G., Surface Engineering for Wear Resistance, Prentice-Hall Pub., 1998
- 25 Waszink, J.H., Graat, L.H.J., "Experimental Investigation of the Forces Acting on a Drop of Weld Metal", Welding Journal, Vol. 62, No. 4, 1983, pp. 108S-116S
- 26 Lancaster, J.F., "The Physics of Fusion Welding – Part 2: Mass Transfer and Heat Flow", IEE Proceedings, Vol. 134, Pt. B., No. 6, November 1987, pp 297-316
- 27 Needham, J.C., Cooksey, C.J., Milner, D.R., "Metal Transfer in Inert-Gas Shielding-Arc Welding", British Welding Journal, Vol. 7, No. 2, 1960, pp. 101-114
- 28 Cooksey, C.J., Milner, D.R., "Metal Transfer in Gas-Shielded Arc Welding", Physics of the Welding Arc – A Symposium, Institute of Welding, London, 1962
- 29 Lucas W., "Choosing a Shielding Gas – Part 2", Welding & Metal Fabrication, Vol. 60, No. 6, 1992, pp. 269 – 276
- 30 Lindberg, R.A., Braton, N.R., Welding and Other Joining Processes, Boston: Allyn and Bacon, Inc. Publ., 1976
- 31 Irving, B., "Trying to Make Some Sense Out of Shielding Gases", Welding Journal, Vol. 73, No. 5, 1995, pp. 65 – 70
- 32 Smith, A.A., "Characteristics of the Short-Circuiting CO₂ Shielded Arc", British Welding Journal, Vol. 10, No. 9, 1963, pp. 571 – 586
- 33 Anon, "Linde Unveils Inert-Gas Tungsten-Arc Cutting of Aluminum", Welding Journal, Vol. 34, No. 11, 1955, pp. 1097 – 1098
- 34 Cooper, G., Palermo, J., Browning, J.A., "Recent Developments in Plasma Welding", Welding Journal, Vol. 44, No. 4, 1965, pp. 268 – 276
- 35 Browning, J.A., "Plasma – A Substitute for the Oxy-Fuel Flame", Welding Journal, Vol. 38, No. 9, 1959, pp. 870 – 875
- 36 Ashauer, R.C., Goodman, S., "Automatic Plasma Arc Welding of Square Butt Pipe Joints", Welding Journal, Vol. 46, No. 5, 1967, pp. 405-415

-
- 37 Burhorn, F., Maecker, H., Peters, T., "Temperatur messungen an wasserstabilisierten Hochleistungsboegen (Temperature measurements in water [wall] stabilized heavily loaded arcs)", Zeitschrift für Technische Physik, vol. 131, 1951, pp 28 -40
- 38 Gage, R.M., "The principles of the Modern Arc Torch", Welding Journal, Vol. 38, No. 10, 1959, pp. 959 – 962
- 39 Groman, E.F., "New Developments and Applications in Manual Plasma Arc Welding", Welding Journal, Vol. 48, No. 7, 1969, pp. 547 – 555
- 40 Norrish, J., "Plasma welding developments", Proceedings of the Conference on Advances in Welding Processes, The Welding Institute, Cambridge, UK, 1971
- 41 Pinfold, B.E., Jubb, J.E.M., "Plasma-Arc Welding – Part 1", Welding Technology Data Sheets Series 2 – Processes, Reprinted from Welding and Metal Fabrication
- 42 Harris, I.D., "Plasma Arc Welding", ASM Handbook, Volume 6 - Welding, Brazing and Soldering, ASM International Pub. 1993
- 43 Nishiguchi, K., "Plasma Arc Welding and Cutting", in Advanced Joining Technologies – Proc. Of the International Institute of Welding Congress on Joining Research, July, Chapman and Hall Publ., 1990
- 44 Mendez, P.F., Eager, T.W., "Penetration and Defect Formation in High-Current Arc Welding", Welding Journal, Vol. 82, No. 10, 2003, pp. 296S-306S
- 45 Lucas, W., TIG and Plasma Welding – Process technique, recommended practices and applications, Abington Publ., Cambridge UK, 1990
- 46 Pang, Q., Pang, T., McClure, J.C., Nunes, A.C., "Workpiece Cleaning During Variable Polarity Plasma Arc Welding of Aluminum", Journal of Engineering for Industry – Transactions of the ASME, Vol. 116, No. 11, 1994, pp. 463 – 466
- 47 Fuerschbach, P.W., "Cathodic Cleaning and Heat Input in Variable Polarity Plasma Arc Welding of Aluminum", Welding Journal, Vol. 77, No. 2, 1998, pp. 76s – 85s
- 48 Nunes Jr., A.C., Bayless Jr., E.O., Jones III, C.S., Munafo, P.M., Biddle, A.P., Wilson, W.A., "Variable Polarity Plasma Arc Welding on the Space Shuttle External Tank", Welding Journal, Vol. 63, No. 9, 1984, pp. 27-35
- 49 Helmbrecht, W.H., Oyler, G.W., "Shielding Gases for Inert-Gas Welding", Welding Journal, Vol. 36, No. 10, 1957, pp. 969 – 979
- 50 Patchett, B.M., "Mig Welding of Aluminium with an Argon - Chlorine Mixture", Metal Construction, Vol. 10, No. 10, 1978, pp. 484 - 487
- 51 Bicknell, A.C., Patchett, B.M., "GMA Welding of Aluminum with Argon - Freon Shielding Gas Mixtures", Welding Journal, Vol. 64, No. 5, 1985, pp. 21
- 52 Marya, M., Edwards, G.R., Liu, S., "An Investigation on the Effects of Gases in GTA Welding of a Wrought AZ80 Magnesium Alloy", Welding Journal, Vol. 83, No.7, 2004, pp. 203s-212s
- 53 Norrish, J., Advanced Welding Processes, IOP Publishing Ltd. Publ, 1992

-
- 54 Jenkins, N.T., Eagar, T.W., "Chemical Analysis of Welding Fume Particles", Welding Journal, Vol. 84, No. 6, 2005, pp. 87s - 93s
- 55 Salter, G.R., Milner, D.R., "Gas Metal Reactions in Arc Welding", British Welding Journal, Vol. 12, No. 5, 1965, pp. 222 – 228
- 56 Polard, B., Milner, D.R., "Gas Metal Reactions in Carbon Dioxide Arc Welding", Journal of the Iron and Steel Institute, Vol. 209, No. 4, 1971, pp. 291 – 300
- 57 Menzel, M., "The Influence of individual components of an industrial gas mixture on the welding process and the properties of welded joints", Welding International, Vol. 17, No. 4, 2003, pp. 262 – 264
- 58 Lyttle, K.A., "Shielding Gases for Welding", ASM Handbook, Volume 6 - Welding, Brazing and Soldering, ASM International Pub. 1993
- 59 Houldcroft, P.T., Welding Process Technology, Cambridge University Press Publ., 1977
- 60 Young, B., "Shielding and Purging Gases: Making the Right Selection", Welding Journal, Vol. 74, No. 1, 1995, pp. 47 – 49
- 61 Khrustaleva, E.I., Surgunt, Y.M., "A Nomogram for Determining the Optimum Flow Rate of the Shielding Gas in Arc Welding", Welding International, No. 3, 1989, pp. 241 – 242
- 62 Kuwana, T., "The Oxygen and Nitrogen Absorption of Iron Weld Metal During Arc Welding", in Advanced Joining Technologies – Proc. Of the International Institute of Welding Congress on Joining Research, July, Chapman and Hall Publ., 1990
- 63 Onsoien, M., Peters, R., Olsen, D.L., Liu, S., "Effect of Hydrogen in an Argon GTAW Shielding Gas: Arc Characteristics and Bead Morphology", Welding Journal, Vol. 74, No. 1, 1995, pp. 10s – 15s
- 64 Marques, P.V., Modenesi, P.J., "TIG Arc Characteristics in Different Atmospheres (Part 1)", Welding International, Vol. 14, No. 8, 2000, pp. 626 – 632
- 65 Ramakrishnan, S., Nuon, B., "Prediction of Properties of Free Burning Welding Arc Columns", Journal of Physics D – Applied Physics, Vol. 13, No. 10, 1980, pp. 1845 – 1853
- 66 Suban, M., Tusek, J., Uran, M., "Use of Hydrogen in welding engineering in former times and today", Journal of Materials Processing Technology, Vol. 119, 2001, pp. 193 – 198
- 67 Hunt, C., Bols, I., Ortega, P., "Helium – A Lightweight Gas but a Heavyweight Performer", Welding & Metal Fabrication, Vol. 65, No. 6, 1997, pp. 10 – 14
- 68 Subramaniam, S., White, D.R., "Effect of Shield Gas Composition on Surface Tension of Steel Droplets in a Gas-Metal-Arc Welding Arc", Metallurgical and Materials Transactions B, Vol. 32B, No. 4, 2001, pp. 313 – 318
- 69 Shackleton, D.N., Lucas, W., "Shielding Gas Mixtures for High Quality Mechanized GMA Welding of Q & T Steel", Welding Journal, Vol. 53, No. 12, 1974, pp. 537s – 547s
- 70 Vaidya, V.V., "Shielding Gas Mixtures for Semiautomatic Welds", Welding Journal, Vol. 81, No. 9, 2002, pp. 42 – 48

-
- 71 Wen, J., Lundin, C.D., "Technical Note: Surface Tension of 304SS Stainless Steel Under Welding Conditions", Welding Journal, Vol. 65, No. 5, 1986, p. 138s
- 72 Leibzon, V.M., Glushko, V.Ya., Frolov, V.V., "The Energy and Technological Parameters of Arcs Running Between a Non-Consumable Electrode and a Copper Plate in Argon, Nitrogen, Helium", Welding Production, Vol. 24, No. 8, 1977, pp. 12 – 14
- 73 Blake, P.D., Jordan, M.F., "Nitrogen Absorption during the Arc Melting of Iron", Journal of the Iron and Steel Institute, Vol. 209, No. 4, 1971, pp. 197
- 74 den Ouden, G., Hoojimans, J.W., "The Influence of Oxygen on Nitrogen Absorption during Arc Melting of Iron", Welding Journal, Vol. 71, No. 10, 1992, pp. 377s
- 75 Du Toit, M., Pistorius, P.C., "Nitrogen Control during Autogenous Arc Welding of Stainless Steel – Part 1: Experimental Observations", Welding Journal, Vol. 82, No. 8, 2003, pp. 219s – 224s
- 76 Lucas, W., "Shielding Gases For Arc Welding – Part 1", Welding & Metal Fabrication, Vol. 60, No. 5, 1992, pp. 220 – 225
- 77 Bennett, G., "Gases for TIG and plasma arc welding", Welding and Metal Fabrication, Vol. 58, No. 6, 1990, pp. 335 – 336
- 78 Tseng, K.H., Hsieh, S.T., Tseng, C.C., "Effect of Process Parameters of Micro-Plasma Arc Welding on Morphology and Quality in Stainless Steel Edge Joint Welds", Science and Technology of Welding and Joining, Vol. 8, No. 6, 2003, pp. 423 – 430
- 79 Sun, Z., Huang, Z.H., "Micro-PTA Powder Cladding on a Hot Work Tool Steel", Journal of Materials and Product Technology, Vol. 13, No. 3-6, 1998, pp. 146 – 154
- 80 Metcalfe, J.C., Quigley, M.B.C., "Automatic Control of Plasma Welding Utilizing The Keyhole Efflux Plasma", Welding and Metal Fabrication, Vol. , No. 11, 1975, pp. 674 - 676
- 81 Metcalfe, J.C., Quigley, M.B.C., "Keyhole Stability in Plasma Arc Welding", Welding Journal, Vol. 54, No. 11, 1975
- 82 Metcalfe, J.C., Quigley, M.B.C., "Heat Transfer in Plasma-Arc Welding", Welding Journal, Vol. 54, No. 3, 1975
- 83 Hou, R., Evans, D.M., McCluure, J.C., Nunes, A.C., Garcia, G., "Shielding Gas and Heat Transfer Efficiency in Plasma Arc Welding", Welding Journal, Vol. 75, No. 10, 1996, pp. 305s – 310s
- 84 Fan, H.G., Kovacevic, R., Zheng, B., Wang, H.J., "Numerical and Experimental Study on the Transport Phenomena in the Plasma Arc Welding", NIST Special Publication, Vol. 949, 2000, pp. 91 – 100
- 85 Keanini, R.G., "Simulation of weld pool flow and capillary interface shapes associated with the plasma arc welding process", Finite Elements in Analysis and Design, Vol. 15, No. 1, 1993, pp. 83 – 92
- 86 Shchitsyn, Y.D., "Stability of molten pool in plasma welding with a penetrating arc", Welding International, Vol. 12, No. 4, 1998, pp. 303 – 305
- 87 Zhang, Y.M., Zhang, S.B., "Observation of the Keyhole during Plasma Arc Welding", Welding Journal, Vol. 78, No. 2, 1999, pp. 53s – 58s

-
- 88 Bashenko, V.V., Sosnin, N.A., "Optimization of the Plasma Arc Welding Process", Welding Journal, Vol. 67, No. 10, 1988, pp. 233s-237s
- 89 Choi, H.K., "Operating Characteristics and Energy Distribution in Transferred Plasma Arc Systems" Ph.D. Dissertation, McGill Univeristy, Montreal, Quebec, Canada, 1980
- 90 Mehmetoglu, M.T., Gauvin, W.H., "Characteristics of a Transferred-Arc Plasma", AIChE Journal, Vol. 29, No. 2, 1983, pp. 207 – 215
- 91 Richardson , I.M., "Properties of Constricted Gas Tungsten (Plasma) Welding Arcs at Elevated Pressures", Ph.D. Dissertation, Cranfield University, UK, 1991
- 92 Hou, H., "Study of Gas Flow Pattern, Undercutting and Modification of the Welding Torch in Variable Polarity Plasma Arc Welding", B.S. Thesis, The University of Texas at El Paso , USA, 1994
- 93 Evans IV, D.M., "Melting and Arc Efficiency of Plasma Arc Welding", M.S. Thesis, The University of Texas at El Paso, USA, 1996
- 94 Martinez, L.F., Matlock, C., Marques, R.E., McClure, J.C., Nunes Jr., A.C., "Effect of Welding Gases on Melt Zone Size in VPPA Welding of Al 2219", Welding Journal, Vol. 73, No. 10, 1994, pp. 51 – 55
- 95 Harris, I.D., "Plasma-MIG Welding", ASM Handbook, Volume 6 - Welding, Brazing and Soldering, ASM International Pub., 1993
- 96 Areskoug, M., Widgren, H., "Recent Developments and Applications of the Gas-Metal-Plasma-Arc Process", in Advances in Welding Processes – Fourth International Conference, Harrogate, UK, 9 – 11 May, 1978, pp. 401 – 414
- 97 Schultz, J.F., "TIG Process With Dual Shield: Intermediate Process Between TIG and Plasma Arc Welding", Welding in the World, Vol. 24, No. 11/12, 1986, pp. 248 – 258
- 98 Rybicki, D.J., McGee, W.F., "Ternary-Gas Plasma Arc Welding", NASA Technical Briefs, Vol. 20, No. 12, 1996, pp. 118
- 99 McGee, W.F., Rybicki, D.J., Waldron, D.J., Ternary Gas Plasma Welding Torch, U.S. Patent 5,399,831, March 21, 1995
- 100 Lundin, C.D., Ruprecht, W.J., "Influence of Shield Gas Composition on Plasma-Arc Penetration", in AWS 55th Annual Meeting, May 6 – 10, 1974, pp. 3 – 4
- 101 Lundin, C.D., Ruprecht, W.J., "The Effect of Shielding Gas Additions on the Penetration Characteristics of Plasma-Arc Welds", Welding Journal, Vol. 56, No. 1, 1977, pp. 1s – 7s
- 102 McLean, W., Pinfeld, B.E., "Operational envelopes for plasma keyhole welding", in Advances in Welding Processes – Third International Conference, Harrogate, UK, 7 – 9 May, 1974, pp. 93 – 104
- 103 Martikainen, J.K., Moisis, T.J.I., "Investigation of the Effect of Welding Parameters on Weld Quality of Plasma Arc Keyhole Welding of Structural Steels", Welding Journal, Vol. 72, No. 7, 1993, pp. 329s – 340s

-
- 104 Jerstrom, P.J., Martikainen, J.K., "On the Effects of Shielding Gas Efficiency of Plasma Arc Keyhole Welding" in ASM Conference on Welding and Joining Science and Technology, Madrid, Spain, 10 – 12 March, 1997, pp. 27 – 36
- 105 Martikainen, J., "Conditions for achieving high-quality welds in the plasma-arc keyhole welding of structural steels", Journal of Materials Processing Technology, Vol. 52, No. 1, 1995, pp. 68 – 75
- 106 Key, J.F., "Anode/Cathode Geometry and Shielding Gas Interrelationships in GTAW", Welding Journal, Vol. 59, No. 12, 1980, pp. 364s – 370s
- 107 MKS Instruments Inc. Application Specialist, "Flow Measurement and Control FAQ's & Application Notes", 1994, <http://www.mksinst.com/techfaq.html>
- 108 MKS Instruments Inc. Application Specialist, Private Communication.
- 109 Bradstreet, B.J., "Effect of Surface Tension and Metal Flow on Weld Bead Formation", Welding Journal, Vol. 47, No. 7, 1968, pp. 314s – 322s.
- 110 Lin, M.L., Eagar, T.W., "Influence of Arc Pressure on Weld Pool Geometry", Welding Journal, Vol. 64, No. 6, 1985, pp. 163s – 169s.
- 111 Lin, M.L., Eagar, T.W., "Effects of Surface Depression and Convection in GTA Welding", in Advances in Welding Science and Technology - Proceedings of an International Conference on Trends in Welding Research, Gatlinburg, Tennessee, USA, 18 – 22 May, 1986
- 112 Rokhlin, S.I., Guu, A.C., "A Study of Arc Force, Pool Depression, and Weld Penetration During Gas Tungsten Arc Welding", Welding Journal, Vol. 72, No. 8, 1993, pp. 381s – 390s
- 113 Choo, R.T.C., Szekely, J., Westhoff, R.C., "Modeling of High-Current Arcs with Emphasis on Free Surface Phenomena in the Weld Pool", Welding Journal, Vol. 69, No. 9, 1990, pp. 346s – 361s.
- 114 Shimada, W., Hoshinouchi, S., "A Study on Bead Formation by Low Pressure TIG Arc and Prevention of Undercut Beads", Quarterly Journal of the Japan Welding Society, Vol. 51, No. 3, 1982, pp. 280 - 286
- 115 Savage, W.F., Nippes, E.F., Agusa, K., "Effect of Arc Force on Defect Formation in GTA Welding", Welding Journal, Vol. 58, No. 7, 1979, pp. 212s – 224s.
- 116 Matsunawa, A., Nishiguchi, K., "Arc Behaviour, Plate Melting, and Pressure Balance of the Molten Pool in Narrow Grooves", in Arc Physics and Weld Pool Behaviour, Vol. 1, London, UK, 8 – 10 May, 1979, pp. 301 – 310.
- 117 Ishizaki, K., "Interfacial Tension Theory of the Phenomena of Arc Welding – Mechanism of Penetration", in Physics of the Welding Arc – A Symposium, London, UK, 29 Oct – 2 Nov, 1962, pp. 195 - 209
- 118 Gratzke, U., Kapadia, P.D., Dowden, J., Droos, J., Simon, G., "Theoretical Approach to the Humping Phenomenon in Welding Processes", Journal of Physics D: Applied Physics, Vol. 25, pp. 1640 - 1647
- 119 Kern, M., Berger, P., Hügel, H., "Magneto-Fluid Dynamic Control of Seam Quality in CO₂ Laser Beam Welding", Welding Journal, Vol. 79, No. 3, 2000, pp. 72s – 78s.
- 120 Mendez, P.F., Neice, K.L., Eagar, T.W., "Humping Formation in High Current GTA Welding", in Proceedings of the International Conference on Joining of Advanced and Specialty Materials II, Cincinnati, OH, USA, November, 1998
- 121 Heiple, C.R., Burhardt, P., "Fluid Flow Phenomena During Welding", ASM Handbook, Volume 6 - Welding, Brazing and Soldering, ASM International Pub., 1993

-
- 122 Heiple, C.R., Roper, J.R., "Mechanism for Minor Element Effect on GTA Fusion Zone Geometry", Welding Journal, Vol. 61, No. 4, 1982, pp. 97s – 103s
- 123 Walsh, D.W., Savage, W.F., "The Mechanism of Minor Element Interaction in Autogenous Weld Pools", in Advances in Welding Science and Technology - Proceedings of an International Conference on Trends in Welding Research, Gatlinburg, Tennessee, USA, 18 – 22 May, 1986
- 124 Heiple, C.R., Burgardt, P., Roper, J.R., Long, J.L., "The Effect of Trace Elements on TIG Weld Penetration", in The Effect of Residual, Impurity, and Microalloying Elements on Weldability and Weld Properties – An International Conference, London, UK, 15 – 17 November, 1983, pp. P36-1 to 36-10
- 125 Keene, B.J., Mills, K.C., Bryant, J.W., Hondros, E.D., "Effects of Interaction Between Surface Active Elements on the Surface Tension of Iron", Canadian Metallurgical Quarterly, Vol. 21, No. 4, 1982, pp. 393 - 403
- 126 Hsieh, R.I., Pan, Y.T., Liou, H.Y., "The Study of Minor Elements and Shielding Gas on Penetration in TIG Welding of Type 304 Stainless Steel", Journal of Materials Engineering and Performance, Vol. 8, No. 1, 1999, pp. 68 - 74
- 127 Mills, K.C., Keene, B.J., "Factors Affecting Variable Weld Penetration", International Materials Reviews, Vol. 35, No. 4, 1990, pp. 185 -216
- 128 Heiple, C.R., Roper, J.R., "The Geometry of Gas Tungsten Arc, Gas Metal Arc, and Submerged Arc Weld Beads", Welding: Theory and Practice, edited by D.L. Olsen, R. Dixon, and A.L. Liby, Elsevier Science Publ. B.V., 1990
- 129 Humenik, Jr., M., Whalen, T.J., "Physiochemical Aspects of Cermets", Cermets, Eds. Tinklepaugh, J.R., Crandall, W.B., Reinhold Publ., 1960
- 130 Lee, J., Morita, K., "Effect of Surface Active Element Sulfur on the Interfacial Energies Between Gas, Solid, and Molten Fe-C-S Alloys", in Steelmaking Conference Proceedings, Vol. 85, 2002, pp. 763 - 773
- 131 Martikainen, J.K., Moisio, T.J.I., "Investigation of the Effect of Welding Parameters on Weld Quality of Plasma Arc Keyhole Welding of Structural Steels", Welding Journal, Vol. 72, No. 7, 1993, pp. 329s – 340s
- 132 Wen, J., Lundin, C.D., "Technical Note: Surface Tension of 304SS Stainless Steel Under Welding Conditions", Welding Journal, Vol. 65, No. 5, 1986, p. 138s
- 133 Salter, G.R., Milner, D.R., "Gas-Metal Reactions in Arc Welding", British Welding Journal, Vol. 12, No. 5, 1965, pp. 222 - 228
- 134 Babiak, Z., Dudzinski, W., "Tungsten Carbide Stability in Plasma Weld Surfacing", Surfacing Journal International, Vol. 1, No. 3, 1986, pp. 87 – 90
- 135 Yan, M. *et al* "The Microstructure and Wear Resistance of Plasma-arc Remelted Ni-base Overlay", Journal of Materials Science Letters, Vol. 15, 1996, pp 2038-2041
- 136 Llewellyn, R., Tuite, C., "Hardfacing Fights Wear in Oil Sands Operation", Welding Journal, Vol. 74, No. 3, 1995, pp. 55-60
- 137 Dören, H., Wernicke, K., "Influence of Welding Parameters in Plasma-Arc Overlay Welding With Powder", Deutscher Verband für Schweisstechnik (DVS) - Berichte, Vol. 100, 1985, pp. 72 – 77

-
- 138 Herrströme, C., Hallén, H., Höganäs, Ait-Meckideche, A., Erlenbach, Lugscheider E., Aachen, "Factorial Analysis Applied to the PTA Process" in TS93: Thermal Spray Conference, Aachen, Germany, 3 – 5 March, 1993, pp. 409 – 412
- 139 Marimuthu, K., Murugan, N., "Prediction and Optimization of Weld Bead Geometry of Plasma Transferred Arc Hardfacing Valve Seat Rings", Surface Engineering, Vol. 19, No. 2, 2003, pp. 143 – 149
- 140 Deuis, R.L., Yellup, J.M., Subramanian, C., "Metal-Matrix Composite Coatings by PTA Surfacing", Composites Science and Technology, Vol. 58, No.2, 1998, pp. 299-309
- 141 Harris, P., Smith, B.L., "Factorial Techniques for Weld Quality Prediction", Metal Construction, Vol. 15, No. 11, 1983, pp. 661 – 666
- 142 Greenhut, V.A., Haber, R.A., "Ceramics, Ceramic-Metal Systems", Ullmann's Encyclopedia of Industrial Chemistry, Wiley-VCH Verlag GmbH & Co., Article Online Posting Date: June 15, 2000
- 143 Tinklepaugh, J.R. and Crandall, W.B., Cermets, Reinhold Publ., 1960
- 144 Llewellyn, R., Hurtubise, G., "The Use of Ceramics and Cermets for Wear Protection Applications in the Oil Sands Industry", in International Symposium on Advanced Ceramics for Structural and Tribological Applications, Vancouver, Canada, 1995, pp. 401 – 412
- 145 Harper, D., Gill, M., Hart, K.W.D., Anderson, M., "Plasma Transferred Arc Overlays Reduce Operating Costs in Oil Sands Processing", in International Thermal Spray 2002, Essen Germany, March, 2002
- 146 McKee, B., Wu, J.B.C., "An Overview of Wear-Resistant Alloys for the Mining Industry", CIM Bulletin No. 1012, Vol. 90, July-August, 1997, pp. 71 - 74
- 147 Hutchings, I.M., Tribology: Friction and Wear of Engineering Materials, Edward Arnold Publishing, 1992
- 148 Budinski, K.G., Surface Engineering for Wear Resistance, Prentice-Hall Publishing, 1998
- 149 Budinski, K.G., "Overview of Surface Engineering and Wear", ASTM STP 1278 - Effect of Surface Coating and Treatments on Wear, ASTM International Publ., 1996, pp. 4 - 21
- 150 Bradford, S.A., Corrosion Control, 2nd Ed., CASTI Publishing, ASM International, 2002
- 151 Llewellyn, R., "Resisting Wear Attack in Oil Sands Mining and Processing", CIM Bulletin No. 1012, Vol. 90, July-August 1997, pp. 75 - 82
- 152 Anderson, M., Chiovelli, S., Llewellyn, R., "The Use of Tungsten Carbide Materials for Oilsand wear Applications", in Thermal Spray 2003: Advancing the Science and Applying the Technology, ASM International, 2003, pp. 509- 518
- 153 Smith, W.F., Structure and Properties of Engineering Alloys, 2nd Ed., McGraw-Hill, 1993
- 154 Nestor, M.C., Nicoll, A.R., Erning, U., "Metals, Surface Treatment – 5. Thermal Spraying", Ullmann's Encyclopedia of Industrial Chemistry, Wiley-VCH Verlag GmbH & Co., Article Online Posting Date: June 15, 2000

-
- 155 Davis, J.R., "Hardfacing, Weld Cladding, and Dissimilar Metal Joining", ASM Handbook, Volume 6 - Welding, Brazing and Soldering, ASM International Pub., 1993
- 156 Anderson, M., Chiovelli, S., Reid, D., "Wear Resistant Materials for Use in the Oil Sands Hydraulic Transportation Process", in International Symposium on Materials for Resource Recovery and Transport, Calgary, Canada, 16 – 19 August, 1998, pp. 451 – 465
- 157 Merrick, S., Kotecki, D., Wu, J., "Surfacing", AWS Welding Handbook, Volume 4 Materials and Applications – Part 2, 8th ed., American Welding Society (AWS), 1998
- 158 Deuis, R.L., Bee, J.V., Subramanian, C., "Investigation of Interfacial Structures of Plasma Transferred Arc Deposited Aluminum Based Composites by Transmission Electron Microscopy" Scripta Materialia, Vol. 37, No. 6, 1997, pp. 721-727
- 159 Deuis, R.L., Subramanian, C., "Dry sliding wear behaviour at ambient and elevated temperatures of plasma transferred arc deposited aluminium composite coatings", Materials Science and Technology (UK), Vol. 16, No. 2, 2000, pp. 209-219
- 160 Baeslack III, W.A., Bucklow, I.A., Adson, D.J., "High Stress Abrasion Wear Testing of Chromium Boride/Stainless Steel and Tungsten-Vanadium-Carbide/Stainless steel Hard-facing Materials", TWI Journal (UK), Vol. 5, No. 1, 1996, pp. 79 - 114
- 161 Hidaka, K., Tanaka, K., "Characteristics of New Chromium Base Alloys for PTA Process", in Proceedings of the 1993 National Thermal Spray Conference, Anaheim, USA, 7 – 11 June 1993, pp. 391 - 196
- 162 Yamamoto, A., Hashimoto, Y., "New Surface Treatment Technology with a Plasma Transferred Arc Welding Process", Kobelco Technology Review, No. 20, 1997, pp. 34 – 38
- 163 Ayers, J.D., Bolster, R.N., "Abrasive Wear with Fine Diamond Particles of Carbide-Containing Aluminum and Titanium Alloy Surfaces", Wear, Vol. 93, No. 2, 1984, pp. 193 - 205
- 164 Deuis, R.L., Yellup, J.M., Subramanian, C., "Aluminum Composite Coatings Produced by Plasma Transferred Arc Surfacing Technique", Materials Science and Technology, Vol. 13, No. 6, 1997, pp. 511 – 522
- 165 Dehaut, P., Rochette, P., "Parametric Study of Plasma Transferred Arc Surfacing", in Advances in Thermal Spraying – ITSC '86 Eleventh International Thermal Spraying Conference, Montreal, Canada, 8 – 12 September, 1986, pp. 711 - 718
- 166 Matsuda, F., Nakata, K., Shimizu, S., Nagai, K., "Carbide Addition on Aluminum Alloy Surface by Plasma Transferred Arc Welding Process", Transactions of JWRI, Vol. 19, No. 2, 1990, pp. 81 – 87
- 167 Xibao, W., Hua, L., "Metal Powder Thermal Behaviour During the Plasma Transferred-Arc Surfacing Process", Surface and Coating Technology, Vol. 106, 1998, pp. 156 – 161
- 168 Xibao, W., Wenyue, Z., "The Theoretical Evaluation of Powders Transportation in Plasma Transferred-Arc Space Under Coaxial Powder Feeding Conditions", China Welding, Vol. 10, No. 2, 2001, pp. 104 – 110

-
- 169 Kamalyan, G.M., Alèksandryan, L.O., Davtyan, G.A., "A Study of the Possibility of Replacing Argon as a Shielding Gas with Nitrogen in Plasma Arc Surfacing", Avtomaticeskaya Svarka, No. 1, 1976, pp. 57 – 58
- 170 Wahl, W., Krauskopf, F., "Plasma-arc Powder Surfacing of Ferrous Materials", Welding Research Abroad, Vol. 40, No. 8, 1994, pp. 15 – 16
- 171 Hallen, H., Mathesius, H., Ait-Mekideche, A., Hettiger, F., Morkramer, U. and Lugscheider, E., "New application for high power PTA surfacing in the steel industry", in Proceedings of the International Thermal Spray Conference & Exposition, Orlando, USA, 28 May 5 June, 1992, pp. 899 – 902
- 172 Wlosinski, W., Mustafa, A.S., and Pikor, N., "Plasma Arc Hardfacing of Steel by Used Composites Powders" in Proceeding of the 6th International Conference on the Joining of Materials, Helsingor, Denmark, 5 - 7 April, 1993, pp. 229 - 233
- 173 Lugscheider, E., Oberländer, B. C., "A comparison of the properties of coatings produced by laser cladding and conventional methods", Materials Science and Technology, Vol. 8, No. 8, 1992, pp. 657 – 665
- 174 Araki, T., Nishida, M., Hirose, A., and Fujita, H., "Effects of Particle Size of Carbide Powder and Silica Sand on Abrasive Wear Resistance of an Overlay Composite Alloy", Welding International, Vol. 8, No. 1, 1994, pp. 23 - 29
- 175 Sasaki, K., Shimada, M., Kato, Y., Shinoda, T., "Improving Wear Resistant Characteristics of Surface Deposited by Plasma Transferred Arc", in Proceedings of the 1993 Thermal Spray Conference, Anaheim, USA, 7 - 11 June, 1993, pp. 385 - 389
- 176 Ueda, U., Notomi, A., "Method for Welding For Hard Surfacing", U.S. Patent 4,472,619, September 18, 1984
- 177 Owa, T., Shinoda, T., Kato, Y., "NiTi coatings produced by the transferred arc welding process and their wear characteristics", Welding International, Vol. 16, No. 4, 2002, pp. 276 – 283
- 178 d'Oliveira, A.S.C.M., Vilar, R., Feder, C.G., "High Temperature Behaviour of Plasma Transferred Arc and Laser Co-based Alloy Coatings", Applied Surface Science, Vol. 201, 2002, pp. 154 – 160
- 179 Bourithis, L., Milonas, A., Papadimitriou, G.D., "Plasma Transferred Arc Surface Alloying of a Construction Steel to Produce a Metal Matrix Composite Tool Steel With TiC as Reinforcing Particles", Surface and Coatings Technology, Vol. 165, 2003, pp. 286 - 295
- 180 Wu, W., Lung-Tien, W., "The Wear Behaviour Between Hardfacing Materials", Metallurgical and Materials Transactions A, Vol. 27A, No. 11., 1996, pp. 3639 - 36483
- 181 Baeslack III, W.A., Bucklow, I.A., Adson, D.J., "High Stress Abrasive Wear Testing of Chromium Boride/Stainless Steel and Tungsten-Vanadium-Carbide/Stainless Steel Hard-Facing Materials", TWI Welding Journal (UK), Vol. 5, No.1, 1996, pp. 79 - 114
- 182 Araki, T., Nishida, M., Hirose, A., Yano, K., Fujita, H., "Abrasive Wear Resistance of Overlay Composite Alloy with Addition of Carbide Powders", Transactions of the Japan Welding Society, Vol. 24 No. 2, 1993, pp. 74 - 80

-
- 183 Kammer, P.A., Weinstien, M., DuMola, R.J., "Characteristics and Applications for Composite Wear-Resistant Overlays" in Proceedings of the Fourth National Thermal Spray Conference, Pittsburgh, USA, 4 - 10 May, 1991, pp. 513 - 518
- 184 Ohriner, E.K., Wada, T., Whelan, E.P., Ocken, H., "The Chemistry and Structure of Wear Resistant, Iron-Base Hardfacing Alloys", Metallurgical Transactions A, Vol. 22A, No. 5, 1991, pp. 983 - 991
- 185 Iakovou, R., Bourithis, L., Papadimitriou, G., "Synthesis of Boride Coatings on Steel Using Plasma Transferred Arc (PTA) Process and its Wear Performance", Wear, No. 252, 2002, pp. 1007 - 1015
- 186 Kim, H.J., Kim, Y.J., "Wear and Corrosion Resistance of PTA Weld Surfaced Ni and Co Based Alloy Layers", Surface Engineering (UK), Vol. 15, No. 6, 1999, pp. 495 - 501
- 187 Yan, M., Zhang, X.B., Zhu, W.Z., "The Microstructure and Wear Resistance of Plasma-Arc Remelted Ni-base Overlay", Journal of Materials Science Letters, Vol. 15, No. 23., 1996, pp. 2034 - 2041
- 188 Hallen, H., Lugscheider, E., Ait-Mekideche, A., "Plasma Transferred Arc Surfacing with High Deposition Rates", in Proceedings of the Fourth National Thermal Spray Conference, Pittsburgh, PA, USA, 4 - 10 May, 1991. pp. 537 - 539
- 189 Lou, D., Hellman, J., Luhulima, D., Liimatainen, J., Lindroos, V.K., "Interactions Between Tungsten Carbide (WC) Particulates and Metal Matrix in WC-reinforced Composites", Materials Science and Engineering, Vol. A320, 2003, pp. 155 - 162